MANCHESTER 1824

The University of Manchester

Conversion of CO_2 by Plasma Catalysis and Thermal Catalysis

A thesis submitted to The University of Manchester for the degree of

Doctor of Philosophy

in the Faculty of Science and Engineering

2021

Shanshan Xu

Department of Chemical Engineering and Analytical Science

Table of Content

List of tables

List of figures

List of abbreviations

Abbreviation	Full name
DRM	Dry reforming of methane
NTP	Non thermal plasma
DRIFTS	Diffuse reflectance infrared Fourier transform spectroscopy
MS	Mass spectrometry
CO_2	Carbon dioxide
CO	Carbon monoxide
CH_4	Methane
CCS	Carbon capture and storage
CCU	Carbon capture and utilization
TGA	Thermogravimetric analysis
P2G	Power-to-gas
WHSV	Weight hourly space velocity
RWGS	Reverse water gas shift reaction
DBD	Dielectric barrier discharges
DFT	Density functional theory
OES	Optical emission spectroscopy
TOF	Turnover frequency
MOF	Metal-organic framework
LDHs	Layered double hydroxides
LDOs	Layered double oxide
EXAFS	Extended X-ray absorption fine structure
SEM	Scanning electron microscope
TEM	Transmission electron microscopy
HAADF-STEM	High-angle annular dark field scanning transmission electron microscopy

BET	Brunauer-Emmett-Teller
ICP-OES	Inductively coupled plasma optical emission spectrometer
GC	Gas chromatography
ToS	Time-on-stream
XRD	X-ray diffraction
TPR	Temperature programmed reduction
TCD	Thermal conductivity detector
FID	Flame ionisation detector
SIE	Specific input energy
WGSR	Water gas shift reaction
S-1	Silicalite-1
XPS	X-ray photoelectron spectra
B.E	Binding energy

Abstract

Catalytic conversion of CO_2 (*e.g.,* CO_2 hydrogenation and dry reforming of methane with CO_2, DRM) to valuable chemicals and fuels can be promising for addressing the issues associated with carbon emissions, benefiting the development of sustainable carbon cycling processes. The activation of CO_2 by the conventional thermocatalytic conversions remains challenging due to the high thermodynamic stability of CO_2. Non thermal plasma (NTP) can activate CO_2 effectively and subsequently convert the activated species over heterogeneous catalysts under mild conditions compared with thermal catalysis, known as NTP-catalysis. Catalysts are the key in both the thermal and the hybrid NTP catalytic systems regarding efficiency, selectivity and stability. This PhD project was focused on the catalysts and catalytic processes development for CO_2 hydrogenation and DRM, aiming at progressing the catalytic CO_2 valorisation technologies.

Specifically, the PhD project conducted (i) the development of supported Ru catalysts on MgAl layered double hydroxide for NTP-catalytic CO_2 hydrogenation; (ii) the mechanistic study of CO_2 hydrogenation over the Ru/MgAl catalysts under thermal and NTP conditions using *in situ* diffuse reflectance infrared Fourier (DRIFTS) coupled with mass spectrometry (MS) characterisation; (iii) the investigation of catalyst deactivation in CO_2 hydrogenation, especially due to CO poisoning, under thermal and plasma condition to show the intrinsic benefits of NTP activation compared to the thermal counterpart; and (iv) the development of the encapsulated Ni catalysts and study of the effect of their different properties (*e.g.*, metal dispersion and degree of encapsulation) on DRM reaction to provide rationales for further development of stable reforming catalysts for CO_2 and CH_4 co-conversion.

Declaration

I declare that this research is the result of my own work except as cited in the references and no portion of the work in the thesis has been submitted in support of an application for another degree or qualification of this or any other university or other institute of learning.

Copyright

Acknowledgements

First and foremost, I would like to express my deep and sincere appreciation to my both supervisors, Professor Christopher Hardacre and Dr Xiaolei Fan. Their knowledge, inspiration, and patience encourage me to overcome all the difficulties and finish my PhD project. They gave me so much support and understanding on my research work. Every insightful discussion on my experimental design and results inspired me so much and their advice is of great value for me. Their enthusiasm for scientific research encourages me to pursue a highly qualified research career.

My sincere thanks also go to my internal examiners, Professor Arthur Garforth, in my first and second year of PhD. His thoughtful discussion and useful advice help me a lot in my work.

I feel very lucky and happy to be part of the group, and I am very appreciated for the help from my lovely colleagues: Cristina, Adam, Xiaoxia, Helen, Lan, Terri, Huanhao, Rebecca, Min…I am deep indebted to Dr Sarayute Chansai for giving me plentiful guidance and help in my study. He is always so nice, dedicated and patient.

I am grateful to the technicians at the Department of Chemical Engineering and Analytical Science Dr Desmond Doocey, Miss Gemma Chapman, Mrs Shahla Khan, Mr Loris Doyle for their helps and assistances during my PhD.

Thanks all my friends for their company and support. They give me so many beautiful and happy memories during my life.

I am so grateful to the Dean's Doctoral Scholar Awards from the University of Manchester for the financial support for my study.

Last but not the least, I would like to thank my parents and younger brother. I would never be me without their love, encouragement and understanding. I love you!

Chapter 1 Background, motivation and achievements

1.1 Background

In recent years, due to growing energy demand and industrial activities, fossil fuels, such as the coal, petroleum and natural gas, are being consumed on an unprecedented scale, which lead to the significant emission of carbon dioxide (CO_2) [1, 2]. The global CO_2 concentration in the atmosphere has increased from ~270 ppm in the preindustrial age to ~416.47 ppm in May, 2020 [3], leading to the catastrophic consequences including the global warming, serious climate changes and the associated energy and environmental issues. Thus, many concepts including carbon capture and storage (CCS) and utilization (CCU) have been proposed and explored to address the issue of CO_2 emission [4, 5]. Catalytic conversion of CO_2 to renewable and valuable chemicals and fuels (*i.e.,* CO_2 as a C1 building block) is a method to reduce CO_2 emission and contributes to the development of sustainable low-carbon economy [6]. Especially, catalytic CO_2 hydrogenation and CO_2 reforming with methane (*i.e.,* DRM) have been regarded as the promising routes for potential practical CO_2 conversion [7]. The former, also known as "Sabatier reaction", reduces CO_2 using H_2 into methane, whilst the latter reaction reforms CO_2 and CH_4 to produce syngas.

Theoretically, CO_2 conversion is challenging due to the high thermodynamic stability of the linear CO_2 molecule. Typically, high temperatures and/or pressures are required to activate CO_2 under conventional thermal conditions which are associated with high energy demand and cause catalyst deactivation [8]. Specifically, under the thermal conditions, catalysts suffered from deactivation problems due to metal sintering, coking and poisoning. For common Ni based reforming catalysts, metal sintering and carbon formation during DRM at high temperatures (*e.g.,* 700 °C) can lead to the rapid catalyst deactivation [9]. Previous study also shows that small amounts of CO in the feed could deactivate the catalysts and contribute to a significant decrease of CO_2 conversion due

to CO poisoning under the thermal conditions [10]. Therefore, developing highly active and stable catalysts is still challenging for progressing catalytic CO_2 conversion technologies towards practical applications.

In addition to the traditional thermal catalysis, several alternative technologies have been proposed for CO_2 conversion, such as electro-, photo- and plasma-catalysis [11-13]. Among these, hybrid non-thermal plasma (NTP) and catalysis systems, that is, NTP-catalysis, enables the activation of stable CO_2 molecular and promote catalytic CO_2 conversions at relatively mild bulk temperatures and atmospheric pressure in comparison with the conventional thermal catalysis, being promising for energy-efficient conversion of CO_2 [14].

In NTP-catalysis, catalysts play an important role in the hybrid system regarding efficiency and selectivity. However, the current catalysts used in NTP-catalysis are still those which have been designed for thermal catalysis, and the relevant investigation on the design principles regarding this aspect are still lacking. Previous studies have shown that the intrinsic properties of the catalysts including the active metal species, metal particle size and dispersion and location of active sites, and catalyst supports are the dominant factors for the performance of NTP-catalysis [15]. However, the correlation between the structure, composition and activity of the catalysts in the hybrid system is still largely unknown, which hinders the rational design cost-effective, highly selective and efficient catalysts bespoke for NTP-catalysis.

The NTP-catalysis system is highly complex including, not exhaustively, plasma discharge, ionisation/activation of molecules, adsorption/desorption process, surface reaction, species collisions, species transport in/between the gas and solid phase [16, 17]. In the presence of a catalyst, the electric field can be enhanced associated with the formation of surface discharge, benefiting CO_2 activation in multiple surface reactions, thus lowering the reaction barriers and altering the reaction pathways of the catalysis. However, both chemical and physical effects are intertwined, and hence being challenging to be fully decoupled. Therefore, further understanding the mechanism of

NTP-catalytic CO_2 conversion is also urgently required to advance the technology.

The research in this PhD project was dedicated to the development of catalytic CO_2 conversion technologies, that is, CO_2 hydrogenation and DRM, with special focus on mechanistic understanding of the catalysis. Firstly, CO_2 hydrogenation under thermal and NTP conditions were comparatively studied, and the relevant mechanisms were investigated using in situ diffuse reflectance infrared Fourier transform spectroscopy–mass spectrometry (DRIFTS–MS), which can contribute to the rational design of the efficient and effective catalysts for the NTP-catalysis. The mechanisms of catalyst deactivation in CO_2 hydrogenation, especially due to CO poisoning, were also investigated under both thermal and NTP conditions, which advanced our understanding of the nature of catalysts deactivation in the hybrid system, being significant to move the development towards the real-world applications for CO_2 conversions. Since the stability and longevity of the catalysts are important factors under both thermal and NTP conditions, zeolite-encapsulated Ni catalysts with different configurations regarding the metal dispersion, degree of encapsulation and metal-support interaction were further designed and evaluated for DRM reaction, paving the way to further development of stable catalysts for CO_2 conversion.

1.2 Thesis structure

The main aims of this PhD project are to (i) design highly efficient catalyst for CO_2 hydrogenation and demonstrate the application of NTP-catalysis system for CO_2 conversions, (ii) perform comparative study of the mechanism of CO_2 hydrogenation and related catalyst deactivation under thermal and NTP conditions to provide some guidance on designing suitable catalysts and developing mature catalysis systems for practical CO_2 utilization, and (iii) develop high active and stable catalyst for DRM reaction to mitigate metal sintering and coking deposition, especially at high reaction temperatures. This PhD thesis is presented in journal format and follows the thesis

submiss ion guidelines approved by The University of Manchester*. The brief summary of the content to be presented in each chapter is summarised below:

Chapter 2 reviews the state-of-the-art of widely studied catalytic processes for CO_2 conversions, including CO_2 hydrogenation and CO_2 reforming with methane. The general knowledge of plasma technology and associated plasma-catalysis for CO_2 hydrogenation are also discussed briefly.

Chapter 3 presents the development of the Ru/MgAl layered double hydroxide (LDH) catalysts and comparative study of CO_2 hydrogenation over the catalysts under thermal and NTP conditions. LDH was found to facilitate chemisorption and activation of CO_2 and the unsaturated active sites on the surface can promote the metal dispersion, being beneficial to be employed as catalyst supports in CO_2 conversions. The Ru/MgAl LDH catalysts enabled significantly higher CO_2 conversions (~85%) and CH_4 yield (~84%) at relatively low temperatures under the NTP conditions as compared with the thermally activated counterpart. Regarding the catalyst preparation, the reduction temperature can affect the physical and chemical properties of catalysts, and thus altering the activity of the catalysts in NTP-driven catalytic CO_2 hydrogenation. Comparative *in situ* DRIFTS-MS characterisation of the catalysis was carried out under thermal and plasma conditions, which established the alternative pathways for CO_2 hydrogenation in NTP-catalysis.

Chapter 4 presents the crucial effect of intrinsic properties of catalyst, such as surface area and metal dispersion, on CO_2 conversion under both thermal and NTP condition. Then, a comparative study of CO poisoning of the supported Ru catalyst was performed under the thermal and NTP conditions and demonstrate the advantage of the hybrid NTP-catalysis system over the thermal counterpart to mitigate CO poisoning of the

* http://documents.manchester.ac.uk/display.aspx?DocID=7420

catalyst. Specifically, in the thermal catalysis, the catalyst suffered from a significant decrease of CO_2 conversion and deactivation due to strong CO adsorption and associated metal sintering, whilst in the NTP-catalysis, the collisions of active species in NTP-catalysis dynamically removed the strongly adsorbed carbon species, leading to the recovery of the additional active sites for CO_2 adsorption. Thus, the catalyst showed the comparatively good stability and regenerability under the NTP conditions.

Chapter 5 examines the proof-of-concept of developing a novel class of catalysts with the feature of spatially confined/encapsulated metal nanoparticles in zeolite's framework by different methods. Such design can potentially prevent aggregation and deactivation of metallic species during DRM, however, the nature of catalysts developed by different methods is crucial in preventing metal sintering and coking formation at high reaction temperatures. In detail, the developed Ni@SiO_2-S1 catalyst by seed-directed synthesis method showed the complete encapsulation of Ni in its structure and the comparatively best catalytic performance with stable CO_2 and CH_4 conversions of ~80% and ~73%, respectively, during 28 h on stream evaluation. Conversely, the catalysts developed by the post treatment and direct hydrothermal methods promoted the incomplete encapsulation of Ni, being prone to deactivate due to the presence of Ni phases on their external surface. The findings show clearly that the full encapsulated Ni in the support with small Ni particle sizes and strong metal-support interactions in the Ni@SiO_2-S1 catalyst could protect Ni aggregation and inhibit coke formation during DRM.

Chapter 6 concludes all the experimental results and findings and provides the recommendations for future work.

1.3 Achievements

This PhD research has led to research outputs, including peer-reviewed journal

publications and national/international conference presentations, as summarised below.

1.3.1 Peer-reviewed publications

1. S. Xu, H. Chen, C. Hardacre, X. Fan, Non-thermal plasma catalysis for CO_2 conversion and catalyst design for the process, *Journal of Physics D: Applied Physics*, DOI: 10.1088/1361-6463/abe9e1.

2. S. Xu, S. Chansai, S. Xu, C. Stere, Y. Jiao, S. Yang, C. Hardacre, X. Fan, CO Poisoning of Ru Catalysts in CO_2 Hydrogenation under Thermal and Plasma Conditions: A Combined Kinetic and Diffuse Reflectance Infrared Fourier Transform Spectroscopy–Mass Spectrometry Study, *ACS Catalysis*, 2020, 10 (21), 12828-12840.

3. S. Xu, S. Chansai, Y. Shao, S. Xu, Y. Wang, S. Haigh, Y. Mu, Y. Jiao, C. Stere, H. Chen, X. Fan, C. Hardacre, Mechanistic Study of Non-Thermal Plasma Assisted CO_2 Hydrogenation over Ru Supported on MgAl Layered Double Hydroxide, *Applied Catalysis B: Environmental*, 2020, 268, 118752.

Publications not included in this thesis:

1. H. Chen, Y. Mu, S. Xu, S. Xu, C. Hardacre, X. Fan, Recent advances in non-thermal plasma (NTP) catalysis towards C1 chemistry, *Chinese Journal of Chemical Engineering* 2020, 28 (8), 2010-2021.

Publications under preparation:

1. S. Xu, et al. Silicalite-1 encapsulated Ni nanoparticles prepared by different synthesis methods as sintering-/coking-resistant catalysts for dry reforming of methane.

1.3.2 Presentations

1. September 2020, CO Poisoning of Ru Catalyst in CO_2 Hydrogenation under Thermal and Plasma Conditions **(Oral)**, 11th International Conference on Environmental Catalysis, Manchester, UK.

2. January 2020, Non-thermal Plasma assisted CO_2 Hydrogenation on Ru supported on the MgAl Layered Double Hydroxide **(Oral)**, 6th UK Catalysis Conference, Loughborough, UK.

3. September 2019, Non-thermal Plasma assisted CO_2 Hydrogenation on Ru supported on the MgAl Layered Double Hydroxide (**Oral**), The 26th Annual SCI-CSCST Conference, London, UK.

4. August 2019, Non-thermal plasma assisted catalytic methanation of CO_2 (**Oral**), EuropaCat 2019, Aachen, Germany.

5. January 2019, Preparation of graphene-supported Pd catalysts for the selective hydrogenation of acetylene **(Poster)**, 5th Catalysis Conference, Loughborough, UK.

6. May 2018, Palladium nanoparticles supported on graphene as highly active catalysts for the selective hydrogenation of acetylene **(Poster)**, CEAS PGR Conference, Manchester, UK.

1.3.3 Awards

1. International Conference Bursaries 2019 from RSC

2. Rideal Travel Bursary 2019 from SCI.

Chapter 2 Overview

This chapter consists of the published content in Journal of Physics D: Applied Physics, DOI: 10.1088/1361-6463/abe9e1. Permission obtained from IOP Publishing to use the manuscript of the paper in this thesis.

2.1 CO_2 mitigation and utilization

Energy production and utilization from the carbonaceous fossil fuels has contributed to the unprecedented development of human civilization. However, this comes with enormous pressure on the natural carbon cycle, which has been changed significantly due to the increasing CO_2 emission from fossil fuel burning [2]. Consequently, the CO_2 concentration in the atmosphere reached ~416.47 ppm in May 2020, an increase of ca. 54% compared with that of preindustrial age, leading to global warming, severe climate change and related energy and environmental issues [3]. The 2019 UN Climate Action Summit announced that 77 countries, 10 regions and over 100 cities aimed to achieve net zero carbon emission by 2050 to prevent the global temperature from rising by more than 1.5 °C. Carbon capture, storage (CCS) and utilization (CCU) technologies are proposed as promising approaches to address the issue of CO_2 emission [18]. As an important part of CCU, catalytic conversion of CO_2 as a renewable carbon source for producing value-added chemicals and fuels such as syngas, hydrocarbons and oxygenates (alcohols and dimethyl ether) contributes to alleviating climate change impact and offers good opportunities for sustainable development in the cyclic C-economy. Specifically, among the catalytic conversions of CO_2, CO_2 hydrogenation and CO_2 reforming with methane have been identified as the promising approaches for potential large-scale utilization of CO_2.

Since CO_2 molecule is thermodynamically and chemically stable, it is challenging and energy-demanding to activate CO_2, where a high energy input of 5.5 eV/molecule is

required to break the chemical bond of CO_2 [19]. Currently, different technologies including thermal-, electro-, photo- and plasma-chemical processes have been investigated for CO_2 conversion [20]. Among these, non-thermal plasma (NTP) activation of catalysts (in which plasma discharge dissociates reactant molecules in the gas phase and contributes to surface reactions) shows the great potential in activating and converting stable CO_2 molecules into value-added fuels and chemicals under comparatively mild conditions [21]. Therefore, in this chapter, we will first focus on the application of thermal- and plasma-catalysis system for CO_2 conversions. Then, the strategy on the development of suitable catalysts for CO_2 conversions will be proposed.

2.2 Thermal-catalytic CO_2 conversion

2.2.1 CO_2 hydrogenation

CO_2 hydrogenation provides the prospect of highly desirable routes for recycling CO_2 into fuels and chemicals. The hydrogenation of CO_2 at atmospheric pressure yields mainly CH_4 (*i.e.*, CO_2 methanation, Eq. 2.1), and/or CO (*via* the reverse water-gas shift reaction, RWGS, Eq. 2.2). CO_2 methanation (*i.e.,* Sabatier reaction) is considered important in the "power-to-gas" (P2G) concept [22]. Typically, P2G concept consisted of two processes: (a) hydrogen (H_2) production by water electrolysis (using the electricity generated from sustainable pathways such as solar energy and hydropower) and (b) subsequent hydrogenation of CO_2 (captured from various industrial sources such as biogas and flue gas) into CH_4 [23]. Therefore, CO_2 hydrogenation is the crucial reaction to determine the effectiveness and efficiency of P2G process. Catalytic CO_2 methanation is thermodynamically favourable ($\Delta H^0_{298K} = -164.94$ kJ mol^{-1}) at low temperatures, however, it suffered from kinetic limitation due to the high stability of CO_2 molecule [24]. Additionally, the RWGS reaction can occur at high temperatures (*e.g.,* > 450 °C), and thus inevitably producing by-product of CO with the reduced selectivity to CH_4. Therefore, the main challenge for CO_2 methanation is to develop

suitable catalyst and systems for improving the reaction rate and selectivity at low temperatures (< 300 °C). Accordingly, metal catalysts such as supported Ni, Ru, and Rh catalysts have been intensively investigated for CO_2 hydrogenation, showing relatively high CO_2 conversions (e.g., >70%) and selectivity to CH_4 (e.g., >94%) at temperature of >300 °C (as shown in Table 2.1) [25].

$$CO_2 + 4H_2 \rightarrow CH_4 + 2H_2O \qquad \Delta_r H^0_{298\ K} = -164.94\ kJ\ mol^{-1} \qquad \text{Eq. 2.1}$$

Table 2.1 Performance of thermal catalytic CO_2 methanation over different catalysts.

Catalyst	WHSV[a] ($mL\ g_{cat}^{-1}\ h^{-1}$)	Temperature[b] (°C)	CO_2 Conv. (%)	CH_4 Sel. (%)	Ref.
10% Ni/CeO_2	10,000	340	88	94.8	[26]
10% Ni/TiO_2	60,000	350	73.2	–	[27]
15%Ni-La/MgAl	12,000	350	78	98	[28]
10% $Ni/MgAl_2O_4$	15,000	350	87	99	[29]
3% Ru/ZrO_2	20,000	250	73	~100	[30]
$RhNi/Al_2O_3$	48,000	300	95	>90	[31]
5% Ru/Al_2O_3	150,000	300	32	94	[32]
5% Ru/CeO_2		300	83	99	
20% Co/KIT-6	22,000	300	51	98.9	[33]

[a]WHSV: weight hourly space velocity; [b]all at atmospheric pressure.

In addition to CH_4, selective hydrogenation of CO_2 to methanol is another potentially profitable process for CCU, since methanol is an important chemical feedstock in the synthesis of chemicals such as formaldehyde, acetic acid, dimethyl ether (DME). Methanol is also considered as a gasoline substitute for combustion engines. From the thermodynamic point of view, low temperatures and high pressures are favorable for methanol formation direct from CO_2 hydrogenation. Currently, on an industrial scale, methanol is mainly produced by catalytic reaction from syngas (Eq. 2.4) produced from steam methane reforming, while CO_2 is introduced to consume excess H_2 to balance the C/H ratio (Eq. 2.2). The heterogeneous catalyst of $Cu/ZnO/Al_2O_3$ is employed by

industry for methanol synthesis at elevated pressures (50–250 bar) and temperatures (200–350 °C) [4] [34]. Under this reaction pathway, several million tons of CO_2 are converted into methanol each year [2]. In addition, the pathway for methanol synthesis *via* direct hydrogenation of CO_2 (Eq. 2.3) has also been demonstrated to occur during the industrial process. Regarding the direct CO_2 hydrogenation to methanol, commercially used catalysts based on Cu/ZnO are not suitable as the catalysts are prone to deactivate caused by the produced water during the reaction [35]. Therefore, further development of efficient catalysts with high stability is needed for CO_2 hydrogenation to methanol.

$$CO_2 + H_2 \rightarrow CO + H_2O \qquad \Delta_r H^0_{298\,K} = +41.2 \text{ kJ mol}^{-1} \qquad \text{Eq. 2.2}$$

$$CO_2 + 3H_2 \rightarrow CH_3OH + H_2O \qquad \Delta_r H^0_{298\,K} = -49.4 \text{ kJ mol}^{-1} \qquad \text{Eq. 2.3}$$

$$CO + 2H_2 \rightarrow CH_3OH \qquad \Delta_r H^0_{298\,K} = -90.4 \text{ kJ mol}^{-1} \qquad \text{Eq. 2.4}$$

2.2.2 Dry reforming of methane

Catalytic carbon dioxide reforming of methane, *i.e.,* DRM, converts two major greenhouse gases into syngas (Eq. 2.5). This reaction is highly endothermic, and hence high temperatures (600–1000 °C) and low pressures are preferred to encourage the reaction. Additionally, the H_2/CO molar ratio from DRM is approximately 1, but the simultaneous occurrence of RWGS reaction (Eq. 2.2) can consume hydrogen, leading to the relatively high CO_2 conversion (as compared with CH_4 conversion) and the H_2/CO ratio of <1. Supported nickel catalysts are promising candidates to be used for DRM reaction in large-scale industrial application due to their good catalytic activities, high availability and low cost as compared with noble metal catalysts [36]. However, it is well-known that the major limitation for DRM is the rapid deactivation of the catalysts during the reaction which caused by (i) metal particle sintering at high reaction temperatures (*e.g.,* 700 °C) and (ii) carbon deposition induced by methane

decomposition (Eq. 2.6) and Boudouard reaction (*i.e.,* CO disproportionation, Eq. 2.7) [37, 38]. Therefore, developing sinter- and coke-resistant nickel-based catalysts remains a main challenge for DRM in the potential practical applications. Various strategies have been proposed to address this challenge including (i) improving Ni dispersion and reducing the particle sizes [39], (ii) developing bimetallic catalysts and using promoters [40], and (iii) encapsulation of metal nanoparticles (NPs) within unique architectures to form the core-shell or yolk-shell structures [41]. For example, Ni-noble metal (*e.g.,* Pt, Ru and Rh) bimetallic catalysts contribute to the high activity and good carbon resistance for DRM, which can be attributed to a higher Ni dispersion, improved reducibility of nickel and surface reconstruction [42, 43]. Ni encapsulated in a thermal stable shell (*i.e.,* core-shell) catalysts have been demonstrated to prevent metal agglomeration and protect the active phase from carbon deposition, leading to good stability during DRM reaction for more than 100 h [44].

$$CO_2 + CH_4 \rightarrow 2CO + 2H_2 \qquad \Delta_r H^0_{298\ K} = +247.3\ kJ\ mol^{-1} \qquad \text{Eq. 2.5}$$

$$CH_4 \rightarrow C(s) + 2H_2 \qquad \Delta_r H^0_{298\ K} = +75\ kJ\ mol^{-1} \qquad \text{Eq. 2.6}$$

$$2CO \rightleftharpoons CO_2 + C(s) \qquad \Delta_r H^0_{298\ K} = -172\ kJ\ mol^{-1} \qquad \text{Eq. 2.7}$$

2.3 Non-thermal plasma (NTP) catalysis for CO_2 conversion

2.3.1 Plasma type

A plasma is a fully or partially ionised gas and is considered as the fourth state of matter. In this state, at least one electron is unbound, creating positively charged ions. In addition to the charged ions, large amounts of neutral species such as atoms, molecules, radicals and excited species are also present in the plasma. Hence, plasma is a highly reactive chemical environment for various potential applications [19].

Table 2.2 Classification of plasma [45].

Plasma	State	Example
High temperature plasma (Equilibrium plasma)	$T_e \approx T_i \approx T_g \approx Tv = 10^6 – 10^8$ K $n_e \geq 10^{20}$ m^{-3}	Laser fusion plasma
Low temperature plasma		
Thermal plasma (Quasi-equilibrium plasma)	$T_e \approx T_i \approx T_g \leq 2\times10^4$ K $n_e \geq 10^{20}$ m^{-3}	Arc plasma, plasma torches, RF inductively coupled discharge
Non thermal plasma (Non-equilibrium plasma)	$T_e >> Tv > T_i \approx T_g = 300 – 10^3$ K $n_e \approx 10^{10}$ m^{-3}	Glow discharge, Corona, DBD, Microwave discharge, Atmosphere plasma jet

T_e: electron temperature, T_v: temperature of vibrationally excited molecules, T_i: ion temperature, T_g: gas temperature, and n_e: electron density.

Plasmas can be divided into high-temperature plasma (or fusion plasma) and low-temperature plasma, which is shown in Table 2.2 [45]. For high temperature plasma, all the species (electrons, ions, and neutral species) are typically in a thermal equilibrium state with a high temperature of 10^6–10^8 K. Low temperature plasma is further subdivided into thermal plasma and non-thermal plasma (NTP). The species in thermal plasma is under a quasi-equilibrium, *i.e.,* local thermodynamic equilibrium state at a temperature of $\leq 2\times10^4$ K. By contrast, NTP is a non-equilibrium system, in which the electrons have a higher temperature than the heavy particles (*e.g.,* ions and neutral species). The high electron temperature can be attributed to the small mass of the electrons, allowing them to be accelerated by the electric fields, whereas the heavy particles are not easily accelerated. Hence, the temperature order in NTP is: $T_e >> Tv > T_i \approx T_g$. Accordingly, the electron temperature is in the order of 1 eV (~10 000K), while the gas temperature remains close to room temperature [20].

There are several advantages for the technology based on NTP: (i) it enables to activate and dissociate ground-state gas molecules to generate various active species, allowing reactions to occur at relatively mild bulk temperatures and atmospheric pressure, (ii) it is flexible for the electric field to be switched on and off, beneficial to scale-up and

regulate the power consumption and (iii) it is easy to pack the catalyst into the reactors, combining the advantage of NTP and catalysis. Different types of NTP have been investigated and reported in the literature, such as the dielectric barrier discharges (DBD), microwave (MW) discharge, corona and glow discharge [46]. Among these, DBD reactor is a typical configuration of non-thermal plasma, which consists of two plane-parallel or concentric metal electrodes and dielectric barrier between them [47]. A gas flow is applied between the discharge gap. After the discharge is ignited, the electric field is high enough to cause breakdown of the gas molecular. The dielectric barrier prevents the formation of sparks and/or arcs. Therefore, the simple configuration of DBD reactor and ambient operating conditions (*i.e.,* at atmospheric pressure and low temperatures) make the effective and efficient conversion of CO_2 at scales possible [48]. Therefore, in this chapter, we will specifically focus on the NTP-catalytic CO_2 conversions using DBD reactors.

2.3.2 CO_2 hydrogenation

CO_2 hydrogenation with molecular H_2 can produce a range of chemicals including CO, CH_4, hydrocarbons and oxygenates (methanol, dimethyl ether, ethanol, etc) under NTP conditions. Conversion of CO_2 to CO *via* RWGS reaction and CH_4 *via* CO_2 methanation under NTP conditions has been investigated [49, 50]. Zhu *et al* [51] studied the effect of a plasma on RWGS over a Au/CeO_2 catalyst. Therein, the plasma enabled a CO_2 conversion of ~25.5% which was higher than the thermodynamic equilibrium value of ~22% at 400 °C. As compared with the conventional thermal catalysis, NTP-catalysis can create high concentrations of reactive species which improves the CO_2 methanation rate and CH_4 yield at low operating temperatures [52]. For example, Biset-Peiró *et al* [53] compared catalytic CO_2 methanation over a $Ni\text{-}CeO_2/Al_2O_3$ catalyst under thermal and NTP conditions. A CO_2 conversion of 70% and CH_4 selectivity of 96% were achieved under NTP conditions (at ~150 °C), whereas under thermal conditions, a temperature in excess of 350 °C was required to achieve a similar performance. Similar

results were reported by other studies as well [54]. In NTP-catalysis, highly reactive species contribute to CO_2 methanation, for example, vibrationally excited CO_2 can adsorb on the catalyst surface to lower the energy barrier as compared with the ground-state CO_2 and facilitate the formation of reactive intermediates on the catalyst surface [55]. Conversely, in thermal catalysis, CO_2 needs to be adsorbed and activated by the catalyst surface before surface reactions can take place, leading to the need for high temperatures [56]. Additionally, the NTP-induced excited states of other reactive species such as CO, OH and CH radicals in the gas phase can also readily interact with the catalyst to promote relevant surface reactions [57, 58].

In addition to CO and CH_4, hydrocarbons and oxygenates, especially methanol, are valuable fuel substitutes and key feedstocks for a wide range of products such as polymers, solvents, and drugs. Catalytic CO_2 hydrogenation to hydrocarbons and methanol under thermal conditions is usually conducted at elevated temperatures (200–300 °C) and pressures (30–300 bar) [59], thus the integration of plasma with catalysts to enable these conversions efficiently under mild conditions is important. Lan *et al* [60] reported that Co/ZSM-5 catalysts promoted hydrocarbon formation with a C_2-C_4 selectivity of 13.7% at 45.0% CO_2 conversion under NTP. CO_2 hydrogenation to methanol under NTP conditions was explored by Eliasson and co-workers [61]. Therein, the methanol yield/selectivity was enhanced by a factor of >10 by coupling NTP with a commercial $CuO/ZnO/Al_2O_3$ catalyst at ~100 °C compared with the results under NTP only condition. Recently, Wang *et al* [62] presented a significant improvement of CO_2 hydrogenation to methanol (*i.e.,* 14% CO_2 conversion and 53.7% methanol selectivity) using a specially designed DBD reactor with a water-cooled electrode (as shown in Figures 2.1a and b). This setup efficiently removed the heat generated by Joule heating and the reaction exothermicity to maintain the NTP system at ~30 °C. In this work, the catalytic performance of the Pt/γ-Al_2O_3 and Cu/γ-Al_2O_3 catalysts was investigated, as shown in Figures 2.1c, in which Cu/γ-Al_2O_3 presented a relatively good catalytic performance (*i.e.,* 21.2% CO_2 conversion and 11.3% methanol yield), showing

that both plasma reactor and catalyst design can affect the catalysis under NTP conditions. However, it is obvious that CO_2 hydrogenation to methanol is still some way from a practical application due to the relatively low CO_2 conversion and methanol yield (<50%). Therefore, the development of highly active and selective catalysts, as well as the optimisation of the NTP reactor design, is necessary to further improve NTP enabled catalytic CO_2 conversion to methanol. Men *et al* [63] prepared a highly dispersed Pt/film/In_2O_3 catalyst *via* the plasma-assisted peptide-assembly method and used it for the NTP-assisted CO_2 hydrogenation, which achieved a high CO_2 conversion of ~37% with a methanol selectivity of ~62.6% due to the high Pt dispersion.

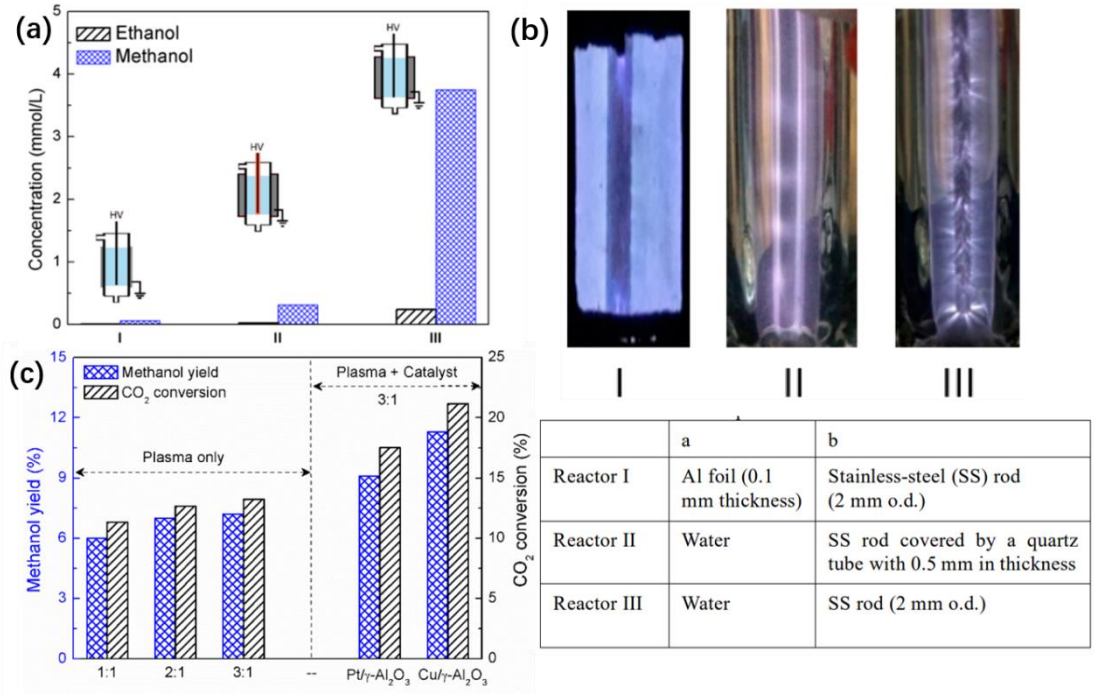

	a	b
Reactor I	Al foil (0.1 mm thickness)	Stainless-steel (SS) rod (2 mm o.d.)
Reactor II	Water	SS rod covered by a quartz tube with 0.5 mm in thickness
Reactor III	Water	SS rod (2 mm o.d.)

Figure 2.1 (a) The influence of DBD reactor configurations on CO_2 hydrogenation to methanol under NTP conditions. (b) Images of H_2/CO_2 discharge generated in different DBD reactors. (c) Effect of H_2/CO_2 molar ratio and catalysts on the reaction performance. Reprinted from ref.[62].

2.3.3 Dry reforming with methane

For DRM, activation of CH_4 molecule is also energy intensive (600–1100°C) due to the stable C-H bands (E_{diss} = 4.5 eV) [64]. From the thermodynamic point of view, DRM

cannot occur at low temperatures because of the endothermic characteristic of the reaction [65]. Alternatively, NTPs can activate the catalysts at ambient conditions without the issues of coke formation and metal sintering experienced by the thermal catalysis [66]. The target product of DRM is syngas, but hydrocarbons can also be produced [67, 68], depending on the selectivity of the catalyst, as well as other process parameters. For example, the reaction selectivity was found to be sensitive to the gas composition [69], with a CH_4-rich feed contributing to high selectivity towards hydrocarbons, whilst the CO_2-rich feed increased the CO selectivity [70].

NTP combined with a suitable catalyst can tune the reaction selectivity towards the valuable hydrocarbons and liquid oxygenates. For example, the selectivity of DRM to C_2 to C_4 hydrocarbons was enhanced over NaX zeolite catalysts under NTP conditions [69]. Similarly, Vakili *et al* [71] reported that the combination of NTP with the UiO-67 metal organic framework (MOF) facilitated the formation of C_2H_2 and C_2H_4, whereas the Pt/UiO-67 catalyst decreased the selectivity to hydrocarbons by ~30% due to the dehydrogenation process on the Pt surface. Recently, Wang *et al* [72] demonstrated the one-step synthesis of liquid chemicals/fuels including acetic acid, methanol, ethanol and formaldehyde from NTP-assisted DRM (as shown in Figure 2.2) by careful selection of the catalysts and operation parameters. The NTP only system promoted the formation of oxygenates (selectivity of 59.1%) with acetic acid as the major product. In contrast, by varying the catalysts within the DBD reactor, the distribution of liquid products could be tuned due to the presence of both gas-phase and plasma-assisted surface reactions. For example, the Cu/γ-Al_2O_3 catalyst increased the selectivity to acetic acid to ~40.2% as compared with the plasma system with the γ-Al_2O_3 packing (~20.2%). Conversely, supported noble metal catalysts (*i.e.,* Au/γ-Al_2O_3 and Pt/γ-Al_2O_3) produced the formaldehyde under NTP conditions, suggesting that the nature of the catalysts is crucial for the NTP-catalysis (as shown in Figure 2.2b). Optical emission spectral (OES) characterisation of the NTP-catalysis system showed the presence of CO, CH, CH_3, CO_2, CO_2^+, OH and H_a as potential key species in the NTP-activated

DRM. Therefore, the possible reaction pathways on the catalyst surface for producing oxygenates were proposed, as shown in Figure 2.2c, which demonstrated the effect of the NTP-assisted surface reactions on the distribution of liquid products. This study confirmed that NTP combined with heterogeneous catalysts can provide selective pathways to value-added products which cannot be achieved by the NTP only condition.

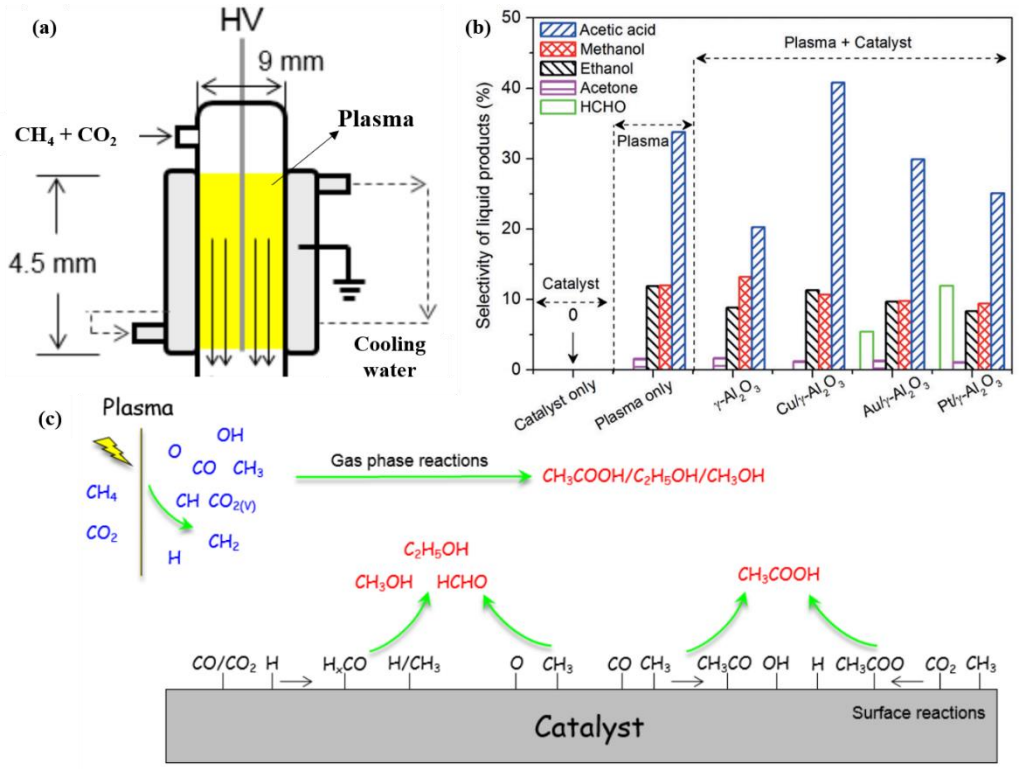

Figure 2.2 (a) The reactor configuration for one-step plasma-assisted DRM for producing liquid chemicals/fuels. (b) Selectivity to oxygenates and (c) possible reaction mechanisms for the formation of CH_3COOH, CH_3OH, C_2H_5OH and HCHO using NTP-catalysis. Reprinted from ref.[72].

2.3.4 Mechanism of plasma-catalysis

As compared with the conventional thermal activation, NTP activation of catalysts shows the great potential in activating and converting stable CO_2 molecules into value-added fuels and chemicals under comparatively mild conditions. However, NTP-catalysis system is highly complex and require further understanding to advance the technology. Specifically, the catalysts have been demonstrated to enhance the local

electric field, affect the plasma discharge type and form microdischarges in porous catalysts, while the plasma may modify the catalysts including their microscopic structure, metal dispersion and chemical state (as shown in Figure 2.3) [17]. Additionally, the interplay between catalyst and plasma-induced active species can be divided into (i) adsorption processes including the adsorption of neutral species, charge carriers and surface charging, and (ii) surface reaction processes including photon-induced surface reactions and collision-induced surface reactions [57]. A higher adsorption ability and a lower activation barrier were observed in the case of plasma-induced vibrationally excited molecules due to the increasing energy of the reactants compared with the ground state, which may promote the subsequent surface reactivity [73, 74]. The presence of free electrons and ions, *i.e.,* free charges in the plasma state could also improve the synergy of plasma catalysis by affecting the bond breaking and formation processes on the catalyst surface. For example, Jafarzadeh *et al* [75] investigated the effect of plasma-induced electrons on the adsorption and activation of CO_2 on titania-supported Cu_5 and Ni_5 clusters by using spin-polarised and dispersion-corrected density functional theory (DFT) calculations. It was found that the electrons affected the adsorption process by shifting the antibonding states of CO_2 towards the valence band, increasing the polarisation effects and changing the adsorption site of CO_2, which lead to improved stabilisation of dissociated CO_2 on the catalyst surface. On the catalyst surface, in addition to the electrons, plasma-produced photons may also induce electronic excitations, which in turn initiate catalytic surface reactions (*i.e.,* photocatalysis). The plasma-induced photocatalysis has been proposed for catalytic VOC abatement over TiO_2, in which 3.2 eV was required to excite an electron in anatase TiO_2 [76]. However, other studies demonstrated that the photocatalytic effect was negligible in the plasma catalysis [77, 78]. Currently, the role of radiation in the NTP-catalytic CO_2 conversions has not yet been reported. Therefore, further research on the effect of photons on the plasma-catalytic systems is still needed. In the collision-induced surface reactions, some energy may be delivered from the vibrational/electronically excited species, and/or impinging photons and electrons to

overcome the surface reaction barrier, thus lowering the activation barrier for surface reactions. On the catalyst surface, the surface reactions were demonstrated to proceed *via* Langmuir-Hinshelwood or Eley-Rideal reaction mechanisms [79]. Therefore, developing a suite of *in situ* techniques for NTP-catalysis are required to provide the fundamental insights into the behaviors of the reactive species in the gas phase and/or on the catalytic surface for the reactions.

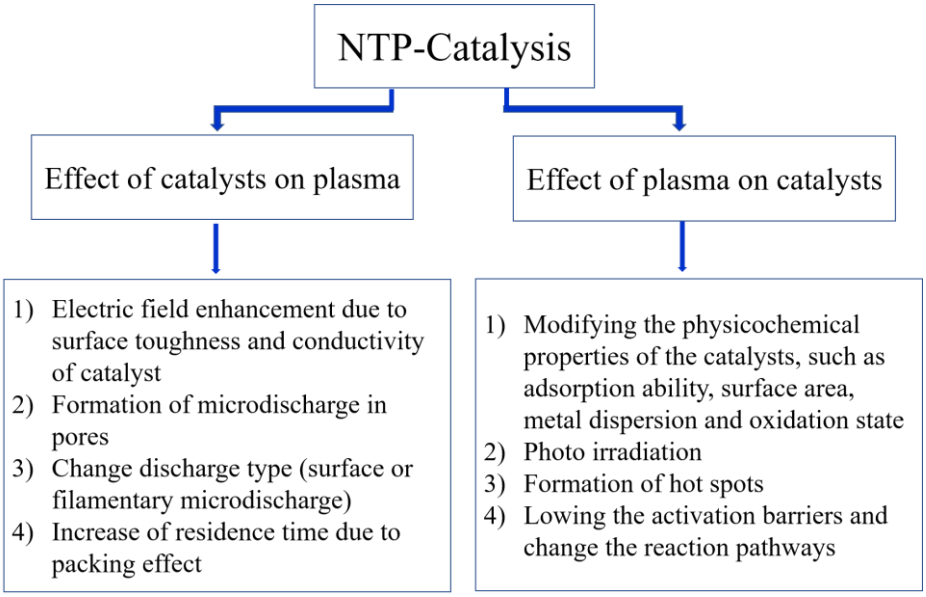

Figure 2.3 The overview of the various effects of the catalyst on the plasma and of the plasma on the catalyst.

Optical emission spectroscopy (OES) is an important technique to identify, in situ, the reactive species in the gas phase which can facilitate an understanding of the relevant reaction mechanisms. Various activated species such as H radicals, CO, CH, OH, C, CHO, CO_2 and CO_2^+ are detected in NTP-assisted CO_2 hydrogenation, confirming that the plasma can activate relevant molecules for catalysis [54, 56]. OES detection also revealed the direct collisions of the reactive gas species with the adsorbed species on the catalyst surface, showing the presence of the Eley-Rideal mechanism [56]. Since in NTP-catalysis, reactions occur simultaneously in the gas-phase and on the catalyst surface, decoupling the contribution of the gas phase reactions from the surface reactions can be highly beneficial in understanding the mechanism of NTP-catalysis,

though it is highly challenging.

Although OES can provide valuable information on the reactive species in the gas phase, direct measurements of the surface reactions on the microscopic scale under NTP conditions are also valuable. Thus, direct operando observation of catalyst structures regarding the evolution and the formation of active surface species using *in situ* techniques has been performed to elucidate and understand the catalysis under NTP. Azzolina-Jury *et al* [80] employed a microsecond time-resolved FTIR spectroscopy to study the intermediates of plasma-activated CO_2 hydrogenation over the Ni-USY catalysts. The findings showed that NTP-induced partial dissociation of CO_2 (to CO) contributed to the gas phase reactions, whilst, on the catalyst surface, the adsorption of vibrationally excited CO_2 contributed to the formation of formates, which was further hydrogenated into carbonyls species. They also found that CO in the gas phase can adsorb on the Ni surface to form the reactive intermediates for CO_2 hydrogenation, demonstrating the existence of multiple pathways under the NTP condition. Recently, a DRIFTS technique (as shown in Figure 2.4) was developed by Stere *et al* [81] for NTP-catalysis to probe the dynamics of the surface species and intermediates on the catalyst surface, including selective catalytic reduction of NO_x [82], WGS [83], CO_2 hydrogenation [84] and DRM [71], which provided valuable information on the explanation of the possible mechanisms and reaction pathways using NTP-catalysis. By combining in situ DRIFTS with the mass spectrometry (MS) study, Chen *et al* [85] confirmed the co-existence of Langmuir-Hinshelwood and Eley-Rideal mechanisms in NTP-catalytic CO_2 hydrogenation, *i.e.* both the surface reactions (between the adsorbed species) and interactions between the adsorbed and gas phase species contributed to the formation of CH_4. *In situ* DRIFTS of the plasma-activated DRM over the Ni/Al_2O_3 catalyst with La as a promotor also found that the vibrational states of CH_4 and plasma-induced CO_2 activation contributed to the improved performance of NTP-catalysis [86]. Specifically, plasma could facilitate CO_2 activation to produce 1.7-fold enhancement for surface carbonate formation on La as compared with the thermal activation. The

surface reaction between CH_x* and carbonates species promoted the improved CH_4 conversion in the plasma-assisted DRM.

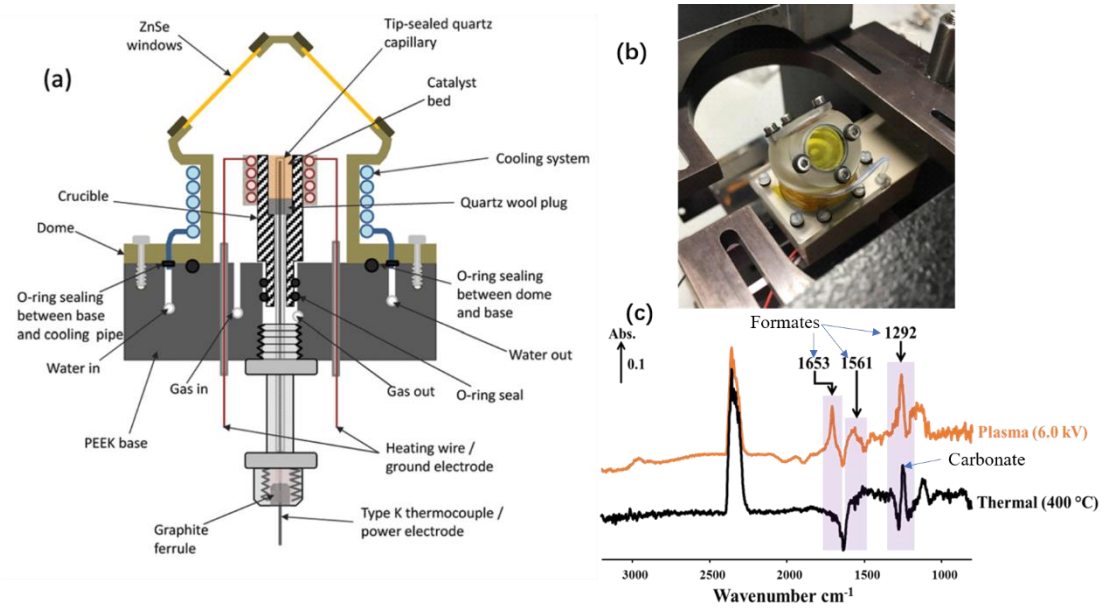

Figure 2.4 (a-b) Schematic and photograph of in situ plasma flow cell for DRIFTS study. Reprinted from ref.[81]. (c) Comparison of in situ DRIFTS spectra of CO_2 hydrogenation over 15Ni-20La/Na-BETA catalyst under the NTP and thermal condition. Reprinted from ref. [85].

Kinetic studies are also a useful experimental method to understand the NTP-catalyst interactions, which allows the understanding of the effect of relevant variables, such as discharge power, reactant concentration and catalysts, on the chemical reaction (*e.g.,* reaction rate and activation barrier) in order to maximise the efficiency of the hybrid system. The pioneering work by Kim *et al* [87] on the kinetic evaluation of CH_4 activation over the Ni catalyst in a thermal-DBD plasma hybrid reactor, as shown in Figure 2.5, established the correlation between the reaction rate and input power for calculating the activation energy of the NTP-catalysis. Subsequently, a comparative kinetic study of CO_2 hydrogenation (over Ni@SiO_2) under thermal and plasma activation was performed [88], showing that the activation energy of the NTP-catalysis was estimated to be ~29 kJ mol^{-1}, which was significantly lower than that of the thermal catalysis (~80 kJ mol^{-1}). These findings suggested that NTP activation can lower the activation barrier required to initiate the catalysis.

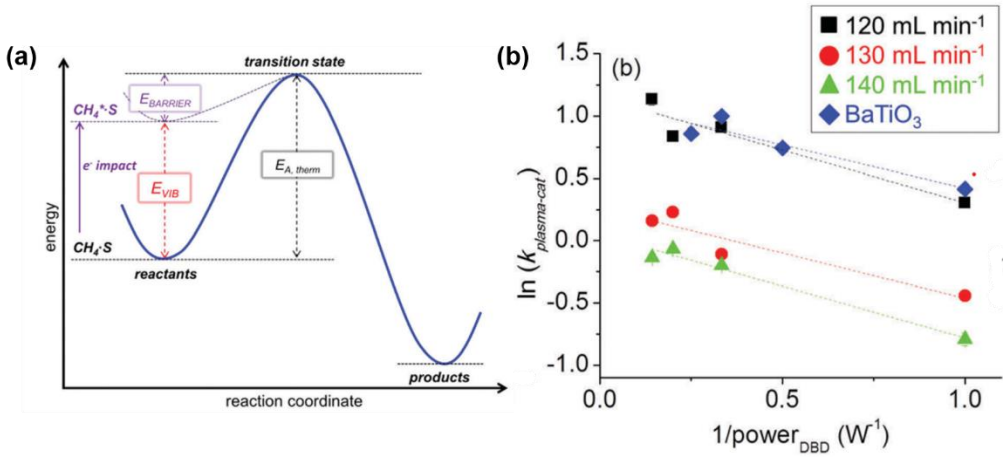

Figure 2.5 (a) Progress of thermal and plasma-assisted catalysis requiring energies of $E_{A,therm}$ and $E_{BARRIER}$ to reform CH_4 species at 790–890 K, respectively. (b) Logarithmic reaction rate constant (ln $k_{plasma-cat}$) vs. 1/power$_{DBD}$ under different reaction environments (unit of reaction rate constant is $s^{-1}kPa^{-1}$). Reprinted from ref.[87].

In summary, *in situ* characterisation is crucial for NTP-catalysis, as it will allow us to (i) identify the critical steps of surface reactions, (ii) understand the catalyst changes during NTP-catalysis, and (iii) establish ideal NTP conditions that optimally exploit the NTP-catalysis. Therefore, further development and implementation of *in situ* measurements coupling plasma and catalysts are significant to progress our understanding of NTP-catalysis.

2.4 Catalysts design for CO_2 conversion

As discussed above, catalysts play an important role in both thermal and plasma systems regarding efficiency and selectivity. Thus, developing suitable catalysts is critical to optimise the systems for CO_2 conversion, making it more competitive and economically attractive for practical applications. Currently, the catalysts used in NTP-catalysis are still those which have been designed for thermal catalysis. And the relevant investigation and fundamental design principles regarding this aspect are still lacking. Therefore, in this section, the recent progress of the catalysts used for thermal catalytic

CO_2 conversion will be briefly discussed first, then a strategy for designing specific heterogeneous catalysts for NTP-catalysis will also be proposed.

2.4.1 Catalysts for thermally activated CO_2 conversion

Under thermal conditions, the group 8–10 metals (*e.g.,* Ru, Rh, Pd, Ni, Co) have been demonstrated to be efficient for CO_2 conversion, as shown in Table 2.1 [89, 90]. Ni-based catalysts are the most widely used catalysts for CO_2 conversion due to their cost-effectiveness and high activity. However, the main issue of the Ni-based catalysts is their stability, especially at high reaction temperatures, because the Ni catalysts are prone to deactivation due to carbon deposition and metal sintering. Ni particle sintering can reduce the metal surface area and overall CO_2 adsorption capacity, and hence leading to the deactivation (of the Ni/AlO_x catalyst) [8]. In comparison, the Rh- and Ru-based catalysts are relatively stable and show a higher activity than the Ni-based counterparts. However, their limited availability and relatively high price make them less attractive for applications at a large scale. Recently, efforts have been made to study the influence of the metal particle size and dispersion on the catalyst performance in order to develop more efficient catalysts for CO_2 conversion [91]. For example, Guo *et al* [92] investigated the effect of Ru particle size (*i.e.,* Ru single atoms, nanoclusters (~1.2 nm) and nanoparticles (~4 nm)) of the Ru/CeO_2 catalysts on CO_2 hydrogenation. Compared with Ru single atoms, the nanoclusters and nanoparticles showed weaker metal-support interactions, thus promoting the activation process; however, they showed higher H spillover, thus inhibiting the removal of H_2O from the catalyst surface. The trade-off of these two factors led to the nanoclusters achieving the highest activity at 190 °C with a turnover frequency (TOF) of 7.41×10^{-3} s^{-1} and 98–100% selectivity to CH_4. Similarly, the correlation between product selectivity and Ru particle size was studied by Kwak *et al* [93] and Yan *et al* [94]. It was revealed that Ru single atoms tended to form CO via RWGS, whereas Ru nanoclusters and nanoparticles favoured the production of CH_4. Regarding Ni catalysts, well dispersed Ni particles are beneficial

for the efficient conversion of CO_2 to CH_4. For example, Ni nanoparticles of 2.7–4.7 nm (confined in the cage-type mesopores of SBA-16) enabled strong adsorption of CO_2 and high catalytic rates in CO_2 hydrogenation [95]. Moreover, it has been demonstrated that controlling the size of Ni NPs below 7 nm could effectively inhibit coke deposition and, thereby, affects the catalytic activity in DRM [96]. For example, a Ni single-atom catalyst dispersed on hydroxyapatite was prepared by co-precipitation method and applied for DRM, showing a high activity and stability for 100 h with negligible carbon deposition [97]. High Ni dispersion can be achieved by using porous catalyst supports, such as structured silica, zeolite and MOFs, with high surface areas and/or micro-/meso-porosity structures [98]. Additionally, porous supports could confine the metal particles inside the pores/channels, preventing metal aggregation and coking formation. For example, Ni confined on the surface of dendritic mesoporous silica was used as the catalyst for DRM, presenting good activity (76% CH_4 conversion at 700 °C) and stability (145 h) [99].

Surface properties of the catalyst support are also very important because (i) the support-metal interactions can tune the property of metals such as reducibility of metal species, metal dispersion and particle size and (ii) the basicity/acidity and the oxygen vacancy can influence CO_2 adsorption. Different supports including Al_2O_3 [100], SiO_2 [101], TiO_2 [102], ZrO_2 [30], CeO_2 [103] and zeolites [104] have been applied to prepare catalysts for CO_2 conversion. Lin *et al* [105] found that Zr doping of the Ni/Al_2O_3 catalysts can improve the Ni dispersion and the reducibility of the Ni phase, thus promoting CO_2 hydrogenation at low temperatures of <300 °C. Le *et al* [106] investigated CO_2 methanation over the supported Ni catalyst on various supports with the activity found to be in the following order: $CeO_2 > ZrO_2 > SiO_2 > Al_2O_3 > TiO_2$. The high catalytic activity of the Ni/CeO_2 catalyst was attributed to the small Ni particle size, as well as the presence of oxygen vacancy, which facilitated CO_2 chemisorption and activation [107]. Operando diffuse reflectance infrared Fourier transform spectroscopy (DRIFTS) studies of CO_2 hydrogenation over the Ru/CeO_2 (with oxygen

vacancy) and Ru/Al_2O_3 (without oxygen vacancy) catalysts showed that the oxygen vacancy in CeO_2 facilitated the dissociation of formate species for CH_4 formation [108]. Additionally, mechanistic investigation of CO_2 hydrogenation over the Ni/CeO_2 catalysts by Cárdenas-Arenas *et al* [109] and Ye *et al* [26] also showed that, in these catalysts, the existence of both Ni^0 sites (for H_2 dissociation) and Ce^{3+} sites (for CO_2 adsorption and activation) was important to enable the selective CO_2 conversion to CH_4. Therefore, developing the next-generation catalysts with highly dispersed metal active sites, a large surface area and enhanced CO_2 adsorption is important to improve the thermal catalytic CO_2 conversion at low temperatures [22]. An understanding of structure-composition-activity correlation in thermal catalysis will provide useful guidance for the NTP-catalysis system in designing highly selective catalyst to improve the performance of the hybrid system.

2.4.2 Role of metal active sites in NTP-catalytic CO_2 conversion

In thermal catalysis, reactions occur only on the catalyst surface, and the highly dispersed catalysts on appropriate supports can convert CO_2 effectively. In contrast, in plasma-catalysis, the combination of gas phase and surface reactions, the complex interactions between plasma and catalysts such as the plasma discharge properties, transport of reactive species and modification of catalyst by plasma are coupled to one another, all affecting the performance of the hybrid system.

Table 2.3 summarises the performance of various supported metal catalysts in NTP-assisted CO_2 hydrogenation. Clearly, combination of plasma and catalysis can effectively improve CO_2 conversion. CO_2 hydrogenation over the Cu/Al_2O_3, Mn/Al_2O_3 and $Cu\text{-}Mn/Al_2O_3$ catalysts was carried out, showing the enhanced CO_2 conversion by 6.7%–36% as compared with the NTP only system [110]. As found for the thermal systems, Ru and Ni catalysts have been widely used for CO_2 hydrogenation under NTP and showed improved CO_2 conversions (generally >50%) compared with that achieved by plasma only systems. Other metals, such as Pt, Pd, Co, Fe and Cu, have also been

explored for NTP-catalytic CO_2 hydrogenation. Oshima *et al* [111] investigated Pt, Pd, Ni, Fe and Cu metals supported on La-ZrO_2 for NTP-activated CO_2 hydrogenation, in which the noble metals showed higher CO_2 conversions than using transition metal catalysts. It was also found that the Pt, Pd, Fe and Cu catalysts for CO_2 hydrogenation were selective to CO, whilst the Ni catalysts were CH_4 selective [50, 112]. Additionally, the Ni particle size and dispersion were also found to affect the catalyst performance. Liu *et al* [113] investigated CO_2 hydrogenation over Ni/La_2O_3 catalysts as a function of the calcination temperature from 600 to 900 °C. A maximum CO selectivity of 78% was achieved with the Ni/La_2O_3 catalyst calcined at 600 °C, which was due to the small Ni particle size (~7.3 nm) and high Ni dispersion achieved under the specific preparation condition.

NTP can facilitate catalyst preparation, resulting in the formation of small and highly dispersed metal nanoparticles on the support [114]. For example, H_2 plasma reduction was used to prepare the Pd, Pt, Ag and Au supported on SBA-15 catalysts, which showed the improved activity in catalytic CH_4 conversion to value-added fuels [115]. Characterisation of these catalysts confirmed that the plasma treatment resulted in high metal dispersions, e.g. the particle sizes of Pd, Pt and Au were 6, 2 and 6 nm, respectively, which were able to fit into the ordered SBA channels (average diameter of 7.6–8.5 nm). Benrabbah *et al* [50] compared the effect of thermal and H_2 plasma reduction on the preparation of Ni/$CeZrO_2$ catalysts for plasma-catalytic CO_2 hydrogenation, showing that the catalysts reduced by H_2 plasma resulted in a strong interaction between Ni and ceria, thus leading to a higher CO_2 conversion (~80%) at low power (~5W) than the catalysts reduced by the thermal treatment (at 470 °C). These studies demonstrate that it is promising to employ the plasma reduction process to prepare the highly dispersed metal catalysts *in situ* for NTP-catalysis.

Table 2.3 Comparison of NTP-assisted catalytic CO_2 hydrogenation over different catalysts.

Catalysts	DBD Power (W)	WHSV (mL g_{cat}^{-1} h^{-1})	CO_2 Conv. (%)			CO_2 rate (mol s^{-1} g^{-1}, $\times10^{-3}$)	CH_4 yield (%)	Ref.
			NTP only	Catalyst thermal[a]	NTP + Catalyst			
6% Ru/γ-Al_2O_3	33	18,625	8.2	0.01 (25°C)	23	0.06	21	[54]
2% Ru/UiO-66	13	–	22	–	41	–	39	[116]
2.8%Ru@UiO-66	13	6,000	20	–	72	0.11	69	[117]
15% Ni/$Ce_xZr_{1-x}O_2$	>13	20,000	–	–	80	0.26	76	[50]
10% Ni/γ-Al_2O_3	15–18	20,000	9	2 (150°C)	60	1.5	59	[56]
Ni/La_2O_3	90	18,000	52	–	97	–	45	[113]
NiFe/$MgAlO_x$	12	12,000	–	76 (250°C)	73	0.08	–	[118]
8% Cu/γ-Al_2O_3	35	2,076	7.5	–	8	0.01	0.7	[110]
8% Mn/γ-Al_2O_3	35	2,076			10	0.02	0.76	
2% Pd/ZnO	30	3,600	19.8	1.5 (230°C)	32.5	0.18	–	[112]
2%Pd/SiO_2	30	3,600			25.3	0.14	–	
1% Pt/La-ZrO_2	5.6	60,000	18	–	41	7.8	–	[111]
1% Pd/La-ZrO_2	3.5	60,000			31	5.7	–	
1% Fe/La-ZrO_2	4.1	60,000			27	5.0	–	

[a]Catalyst thermal: CO_2 conversions achieved by catalysts activated under thermal conditions at different temperatures for comparison.

2.4.3 Role of catalyst supports in NTP-catalytic CO_2 conversion

Properties of the catalyst support (*e.g.,* morphology, dielectric property and pore structures) are important in NTP-catalysis as they affect the metal dispersion, adsorption/desorption properties and plasma discharge. A summary of Ni catalysts supported on various supports for NTP-catalytic CO_2 hydrogenation is presented in Table 2.4.

Table 2.4 Comparison of the performance of CO_2 hydrogenation over Ni-supported on various supports in DBD reactors under NTP conditions.

Catalysts	DBD Power (W)	WHSV (mL g_{cat}^{-1} h^{-1})	CO_2 Conv. (%)			CH_4 selectivity (%)	CH_4 yield, (%)	Ref.
			NTP only	Catalyst thermal	NTP+ Catalyst			
15Ni-CeO_2/Al_2O_3	15–40	40,000	3	4 (250°C)	70	96	67	[53]
15Ni/$Ce_{0.1}Zr_{0.9}O_2$	1–3	50,000	–	0 (280°C)	80	99.7	79.8	[119]
15Ni-TiO_2/Al_2O_3	–	1100	13	5 (220°C)	50	–	–	[120]
15Ni/UiO66	1–3	30,000	5	5 (200°C)	85	99	84.2	[84]
15Ni/CZ/SBA-15	–	20,000	–	<1 (200°C)	80	99	79	[121]
15NiLa/Na-BETA	1–3	23,007	10	0 (200°C)	84	97	81	[85]
NiCe/Cs-USY	35	40,000	<5	20 (250°C)	79	98	77	[122]

2.4.3.1 Catalysts supported on metal oxides

γ-Al_2O_3 is the most common support used for NTP-assisted CO_2 conversion due to its relatively high surface area (~150 m^2 g^{-1}) and high stability [56]. However, the acidic nature of γ-Al_2O_3 suppresses CO_2 adsorption, and hence CO_2 conversion over the catalysts supported on γ-Al_2O_3 is relatively low in NTP-catalysis. For example, in the NTP-assisted DRM, the Ni/γ-Al_2O_3 catalyst achieved a CO_2 conversion of 26.2% and CH_4 conversion of 44.1% [123], and in NTP-catalytic CO_2 methanation (as shown in Table 2.3), only 23% CO_2 conversion was achieved by the Ru/γ-Al_2O_3 catalyst [54]. Catalyst supports with basic sites and oxygen vacancies have also been explored for NTP-catalytic CO_2 conversion. For example, Nizio *et al* [119, 124] developed Ni catalysts supported on $CeZrO_2$ with different Ce/Zr ratios for the NTP-assisted CO_2 hydrogenation. The highest CO_2 conversion of ~80% and CH_4 selectivity of ~95% was achieved when the Ce/Zr ratio was 1.40. In these catalysts, ceria acted as an oxygen

reservoir, which promoted the adsorption of CO_2 and subsequently produced CO and O active species with the assistance of plasma. Recently, hydrotalcite-derived/supported metal catalysts showed potential in C1 chemistry due to their compositional flexibility, good thermal stability and basic properties, which facilitated chemisorption and activation of CO_2 [125]. Additionally, the coordinatively unsaturated active sites in hydrotalcite such as the steps, edges and corner atoms can also promote the metal dispersion, favouring the catalysis [126]. Therefore, hydrotalcite-supported catalysts are promising catalysts for NTP-assisted CO_2 conversion, particularly CO_2 hydrogenation and DRM.

2.4.3.2 Catalysts supported on zeolites

Zeolites have been widely used for heterogeneous catalysis due to their uniform micropores, high surface area, tunable acidities and high thermal stabilities [127]. Zeolite also have the ability to spatially confine the reactions, thus preventing the aggregation and deactivation of metallic species[128]. Zeolite-supported Ni catalysts have been explored for CO_2 hydrogenation under the NTP conditions. Bacariza *et al* [122] evaluated the NTP-assisted CO_2 methanation over a Ni/USY zeolite catalyst and investigated the effect of Si/Al ratio and Ce addition on the catalytic performance. It was found that a higher Si/Al ratio could lead to lower affinity towards water, reducing the inhibiting effect of H_2O on the catalyst activity for CO_2 methanation. The addition of Ce as promoter in the Ni/USY catalyst favoured CO_2 activation and improved the dielectric constant of the catalyst (ε_r = 24 for CeO_2 versus ε_r = 1.5–5 for zeolites), leading to high CO_2 conversions (~70%) and CH_4 yields (~75%). Chen *et al* [85] investigated the performance of BETA zeolite supported Ni catalysts in the NTP-assisted catalytic CO_2 hydrogenation. It was found that, as compared with H-form BETA, Na-form BETA benefits CO_2 adsorption, which can be further improved by La doping.

Additionally, the effect of porous catalysts on the plasma discharge properties also

deserves attention. Both experimental and modelling studies showed that the pore structure of catalysts can intensify the electric field due to the formation of strong micro-discharges [129]. A two-dimensional fluid model predicted that plasma could be formed and penetrate the pores with the pore diameter greater than the Debye length (typically >2 μm) [130]. On the other hand, the lifetime of the plasma-induced reactive species is short, ranging from a few nanoseconds (for electronically excited atoms/molecules) to microseconds (for radicals) [131]. Thus, the plasma-induced reactive species may lose their energy due to collisional quenching before participating into surface reactions. Accordingly, the diffusion of the short-lived reactive species to the active sites is a key parameter in determining the efficiency of plasma-catalysis, and an understanding of the diffusion mechanisms within the porous network of the catalysts is necessary for NTP-catalysis [132]. Recently, Chen *et al* [15] investigated how the catalyst structure, for example the location of the active sites and support pore structures, affects the diffusion of the reactive species and the catalytic performance in CO_2 hydrogenation by designing a series of Ni supported on silicalite-1 (with different pore structures) catalysts (as shown in Figure 2.6). Specifically, at low input energy, the availability of NTP-reduced reactive species in the gas phase is limited, thus they prefer to interact with the exposed Ni active sites on the external surface of the catalysts with less diffusion resistance. Conversely, at high input energy, the abundant existence of the reactive species enables diffusion into the pore of the zeolite and allows interactions with the highly dispersed active sites. Thus, catalysts with a hierarchical meso-micro-porous network and the associated highly dispersed Ni species may benefit the accessibility of the short-lived reactive species towards Ni active sites, leading to the relatively high CO_2 conversion of ~75%. This work demonstrated that the intrinsic nature of catalysts (*e.g.,* the pore structure, metal dispersion and the location of active sites) plays a key role in NTP-catalysis, and the development of catalysts with highly dispersed and easily accessible metal sites may benefit NTP-catalysis towards practical applications.

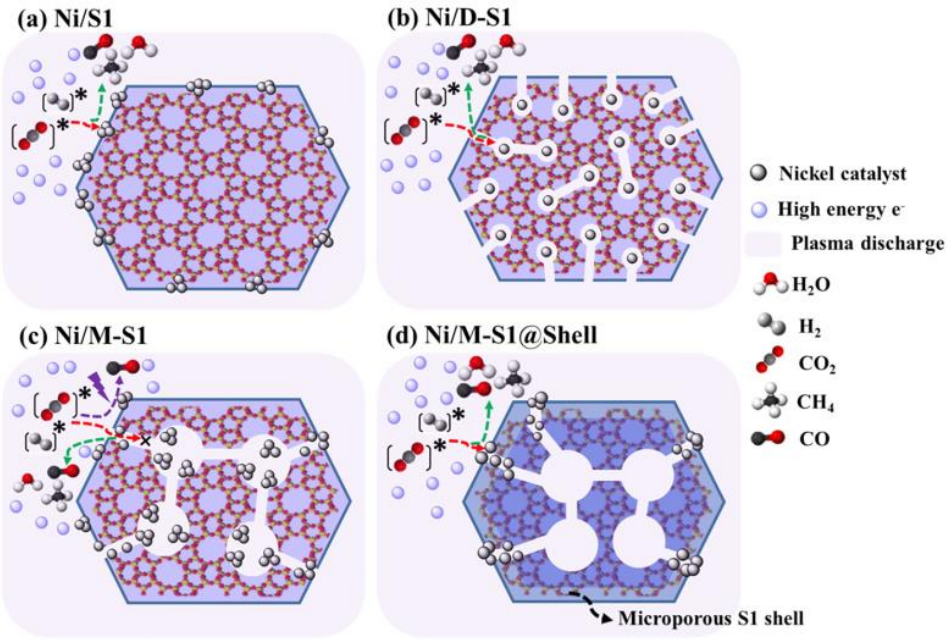

Figure 2.6 Mechanistic scheme of catalysts with different pore structures for NTP-assisted CO_2 hydrogenation. Reprinted from ref.[15].

2.4.3.3 Catalysts supported on MOFs

MOFs have exceptionally high specific surface areas, structure diversity and tailorability, tunable pore size distribution and confined microenvironment, which enable flexible catalyst design by allowing active guest species to be anchored into their pores/cages/channels [133]. However, under thermal conditions, catalysts based on MOFs are often unstable. This can potentially be solved using NTP activation. In addition, it is well known that MOFs have much stronger CO_2 adsorption capacities than other materials, such as zeolites and silica, which inspired the development of MOF-based catalysts for CO_2 fixation and conversion under NTP conditions [134]. Chen *et al* [84] developed Ni supported on UiO-66 catalysts for catalytic CO_2 hydrogenation under NTP conditions. The turnover frequency of the NTP-catalysis system had a nearly two-fold improvement as compared with the thermal catalysis (1.8 s^{-1} *vs.* 0.06 s^{-1}) and the structure of the catalyst showed insignificant change after 20 h testing, confirming that a high stability of the MOF-based catalyst under NTP conditions could be achieved. Vakili *et al* [71] investigated the performance of the

Pt@UiO-67 catalyst in the plasma-assisted DRM. Therein, it was found that, in addition to the high stability of the catalyst, the high surface area and the porous structure of UiO-67 also favoured the formation of micro-discharges on catalyst surface, improving the conversion of CH_4 and CO_2 by 18% and 10%, respectively. These studies demonstrated the potential of the MOF-based catalysts to improve NTP catalysis, as well as the use of NTP activation to sustain the MOFs-based catalysts activity. However, to date, the bespoke design of the MOFs-based catalysts for NTP-assisted CO_2 conversions and relevant mechanistic understanding are lacking, which requires further investigation.

2.4.3.4 Promoter modified supported catalysts

The addition of promoters such as alkali and rare earth metal oxides to metal-supported catalysts has been shown to be effective in improving the metal dispersion and reducibility as well as the acid/base properties of the catalysts, resulting in enhanced activity and stability of catalysts under thermal activation [135-137]. Accordingly, relevant research on the evaluation of promoter modified catalysts in plasma-catalytic CO_2 conversions was conducted, as shown in Table 2.5. Khoja *et al* [68] found that the La-promoted Ni/$MgAl_2O_4$ catalysts improved CO_2/CH_4 conversion to 84.5% and 86%, respectively, in the NTP-assisted DRM. Similarly, Chen *et al* [85] developed La-promoted Ni/Na-BETA zeolite catalysts for CO_2 hydrogenation, which showed improved CO_2 conversion (in comparison with the Ni/Na-BETA zeolite catalyst) under NTP conditions. Ray *et al* [138] compared the performance of the MgO- and CeO_2-promoted Ni/γ-Al_2O_3 catalysts for the NTP-assisted DRM. The results showed that the MgO-promoted catalyst had the smallest particle size (~12 nm) and the highest surface area (~201 m^2 g^{-1}) with a uniform distribution of Ni on the surface of the catalyst, leading to better catalytic performance with 34.7% and 13% conversions of CH_4 and CO_2, respectively, as compared with the NTP system with Ni/γ-Al_2O_3. In comparison, the CeO_2-promoted catalysts provided the oxygen vacancy for CO_2 activation, resulting

in the improved anti-carbon deposition property and maximum selectivity to CO. The effect of the promoters depends on their distribution and loading. Excessive addition of the promoters may block the active sites, leading to a decrease in the catalytic activity [139, 140]. On the other hand, Zeng *et al* [141] compared catalytic DRM over the K, Mg, and Ce promoted Ni/Al_2O_3 catalyst under the NTP and thermal conditions. Under thermal activation, the addition of the promoters reduced the CH_4 conversion. Conversely, in NTP-catalysis, the K promoted catalyst improved the CO_2/CH_4 conversions, the yield of H_2, CO and C_2-C_4 alkanes and the energy efficiency of the system, whilst the Mg-promoted catalyst increased the H_2/CO molar ratio due to the decreased CO_2 conversion. This work suggests that the catalysts presenting poor performance in thermal catalysis may perform well under NTP activation and vice versa. Therefore, fundamental research into the role of promoter in NTP-catalysis and their mechanism of enhancement needs further research to advance NTP-catalysis.

Table 2.5 Summary of NTP-catalytic DRM over supported catalysts modified with various promoters.

Catalyst	Power (W)	CH_4/CO_2	CO_2 Conv. (%)		CH_4 Conv. (%)		Ref.
			NTP only	NTP+ catalyst	NTP only	NTP+ catalyst	
Ni-K/Al_2O_3	16	1.5		22.8		31.6	
Ni-Mg/Al_2O_3	16	1.5	18.2	15	25.1	22	[141]
Ni-Ce/Al_2O_3	16	1.5		21		32	
Ni/ γ-Al_2O_3-MgO	100	1.0	58	73.5	64	74.5	[142]
Ni-Mn/ γ-Al_2O_3	2.1	1.0	6	12	12	28.4	[67]
Na/La_2O_3-$MgAl_2O_4$	100	1.0	59	84.5	62	86	[68]
NiCeC	40	1.0	–	53.7	–	55.6	[140]
Ni/MgO-Al_2O_3	2.7	1.0	9.5	13	20	34.7	[138]
Ni/CeO_2-Al_2O_3	2.7	1.0		12.1		30	

This review presented in this chapter briefly discusses the general aspects of thermal- and plasma-activated CO_2 conversions and their relevant mechanisms, as well as the principle of catalyst design for CO_2 conversion. Specific reviews related to the detailed research are presented in the individual chapters of Chapter 3–5.

Chapter 3 Mechanistic Study of Non-Thermal Plasma Assisted CO_2 Hydrogenation over Ru Supported on MgAl Layered Double Hydroxide

This chapter was published in Applied Catalysis B: Environmental, 2020, 268, 118752.

DOI: https://doi.org/10.1016/j.apcatb.2020.118752. Permission obtained from Applied Catalysis B: Environmental to use the manuscript of the paper in this thesis.

3.1 Introduction

Catalytic hydrogenation of carbon dioxide (CO_2) is an appealing way to produce fuels and chemical building blocks such as methane (CH_4) and methanol. The hydrogenation of CO_2 at atmospheric pressure yields mainly CH_4 (*i.e.* CO_2 methanation), and/or CO (*via* the reverse water-gas shift reaction) [143]. CO_2 methanation is considered important in the "power-to-gas" process, enabling the large-scale chemical storage of hydrogen (H_2) generated by sustainable pathways (*e.g.* using solar energy and hydropower) [144]. Additionally, the synthetic (or substitute) natural gas from the reaction can be easily stored and transported, or directly injected into the existing industrial natural gas infrastructures [145]. The reaction (Eq. 3.1) is highly exothermic and kinetically limited accordingly, catalytic CO_2 methanation with high conversions at low temperatures is challenging. Therefore, to promote direct CO_2 activation, the development of highly active and stable catalysts at mild thermal conditions (*e.g.* T < 250 °C) [146], as well as new processes for activating the catalysis, is still urgently needed.

$$CO_2 + 4H_2 \rightarrow CH_4 + 2H_2O \qquad \Delta_r H^0_{298\,K} = -164.94\ \text{kJ mol}^{-1} \qquad \text{Eq. 3.1}$$

Extensive studies have been performed to develop metal catalysts for CO_2 methanation, among which Ni, Ru and Rh have been revealed as effective candidates [25]. Although nickel-based catalysts are relatively cost-effective and earth abundant, they are prone to deactivation due to carbon deposition, sintering and chemical poisoning [147]. Conversely, Ru-based catalysts are relatively stable, as well as being highly active for CO_2 methanation. Layered double hydroxides (LDHs) have the general formula of $[M^{2+}_{1-x} M^{3+}_{x} (OH)]^{z+} A^{n-}_{z/n} \cdot mH_2O$, in which M^{2+} and M^{3+} occupy the octahedral holes in a brucite-like layer and A^{n-} represents the exchangeable interlayer anions to compensate the positive charge on the layers, being widely employed as catalysts, catalyst precursors and catalyst supports [148]. As the catalyst support, LDH offers: (*i*) 6-fold coordinated OH– groups with divalent and trivalent cations, which can facilitate chemisorption and activation of CO_2, (*ii*) turntable electronic structure (or basicity) of the surface of LDHs as well as the layered double oxide (LDOs) produced by calcination of LDH, and (*iii*) coordinatively unsaturated active sites (*e.g.* low-coordinated steps, edges and corner atoms) to promote the metal dispersion [125, 149]. To date, Ni−Al catalysts derived from Ni_3Al LDH has shown high CO_2 conversions (*e.g.* 86%) at 300 °C due to the high metal surface area (*e.g.* ~52 $m_{Ni}^2\ g_{cat}^{-1}$) and dispersions (*e.g.* 16%) [150].

Non-thermal plasma (NTP) dissociates and activates gaseous species to produce a variety of active electrons, ions and radicals, being able to participate in surface reactions over a catalyst under relatively mild conditions (*i.e.* atmospheric pressure and low bulk temperatures < ~200 °C) compared to the conventional thermally activated catalysis [20, 73]. Previously, NTP-catalysis was highly effective for promoting kinetically limited reactions, such as CO_2 dry reforming [151] and water gas shift reactions [83, 152], without an external heat source. Recently, NTP-assisted catalytic CO_2 hydrogenation over Ni/Al_2O_3 catalysts has been demonstrated, in which the conversion of CO_2 was improved significantly (by 60% compared to the NTP-promoted gas-phase reactions) at ~150 °C [49]. Therefore, NTP-catalysis represents an alternative

to thermal catalysis due to the presence of the plasma-generated reactive species and plasma-catalyst interactions [153]. However, the specific activation mechanism in NTP-catalysis depends on various factors including the type of catalyst and reaction, and *in situ* characterisation of the NTP-catalysis (such as diffuse reflectance infrared Fourier transform, DRIFTS, and extended X-ray absorption fine structure, EXAFS) was proven to be beneficial to develop insights into the complex system [82, 152, 154].

Herein, a series of Ru catalysts with different Ru loadings (0.4%, 1.0%, 2.5% and 5%) supported on MgAl LDHs were developed and reduced at different temperatures (160–600 °C). The developed Ru catalysts were used in the comparative and systematic catalytic tests for CO_2 hydrogenation under both NTP and thermal (at 250 °C or 300 °C) conditions, aiming at understanding the synergetic effect of plasma and catalyst in NTP-assisted catalytic CO_2 hydrogenation. It was found that the catalysis under the NTP conditions enabled significantly higher CO_2 conversions (~85%) and CH_4 yield (~84%) at relatively low temperatures. Regarding the catalyst preparation, the reduction temperature can affect the chemical state of the metal and metal-support interaction significantly, and thus altering the activity of the catalysts in NTP-driven catalytic CO_2 hydrogenation. NTP-catalysis systems were also investigated *in situ* using a combined DRIFTS-mass spectrometry (MS), in which the dynamics of surface species during the NTP-activated CO_2 hydrogenation provide useful information to allow the development of reaction mechanism of the system under study.

3.2 Experimental Section

3.2.1 Chemicals

Ruthenium(III) chloride trihydrate **(**$RuCl_3 \cdot 3H_2O$), magnesium nitrate hexahydrate ($Mg(NO_3)_2 \cdot 6H_2O$, >99%), aluminum nitrate nonahydrate ($Al(NO_3)_3 \cdot 9H_2O$, >98%) and

urea (BioUltra, >99.5%) were purchased from Sigma-Aldrich and used without further purification.

3.2.2 Synthesis of MgAl layered double hydroxides (LDHs)

MgAl LDH was synthesised using a urea-assisted coprecipitation method. Typically, $Mg(NO_3)_2 \cdot 6H_2O$ (0.01 mol), $Al(NO_3)_3 \cdot 9H_2O$ (0.005 mol) and urea (0.005 mol) were first dissolved in 50 mL deionised water and stirred for 30 min. The resulting homogeneous solution was then transferred into a Teflon-lined stainless-steel autoclave, sealed and hydrothermally treated at 110 °C for 24 h. After cooling the system down to room temperature (RT), the solid product was separated by centrifugation, washed repeatedly with deionised water, and finally dried at 70 °C overnight.

3.2.3 Preparation of Ru/MgAl catalysts

Ru/MgAl catalysts were prepared using the conventional wet impregnation method. Firstly, the obtained MgAl LDH (1.5 g) was suspended in water (30 mL), then 0.07 g $RuCl_3 \cdot 3H_2O$ was added in the suspension. After vigorous stirring for 3 h (by using the magnetic stirrer), the precipitate was filtered, washed with deionised water and dried at 60 °C for 12 h. Different theoretical loadings of Ru (0.4%, 1.0%, 2.5% and 5%) on MgAl LDH were achieved by adjusting the concentration of $RuCl_3 \cdot 3H_2O$ during impregnation. The obtained dry solids were subsequently reduced under a H_2 atmosphere at different reduction temperatures ranging from 160 to 600 °C for 2 h, with a heating rate of 5 °C min^{-1}. After reduction, the samples were cooled to RT naturally. Based on the theoretical metal loading and the reduction temperature, the catalysts developed have been denoted as *x*% Ru/MgAl-R*y* (where *x* refers to the theoretical Ru loading and *y* is the reduction temperature). The actual metal loading was determined by ICP-OES.

3.2.4 Characterisation of catalysts

The morphology of the samples was investigated using a TESCAN Mira 3 scanning electron microscope (SEM) at an accelerating voltage of 5 kV. The bright-field transmission electron microscopy (TEM) was performed on an FEI Tecnai G20 transmission electron microscope operating at 200 kV. And high-angle annular dark field scanning transmission electron microscopy (HAADF-STEM) and elemental mapping were carried out on FEI Titan G2 STEM operating at 200 kV. X-ray diffraction (XRD) patterns of the materials were obtained on a PANaytical X'Pert Pro diffractomer using Cu Kα_1 radiation (λ = 1.5406 Å) at 40 kV, 40 mA, a scanning rate of 2° min^{-1}, a step size of 0.03° s^{-1}, and a 2θ angle from 3 to 100°. X-ray photoelectron spectra (XPS) were recorded on a Kratos AXIS Ultra DLD apparatus with monochromated Al Kα radiation X-rays source, a charge neutraliser and a hemispherical electron energy analyser with a pass energy of 160 eV. The binding energies (B.E) were calibrated by the C 1s peak at 284.8 eV. The actual metal loading of samples was analysed by using ICP-OES (PQ 9000 Elite system). Prior to analysis, the sample (20 mg) was dissolved in concentrated sulfuric acid (5 mL) and concentrated nitric acid (5 mL) by microwave digestion (ETHOS UP microwave digester).

Temperature programmed reduction (H_2-TPR), CO_2 desorption (CO_2-TPD) analyses were performed using Quantachrome ChemBet Pulsar equipped with a thermal conductivity detector (TCD). For H_2-TPR, 30 mg of the sample was loaded in a quartz tube reactor and then pre-treated with helium at 160 °C for 1 h. After cooling to RT, a gaseous mixture of 5% H_2 in Ar was introduced into the reactor (at 40 mL min^{-1}), and the system temperature was increased to 800 °C with a heating rate of 10 °C min^{-1}. TPR of commercial RuO_2 catalyst was performed as well for comparison. For CO_2-TPD, 30 mg of sample was first reduced at 250 °C under 5% H_2/Ar steam for 1 h (10 °C min^{-1}, 40 mL min^{-1}). Then, the reactor was cooled down under the Ar to RT, and a flow of 1% CO_2/He (55 mL min^{-1}) was introduced into the reactor for 1.5 h.

Subsequently, the catalyst was purged with helium for 1 h to remove the gas-phase and physiosorbed CO_2. The CO_2-TPD was performed by raising the temperature from RT to 900 °C under He flow with a temperature ramp of 10 °C min^{-1}. For the CO pulse chemisorption, the sample was reduced under H_2/He at 300 °C for 1 h and then was purged by He for 1.5 h to remove the H_2 from the catalyst and finally cooled down to RT. The CO pulse was performed with 1% CO/He at RT. For temperature-programmed oxidation (TPO) of the spent samples was carried out by using 10% O_2/Ar (50 mL min^{-1}) from RT up to 750 °C under a 10 °C/min temperature ramp. The CO_2 concentration at the outlet was measured using Hiden™ HPR-20 mass spectrometer.

3.2.5 NTP-activated catalytic CO_2 hydrogenation

The catalytic activity, selectivity and stability of the prepared catalysts were assessed at atmospheric pressure in a dielectric barrier discharge (DBD, 6 mm O.D. × 4 mm I.D.) flow reactor (Figure 3.1). An aluminium foil wrapped around outside of the quartz tube served as the high voltage electrode, while a stainless-steel rod (1 mm O.D.) placed in the centre of the quartz tube was used as the ground electrode. The discharge length and gap of the DBD reactor were 10 mm and 1.5 mm, respectively. The electrical parameters of NTP were monitored using an oscilloscope (Tektronix TBS1072B) which was connected to the reactor through a high voltage probe (Tektronix, P6015). Typically, 100 mg catalysts (pelletised with particle size of 250–425 μm) were loaded in the discharge zone between two quartz wool plugs. As the catalysts can be re-oxidised due to exposition to air at RT, the catalyst was treated *in situ* before NTP-catalysis (at 6.5 kV) using pure H_2 as the discharge gas (50 mL min^{-1} for 20 mins). For the reaction, the gas mixture of H_2 and CO_2 (molar ratio of 4:1) was fed into the DBD plasma reactor. The total flow rate and space velocity of the gas mixture were 50 mL min^{-1} and 30,000 mL (STP) g_{cat}^{-1} h^{-1}, respectively. The applied voltage was from 5.5 kV to 7.5 kV, corresponding to the increased power from 1.1 W to 2.6 W, while a constant frequency of 20.5 kHz was used. The outlet gas composition was analysed by

a two-channel on-line gas chromatography (GC) equipped with an Elite-Carbon molecular sieve packed column (N 9303926), a thermal conductivity detector (TCD) and a flame ionisation detector (FID). For each measurement, three samples of gas products were taken and analysed under steady-state conditions. The produced water was condensed by a glass water trap cooled by an ice bath and the total flowrate of the gas products was measured by a bubble-flow meter for the calculation of CO_2 conversion and CH_4 selectivity. Control experiments, *i.e.* catalyst-free CO_2 hydrogenation under NTP (gas phase reactions) and NTP-assisted CO_2 hydrogenation over LDHs were performed under the same power.

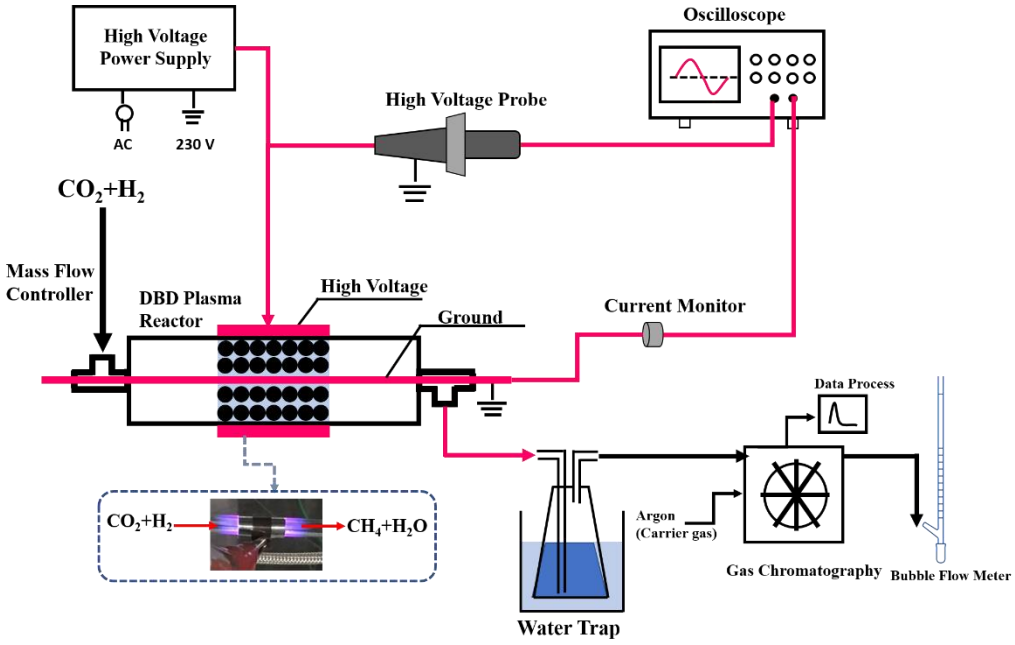

Figure 3.1 Schematic diagram of the DBD plasma system for catalytic CO_2 hydrogenation.

For comparison, thermally activated catalysis at 250 °C and 300 °C was carried out at atmospheric pressure as well. Typically, the Ru/MgAl catalysts were first treated *in situ* at 250 °C for 1 h under a 20% H_2/Ar flow at 100 mL min^{-1}. Then the gas mixture of CO_2 and H_2 (volume ratio = 1:4) was fed into the reactor at 50 mL min^{-1}. The temperature of the catalyst bed was monitored by placing a K-type thermocouple in the middle of the catalyst bed.

CO_2 (X_{CO2}) conversion, selectivity towards CH_4 (S_{CH4}) and CO (S_{CO}), CH_4 yield, Carbon balance and turnover frequency (TOF) were determined as following:

$$X_{CO_2} = \frac{CO_{2,in} - CO_{2,out}}{CO_{2,in}} \times 100 \quad \text{Eq. 3.2}$$

$$S_{CH_4} = \frac{CH_{4,out}}{CO_{2,in} - CO_{2,out}} \times 100 \quad \text{Eq. 3.3}$$

$$S_{CO} = \frac{CO_{out}}{CO_{2,in} - CO_{2,out}} \times 100 \quad \text{Eq. 3.4}$$

$$Y_{CH_4} = X_{CO_2} \times S_{CH_4} \quad \text{Eq. 3.5}$$

$$C_{balance}(\%) = \frac{CO_{2,out} + CO_{out} + CH_{4,out} + 2C_{2,out}}{CO_{2,in}} \times 100 \quad \text{Eq. 3.6}$$

where, X is the conversion, S is the selectivity, Y is the yield, C is carbon balance.

The specific reaction rates were calculated as following:

$$r_{CO_2} = \frac{X_{CO_2} \cdot F_{in}}{W_{cat}} \quad \text{Eq. 3.7}$$

where r_{CO_2} is the conversion rate of CO_2 (mol s^{-1} g_{cat}^{-1}), X_{CO_2} is the conversions of CO_2, F_{in} is the molar flow rate of CO_2 in the inlet of the DBD reactor (mol s^{-1}), W_{cat} is the mass of catalyst used in the catalytic performance measurements (g).

Turnover frequencies (TOF) of CO_2 conversion, defined as moles of CO_2 converted per surface Ru metal atom per second (s^{-1}), were calculated using the results obtained from catalytic performance measurements and metal dispersions which are determined by using CO pulse chemisorption (as shown in Table 3.4):

$$TOF_{CO_2} = \frac{r_{CO_2} \cdot M_{Ru}}{D \cdot X_{Ru}}$$ Eq. 3.8

where M_{Ru} is the metal atomic weight (101.07 g mol^{-1}) and X_{Ru} is the metal content in catalysts (g_{Ru} g_{cat}^{-1}) and D is the Ru dispersion (by CO pulse chemisorption, as shown in Table 3.4).

3.2.6 Kinetic evaluation of catalytic CO_2 hydrogenation under the NTP and thermal conditions

Kinetic study of CO_2 hydrogenation under the thermal conditions was conducted in a continuous-flow fixed-bed quartz reactor (6 mm O.D. × 4 mm I.D.). Approximately 20 mg sample was diluted with glass beads (with particle size of 425–600 μm) in a 1:9 dilution ratio, and then the temperature was adjusted between 230−300 °C to maintain CO_2 conversion below 20%. Prior to catalytic activity test, the catalyst was pre-treated *in situ* in 20% H_2/Ar gas at 250 °C. Then, the reaction mixture consisted of H_2 and CO_2 with a specific molar composition of H_2:CO_2 = 4 was introduced into the reactor *via* two mass flow controllers.

Kinetic study of NTP-catalysis was performed in a DBD reactor (Figure 3.1). Similarly, about 20 mg catalysts were diluted with glass beads to form a 10 mm bed height. Prior to reaction, each catalyst was pre-treated in a pure H_2 flow under NTP for 30 mins (6.5 kV, 20.5 kHz). The gas composition and total flow rate of feed gas mixture keep the same with that of thermal conditions. The applied peak voltage varied from 4 kV to 6 kV to make sure the CO_2 conversion below 20%. The apparent activation energy was measured at conversions below 20%, where these conversions are primarily kinetically controlled to minimise pore diffusion and mass transfer. As NTP can dissociate CO_2 to CO, the NTP-alone experiments with glass beads packing were performed to exclude the relevant gas phase reaction in the calculation of the reaction rate for the NTP-catalysis systems.

Activation energy ($E_{a,thermal}$, kJ mol^{-1}) of the thermal catalysis was determined according to:

$k_{thermal-cat} = A \times e^{-\frac{E_{a,thermal}}{RT}}$	Eq. 3.9
$r_{thermal-cat} = k_{thermal-cat}[CO_2]^a[H_2]^b \times (1-\beta)$	Eq. 3.10

where r is the reaction rate (mol s^{-1} g^{-1}), k is the rate constant, A is the pre-exponential factor, R is the universal gas constant, while T is the reaction temperature (K). [CO] and [H_2] are the feed gas concentrations, and a and b are the reaction orders with respect to CO_2 and H_2, respectively. β is an approach to equilibrium. Since the conversion was limited to lower than 20%, the β can be neglected as the reaction was far from equilibrium.

Energy barrier ($E_{a,\ NTP}$, kJ mol^{-1}) of the NTP-catalysis was obtained using Eq.3.11 according to the method presented in the literature [87]:

$$r_{NTP-cat} = A \times e^{\frac{E_{a,NTP}}{\frac{1}{F_{total}} \times power_{DBD}}} \qquad \text{Eq. 3.11}$$

where F_{total} is the total flow rate of feed gas (0.833 mL s^{-1} (0.037 mmol s^{-1})) in this study), while $power_{DBD}$ is the DBD discharge power (W). Specifically, the DBD discharge power was calculated by using the current and voltage data obtained from a digital oscilloscope (TBS1102B).

3.2.7 In situ DRIFTS-MS characterisation of NTP-activated CO_2 hydrogenation

The experimental setup for the NTP-DRIFTS was described in the Chapter 2 [81] (briefly described as Figure 3.2). The catalyst was loaded into the IR cell and pre-treated in a 10% H_2/Ar flow under the plasma (applied voltage: 5.0 kV, frequency: 23.5 kHz) for 30 min. Then the gas reactant (1 vol.% CO_2 and 4 vol. % H_2 with Ar balance) was

introduced into the cell to initiate the reaction. The use of Ar balance in DRIFTS was to avoid the signal saturation of IR spectra and MS signal. A constant peak voltage of 5.0 kV and pulse frequency of 23.5 kHz were employed to avoid arcing between the electrodes. IR spectra were recorded every 60 s with a resolution of 4 cm^{-1} and analysed by the OPUS software.

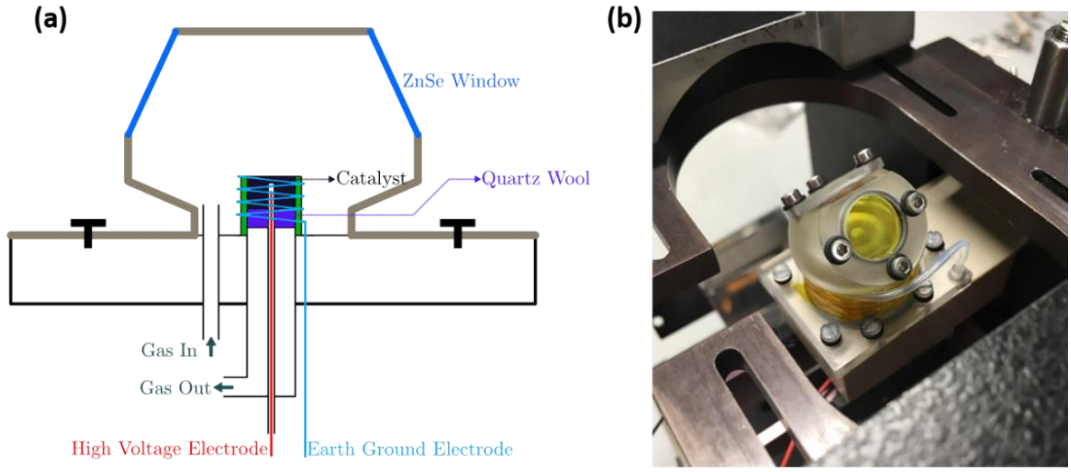

Figure 3.2 (a) Schematic diagram of the *in situ* DRIFTS flow cell and (b) photograph of the *in situ* DRIFTS flow cell.

3.3 Result and discussion

3.3.1 NTP-activated CO_2 hydrogenation.

The performance of the 2.5% Ru/MgAl catalysts in NTP-activated CO_2 hydrogenation was studied in reference to the control experiments (*i.e.* empty tube for gas phase reaction and with the MgAl LDH support packing under the NTP conditions). Figure 3.3a and b shows insignificant CO_2 conversion and selectivity to CH_4 as a function of plasma voltage/power in the two control experiments. For the blank reactor, only 5% conversion of CO_2 was achieved due to the NTP-assisted dissociation of CO_2 to CO in the gas phase. Similarly, the NTP system with the MgAl LDH packing was only

selective to CO with a CO_2 conversion of ~10% (due to the enhanced electric field strength or the CO_2 adsorption on MgAl LDH which facilitates the NPT dissociation [155]. Conversely, the NTP-catalysis system using the packing of 2.5% Ru/MgAl catalysts showed significant CO_2 conversions and selectivity to CH_4 of >68 and >95 %, respectively, at voltages above 6.5 kV, demonstrating the synergy between the catalyst and NTP.

For all 2.5% Ru/MgAl catalysts, the activity profile under NTP conditions (*e.g.* the calculated specific reaction rates, TOF, in Figure 3.3d) shows a similar trend as a function of the discharge voltage/power. Specifically, the CO_2 conversion (Figure 3.3a) and CH_4 selectivity/yield (Figures 3.3b and 3.3c) show an initial steep increase with an increase of the voltage which then decrease slightly on increasing the voltage to 7.5 kV. The initial increase of CO_2 conversion and CH_4 selectivity corresponds to the increased input energy under NTP conditions, *i.e.* the catalysis requires the energy input over the threshold value at ~5.5 kV to be activated by NTP. The gradual decrease in the selectivity to CH_4 may be related to the methane steam reforming reactions under NTP, producing CO and other hydrocarbons [156] (which were detected by GC, as shown in Figure 3.5, *i.e.* the peak for C_2H_x in the outlet gas mixture at 7.5 kV). Interestingly, the reduction temperature used for treating the 2.5% Ru/MgAl catalysts had a considerable effect on their catalytic performance under NTP conditions. The 2.5% Ru/MgAl catalysts reduced at <300 °C showed a higher initial activity compared with the catalysts reduced at >300 °C. For example, at 6.0 kV, the 2.5% Ru/MgAl-R300 catalyst showed about 80% CO_2 conversion with 99.5% selectivity to CH_4 and 79% CH_4 yield, while the catalysts reduced at >300 °C only gave <20% conversion and zero CH_4 formation. Based on the comparison of TOF values at 6.0 kV, 2.5% Ru/MgAl-R250 gives a TOF value of 1.9 s^{-1}, representing a >7-fold increase compared with the TOF value of 2.5% Ru/MgAl-R400. Moreover, the corresponding carbon balance and TPO testing of 2.5% Ru/MgAl-R250 catalyst (Figure 3.4a and b) showed that no carbon deposition was formed on the surface. To explain the effect of reduction temperature

on the catalytic activity of the 2.5% Ru/MgAl catalysts, the catalysts were characterised and these results correlated with the reaction data.

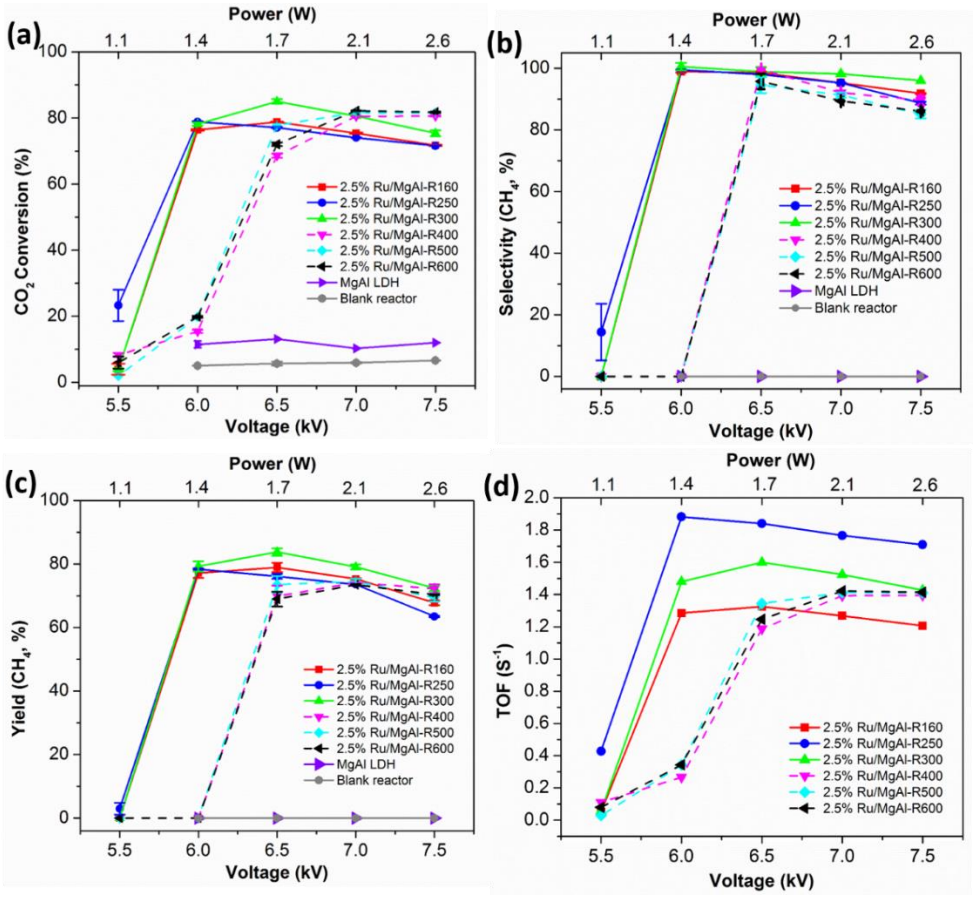

Figure 3.3 Performance of NTP-activated catalytic CO_2 hydrogenation as a function of voltage/power over the 2.5% Ru/MgAl catalysts reduced at different temperatures in reference to the control experiments. (a) CO_2 conversion, (b) CH_4 selectivity, (c) CH_4 yield and (d) TOF (R160, R250, R300, R400, R500 and R600 refers to the reduction temperature of 2.5% Ru/MgAl catalysts at 160, 250, 300, 400, 500 and 600 °C).

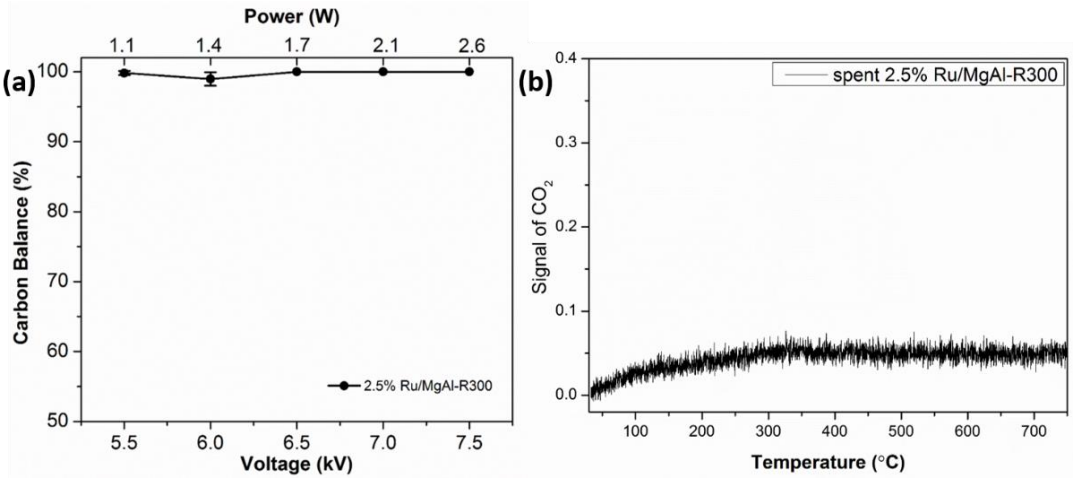

Figure 3.4 (a) Carbon balance of NPT-assisted catalytic CO_2 hydrogenations over 2.5% Ru/MgAl-R300 °C catalyst. (b) TPO analysis of spent 2.5% Ru/MgAl-R300 catalysts.

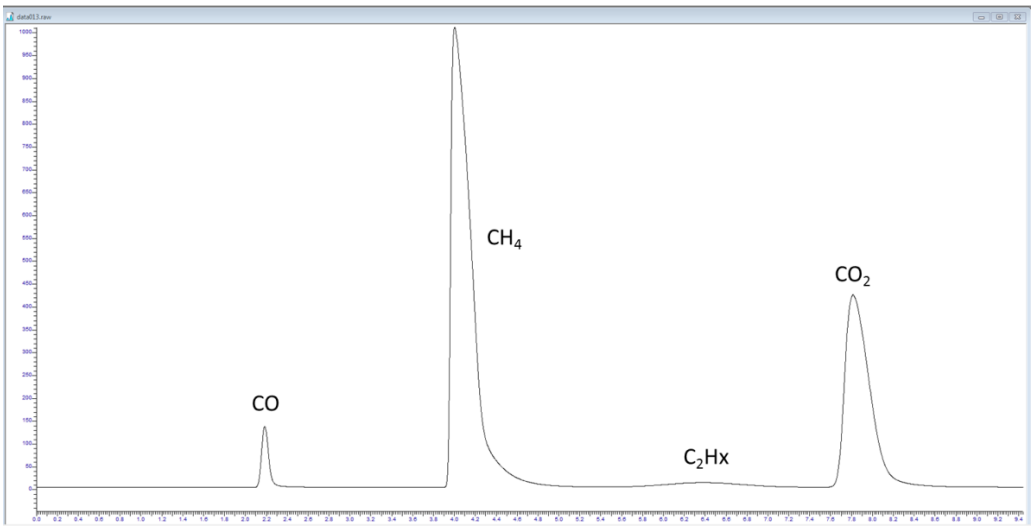

Figure 3.5 Raw GC data for NTP-activated CO_2 hydrogenation at 7.5 kV, 20.5 kHz over the 2.5% Ru/MgAl-R300 catalyst.

Considering that the 2.5% Ru/MgAl-R300 catalyst displayed relatively high CO_2 conversion and CH_4 yield, catalysts with different Ru loading were prepared and reduced at 300 °C, and then used in the comparative evaluations under both NTP and thermal conditions (Figures 3.6 and 3.8). As the Ru loading increased from 0.4% to 2.5%, CO_2 conversion and CH_4 yield increased as well, and the highest CO_2 conversion was obtained with an optimal 2.5% Ru loading. By increasing the Ru loading further to

5%, the catalytic activity decreased (Figure 3.6). This result could be attributed to the aggregation of Ru NPs on the support surface when excessive Ru was loaded, which led to the reduced activity (as shown in Figure 3.7). And on the other hand, for the 0.4% Ru/MgAl-R300 catalyst, CO_2 conversion raised from 5% at 6.0 kV to 70 % at 7.5 kV. However, CO is the main product and CH_4 was formed only at 7.5 kV, which means that the low loading of Ru needs more energy to be activated for CH_4 formation. When the Ru loading increased from 1.0% to 5%, the activity trend with voltage in the CO_2 conversion was similar to that observed for the 2.5% Ru/MgAl-R300 catalyst.

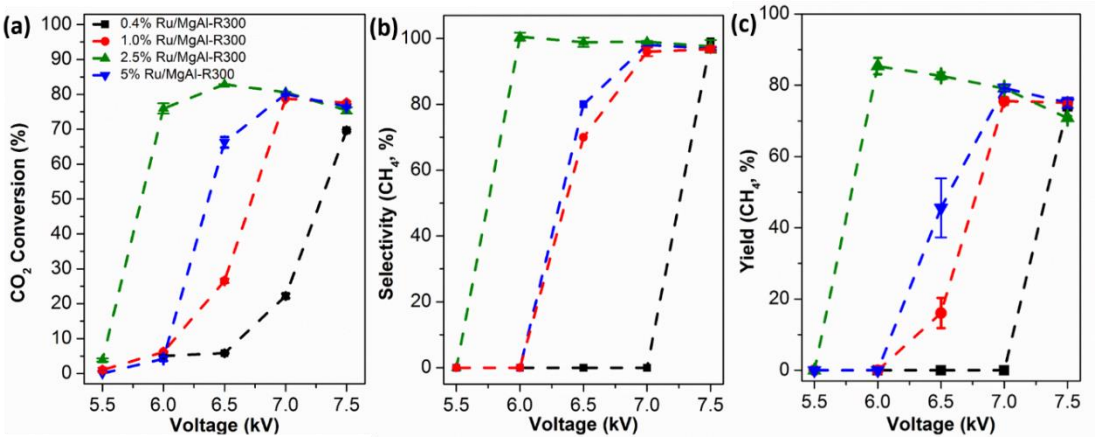

Figure 3.6 Performance of NTP-assisted catalytic CO_2 hydrogenations under different voltages over the catalysts with different loading of Ru. (a) CO_2 conversion, (b) CH_4 selectivity, and (c) CH_4 yield.

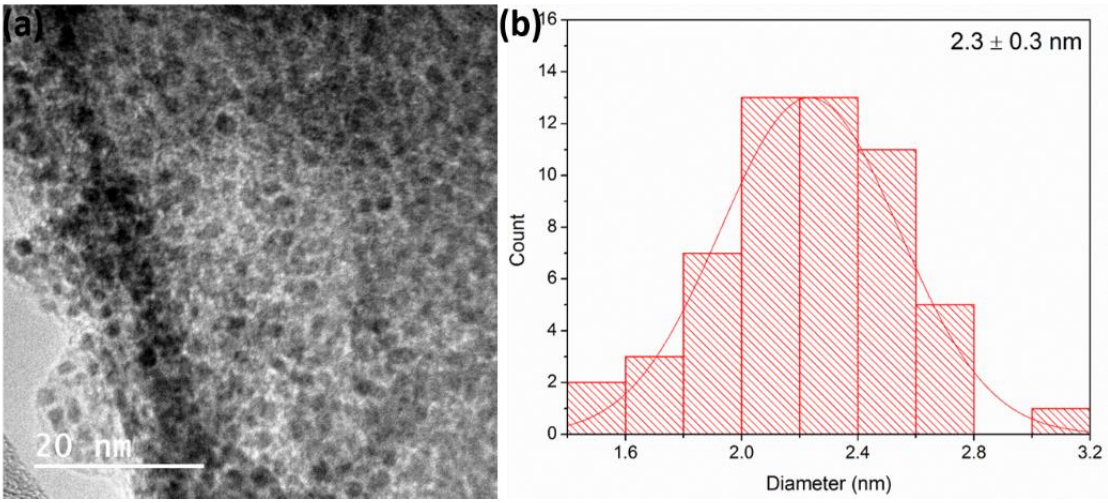

Figure 3.7 TEM images of 5% Ru/MgAl-300 °C catalysts and the corresponding particle size distribution.

In general, regardless the variation of Ru loading on the catalysts, the NTP activation significantly enhanced the CO_2 conversion compared with the thermal activation (Figures 3.8a and 3.8b). In detail, NTP activation enabled high CO_2 conversions (~85%) at 6.5 kV and relatively low average temperature of ~129 °C (by Infrared (IR) thermometer). Conversely, under the thermal condition at 250 °C, only 13.7% and 3.7% CO_2 conversion were achieved, respectively, over 2.5% and 5% Ru/MgAl-R300 catalysts, while no CO_2 conversion was found for the catalysts with low Ru loadings (*i.e.* 0.4% and 1.2% Ru/MgAl-R300 catalysts, which enabled 1.5% and 8.1% CO_2 conversion, respectively, at 300 °C, as shown in Figures 3.8a). Accordingly, to develop a mechanistic understanding of the NTP catalysis, relevant kinetic studies were performed, and the details of the kinetic calculations are presented in the Tables 3.1 and 3.2. Accordingly, Figure 3.8c shows that the thermal system exhibits the typical Arrhenius behaviour with the calculated activation energy over the 2.5% Ru/MgAl-R160, R300 and R600 catalysts being 68, 82 and 113 kJ mol^{-1}, respectively, while the energy barriers of the NTP-catalysis were 30, 21 and 43 kJ mol^{-1}, respectively, which is about 3 times smaller than that required by the thermal activation (Table 3.1–3.3) [87]. The findings from the kinetic study suggest that plasma-catalyst interactions may enable alternative pathways for promoting CO_2 hydrogenation.

Table 3.1 Kinetic parameters obtained for catalytic CO_2 hydrogenation under thermal conditions to calculate the apparent activation energy and the corresponding graph is in Figure 3.8c.

Catalysts	*Temperature* (K)	X_{CO2} (%)	$r_{thermal\text{-}cat}$ ($\times 10^{-3}$ mol s^{-1} g^{-1})	Slope (ln ($r_{thermal\text{-}cat}$) *VS. 1000/T)*	R^2	$E_{a,\ thermal}$ (kJ mol^{-1})
2.5% Ru/MgAl-R160	545.15	5.6	1.0	−8.20 ± 0.42	0.990	68
	557.35	7.3	1.3			
	568.15	10.5	1.9			
	585.25	14.2	2.6			
	599.05	20.8	3.8			
2.5% Ru/MgAl-R300	567.55	3.6	0.6	−9.82 ± 0.52	0.996	82
	580.35	5.1	0.9			
	593.85	8.3	1.3			
	607.85	11.6	1.9			
2.5% Ru/MgAl-R600	564.05	5.1	0.7	−13.63 ± 0.52	0.989	113
	577.75	9.6	1.2			
	590.25	15.5	2.0			
	606.35	18.6	3.6			

Table 3.2 Kinetic parameters obtained for catalytic CO_2 hydrogenation under NTP conditions to calculate the apparent activation energy and the corresponding graph is in Figure 3.8d.

Catalysts	*DBD discharge power (W)*	X_{CO2}[a] (%)	$r_{NTP\text{-}cat}$ ($\times 10^{-4}$ mol s^{-1} g^{-1})	*Slope* (ln ($r_{NTP\text{-}cat}$) *VS. 1/power)*	R^2	$E_{a,NTP}$[b] (kJ mol^{-1})
2.5% Ru/MgAl-R160	0.54	3.5	6.8	−1.09 ±0.04	0.997	29
	0.72	6.1	11.7			
	1.05	9.4	17.8			
	1.22	11.3	21.5			
2.5% Ru/MgAl-R300	0.72	5.6	9.0	−0.79 ±0.03	0.996	21
	0.96	7.1	11.4			
	1.24	8.8	14.2			
	1.56	10.1	16.3			
2.5% Ru/MgAl-R600	0.51	1.9	2.4	−1.60 ±0.09	0.993	43
	0.67	4.1	5.3			
	0.90	7.9	10.2			
	1.20	10.9	14.2			

[a] CO_2 Conversion = CO_2 Conversion (catalysts + glass bead) − CO_2 Conversion (glass bead); [b] $E_{a,NTP}$ calculated according to Eq. 3.11 by accounting total flow rate (0.037 mmol s^{-1} in this study).

Table 3.3 Apparent activation energy calculated for catalytic CO_2 hydrogenation over 2.5% Ru/MgAl catalysts (reduced at 160 °C, 300 °C and 600 °C, respectively) by thermal and plasma activation.

Catalysts	E_a (kJ mol^{-1})	E_a (kJ mol^{-1})
	Thermal activation	NTP activation
2.5% Ru/MgAl-R160	68	30
2.5% Ru/MgAl-R300	82	21
2.5% Ru/MgAl-R600	113	43

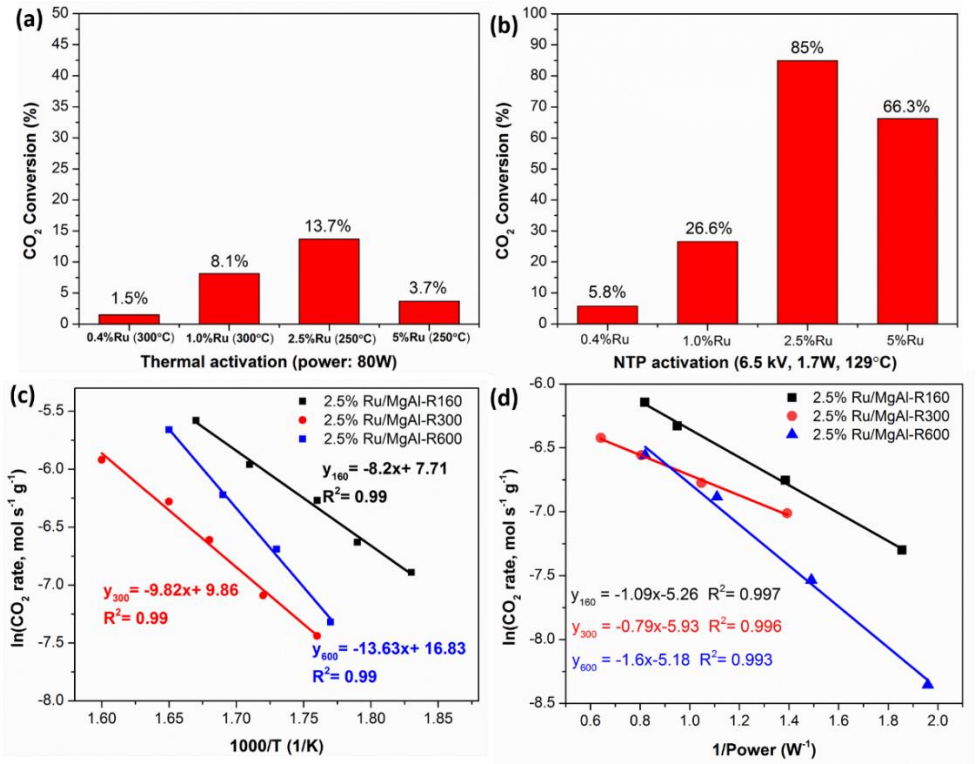

Figure 3.8 Comparison of the performance of catalytic CO_2 hydrogenation over the 0.4%, 1.0%, 2.5% and 5% Ru/MgAl catalysts reduced at 300 °C under (a) thermal conditions at 250 or 300 °C; (b) NTP condition at 6.5 kV (20.5 kHz, 1.7W). Determination of the activation energy over the 2.5% Ru/MgAl catalysts reduced at 160 °C, 300 °C and 600 °C (c) under thermal and (d) NTP conditions.

The NTP-catalysis system (at 6.5 kV, 20.5 kHz) also showed good stability, which was demonstrated by the 2.5% Ru/MgAl-R300 catalyst in the longevity test (Figure 3.9a). Under the NTP condition, the catalyst displayed high activity (about 84% CO_2 conversion) and no deactivation over 600 min time on stream and maintained a high

selectivity to CH_4 of ~98.4%. The stability of the NTP-catalysis system may be due to the absence of metal sintering, which is common in the conventional thermal catalysis, especially at high temperatures. The post-reaction TEM characterisation of the catalyst (as shown in Figures 3.9b and c) provides the information on particle size of Ru NPs after the longevity test, showing 1.9 ± 0.4 nm which is comparable to that of the fresh catalyst.

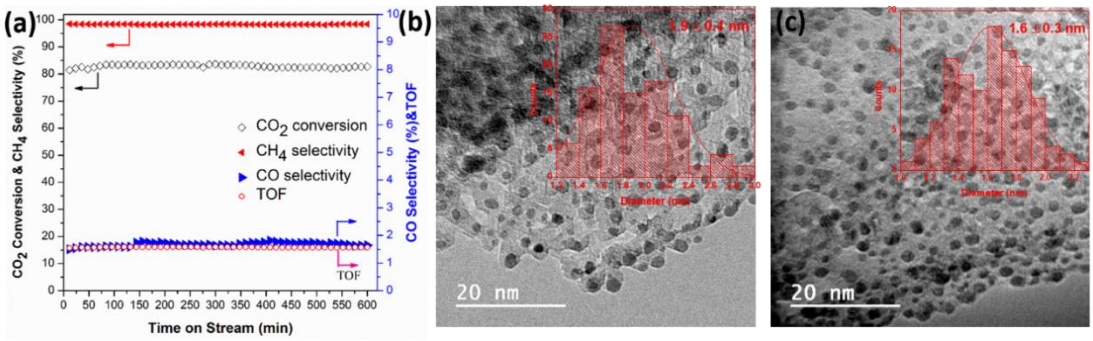

Figure 3.9 (a) Stability test of the 2.5% Ru/MgAl-R300 catalyst for catalytic CO_2 hydrogenation under the NTP condition (H_2/CO_2 = 4, WHSV = 30,000 mL (STP) $gcat^{-1}$ h^{-1}); (b) TEM image and particle size distribution of the used 2.5% Ru/MgAl-R300 catalysts after the longevity test; and (c) TEM image and particle size distribution of the fresh 2.5% Ru/MgAl-R300 catalysts.

3.3.2 Effect of reduction temperature on the property of the catalysts.

To understand the effect of the reduction temperature on the catalytic activity of the resulting catalysts, XRD analysis was performed to characterise the as-reduced catalysts. As shown in Figure 3.10, the characteristic diffraction peaks of MgAl LDH support at 2θ = 12°, 23.9°, 35° and 39.8° are ascribed to the (003), (006), (012) and (015) reflections, corresponding to a well-defined hydrotalcite structure. Accordingly, the basal spacing value (d_{003}) of MgAl-LDH support is calculated as 0.80 nm, being similar to that of the LDH with CO_3^{2-} anions in the layer [157]. All the as-prepared 2.5% Ru/MgAl catalysts did not show the relevant diffraction peaks associated with the crystalline Ru phases, indicating that Ru is finely dispersed on the support which is

consistent with the TEM results. After the reduction of $RuCl_3$-impregnated MgAl LDH at 160 °C, XRD analysis of the resulting catalyst (*i.e.* 2.5% Ru/MgAl-R160) showed the relatively reduced peak intensities and the shift of peak positions. However, the XRD patterns of 2.5% Ru/MgAl-R160 catalyst is still comparable to that of the MgAl LDH support. Conversely, by increasing the reduction temperature from 160 °C to 300 °C, the characteristic diffraction peaks of MgAl support in the resulting catalysts disappeared, leaving two broad diffraction peaks by (003) and (110) facets with comparatively low intensities, which suggests dehydration of the support at high temperatures and a reduced crystallinity of the hydrotalcite structure. By increasing the reduction temperature from 300 °C to 600 °C, diffraction peaks associated with the LDH phase disappeared completely, suggesting the phase transition from LDH to $Mg_2(Al)O$ layer double oxide (LDO) [158]. Additionally, two diffraction peaks at 43.6° and 63.4° (with the low intensity) were detected, corresponding to crystalline MgO phase, confirming the formation of the $Mg_2(Al)O$ mixed oxide phase with the incorporation of Al^{3+} into the MgO lattice [159]. Figure 3.11 also showed that with the increasing of Ru loading, the peaks at 12° and 23.9°, which corresponds to the reflections of (003) and (006) facets, are decreasing, indicating that Ru NPs dispersed on the surface will influence the crystalline nature of supports slightly. However, the XRD patterns show no characteristic peaks for Ru regardless of the loading, which confirmed the well dispersion of Ru species on the MgAl support.

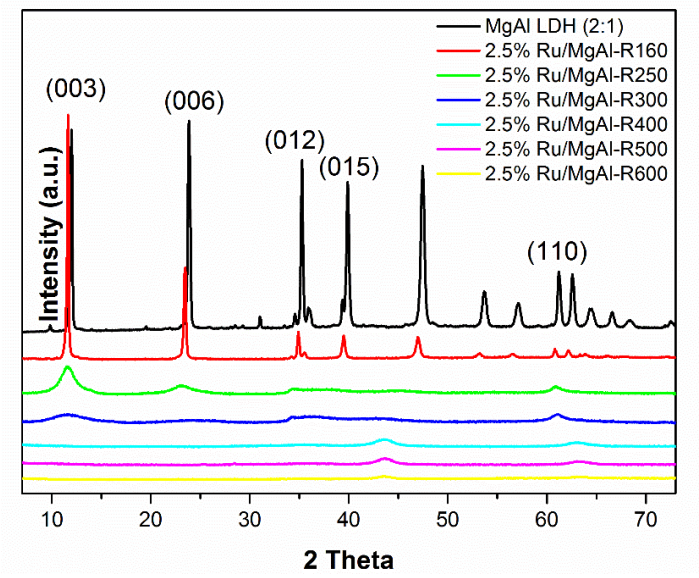

Figure 3.10 XRD patterns of MgAl LDH and fresh 2.5% Ru/MgAl catalysts reduced at different temperatures of 160 °C, 250 °C, 300 °C, 400 °C, 500 °C and 600 °C, respectively, under H_2.

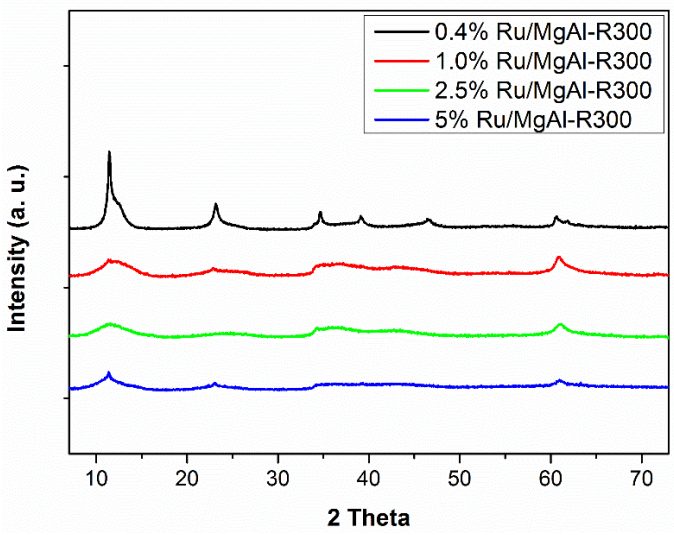

Figures 3.11 XRD patterns of fresh Ru/MgAl-R300 catalysts with different Ru loading reduced at 300 °C.

SEM and HRTEM were performed (Figures 3.12–3.17) to understand the effect of reduction temperature on Ru particle size and dispersion in the catalysts. According to the SEM micrographs (Figure 3.12), the MgAl LDH nanocrystals under study (by hydrothermal synthesis) exhibits the well-defined hexagonal shape with average crystal sizes of ~2.7 μm, being consistent with the XRD results. After the reduction treatments at different temperatures, the shape of LDH remained intact. The elemental mapping

analysis of the materials (Figures 3.13−3.15) shows that the Ru is uniformly distributed on the support. Additionally, TEM analysis revealed the particle size distribution of the resulting catalysts (Figure 3.16). The catalysts reduced at <300 °C showed an average particle size of Ru of 1.6−1.7 nm, while it is 1.9−2.0 nm for the catalysts reduced at above 400 °C (Table 3.4). The slight increase of the Ru NPs size could be attributed to the phase transformation of the support (*i.e.* from LDH to LDO). High-resolution TEM image (Figure 3.17) also revealed that the Ru NPs was dominated by the Ru (002) plane with interlayer spacing of ~0.21 nm regardless of the reduction temperature. Previous study showed that the hydrogenation activity is positively correlated with the Ru particle size, and relatively large Ru NPs (<3 nm) reduced the energy barrier for CO_2 hydrogenation [93]. Conversely, based on the calculated TOFs of the catalysts under study (Figure 3.3d), the Ru/MgAl-R250 catalyst shows the highest TOFs, and the catalysts reduced at >400 °C presents significantly low TOFs. Accordingly, the particle size of Ru catalysts might not play a key role in the NTP-catalysis.

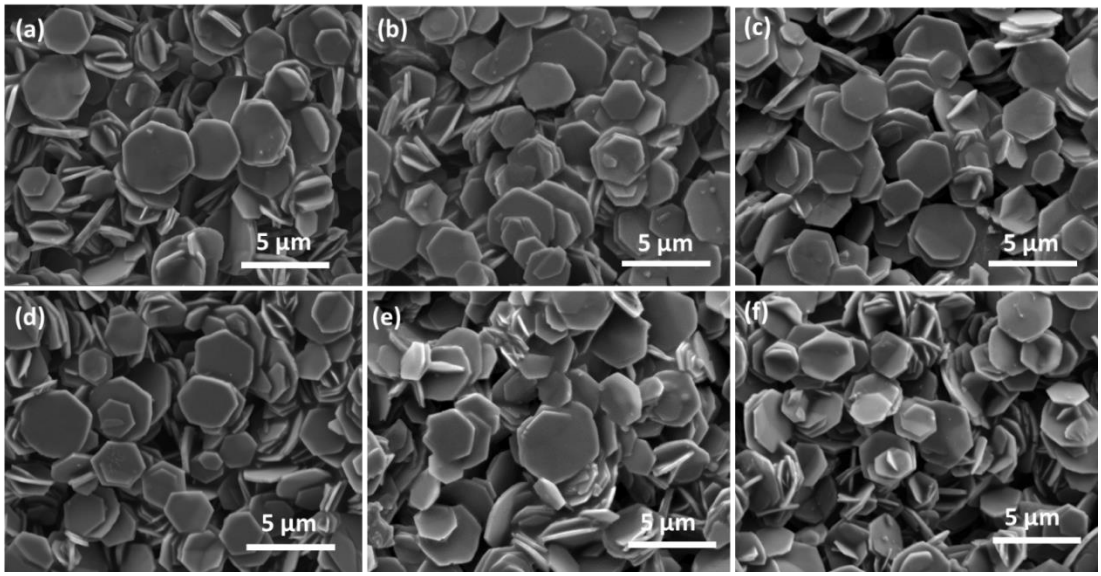

Figure 3.12 SEM images of 2.5% Ru/MgAl catalysts reduced under different temperatures. (a) MgAl LDH, (b) 160 °C, (c) 300 °C, (d) 400 °C, (e) 500 °C, and (f) 600 °C.

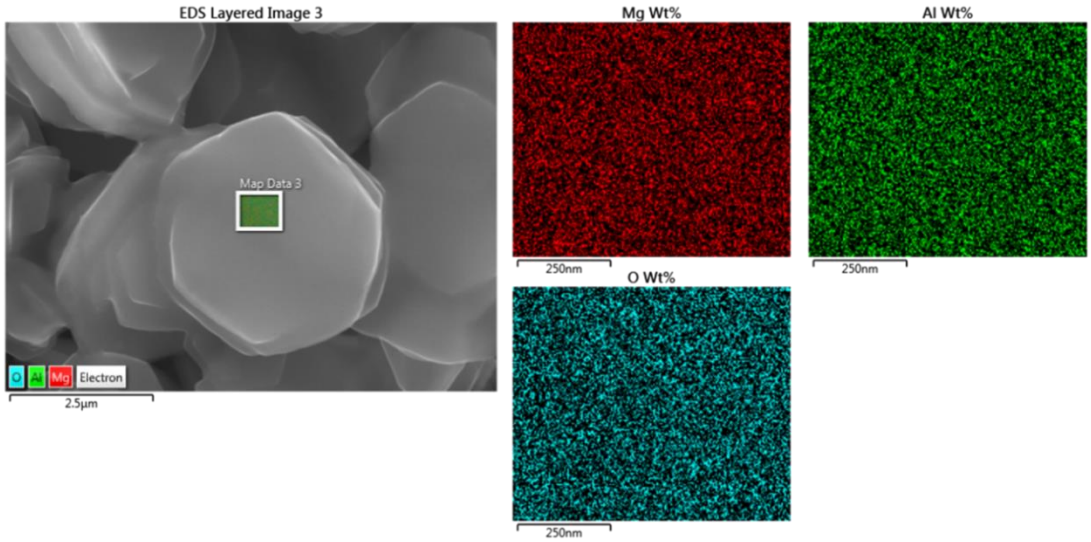

Figure 3.13 SEM and EDX elemental analysis of the as-synthesised MgAl LDH.

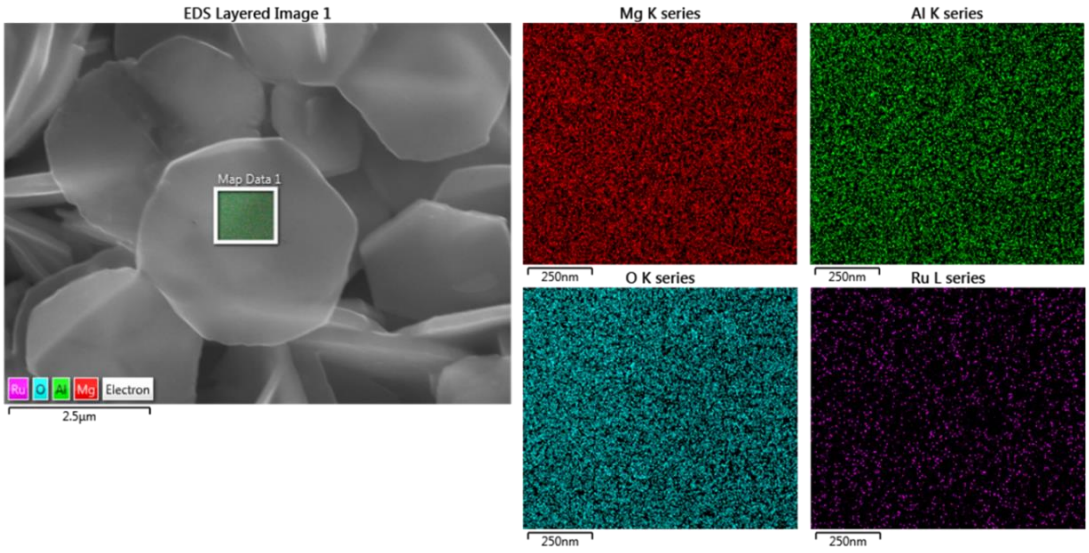

Figure 3.14 SEM and EDX elemental analysis of the as-synthesised 2.5% Ru/MgAl-R300 catalyst.

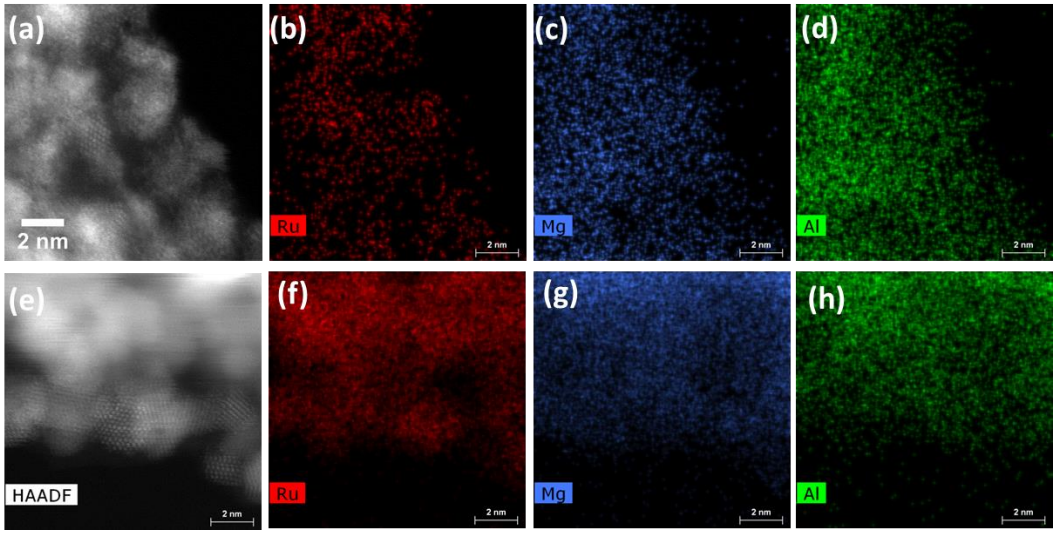

Figure 3.15 HAADF image and selected area of Ru/MgAl catalysts for elemental mapping. (a-d) 2.5% Ru/MgAl- R300; (e-f) 2.5% Ru/MgAl-R500.

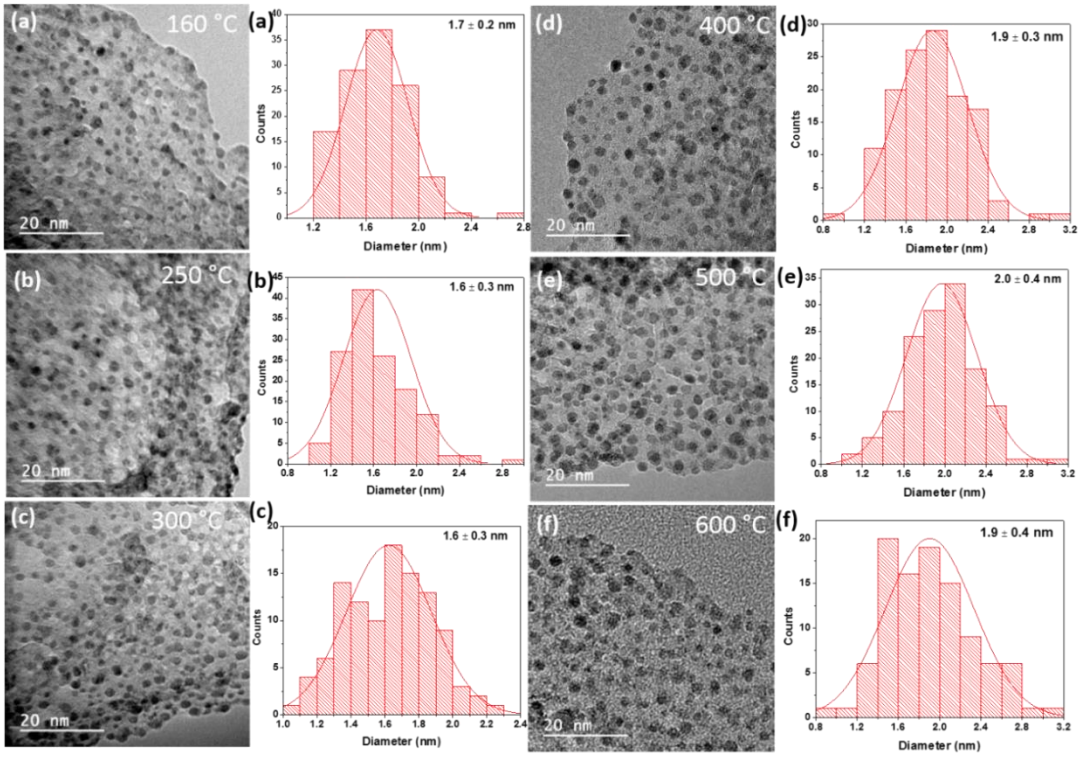

Figure 3.16 TEM images and the corresponding particle size distribution of 2.5% Ru/MgAl catalysts reduced at different reduction temperatures of (a) 160 °C, (b) 250 °C, (c) 300 °C, (d) 400 °C, (e) 500 °C, and (f) 600 °C. Histograms are made by counting more than 100 particles for multiple HRTEM images taken in different sample regions.

Table 3.4 The metal dispersion and particle size information of the as-synthesised catalysts reduced at different temperatures.

Sample (2.5% Ru/MgAl)	Ru loading[a] (wt.%)	Average Ru particle size[b] (nm)	Ru dispersion[c] (%)	Surface metallic Ru concentration[c] (mmol g^{-1})
R160	2.0	1.7	22.38	1.8
R250	2.1	1.6	15.02	1.15
R300	2.1	1.6	19.94	1.74
R400	2.3	1.9	16.23	1.60
R500	2.6	2.0	14.94	1.47
R600	2.7	1.9	12.73	1.35

[a]Actual Ru loading was measured by ICP-OES; [b]Average Ru particle size was determined by TEM; [c]Ru dispersion and surface metallic Ru concentration were calculated based on pulse CO chemisorption measurement at RT.

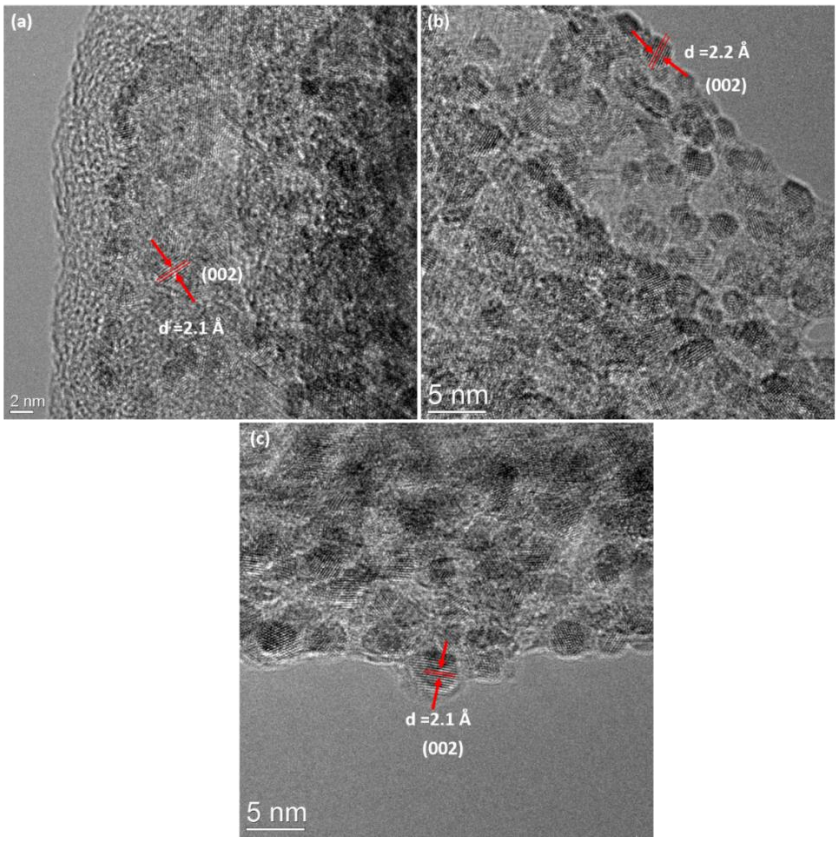

Figure 3.17 High-resolution TEM images of 2.5% Ru/MgAl catalysts reduced at different reduction temperatures of (a) 160 °C, (b) 300 °C, (c) 600 °C.

As the electronic state of the active phase is an important factor to influence the catalytic behaviour, FTIR of CO adsorption and XPS were performed to understand the effect of reduction temperature on the electronic states of surface Ru species on the support. As shown in Figure 3.18, the bands at 2173 cm^{-1} is assigned to physisorbed CO and the bands at 1950–2070 cm^{-1} are attributed to linearly bonded CO [160]. The IR bands located at 2051 cm^{-1} and 2120−2130 cm^{-1} were assigned to the CO species linearly adsorbed on the Ru^0 surfaces and Ru with a higher oxidation state [161], respectively, while the bands at 1983 cm^{-1} were associated with CO adsorbed on the very small Ru NPs [162]. In the case of Ru/MgAl-R600 catalyst, the peak at 1983 cm^{-1} disappeared, and a new shoulder peak at 2070 cm^{-1} emerged, corresponding to the multiply bonded carbonyl species (Ru^0-$(CO)_n$ species) [163]. Additionally, the linear CO bands shifted to higher wavenumber with an increase in reduction temperature, which is due to the variation in Ru particle size and the phase transformation (from LDH to LDO), in agreement with the findings from XRD and TEM [164].

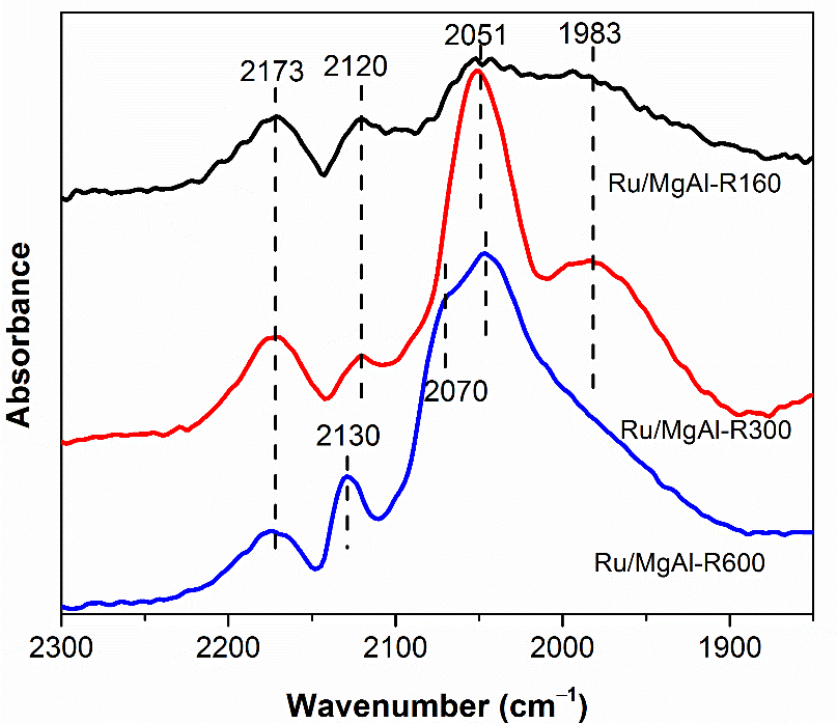

Figure 3.18 FTIR spectra of adsorbed CO (CO-DRIFT) on the reduced 2.5% Ru/MgAl-R160, 2.5% Ru/MgAl-R300 and 2.5% Ru/MgAl-R600 catalysts.

The XPS spectra of 2.5% Ru/MgAl catalysts reduced at 160 °C, 300 °C and 600 °C are shown in Figure 3.19 to understand the effect of reduction temperature on the Ru chemical state, and the summary of the calculated Ru^{x}/Ru^{Total} ($Ru^{Total}=Ru^{0}+Ru^{4+}+Ru^{6+}$) ratios is given in Table 3.5. As the Ru NPs can be oxidised due to air exposure at RT during sample preparation, the XPS peaks of Ru3d were deconvoluted into Ru^{4+} (RuO_2), Ru^{6+} (RuO_3) and Ru^{0} [165]. Regardless of the reduction temperature, the Ru $3d_{5/2}$ peak from RuO_3 slightly shifts within 0.1 eV, indicating that the chemical state of RuO_3 remains unchanged. Conversely, it can be seen that the binding energy of RuO_2 was much higher on the Ru/MgAl catalysts reduced at <300 °C (281.3 eV), which may be due to the relatively strong interaction between Ru NPs and supports or the inadequate reduction [92, 166]. By increasing the reduction temperature from 160 °C to 600 °C, Ru^{6+}/Ru^{Total} ratio of the resulting catalyst decreased by ~28% (Table 3.5), and an additional Ru^{0} peak appeared in the Ru/MgAl-R600 catalyst, confirming the improved reduction level of Ru species in the catalyst after the reduction treatment at high temperatures. Also, O1s score level could be fitted into four peaks at 529.4−530.6 eV, 530.8 eV, 531.7−532.5 eV, and 534 eV, which can be assigned to O^{2-} from RuO_x, surface oxygen, OH− and interlayer H_2O, respectively [167]. The analysis of O1s core level shows that the peak of interlayer H_2O between LDH layers gradually disappeared due to dehydration at elevated temperatures, being in line with the XRD results. The findings from the CO-FTIR and XPS revealed that the electronic features of Ru NPs were different with different reduction temperatures, and thus affecting the catalytic performance for CO_2 hydrogenation.

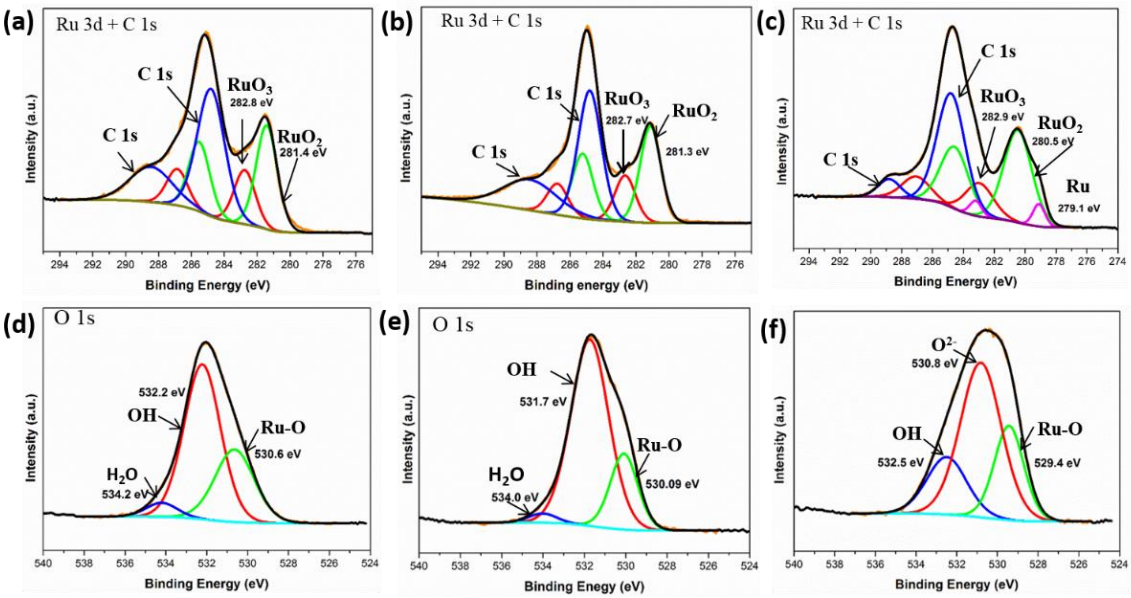

Figure 3.19 XPS spectra of the (a, d) 2.5% Ru/MgAl-R160, (b, e) 2.5% Ru/MgAl-R300 and (c, f) 2.5% Ru/MgAl-R600, Ru 3d, C1s and O1s.

Table 3.5 XPS data of 2.5% Ru/MgAl-R160, 2.5% Ru/MgAl-R300 and 2.5% Ru/MgAl-R600 catalysts.

Catalysts	$Ru^0/(Ru^0+Ru^{4+}+Ru^{6+})$	$Ru^{4+}/(Ru^0+Ru^{4+}+Ru^{6+})$	$Ru^{6+}/(Ru^0+Ru^{4+}+Ru^{6+})$
2.5% Ru/MgAl-R160	–	65.7%	34.3%
2.5% Ru/MgAl-R300	–	67.6%	32.4%
2.5% Ru/MgAl-R600	7.2%	68.2%	24.6%

The metal-support interaction is another factor affecting the catalytic performance, which was determined by H_2-TPR (Figure 3.20). For the control experiment using the commercial RuO_2 catalyst, only one reduction peak at 213 °C was measured, corresponding to the reduction of Ru^{4+} to Ru^0 [168]. Regarding the 2.5% Ru/MgAl catalysts, TPR results show that, in general, the metal-support interaction becomes stronger with an increase in the reduction temperature. In the case of the as-prepared $RuCl_3$/MgAl LDH, the peak at 126 °C can be assigned to reduction of $RuCl_3$ adsorbed on the surface of MgAl LDH [169]. For the reduced 2.5% Ru/MgAl catalysts, three reduction peaks centred at 120−180 °C (peak I), 185−220 °C (peak II), and 320−340 °C

(peak III), which are attributed to the weakly supported RuO_x species on the support, strongly supported RuO_x species and the surface or subsurface oxygens, respectively [92, 166]. For 2.5% Ru/MgAl catalysts reduced at 160−300 °C, the peak I gradually shifts to higher values from 135 °C to 175 °C, suggesting that the improved metal-support interaction promoted by increasing the reduction temperature (<300 °C). Interestingly, when the Ru/MgAl catalysts were reduced at high temperatures, namely >400 °C, the peak I shifted back to 120 °C with a shoulder peak appeared at 132 °C, suggesting the reduced metal-LDO support interaction compared with that of metal-LDH. Coupled with the catalytic performances shown in Figure 3.3, it was found that the strong interaction between Ru species and support favours the catalysis. Accordingly, we proposed that the metal-support interaction plays a key role for the NTP-catalysis activity over the catalysts reduced at 160−300 °C compared with the variation in the Ru particle sizes.

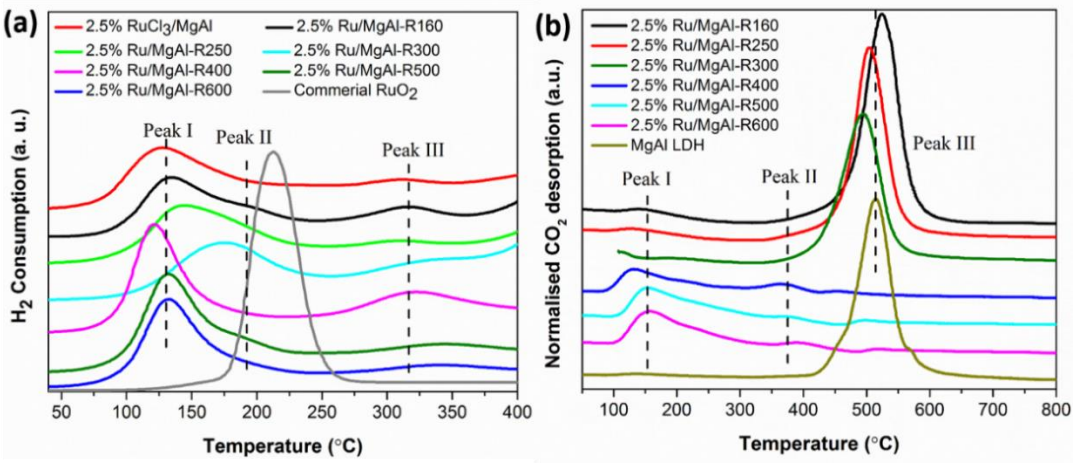

Figure 3.20 (a) H_2-TPR and (b) CO_2-TPD profiles of 2.5% Ru/MgAl catalysts reduced at different temperatures.

The surface basicity of Ru/MgAl catalysts, which is beneficial to the adsorption and activation of CO_2, was evaluated by CO_2-TPD, as shown in Figure 3.20b. For 2.5% Ru/MgAl catalysts reduced at 160−300 °C, only one strong peak appears at about 500 °C, which is from the LDH support (*i.e.* completely decomposition of CO_3^{2-} group in the internal layer). No other CO_2 desorption peaks were detected, as the strong

interaction between Ru and LDH lead to very weak adsorption of CO_2, which can be easily removed by Ar purge. However, for 2.5% Ru/MgAl catalysts reduced at >400 °C, two dominant peaks located at 129−154 °C and 367−399 °C was observed, which can be ascribed to the surface sites of weak (OH)− and strong (unsaturated oxygen pairs) basicity sites, respectively [158, 159]. The peak for CO_2 desorption at 129−154 °C originates from the decomposition of carbonate-like species formed by CO_2 with surface OH− group [166], while the peak at 367−399 °C can be attributed to the migration of Al^{3+} into the MgO framework, forming the unsaturated oxygen on the surface [170], which is in agreement with the XRD results. The findings from the CO_2-TPD shows a relatively strong CO_2 adsorption on the catalysts reduced at >400 °C. Interestingly, these catalysts showed relatively poor activity (Figure 3.3) in the NTP-catalysis. Therefore, these findings suggest that the strongly adsorbed CO_2 on the surface may block the active sites for surface reactions, which is in line with previous findings [171].

3.3.3 Mechanistic study for NTP-assisted CO_2 hydrogenation.

To elucidate the reaction pathway of catalytic CO_2 hydrogenation under NTP activation, *in situ* DRIFTS coupled with mass spectrometry (MS) characterisation of the Ru/MgAl-R300 and Ru/MgAl-R600 catalysts was performed comparatively under both thermal (at 270 °C) and NTP conditions with different feed gases. The 2.5% Ru/MgAl-R300 and Ru/MgAl-R600 catalysts were selected since they showed the distinct catalytic activity due to the catalyst reduction temperature. Under the thermal conditions (at 270 °C), Figure 3.21 shows the evolution of IR bands for the surface species switching from CO_2/H_2 exposure to subsequent purge with H_2 and Ar over the 2.5% Ru/MgAl-R300 catalyst. Under the flow of CO_2 and H_2, intense peaks developed at 3017 and 2018 cm^{-1}, which are characteristic of CH_4 and adsorbed CO, were observed. Moreover, when the feed switched from CO_2+H_2 to H_2 purge, the CO peak disappeared immediately within 2 min, which is due to adsorbed H* reacted with the CO_{ad} to form

CH_4. Conversely, when the feed switched to Ar, CO peak disappeared more slowly (within 5 min) under the Ar purge due to the thermal removal. There is no formation of other carbonaceous species on the surface, indicating that (*i*) CO is the important intermediate and (*ii*) the direct carbon-oxygen bond dissociation to CO and C on the surface dominates CO_2 hydrogenation over the 2.5% Ru/MgAl-R300 catalyst under the thermal conditions (as shown in Table 3.6) [172, 173].

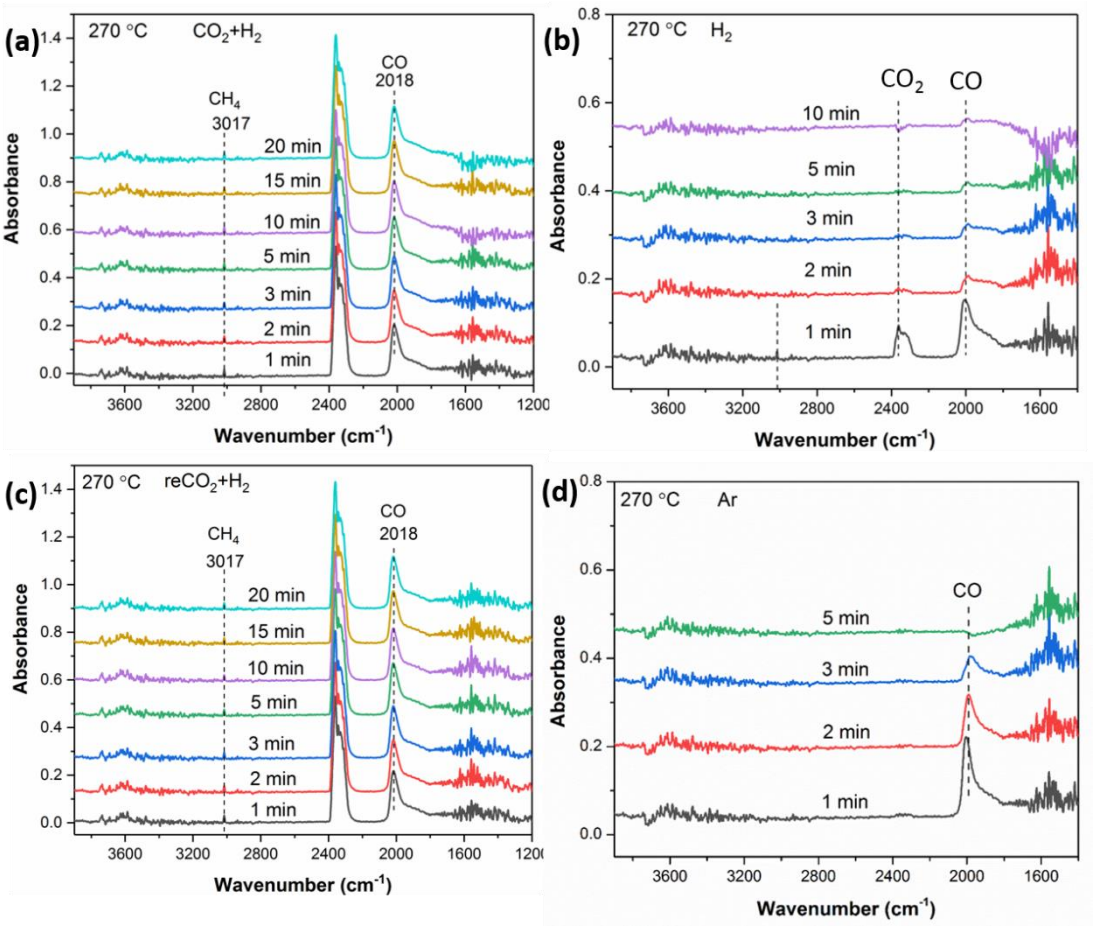

Figure 3.21 *In situ* DRIFTS spectra of surface species collected at 270 °C in thermal activated CO_2 hydrogenation over the 2.5% Ru/MgAl-R300 catalyst. (a) introduce feed: 1% CO_2+4% H_2+ Ar; (b) switch to H_2/Ar; (c) switched back to feed: 1% CO_2+4% H_2+ Ar; and then switch to (d) Ar;

Table 3.6 The reaction pathways of CO_2 hydrogenation over the 2.5% Ru/MgAl-R300 catalyst under thermal conditions.

Thermal activated CO_2 hydrogenation	
$CO_2 \rightarrow CO_{ad} + O_{ad}$	Eq. 3.11
$H_2 \rightarrow 2H_{ad}$	Eq. 3.12
$CO_{ad} \rightarrow C_{ad} + O_{ad}$	Eq. 3.13
$C_{ad} + H_{ad} \rightarrow CH_{ad}$	Eq. 3.14
$CH_{ad} + H_{ad} \rightarrow CH_{2,ad}$	Eq. 3.15
$CH_{2,ad} + H_{ad} \rightarrow CH_{3,ad}$	Eq. 3.16
$CH_{3,ad} + H_{ad} \rightarrow CH_4$	Eq. 3.17
$O_{ad} + 2H_{ad} \rightarrow H_2O$	Eq. 3.18

Comparably, for 2.5% Ru/MgAl-R600 catalyst, under the flow of CO_2 and H_2 (Figure 3.22), in addition to the surface CO_{ad} and methane species (at 2000 and 3017 cm^{-1}), the characteristic peaks of formate species (at 2867, 1601 and 1410 cm^{-1}) were also detected on the surface. And when the feed gas switched from CO_2+H_2 to H_2 purge (Figure 3.22b), the CO peak disappeared immediately while the formate peaks only decreased slightly. Moreover, when the feed gas switched to from CO_2+H_2 to Ar (Figure 3.22d), the formate peaks displayed similar trend with those under the H_2 purge, suggesting that the decrease of formate peaks under H_2 was due to the thermal removal and formate species might not participate in CH_4 formation process. Therefore, CO_2 hydrogenation under the thermal condition over the 2.5% Ru/MgAl-R600 catalyst proceeded with similar pathways to those of the Ru/MgAl-R300 catalyst.

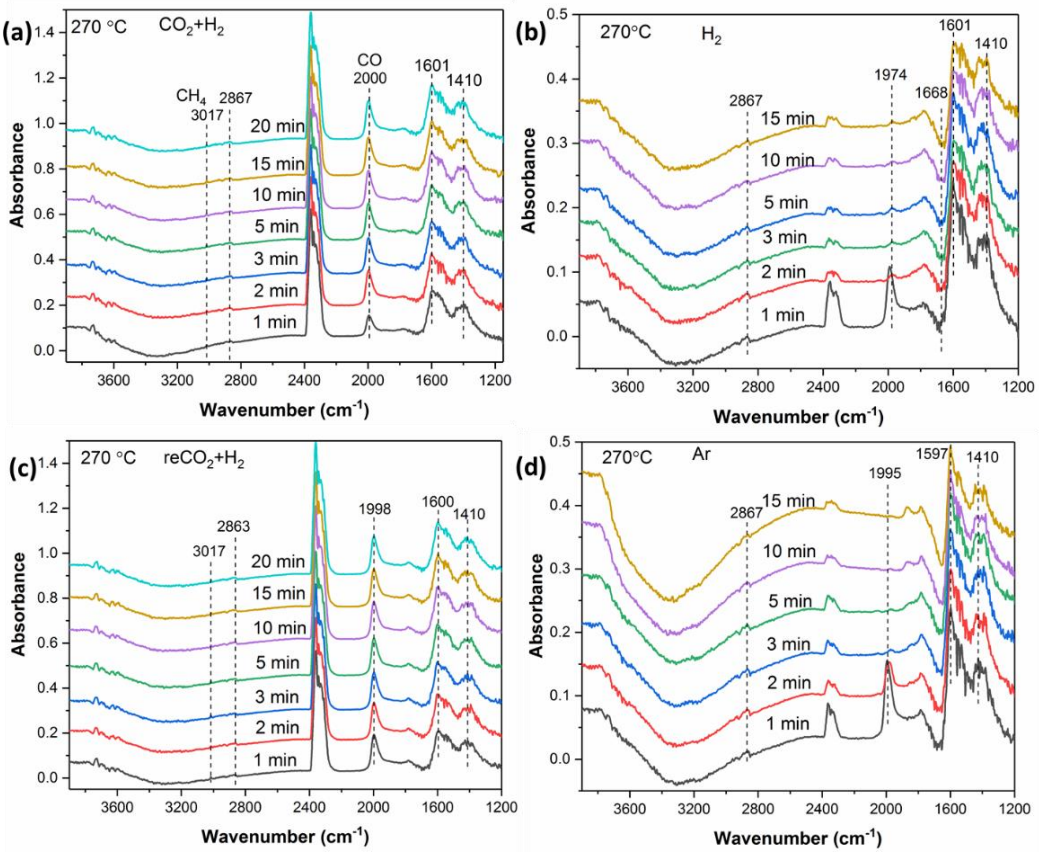

Figure 3.22 *In situ* DRIFTS spectra of surface species collected at 270 °C in thermal activated CO_2 hydrogenation over the 2.5% Ru/MgAl-R600 catalyst. (a) introduce feed: 1% CO_2+4% H_2+ Ar; (b) switch to H_2/Ar; (c) switched back to Feed: 1% CO_2+4% H_2+ Ar; and then switch to (d) Ar.

Under the NTP conditions, more carbon species were detected by DRIFTS, indicating that a more complex pathway for CO_2 conversion is present for the NTP-catalysis. According to the previous studies [80, 174], in the plasma-activated CO_2 hydrogenation with catalysts, both gas-phase reactions and plasma-assisted surface reactions contribute to CO_2 conversion and selectivity to CH_4, *i.e.* (*i*) the dissociation of CO_2 and H_2 in the gas phase, followed by surface hydrogenation reactions to produce CH_4 (the dissociated H species in the gas phase may participate in the surface hydrogenation reactions); (*ii*) absorption of CO_2 molecules (in both ground and excited states) on Ru surfaces, and then NTP-assisted surface hydrogenation reactions to produce CH_4 (due to the low bulk temperatures at ~120 °C, the thermal-assisted surface hydrogenation reactions was assumed not possible).

The gas-phase CO_2 dissociation to CO was confirmed by DRIFTS and MS using 1% CO_2/Ar mixture under the NTP conditions (with 2.5% Ru/MgAl-R300 catalyst, Figure 3.23). Under the plasma-off condition, surface species were not detected with CO_2 flow. When the plasma was on, the linearly adsorbed CO_{ad} peak (at 2125, 2064, 2018 and 1847 cm^{-1}), carbonate (1561 and 1282 cm^{-1}) species were formed immediately, suggesting the adsorption of ground-state or vibrationally excited CO_2 species on the catalyst surface. Moreover, the CO_2 dissociation into CO and O in the gas phase can be confirmed by MS (Figure 3.23d). By switching off the plasma again, the relevant peaks of the carbon species remained, proving the strong adsorption of the species on the surface (Figure 3.23c).

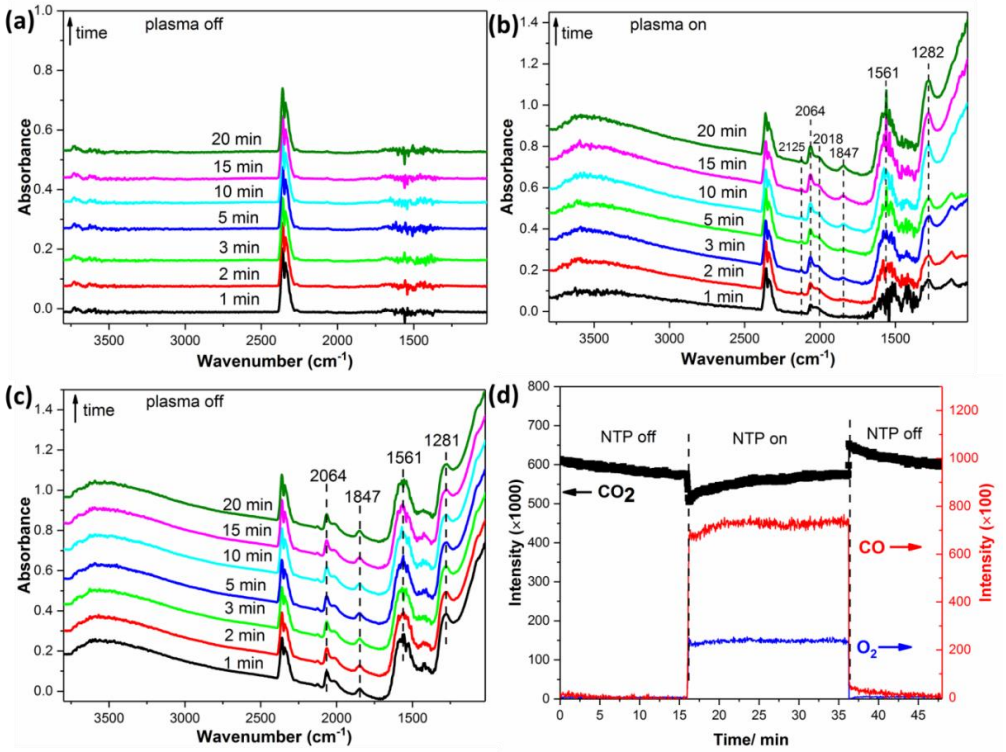

Figure 3.23 *In situ* DRIFTS spectra of surface species on the 2.5% Ru/MgAl-R300 catalyst. (a) Plasma-off condition with the gas mixture of 1% CO_2 + Ar; (b) Plasma-on condition with the gas mixture of 1% CO_2 + Ar (5 kV, 23.5 kHz). (c) Plasma-off condition with the gas mixture of 1% CO_2 + Ar. (d) Corresponding MS signals collected simultaneously from *in situ* DRIFTS cell as a function of time during NTP-on-off conditions.

With the reaction gas mixture (*i.e.* 1% CO_2/4% H_2/Ar), prior to the ignition of plasma, only the gas phase peaks related to CO_2 (at 2361 and 2343 cm^{-1}, as shown in Figure 3.24a) were detected, and MS profile (Figure 3.25) confirmed that the catalyst (2.5% Ru/MgAl-R300) was not active for CO_2 hydrogenation without NTP. Upon the ignition of plasma, the instantaneous appearance of CH_4 signal (m/z = 15) associated with a decrease of CO_2 signal (m/z = 44) in MS profiles (Figure 3.25) confirmed the activity of the NTP-catalysis system. Additionally, characteristic peaks of carbonyl (CO_{ad}, at 2023 and 1945 cm^{-1}), carbon-hydroxyl (COH_{ad}, at 1300 cm^{-1}) and formyl species (HCO_{ad}, at 1756 and 1132 cm^{-1}) were detected by DRIFTS simultaneously on the catalyst surface (Figure 3.24b) [175]. The IR peak at ~1037 cm^{-1} corresponds to methoxy species (OCH_3), showing no changes during the reaction, suggesting the formation of methanol, which was confirmed by the in-line MS analysis with increased intensity of m/z = 31 (corresponding to methanol), as shown in Figure 3.26. The band at 3016 cm^{-1} is normally attributed to surface methane which was not detected under the condition used. This may be caused by the fast desorption of CH_4 from the catalyst surface under the NTP conditions [176]. When the plasma was switched off, MS profile showed that the system was not active anymore (Figure 3.25). Interestingly, by comparing DRIFTS spectra of the NTP system with CO_2/Ar (Figure 3.23) and the CO_2/H_2/Ar (Figure 3.24) feed gases, the presence of H_2 affects the CO binding on Ru, which is evidenced by the CO_{ad} peak shift from 2064 and 2018 cm^{-1} to 2023 and 1945 cm^{-1}, suggesting the transformation of multicarbonyl to monocarbonyl species [163]. Moreover, the interaction between Ru and CO_{ad} was weakened (Figure 3.24c) in the presence of H_2, causing the gradual disappearance of CO_{ad} bands after plasma extinction. This is due to the co-absorption of H* and CO*/O* on the Ru surface [177].

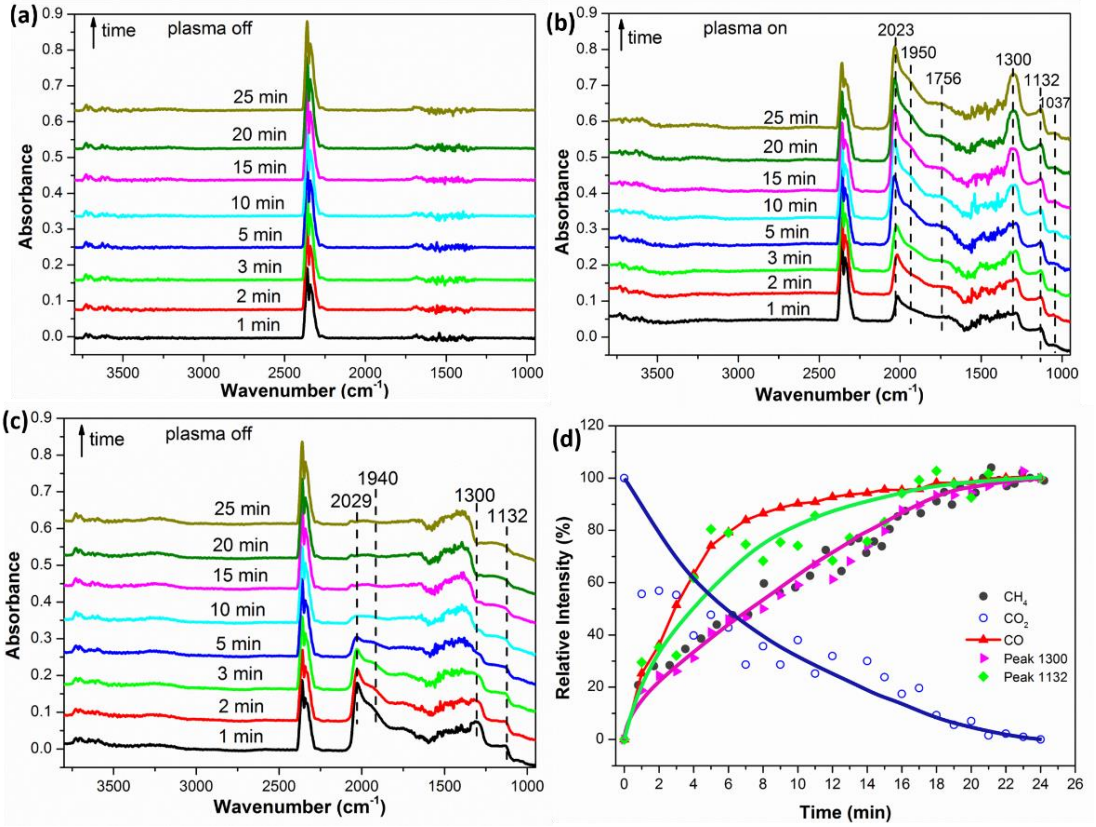

Figure 3.24 *In situ* DRIFTS spectra of surface species on the 2.5% Ru/MgAl-R300 catalyst under (a) plasma-off condition with the feed gas of 1% CO_2 + 4% H_2 + Ar; (b) plasma-on condition with the feed gas (5.0 kV, 23.5 kHz); and (c) plasma-off condition with the feed gas. (d) Relative intensities of surface species as a function of time-on-stream recorded in the *in situ* DRIFTS from (b) and relative intensity change of methane recorded in mass spectra (Figure 3.25) during CO_2 hydrogenation upon NTP on (5.0 kV, 23.5 kHz).

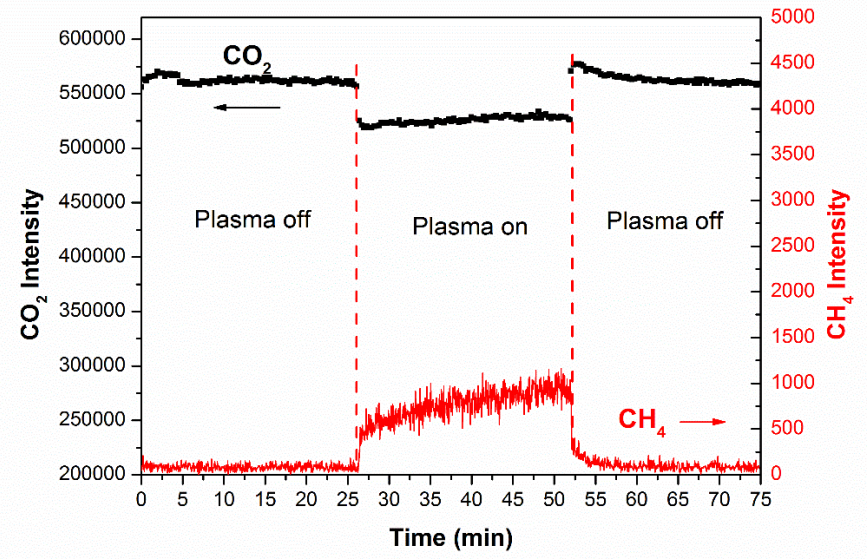

Figure 3.25 Corresponding MS signals collected simultaneously from the DRIFTS cell as a function of time during NTP-assisted CO_2 hydrogenation over the 2.5% Ru/MgAl-R300 catalyst.

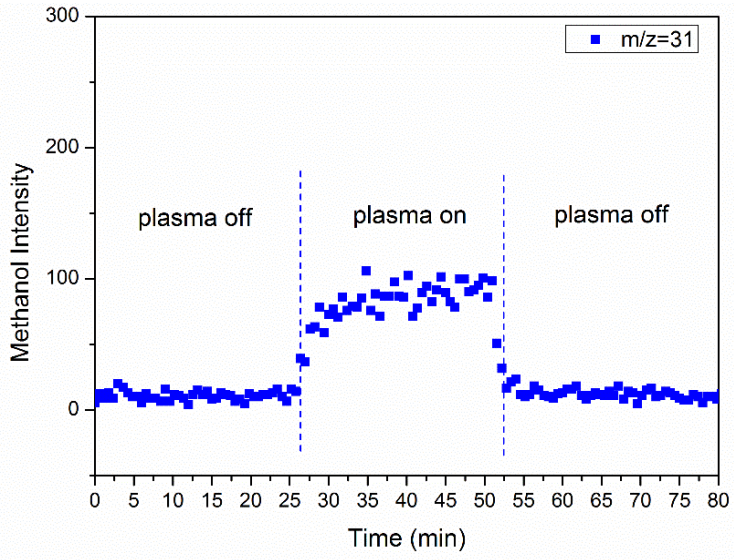

Figure 3.26 Corresponding MS signals of methanol collected simultaneously from the DRIFTS cell as a function of time on stream during NTP-assisted CO_2 hydrogenation over the 2.5% Ru/MgAl-R300 catalyst.

To illustrate the quantitative agreement between the intensity change of the surface species and the formation of CH_4 in the NTP-catalysis system, we include the evolution of the surface species as a function of time from *in situ* DRIFTS (Figure 3.24b), together

with the intensity increase of the CH_4 from MS (Figure 3.25). The intensity of surface CO_2 species shows a significant decrease, while CH_4 signal from MS increased continuously over the course of the reaction, suggesting that CO_2 was hydrogenated to produce CH_4. In addition, the CO signal shows a steeper increase than that of CH_4, confirming the possible CO production both plasma-assisted CO_2 dissociation in the gas phase and the dissociation of adsorbed CO_2 on the catalyst. And the progressive increase of HCO_{ad} species and COH_{ad} profiles are consistent with the rate of CH_4 formation, suggesting that CO_2 hydrogenation in the system under study was *via* the HCO and COH pathway [173, 178, 179]. Also the concentration of HCO_{ad} is higher than that of COH_{ad} groups, due to the low HCO_{ad} formation energy (~1.25 eV) compared to that of COH_{ad} (~1.42 eV) [180]. Accordingly, the key elementary surface reaction steps are proposed for the NTP-catalysis over the 2.5% Ru/MgAl-R300 catalyst, in which CO_2 is dissociated to carbonyl (CO_{ad}) and O* species, then was hydrogenated to formyl intermediate (HCO_{ad} and COH_{ad}) species. The overall reaction schemes are shown in Figure 3.27 and Table 3.8.

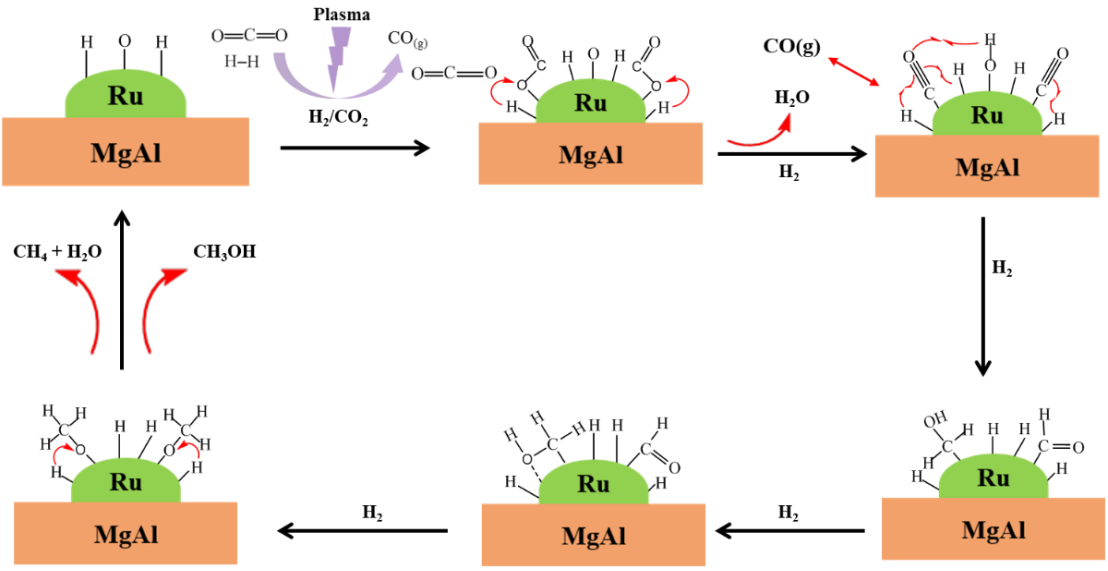

Figure 3.27 Scheme of the reaction pathways of the NTP-activated CO_2 hydrogenation over 2.5% Ru/MgAl-R300 catalyst.

Table 3.7 The reaction pathways of CO_2 hydrogenation over the 2.5% Ru/MgAl-R300 catalyst under the NTP conditions.

Plasma-gas phase CO_2 activation		Plasma-catalyst surface CO_2 activation	
$e^- + CO_2 \rightarrow CO^* + O^* + e^-$	Eq. 3.19	CO_2, ad $\rightarrow CO_{ad} + O_{ad}$	Eq. 3.21
$e^- + H_2 \rightarrow 2H^* + e^-$	Eq. 3.20	$H_{2,ad} \rightarrow 2H_{ad}$	Eq. 3.22
$2H + O \rightarrow H_2O$		$2H + O \rightarrow H_2O$	
$CO^* \rightarrow CO_{ad}$			
$CO_{ad} + H^* \rightarrow HCO_{ad}$			Eq. 3.23
$CO_{ad} + H_{ad} \rightarrow HCO_{ad}$			Eq. 3.24
$CO_{ad} + H^* \rightarrow COH_{ad}$			Eq. 3.25
$CO_{ad} + H_{ad} \rightarrow COH_{ad}$			Eq. 3.26
$HCO_{ad} + 2H \rightarrow H_3CO_{ad}$			Eq. 3.27
$COH_{ad} + 2H \rightarrow CH_3O_{ad}$			Eq. 3.28
Step towards methane		Step towards methanol	
$CH_3O_{ad} + H \rightarrow CH_{3,ad} + OH_{ad}$	Eq. 3.29	$H_3CO_{ad} + H \rightarrow CH_3OH$	Eq. 3.32
$CH_{3,ad} + H \rightarrow CH_4$	Eq. 3.30		
$OH_{ad} + H \rightarrow H_2O$	Eq. 3.31		

For the NTP system employing the Ru/MgAl-R600 catalyst, *in situ* DRIFTS analysis revealed multiple surface species, suggesting a more complex reaction mechanism of CO_2 hydrogenation than the system with the Ru/MgAl-R300 catalyst. Under the plasma-off condition with CO_2/Ar gas at RT, surface bicarbonate with the characteristic IR bands at 1674, 1420 and 1224 cm^{-1} and carbonate at 1538 cm^{-1} were observed, as shown in Figure 3.28, due to the CO_2 interaction with the surface hydroxyl group on the catalyst [181]. This confirms that the high reduction temperature lead to more active sites for CO_2 adsorption, in agreement with our CO_2 TPD result. Upon the plasma ignition, more surface carbon species were produced due to the plasma excitation, including the bridged and linearly adsorbed CO_{ad} peaks (at 2129, 2078, 2027 and 1867 cm^{-1}), bicarbonate (at 1660 and 1415 cm^{-1}) and bidentate carbonate (at 1538 and 1295 cm^{-1}). Similar with the 2.5% Ru/MgAl-R300 catalyst, the carbon species interacted strongly with the surface of catalyst, evidenced by the sustained peaks when the NTP was switched off. CO and O_2 due to the dissociation of CO_2 in the gas phase were also detected by MS as well (Figure 3.28d).

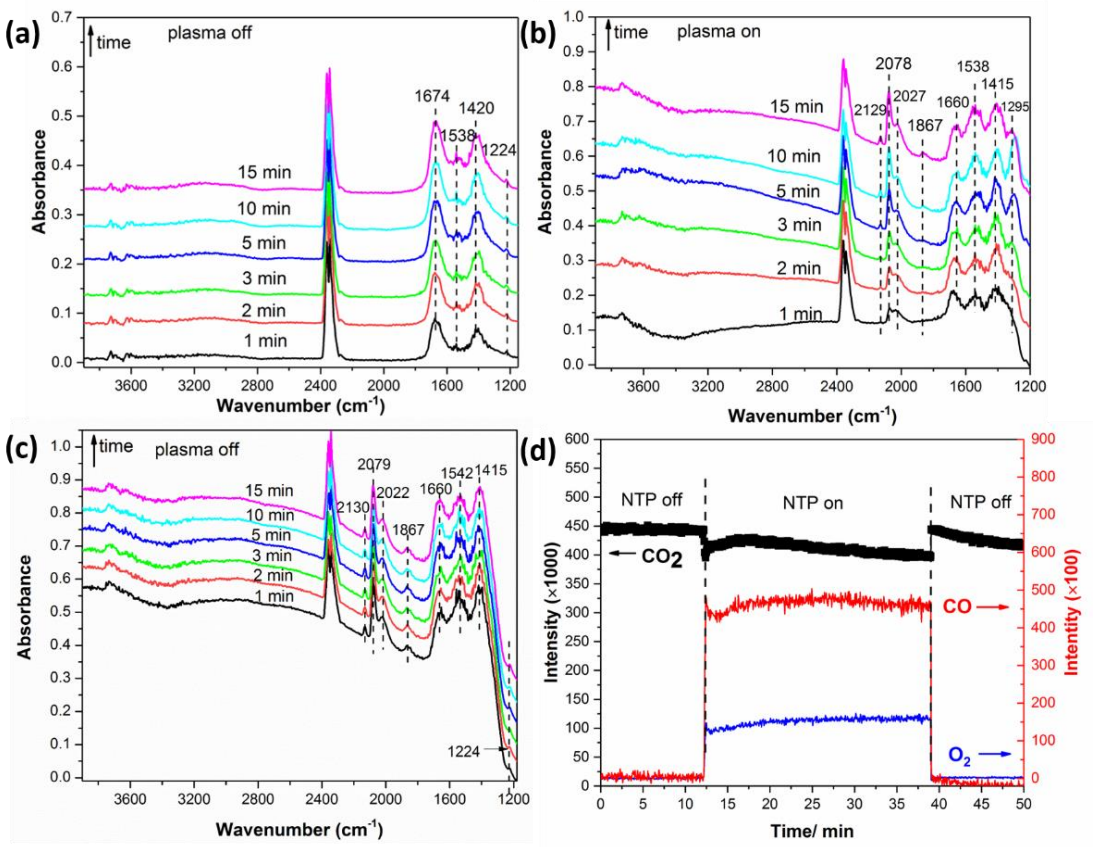

Figure 3.28 *In situ* DRIFTS spectra of surface species on the 2.5% Ru/MgAl-R600 catalyst. (a) Plasma-off condition with the gas mixture of 1% CO_2 + Ar; (b) Plasma-on condition with the gas mixture of 1% CO_2 + Ar (5 kV, 23.5 kHz). (c) Plasma-off condition with the gas mixture of 1% CO_2 + Ar. (d) Corresponding MS signals collected simultaneously from *in situ* DRIFTS cell as a function of time during NTP-on-off conditions.

With the reactant feed gas (*i.e.* 1% CO_2/4% H_2/Ar) (Figure 3.29b), carbonyl (CO_{ad}, at 2038 and 1945 cm^{-1}) and oxygenated species of CH_xO (at 1130 and 1304 cm^{-1}) were measured instantaneously under the plasma-on condition and then disappeared gradually (within 5 min) when plasma was off. This suggests that CHO species and CO_{ad} is active for reactions towards CH_4 formation, and CH_xO species originated from the reaction between CO* and H*, *i.e.* CO* + H* → CHO*, and then CHO* + H* → OCH_3. Finally, OCH_3 reacted with H* to produce CH_4 and H_2O, which is similar to the findings from the Ru/MgAl-R300 catalyst. However, the formation of methanol on Ru/MgAl-R600 catalyst during the catalysis under NTP conditions was insignificant as

no methoxy peak was measured by *in situ* DRIFTS. Conversely, the bicarbonate species (at 1678 and 1410 cm^{-1}) disappeared gradually during the reaction and new IR bands at 2865 and 1601 cm^{-1} emerged which are associated with the adsorbed monodentate formates (HCOO*) (Figure 3.29b) [179], suggesting the bicarbonate species were transformed to formate under plasma. By switching off the plasma, the bicarbonate IR bands at 1662 and 1407 cm^{-1} built up again and overlapped with the formate bands, forming one broad band (Figure 3.29c). Considering that the main location of bicarbonates is on the surface of the support, the decrease of IR intensity of bicarbonate bands under plasma was very likely due to the reaction between bicarbonates and activated H* in the gas phase or at the interface of Ru/support to form formates. A previous study stated that the formate species formed at the interfacial sites are more reactive towards H* than the formates formed on/migrated to the support (to form CH_4), and the latter can accumulate on the surface [182], explaining the remaining formate species on the surface after the NTP-catalysis (when plasma was off). MS profile also showed that when the plasma was switched on, the system was active for CH_4 formation (Figure 3.30). Therefore, based on the *in situ* DRIFT spectroscopic data, the significant evolution of the IR bands supports the assertion of possible reaction pathway of bicarbonate-formate-methane coupled with the formyl pathways for NTP-assisted CO_2 hydrogenation over the Ru/MgAl-R600 catalyst. As shown in Figure 3.29d and Table 3.9, the adsorbed CO_2 reacts with the surface hydroxyl to produce the bicarbonate and carbonate species. The bicarbonate species then combines with the adsorbed hydrogen to produce formate species which undergoes a multistep reaction with hydrogen to produce methane and water (Figure 3.31).

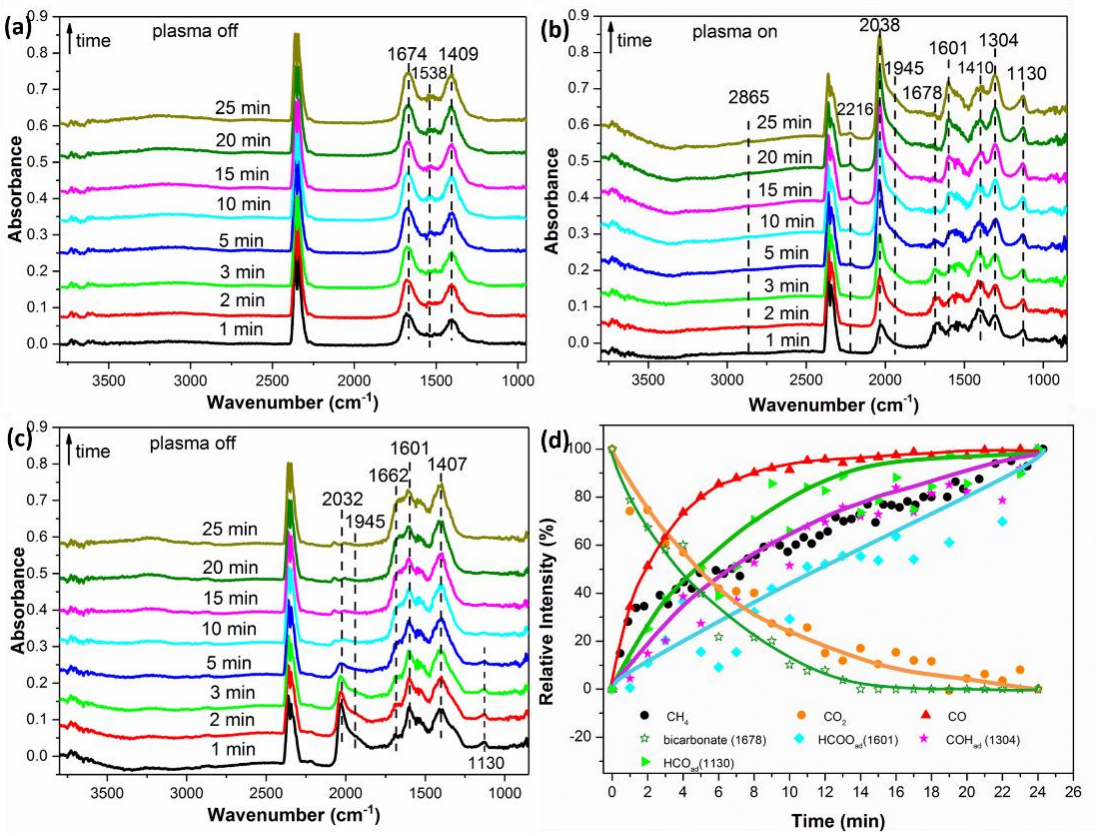

Figure 3.29 *In situ* DRIFTS spectra of surface species on the 2.5% Ru/MgAl-R600 catalyst under (a) plasma-off condition with the feed gas of 1% CO_2 + 4% H_2 + Ar; (b) plasma-on condition with the feed gas (5.0 kV, 23.5 kHz); and (c) plasma-off condition with the feed gas. (d) Relative intensities of surface species as a function of time-on-stream recorded in the *in-situ* DRIFTS from (b) and relative intensity change of methane recorded in mass spectra (Figure 3.30) during CO_2 hydrogenation upon NTP on (5.0 kV, 23.5 kHz).

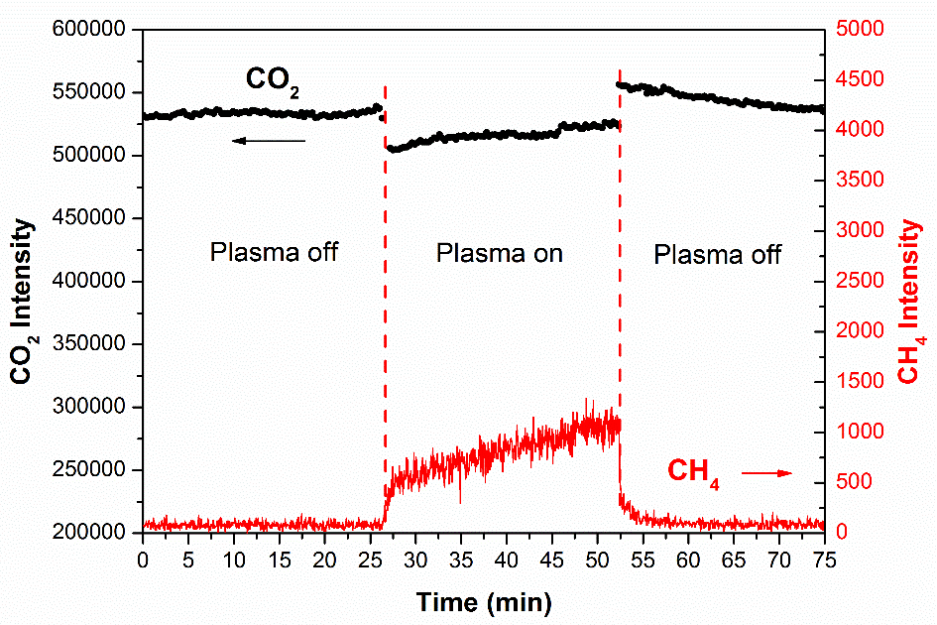

Figure 3.30 Corresponding MS signals collected simultaneously from DRIFTS cell as a function of time during NTP assisted CO_2 hydrogenation over the 2.5% Ru/MgAl-R600 catalyst.

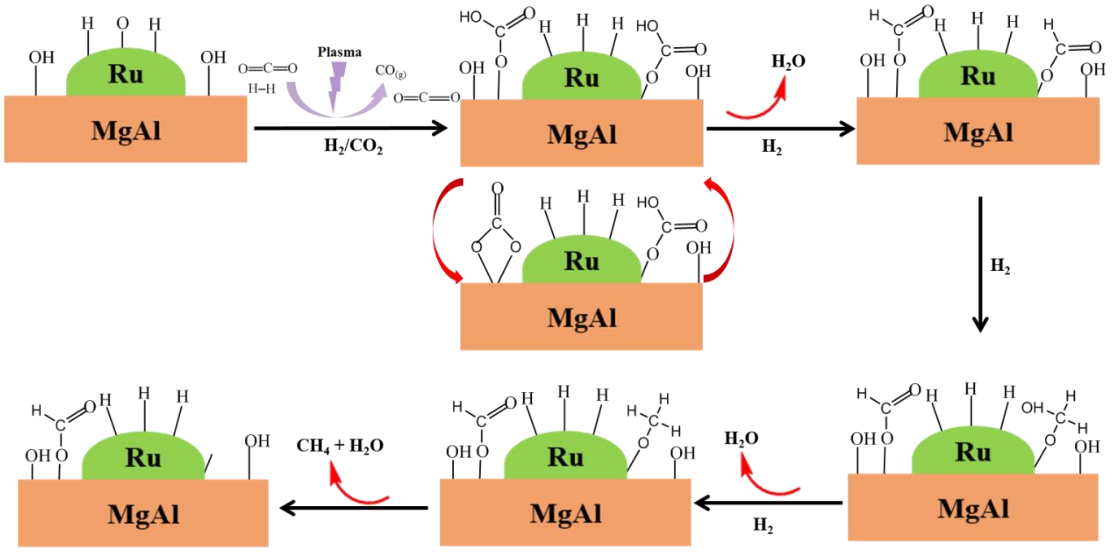

Figure 3.31 Scheme of the bicarbonate-formate-methane reaction pathways of the NTP-activated CO_2 hydrogenation over 2.5% Ru/MgAl-R600 catalyst.

Table 3.8 The reaction pathway of CO_2 hydrogenation over the 2.5% Ru/MgAl-R600 catalyst under the NTP conditions.

Plasma-gas phase CO_2 activation		Plasma-catalyst surface CO_2 activation	
$e^- + CO_2 \rightarrow CO^* + O^* + e^-$	Eq. 3.33	CO_2, ad $\rightarrow CO_{ad} + O_{ad}$	Eq. 3.35
$e^- + H_2 \rightarrow 2H^* + e^-$	Eq. 3.34	$H_{2,ad} \rightarrow 2H_{ad}$	Eq. 3.36
		$2H + O_{ad} \rightarrow H_2O$	Eq. 3.37
		$CO_{2,ad} + OH_{ad} \rightarrow HOCOO_{ad}$	Eq. 3.38
		$HOCOO_{ad} + OH_{ad} \rightarrow CO_{3,ad} + H_2O$	Eq. 3.39
CH_xO pathways		bicarbonate-formate-methane	
$CO_{ad} + H \rightarrow HCO_{ad}$	Eq. 3.40	$HOCOO_{ad} + H \rightarrow HCOO_{ad}$	Eq. 3.44
$HCO_{ad} + 2H \rightarrow H_3CO_{ad}$	Eq. 3.41	$HCOO_{ad} + 2H \rightarrow H_2COH_{ad}$	Eq. 3.45
$CH_3O_{ad} + H \rightarrow CH_{3,ad} + OH_{ad}$	Eq. 3.42	$H_2COH_{ad} + H \rightarrow CH_3O_{ad} + H_2O$	Eq. 3.46
$CH_{3,ad} + H \rightarrow CH_4$	Eq. 3.43	$CH_3O_{ad} + H \rightarrow CH_{3,ad} + OH_{ad}$	Eq. 3.47
		$CH_{3,ad} + H \rightarrow CH_4$	Eq. 3.48
$OH_{ad} + H \rightarrow H_2O$			Eq. 3.49

Based on the comparative *in situ* DRIFTS-MS characterisation of the catalysis over the 2.5% Ru/MgAl-R300 and 2.5% Ru/MgAl-R600 catalysts under thermal and NTP conditions, NTP-catalysis system enables the alternative surface pathways for promoting CO_2 hydrogenations, in line with the kinetic data shown in Figure 2. And the reduction temperature (during the catalysts preparation) affects the metal-support interaction and surface basicity, leading to the different adsorption behaviours of CO_2 on the surface. Therefore, 2.5% Ru/MgAl-R300 and 2.5% Ru/MgAl-R600 catalysts present different active sites for CO_2 hydrogenations, which may alter the reaction pathways [173]. Accordingly, under NTP conditions, different intermediates were formed during CO_2 hydrogenation over 2.5% Ru/MgAl-R300 and 2.5% Ru/MgAl-R600, suggesting different reaction pathways for CO_2 conversion.

3.4 Conclusions

In this study, the hybrid NTP-catalyst system for CO_2 hydrogenation has been investigated in a dielectric-barrier-discharge (DBD) reactor combined with Ru

supported on the MgAl LDH catalysts, in which 85% CO_2 conversion and 84% CH_4 yield can be achieved at 6.5 kV. It was clearly demonstrated that synergistic effect of plasma-catalysts can facilitate CO_2 conversion, which is more than 6 times higher than that under the thermal condition at 250 °C. Kinetic studies further confirmed that NTP-catalysis system presents lower apparent activation energy (21 kJ mol^{-1}) than the thermal system (82 kJ mol^{-1}).

The reduction temperature significantly affects the chemical and physical properties of the prepared catalysts significantly, which in turn strongly influences the CO_2 conversion and surface reactions under the plasma conditions. Comparative *in situ* DRIFTS-MS study confirmed that, under the thermal condition, CO_2 hydrogenation over the Ru/MgAl catalysts proceeds *via* the CO* route with CO as the sole intermediate. In contrast, plasma activation promotes the formation of various active species both in gas-phase and in catalysts-surface including CO*, O*, H*, formates, carbonate, formyl, carbonyl and water, explaining the improved performance of the NTP-catalysis system. Findings of the study confirms that the plasma-induced gas-phase dissociation of CO_2 and the interaction between plasma and catalyst surface opens new reaction routes, contributing to the enhanced CO_2 hydrogenation at low temperatures. However, further investigation into the surface interaction between the plasma, plasma-activated hydrocarbon species and the catalyst surface is needed to fully understand the CO_2 hydrogenation mechanism under plasma condition.

Chapter 4 CO Poisoning of Ru Catalysts in CO_2 Hydrogenation under Thermal and Plasma Conditions

This chapter was published in ACS Catalysis, 2020, 10 (21), 12828-12840.

DOI: https://doi.org/10.1021/acscatal.0c03620. Permission obtained from ACS to use the manuscript of the paper in this thesis.

4.1 Introduction

The work in the Chapter 3 demonstrated that hybrid nonthermal plasma (NTP) and catalysis (NTP-catalysis) systems can effectively activate and convert carbon dioxide (CO_2) into desired products under mild conditions, *e.g.*, ambient pressure and low bulk temperatures (< 200 °C) [73, 132, 183]. Additionally, NTP-catalysis is particularly beneficial to enable kinetically and/or thermodynamically limited reactions, including dry reforming of methane [184], water-gas shift [83, 152], and CO_2 hydrogenation [85]. In comparison with the thermal counterparts, NTP-catalysis has shown the capability of lowering the energy barrier required for the catalysis and/or changing the reaction pathways on the catalyst surface [87]. Recent studies have shown that, being similar with the thermal catalysis, the intrinsic nature of heterogeneous catalysts (including the supports), such as metal dispersion and pore structure, plays a key role in NTP-catalysis. For example, a series of Ni supported on silicalite-1 (with different pore structures) catalysts was designed to study CO_2 hydrogenation under NTP conditions. It was found that the pore structure of the silicalite-1 supports determines the dispersion and location of Ni sites and hence, the accessibility of plasma-generated reactive species, thus affecting the performance of the NTP-catalysis [15]. However, the catalysis (NTP-catalysis) systems is highly complex and require further understanding to advance the technology.

In addition to the activity, the stability and longevity of the catalysts are important factors for CO_2 hydrogenation under both thermal and NTP conditions. Under thermal conditions during CO_2 hydrogenation, catalyst deactivation is mainly caused by (i) metal particle sintering due to high reaction temperatures, (ii) coking caused by carbon deposition, and (iii) catalyst poisoning resulting from the trace impurity in feed gases such as carbon monoxide (CO). Due to the low-temperature activation of catalytic process, the previous work in the Chapter 3 has shown that NTP-assisted CO_2 hydrogenation intrinsically avoids sintering and coking processes, enabling stable catalytic performance of the catalysts. Regarding catalyst poisoning in CO_2 hydrogenation, it is well known that CO poisoning is one of the worst catalyst-deactivating processes under thermal conditions [10, 185]. Under plasma conditions, conversely, previous studies have shown that the plasma could enable the recovery of poisoned catalytic sites *via* dynamic collisions among reactive plasma-derived species, which lead to the desorption of strongly bound surface species [55, 186]. Accordingly, comparative insights into CO poisoning under thermal and NTP conditions, especially relevant deactivation mechanisms, have not yet been studied and need to be assessed to develop mature NTP-catalysis technology for potential practical adoptions. NTP-catalysis is a complex combination of plasma discharge and surface reactions (and other factors) with multifaceted interplays between them. Regarding the surface reactions under NTP conditions, *in situ* techniques, such as diffuse reflectance infrared Fourier transform (DRIFTS) [85, 187] and extended X-ray absorption fine structure (EXAFS) spectroscopy [154], have been proved to be powerful tools to gain insights into the surface dynamics of the catalyst, reaction mechanisms, and catalyst state during NTP-catalysis, which can facilitate the rational design of bespoke catalysts for NTP conditions. However, relevant *in situ* studies of NTP-catalysis toward the understanding of catalyst poisoning are still lacking.

This chapter presents the comparative study of the effect of CO on CO_2 hydrogenation over a supported Ru catalyst (*i.e.*, CO poisoning) under thermal and NTP conditions.

The intrinsic nature of the catalysts on the performance of CO_2 hydrogenation was first studied, and the Ru/SiO_2 catalyst with high activity and stability was chosen for further investigation. To elucidate the mechanism of CO poisoning, the mechanistic investigation of CO_2 hydrogenation including the kinetic and in situ diffuse reflectance infrared Fourier transform spectroscopy–mass spectrometry (DRIFTS–MS) studies was comparatively performed under thermal and NTP conditions, which provide useful information on the intermediates and reaction pathways of CO_2 hydrogenation. Finally, the mechanism of CO poisoning in CO_2 hydrogenation over the Ru/SiO_2 catalyst was investigated. Under the thermal conditions, significant catalyst deactivation due to the strong CO adsorption and metal sintering was observed; conversely, in situ DRIFTS–MS analysis revealed that the collisions of reactive plasma-derived species in NTP-catalysis could remove the strongly adsorbed carbon species to recover the active sites for CO_2 adsorption. Thus, NTP activation was found to mitigate the effect of CO on the performance of the catalyst and regenerate the catalyst efficiently. Additionally, under the NTP conditions, the NTP-enabled water-gas shift reaction of CO with H_2O (which was produced by CO/CO_2 hydrogenation) shifted the equilibrium of CO_2 hydrogenation toward CH_4 production.

4.2 Experimental Section

4.2.1 Preparation of Catalysts

Ruthenium (III) chloride trihydrate **(**$RuCl_3 \cdot 3H_2O$), silicon dioxide, and γ-Al_2O_3 were purchased from Sigma-Aldrich and used without further purification.

Supported Ru catalysts including Ru/SiO_2 and Ru/γ-Al_2O_3 (with the theoretical metal loading of 2 wt %) were prepared using the wet impregnation method. First, the support (1.5 g) was suspended in water (30 mL), and then 6.2 mL of $RuCl_3 \cdot 3H_2O$ solution (10 mg mL^{-1}) was added dropwise. The mixture was vigorously stirred for 3 h, and then evaporated using a rotary evaporator. The resulting precipitate was dried at 70 °C in a

convection oven for 12 h. The obtained dry solid was subsequently reduced in pure H_2 at 300 °C for 2 h with a heating rate of 5 °C min^{-1}. After reduction, the sample was cooled down to room temperature (RT) naturally under the H_2 flow (at 100 mL min^{-1}). The actual metal loading was determined by inductively coupled plasma optical emission spectrometry (ICP-OES). The prepared catalysts were characterised to understand their physical and chemical properties by bright-field transmission electron microscopy (TEM), N_2 physisorption (using the Brunauer–Emmett–Teller (BET) method), hydrogen temperature programmed reduction (H_2-TPR), and CO chemisorption.

4.2.2 Characterization of catalysts

The bright-field transmission electron microscopy (TEM) was performed on FEI Tecnai F20 electron microscope operating at 200 kV. X-ray diffraction (XRD) patterns of the materials were obtained on a PANaytical X'Pert Pro diffractomer using Cu Kα_1 radiation (λ = 1.5406 Å) at 40 kV, 40 mA, a scanning rate of 2° min^{-1}, a step size of 0.03° s^{-1}, and a 2θ angle from 5 to 80°. Elemental analysis of metal in samples was analysed by using ICP-OES (PQ 9000 Elite system). Prior to analysis, the sample (20 mg) was dissolved in concentrated sulfuric acid (5 mL) and concentrated nitric acid (5 mL) by microwave digestion (ETHOS UP microwave digester). N_2 physisorption analysis of samples was carried out at −196 °C using a Micromeritics 3Flex Surface Characterisation Analyser. Prior to N_2 physisorption measurements, the samples (~100 mg) were degassed at 200 °C under vacuum overnight. The Brunauer-Emmett-Teller (BET) method was used to determine the specific surface area of catalysts. Temperature programmed reduction (H_2-TPR) analysis was performed using Quantachrome ChemBet Pulsar equipped with a thermal conductivity detector (TCD). For H_2-TPR, ~25 mg of samples was pre-treated in He at 300 °C for 1h to remove the adsorbed water, and then cooled down to RT. H_2-TPR was performed at 30–700 °C (heating rate of 10 °C min^{-1}) under 5% H_2/He steam. For the CO pulse chemisorption,

the sample was reduced in H_2/He at 300 °C for 1 h and then was purged by He for 1.5 h to remove the H_2 from the catalyst and finally cooled down to RT. The CO pulse was performed with 10% CO/He at RT.

4.2.3 Catalysis

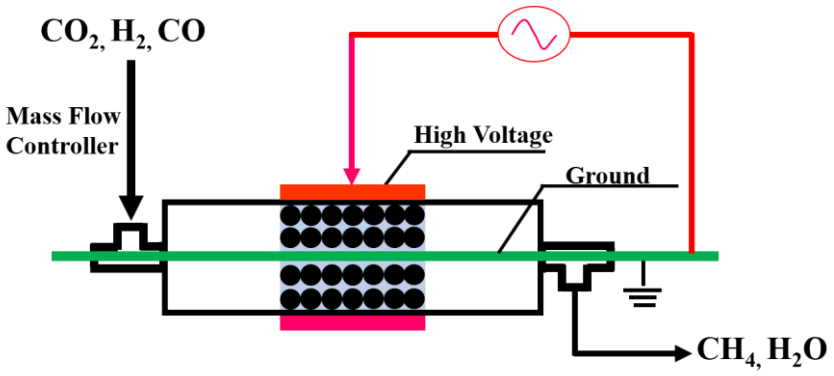

Figure 4.1 Schematic diagram of the DBD plasma system for catalytic CO_2 hydrogenation.

A dielectric barrier discharge (DBD) flow reactor was used for NTP-activated CO_2 hydrogenation (Figure 4.1), and the details of the DBD reactor have been described in the chapter 3. NTP-catalysis was performed at atmospheric pressure without a heating source. Briefly, ~100 mg of catalyst (pellet sizes of 250–425 μm) was packed into a quartz tube (6 mm o.d. × 4 mm i.d.), where an aluminium foil wrapped outside of the tube served as the high-voltage electrode and a tungsten rod (1 mm o.d.) in the centre of reactor acted as the ground electrode. Since the catalyst was exposed to air at RT before being loaded to the DBD reactor, it was treated *in situ* by NTP (at 6.5 kV) using 50% H_2/Ar as the discharge gas for 20 min before catalysis. The feed of CO_2, H_2, and Ar balance (molar ratio of 1:3:3) was introduced by mass flow controllers (Bronkhorst, F-201CV-500-RAD-11-V) with the flowrate of 50 mL min^{-1}. The applied voltage was from 5.5 to 7.5 kV at a constant frequency of 21.0 kHz. The product was analysed by using on line mass spectrometry (MS, Hiden HPR-20) and two-channel on line gas chromatography (GC). An Ar balance in the system was used in the system to avoid the signal saturation of MS signal. For each measurement, three samples of gas products

were analysed under steady-state conditions for an average value and error determination. Control experiments using the empty reactor (catalyst-free) and the reactor with the bare supports as a packing were performed under the same NTP conditions.

CO poisoning study under the NTP condition (at 6.5 kV and 21.0 kHz) was investigated by varying the inlet molar ratio of CO/CO_2 between 0 and 2. The total gas feed flowrate was 50 mL min^{-1}, corresponding to a space velocity of 30,000 mL (STP) g_{cat}^{-1} h^{-1}, which included CO_2, CO, H_2, and Ar balance (molar ratio of $H_2/(CO_2+CO) = 3$). Catalyst deactivation was monitored as a function of time-on-stream (ToS) by switching the CO on and off in the feed. The average bulk temperature of the system between 5.5 kV and 7.5 kV was measured using an infrared (IR) thermometer and was in the range of 110–135 °C. Specifically, the average bulk temperature at 6.5 kV was ~129 °C, which could not activate CO_2 conversion thermally.

For comparison, thermal catalysis was carried out at 250–430 °C at atmospheric pressure. Prior to catalysis, the catalyst (pellets, about 100 mg) was first treated at 300 °C for 1 h in 50% H_2/Ar. Then the feed (CO_2/H_2/Ar = 1:3:3) was introduced into the reactor at 50 mL min^{-1}. The temperature of the catalyst bed was monitored by a K-type thermocouple embedded in the catalyst bed.

CO poisoning of the catalyst under the thermal condition (at 330 °C) was studied using the same gas condition as in the relevant NTP-catalysis. The catalyst deactivation experiment was performed at 330 °C with the same gas conditions as described in the NTP-catalysis (for CO poisoning study).

CO_2 (X_{CO_2}) conversion, CO (X_{CO}) conversion, carbon ($X_C = X_{CO_2+CO}$) conversion, selectivity toward CH_4 (S_{CH_4}), and CH_4 yield (Y_{CH_4}) were determined accordingly to evaluate the catalytic performance.

$$X_{CO_2}\% = \frac{CO_{2,in} - CO_{2,out}}{CO_{2,in}} \times 100\% \quad \text{Eq. 4.1}$$

$$S_{CH_4}\% = \frac{CH_{4,out}}{CO_{2,in} - CO_{2,out}} \times 100\% \quad \text{Eq. 4.2}$$

$$Y_{CH_4}\% = X_{CO_2}\% \times S_{CH_4}\% \quad \text{Eq. 4.3}$$

$$X_{CO}\% = \frac{CO_{in} - CO_{out}}{CO_{in}} \times 100\% \quad \text{Eq. 4.4}$$

$$X_C\% = \frac{CO_{2,in} + CO_{in} - CO_{2,out} - CO_{out}}{CO_{2,in} + CO_{in}} \times 100\% \quad \text{Eq. 4.5}$$

where, *X* is the conversion, *S* is the selectivity, *Y* is the yield.

The specific reaction rates were calculated as following:

$$r_{CO_2} = \frac{X_{CO_2} \cdot F_{in}}{W_{cat}} \quad \text{Eq. 4.6}$$

where r_{CO_2} is the conversion rate of CO_2 (mol s^{-1} g_{cat}^{-1}), X_{CO_2} is the conversions of CO_2, F_{in} is the molar flow rate of CO_2 in the inlet of the DBD reactor (mol s^{-1}), W_{cat} is the mass of catalyst used in the catalytic performance measurements (g).

4.2.4 Kinetic study

The kinetic study of thermal catalysis was performed at 260–320 °C with ~30 mg of catalyst (diluted with inert glass beads to prevent hot spots) to ensure low CO_2 conversions of <20%. The feed mixture containing $CO_2/H_2/Ar$ (molar ratio = 1:3:3) was fed into the reactor for kinetic study. To extract the reaction order with respect to H_2 and CO_2 partial pressures, the composition of the feed was varied; *i.e.*, H_2 partial pressure was changed with a constant partial pressure of CO_2 and vice versa.

Kinetic study of the NTP-catalysis was performed using similar procedures and conditions as described above (about 30 mg of catalyst diluted with glass beads, at 5.0–6.5 kV and 21.0 kHz). The gas conditions were the same as in the kinetic study of the thermal catalysis. Due to the low bulk temperature under the NTP conditions (<129 °C), thermal activation of CO_2 was not possible. To minimise pore diffusion and mass transfer, CO_2 conversion under NTP-catalysis was kept below 20%. Considering the effect of support packing and discharge volume, control experiments using the same amount of bare supports and inert glass beads were performed to extract the information on the relevant gas phase and surface (over the bare supports) reactions under NTP, which was subsequently used to correct the kinetic data of the NTP-catalysis. Specifically, the NTP gas phase experiments were performed under identical reaction conditions to those of NTP-catalysis packed with Ru/SiO_2 and $Ru/\gamma\text{-}Al_2O_3$, but using a different reactor packed with the support (*i.e.*, SiO_2 or $\gamma\text{-}Al_2O_3$) and glass beads.

Activation energy ($E_{a,thermal}$, kJ mol^{-1}) of the thermal catalysis was determined according to Arrhenius equation:

$k_{thermal-cat} = A \times e^{-\frac{E_{a,thermal}}{RT}}$	Eq. 4.7
$r_{thermal-cat} = k_{thermal-cat}[CO_2]^a[H_2]^b \times (1-\beta)$	Eq. 4.8

where r is the reaction rate (mol s^{-1} g^{-1}), k is the rate constant, A is the pre-exponential factor, R is the universal gas constant, while T is the reaction temperature (K). [CO] and $[H_2]$ are the feed gas concentrations, and a and b are the reaction orders with respect to CO_2 and H_2 respectively. β is an approach to equilibrium. Since the conversion was limited to lower than 20%, the β can be neglected as the reaction was far from equilibrium.

Energy barrier ($E_{a,\ NTP}$, kJ mol^{-1}) of the NTP-catalysis was obtained according to the method presented in the literature [87]:

$$r_{NTP-cat} = A \times e^{\frac{E_{a,NTP}}{\frac{1}{F_{total}} \times power_{DBD}}}$$ Eq. 4.9

where F_{total} is the total flow rate of feed gas (0.833 mL s^{-1} (0.037 mmol s^{-1}) in this study), while $power_{DBD}$ is the DBD discharge power (W). Specifically, the DBD discharge power was calculated by using the current and voltage data obtained from a digital oscilloscope (TBS1102B).

Specific input energy (*SIE*, J mL^{-1}) was calculated according to the method presented in the literature [188]:

$$SIE = \frac{power_{DBD}}{F_{total}}$$ Eq. 4.10

where $power_{DBD}$ is the DBD discharge power (W), F_{Total} is the total gas flow rate (0.833 mL s^{-1} in this study).

4.2.5 In Situ DRIFTS–MS

The experimental setup of DRIFTS–MS for NTP-catalysis was described in the chapter 3. The catalyst was pretreated with 50% H_2/Ar gas under NTP at 6.0 kV and 27.0 kHz for 20 min in the flow cell. Then, the gas mixture containing CO_2, CO, H_2 and Ar balance was fed into the cell for the reaction. Kr at 10 mL min^{-1} was also introduced as the internal standard. The use of Ar balance in DRIFTS experiments was to avoid the signal saturation of IR spectra and MS signal. NTP-catalysis in the DRIFTS cell was performed at a constant peak voltage of 5.5 kV to avoid arcing between the electrodes. The IR spectra were recorded every 60 s with a resolution of 4 cm^{-1} and analysed by OPUS software.

4.3 Result and Discussion

4.3.1 Effect of Catalysts in the NTP-Catalysis

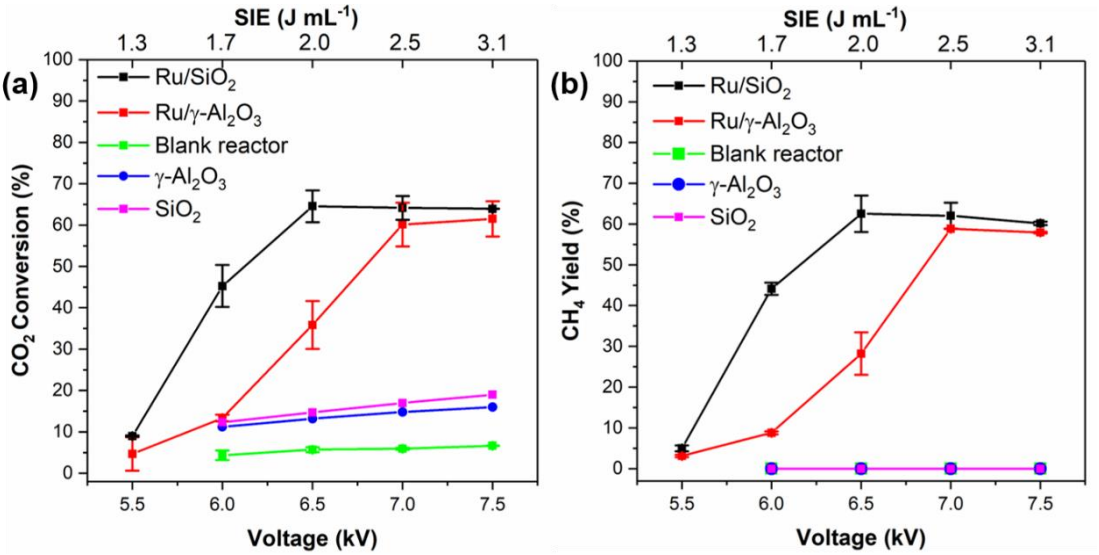

Figure 4.2 Performance of NTP-activated catalytic CO_2 hydrogenation as a function of voltage/input energy over the Ru/SiO_2 and $Ru/\gamma\text{-}Al_2O_3$ catalysts in reference to the control experiments; (a) CO_2 conversion and (b) CH_4 yield. (Experimental conditions: feed gas composition of $CO_2/H_2/Ar$ = 1:3:3, and WHSV of 30,000 mL (STP) g_{cat}^{-1} h^{-1}).

CO_2 hydrogenation over the two supported Ru catalysts under NTP conditions was investigated in reference to the control experiments (*i.e.*, the empty tube for NTP-lonely experiments and with the bare $\gamma\text{-}Al_2O_3$ and SiO_2 support packing under the NTP conditions) to screen the candidate for the following study (as shown in Figure 4.2). Under the NTP conditions without a catalyst, CO_2 was decomposed to CO with a trivial conversion of ~6% at 6.5 kV (with the specific input energy (SIE) of 2.0 J mL^{-1}). Similarly, NTP systems with the bare $\gamma\text{-}Al_2O_3$ and SiO_2 supports were only selective to CO with relevant CO_2 conversions of ~13% and ~15 %, respectively, at 6.5 kV. In comparison with the system without a packing, that is, the blank experiment with an empty tube, the higher CO_2 conversions with the bare supports can be attributed to the enhanced average electric field strength, benefiting CO_2 dissociation [189]. Conversely,

in NTP-catalysis with the voltage above 7.0 kV (SIE > 2.5 J mL^{-1}), regardless of the Ru catalysts used in this work, CO_2 conversion and CH_4 yield increased significantly to >57%. However, Ru catalysts based on different supports showed different behaviours under the NTP conditions, demonstrating the effect of catalyst design on NTP-catalysis [16]. Specifically, the Ru/SiO_2 catalyst showed a higher activity as compared with the $Ru/\gamma\text{-}Al_2O_3$ catalyst, especially at the lower voltage of < 6.5 kV (SIE < 2.5 J mL^{-1}). The highest CO_2 conversion (~65%) and CH_4 yield (~63%) at 6.5 kV were achieved by Ru/SiO_2, while the $Ru/\gamma\text{-}Al_2O_3$ catalyst only showed about 35% CO_2 conversion and 29% CH_4 yield, being less active for NTP-activated CO_2 hydrogenation. Similarly, under thermal conditions (Figure 4.3), Ru/SiO_2 outperformed $Ru/\gamma\text{-}Al_2O_3$ as well throughout all the temperature, suggesting that the intrinsic nature of catalysts dominated the performance of CO_2 hydrogenation regardless of the means of activation. In detail, the XRD analysis (Figure 4.4) of the catalysts did not show the relevant diffraction peaks of the crystalline Ru phases, suggesting that Ru is finely dispersed on the SiO_2 and $\gamma\text{-}Al_2O_3$ supports. The corresponding TEM and CO chemisorption analysis of the Ru/SiO_2 and $Ru/\gamma\text{-}Al_2O_3$ catalysts (Figure 4.5 and Table 4.1) showed that the two catalysts presented similar average particle sizes and Ru dispersions. Additionally, the metal–support interaction of the two catalysts was also similar, as revealed by H_2-TPR, as shown in Figure 4.6. The peaks of each catalyst was deconvoluted into two peaks. The first shoulder peak at 138−142 °C was attributed to the reduction of weakly supported RuO_x species on the support, while the second peak at 198−213 °C was assigned to the strongly adsorbed RuO_x [166]. The position of the two peaks showed insignificant shift, suggesting the metal-support interactions were similar in both catalysts. These findings show that the property of the supported active Ru phases of the two catalysts under study is similar, thus suggesting that the supported Ru might not affect the activity of the two catalysts significantly under NTP conditions.

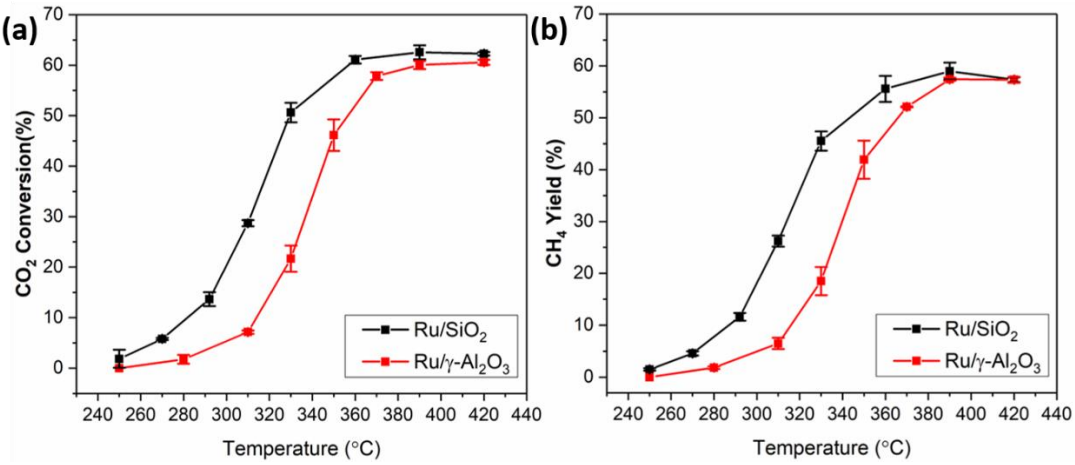

Figure 4.3 (a) CO_2 conversion and (b) CH_4 yield for thermal activated catalytic CO_2 hydrogenation over the Ru/SiO_2 and Ru/γ-Al_2O_3 catalysts.

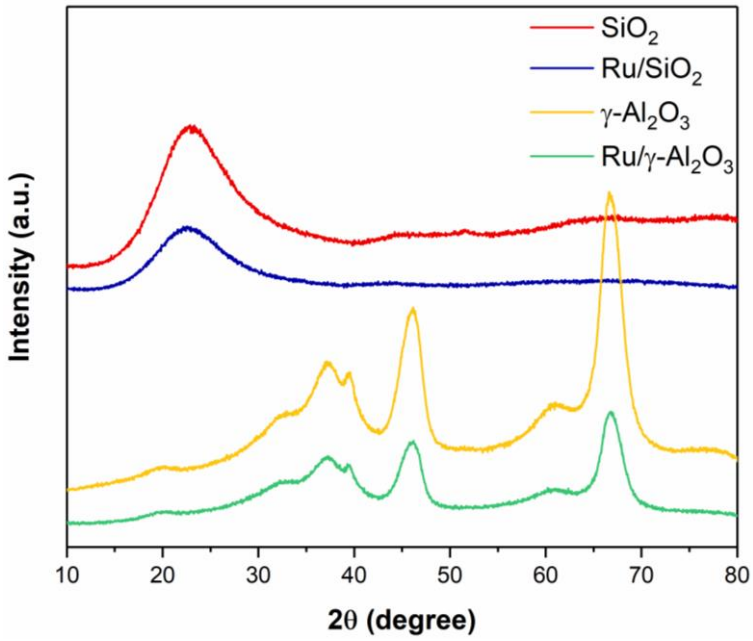

Figure 4.4 XRD patterns of SiO_2 support, Ru/SiO_2, γ-Al_2O_3 and Ru/γ-Al_2O_3 catalysts.

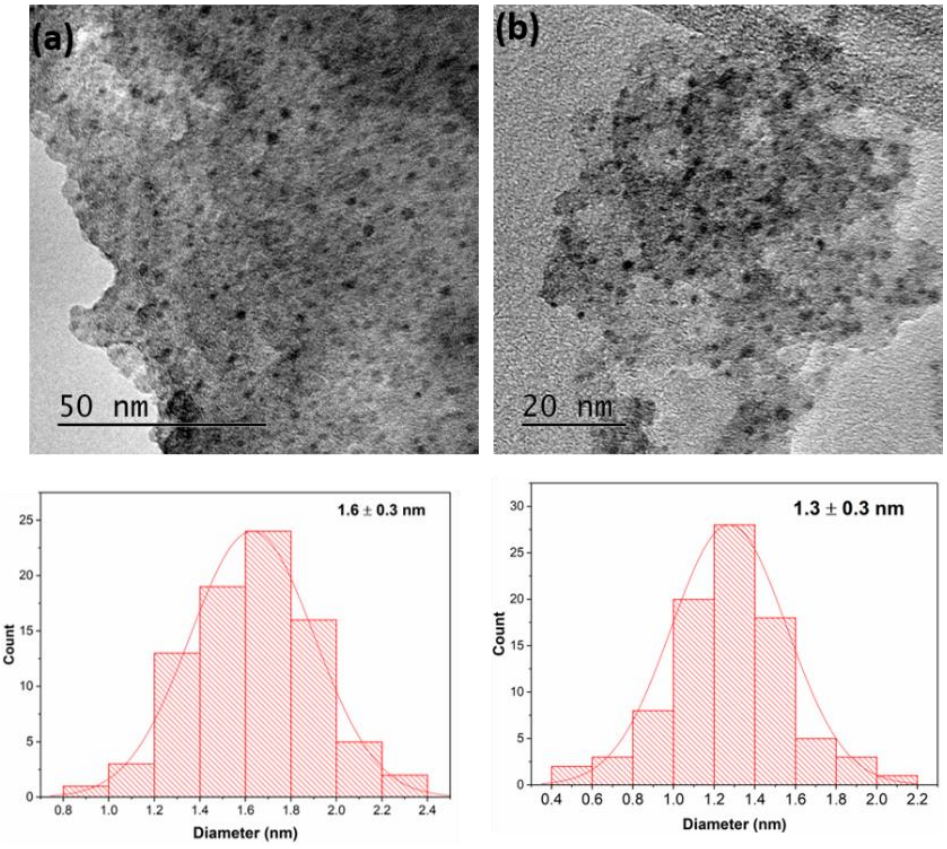

Figure 4.5 TEM image and particle size distribution of fresh (a) Ru/SiO_2 and (b) $Ru/\gamma\text{-}Al_2O_3$ catalysts.

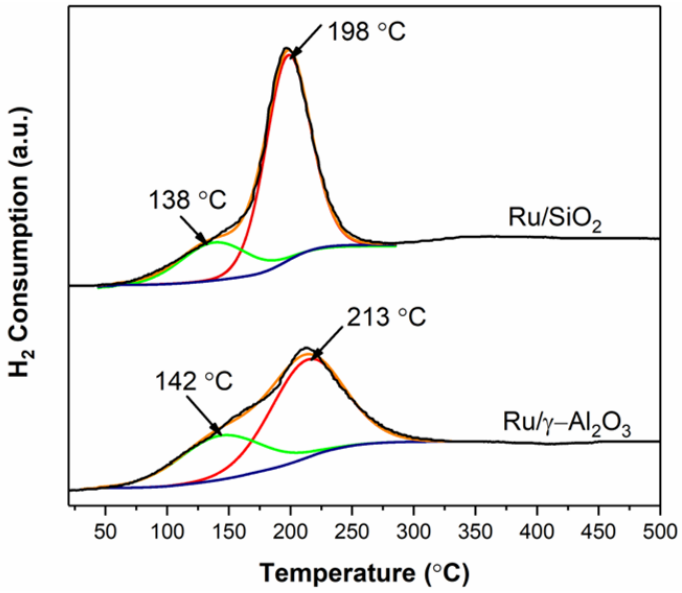

Figure 4.6 H_2-TPR profiles of Ru/SiO_2 and $Ru/\gamma\text{-}Al_2O_3$ catalysts.

Under NTP conditions, the effect of dielectric property of the bare supports on the catalysis was deemed insignificant since γ-Al_2O_3 and SiO_2 have different dielectric constants (~9.1 and ~4.2, respectively), while the reaction results were similar [190]. In addition to the dielectric constant, the porous property of the packing material can also influence the plasma discharge and reaction performance under the NTP conditions [191]. N_2 physisorption analysis (Figure 4.7 and Table 4.1) showed that the Ru/SiO_2 catalyst and Ru/γ-Al_2O_3 catalyst had comparable pore volume of ~0.7 cm^3 g^{-1}. The average pore sizes of the Ru/SiO_2 catalyst and Ru/γ-Al_2O_3 catalyst were ~5 and ~12 nm, respectively, which are much smaller than the Debye length, suggesting that the penetration of plasma into the catalyst pores might be limited. However, a previous study based on Monte Carlo calculation revealed that microdischarges might be formed near the pores of mesoporous catalysts with mesopore sizes of 2–50 nm, and the relatively high surface area promoted the intensified surface discharge on the surface [192]. This may explain the better catalytic performance of Ru/SiO_2 in CO_2 hydrogenation than Ru/γ-Al_2O_3 since the high surface area might promote the surface discharge in NTP-catalysis. The Ru/SiO_2 catalyst has a well-developed micro/meso porous structure with a higher specific BET surface area of 557 m^2 g^{-1} than that of the Ru/γ-Al_2O_3 catalyst (239 m^2 g^{-1}). Thus, a high surface area is expected as the key to determine the catalytic performance of the supported Ru catalysts under NTP and thermal conditions. The calculated apparent activation energy (Figure 4.8) showed that the Ru/SiO_2 catalyst presented lower values, under both conditions, than the Ru/γ-Al_2O_3 catalyst (Table 4.2), *e.g.*, 20 versus 71 kJ mol^{-1} in NTP-catalysis and 66 versus 119 kJ mol^{-1} in thermal-catalysis, respectively [87, 187].

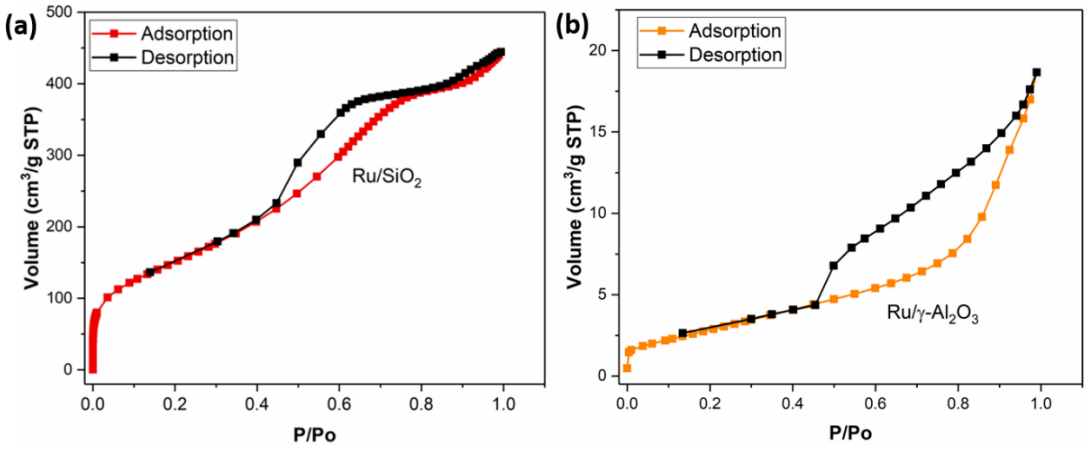

Figure 4.7 N_2 adsorption-desorption isotherms of different samples.

Table 4.1 Textural properties of the supported Ru catalysts under investigation.

Catalyst	Actual Ru content[a] (wt.%)	Ru dispersion[b] (%)	S_{BET} (m^2 g^{-1})	Pore volume (cm^3/g)	Average pore diameter (nm)
Ru/SiO_2	2.0%	2.71	557	0.70	5
$Ru/\gamma\text{-}Al_2O_3$	1.9%	2.49	239	0.71	12

[a]Actual Ru loading was measured by ICP-OES; [b]Ru dispersion were calculated based on pulse CO chemisorption measurement at RT.

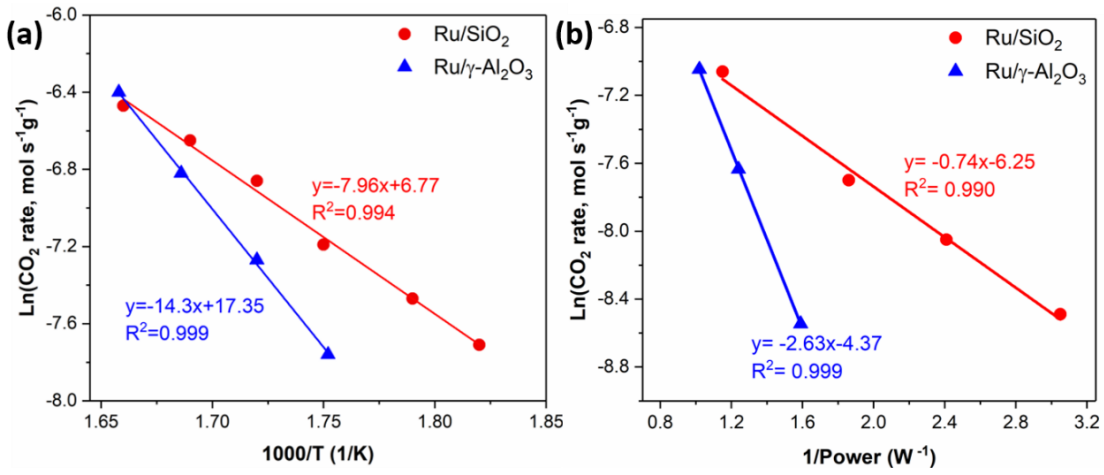

Figure 4.8 Determination of the activation energy over the Ru/SiO_2 and $Ru/\gamma\text{-}Al_2O_3$ catalyst (a) under thermal and (b) NTP conditions.

Table 4.2 Apparent activation energy calculated for catalytic CO_2 hydrogenation over Ru/SiO_2 and Ru/γ-Al_2O_3 catalyst by thermal and plasma activation.

Catalysts	E_a (kJ mol^{-1})	E_a (kJ mol^{-1})
	Thermal activation	NTP activation
Ru/SiO_2	66	20
Ru/γ-Al_2O_3	119	71

4.3.2 Mechanistic Study of CO_2 Hydrogenation over Ru/SiO_2

Preliminary catalytic assessments have shown that the Ru/SiO_2 catalyst presented relatively high CO_2 conversion and CH_4 yield for CO_2 hydrogenation under NTP and thermal conditions (in comparison with the Ru/γ-Al_2O_3 catalyst); thus, the Ru/SiO_2 catalyst was selected for further investigation. To gain insight into the mechanism of CO poisoning in CO_2 conversions, first, the comparatively mechanistic study of CO_2 hydrogenation over the Ru/SiO_2 catalyst was performed. Figure 4.9 and Table 4.3 show correlation between the apparent reaction rate and the CO_2/H_2 partial pressures (p_{H_2} and p_{CO_2}) in CO_2 hydrogenation under the thermal and NTP conditions. Under the thermal condition at 330 °C, the CH_4 formation rate over the Ru/SiO_2 catalyst showed a stronger dependence on p_{H_2} than p_{CO_2} in the feed. Specifically, the reaction order with respect to p_{H_2} was calculated as 1.0, in line with the Langmuir–Hinshelwood mechanism [193]. A previous study showed that H_2 dissociation on the Ru surface was fast with the produced H_{ad} being short-lived [194], and the reaction order regarding p_{H_2} indicated that CO_2 and H_2 were adsorbed on the different active sites on the Ru surface [195, 196]. The reaction order regarding p_{CO_2} was found to be –0.03, which can be approximated as zero order, suggesting that CO_2 concentration has a relatively weak influence on the formation rate of CH_4. This finding suggested (i) the CO_2 chemisorption on the catalyst and (ii) the saturation of relevant active sites on the Ru surface by CO_2 molecules at relatively low CO_2 concentrations [194]. Therefore, under

the thermal condition, CO_2 participated in the reaction *via* the Langmuir–Hinshelwood mechanism, *i.e.*, CO_2 adsorbed on the catalyst, and then dissociated to active intermediates under heating, which further react with H_{ad} to form methane.

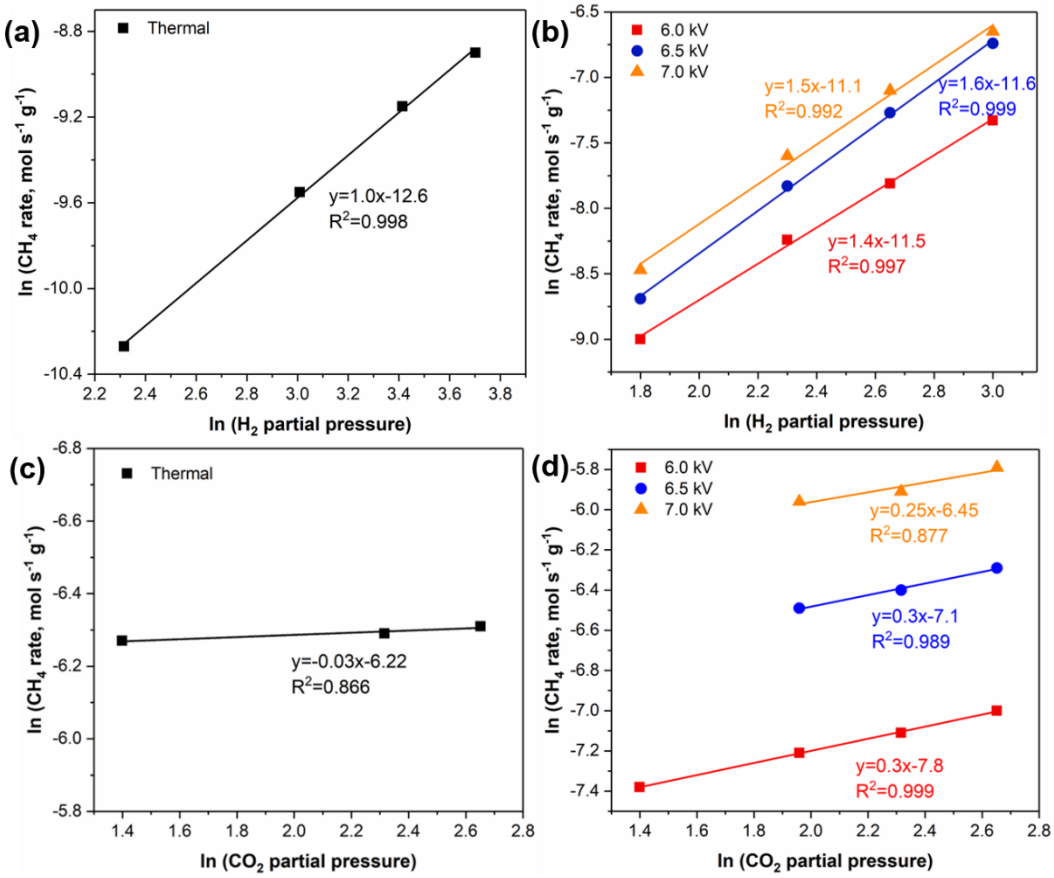

Figure 4.9 Dependence of the reaction rate on p_{H_2} and p_{CO_2} under (a, c) thermal conditions (at 330 °C) and (b, d) NTP conditions.

Table 4.3 Reaction order with respect to p_{H_2} and p_{CO_2} for catalytic CO_2 hydrogenation over Ru/SiO_2 under the thermal (at 330 °C) and NTP conditions.

reaction order	NTP			thermal
	6.0 kV	6.5 kV	7.0 kV	
p_{H_2}	1.40	1.60	1.50	1.0
p_{CO_2}	0.30	0.30	0.25	–0.03

In comparison, under the NTP conditions, the reaction orders with respect to p_{H_2} and p_{CO_2} were 1.50 ± 0.10 and 0.30 ± 0.05, respectively. Additionally, both reaction orders remained almost constant as a function of the input power, suggesting the same surface reaction mechanism at different input powers. The comparatively strong dependence on p_{H_2} and p_{CO_2} under NTP conditions (compared with the thermal condition) indicates the presence of multiple reaction pathways for CO_2 hydrogenation in NTP-catalysis. In addition to the surface reactions under the thermal catalysis, the vibrationally activated and dissociated active species (*e.g.,* electronically excited H radical) in the gas-phase reaction under NTP conditions might also participate in the surface hydrogenation reactions *via* the Eley–Rideal mechanism [80]. To clarify the relationship between the reaction order and reaction mechanism under NTP and thermal conditions, *in situ* DRIFTS–MS were performed, and the relevant results were correlated with the kinetic data.

In situ DRIFTS coupled with MS characterisation of CO_2 hydrogenation over the Ru/SiO_2 catalyst was comparatively performed under thermal and NTP conditions to investigate the mechanism of CO_2 hydrogenation. Under the thermal condition at 250 °C (Figure 4.10), characteristic peaks of surface hydroxyls (OH_{ad}, from ~3596 to ~3730 cm^{-1}), CH_x species ($CH_{3,\,ad}$, at ~3015 cm^{-1}), carbonyl (CO_{ad}, at ~1997 cm^{-1}) and surface-adsorbed CH_4 (at ~3047 cm^{-1}) were detected on the catalyst surface. It was observed that after changing the feed to inert Ar, the CO_{ad} band decreased slowly (within 10 min, Figure 4.10b), whereas the intensity of methane decreased rapidly (Figure 4.10c), suggesting that the gradual decrease of CO_{ad} band was only due to the desorption under the condition used. Conversely, when the feed was changed to H_2, the intensity of CO_{ad} band declined fast (within 2 min) with the associated rapid emergence of peak in the CH_4 signal, which gradually decreased after 2 min. This phenomenon confirms CO_{ad} as the active intermediate, which further reacted with H_2 to produce CH_4, being in line with the kinetic data discussed above (Figure 4.9). Under thermal

conditions, catalytic CO_2 hydrogenation is commonly thought to proceed *via* a direct carbon–oxygen bond dissociation mechanism [173, 197], which involves the dissociation of CO_2 on the catalyst surface (to adsorbed CO_{ad} and surface C) and the subsequent hydrogenation of surface C. Under the thermal condition used in this work, DRIFTS only probed CO_{ad} species on the Ru surface, confirming the direct carbon–oxygen bond dissociation mechanism.

In situ DRIFTS-MS study of CO_2 interaction with the Ru/SiO_2 catalyst under the plasma on and off conditions was performed with the CO_2/Ar mixture, and the relevant findings are shown in Figure 4.11. Initially, under the NTP-off condition (Figure 4.11a), a small peak at 1630 cm^{-1}, corresponding to bicarbonate, appeared on the catalyst surface with CO_2 flowing. With the ignition of plasma (*i.e.*, the NTP-on condition, Figure 4.11b), the linearly and bridged adsorbed CO_{ad} species (at ~2092, 2041, and 1881 cm^{-1}) and bidentate and monodentate carbonate (at ~1274 and ~1311 cm^{-1}, respectively) were measured. Also, the gas-phase CO_2 dissociation to CO and O_2 was confirmed by MS (Figure 4.11d). Since carbonate species were not observed under the thermal condition, the presence of carbonate species under the NTP condition was due to the plasma excitation and could be ascribed to the adsorption of ground-state or vibrationally excited CO_2 species on the catalyst surface. By switching off the plasma (Figure 4.11c), the relevant peaks of the CO_{ad} species remained almost unchanged even after 15 min purging, indicating the strong adsorption of the CO_{ad} on the surface, while the carbonate species gradually disappeared within 5 mins, proving that carbonate species was weakly adsorbed on the catalyst surface.

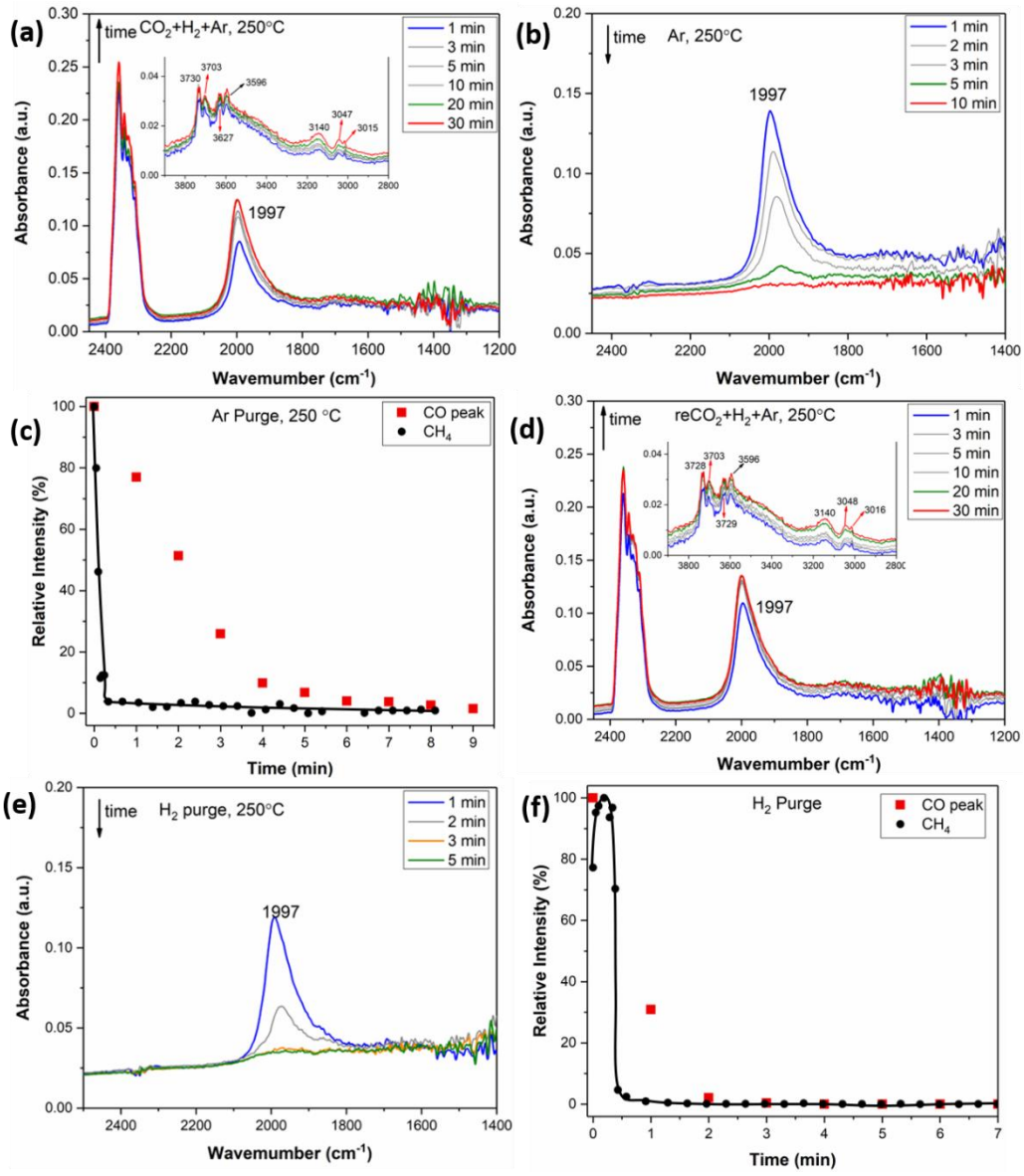

Figure 4.10 In situ DRIFTS spectra of surface species collected at 250 °C in thermal activated CO_2 hydrogenation over the Ru/SiO_2 catalyst. (a) introduce feed: 3% CO_2 + 9% H_2 + Ar, (b) switch to Ar, (c) The relative intensities change of CO_{ad} from *in-situ* DRIFTS and methane from MS as a function of time after changing to Ar at 250 °C, (d) switched back to feed: 3% CO_2 + 9% H_2 + Ar; and then switch to (e) H_2/Ar; (f) The relative intensities change of CO_{ad} from *in-situ* DRIFTS and methane from MS as a function of time after changing to H_2/Ar at 250 °C. (IR spectra were recorded every 60 s with a resolution of 4 cm^{-1}).

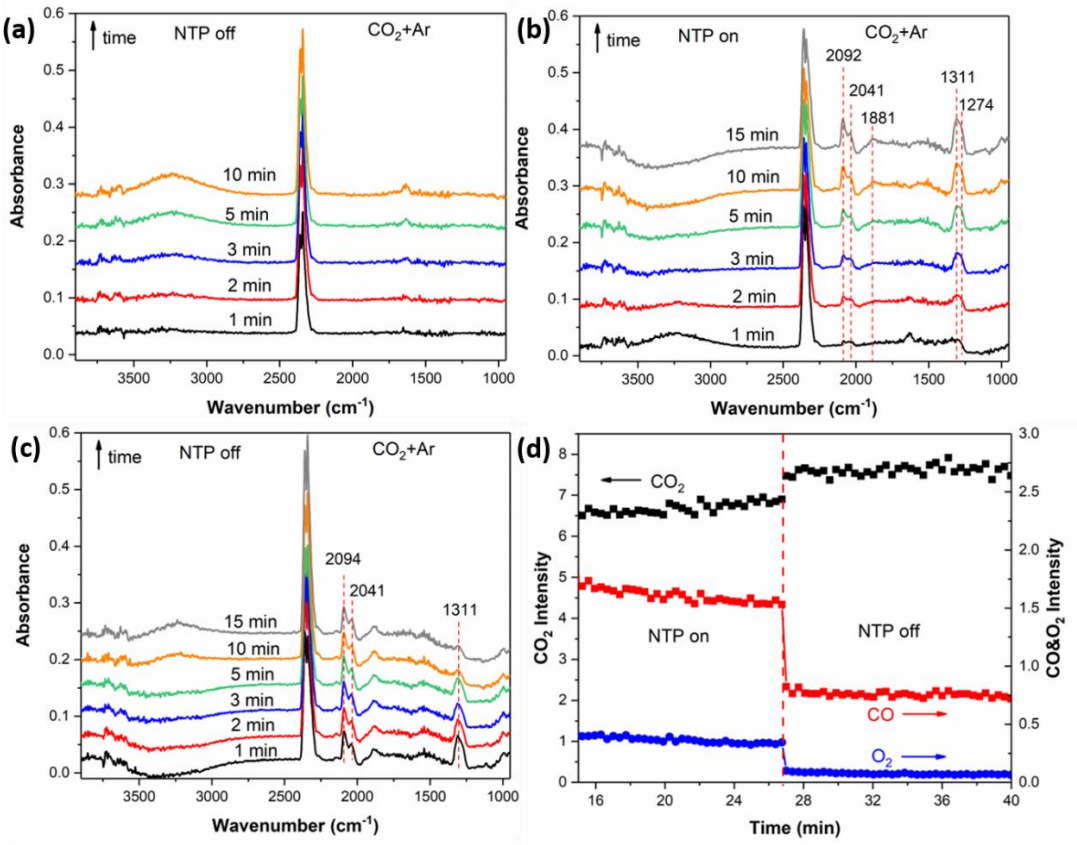

Figure 4.11 In situ DRIFTS spectra of surface species on the Ru/SiO_2 catalyst with 3% CO_2 + Ar flowing. (a) Plasma-off condition with the gas mixture of 3% CO_2 + Ar; (b) Plasma-on condition with the gas mixture of 3% CO_2 + Ar (at 5.5 kV and 27.0 kHz). (c) Plasma-off condition with the gas mixture of 3% CO_2 + Ar. (d) MS signals collected simultaneously from the DRIFTS cell as a function of time, corresponding to the experiments in (b) and (c). (Feed: 3% CO_2 + Ar; DRIFTS experiments were performed according to the procedure of (a) NTP off, (b) NTP on, and (c) NTP off; IR spectra were recorded every 60 s with a resolution of 4 cm^{-1}).

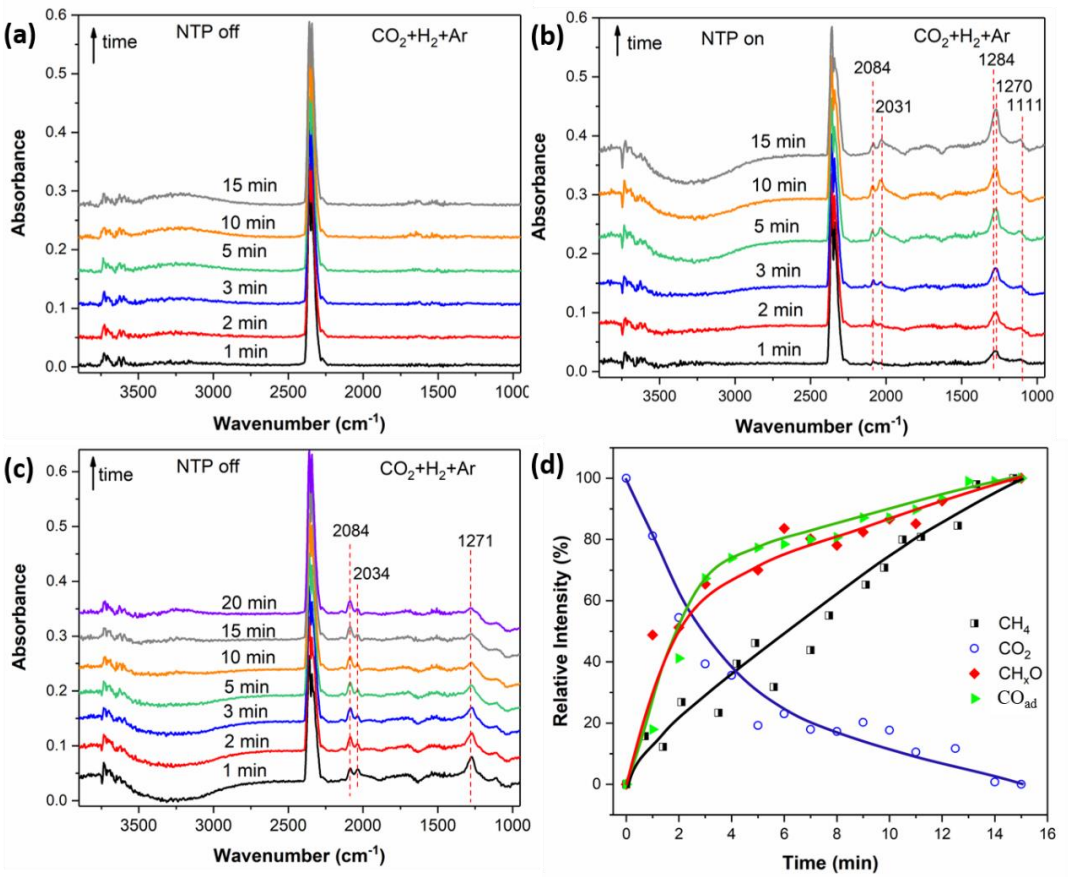

Figure 4.12 In situ DRIFTS spectra of surface species for CO_2 hydrogenation over the Ru/SiO_2 catalyst under (a) the NTP-off condition with the feed gas of 3% CO_2 + 9% H_2 + Ar; (b) NTP-on condition with the feed gas (at 5.5 kV and 27.0 kHz), and (c) NTP-off condition with the feed gas. (d) Relative intensities of surface species as a function of time-on-stream recorded by *in-situ* DRIFTS from (b) and relative intensity change of methane recorded in MS (Figure 4.13a) during CO_2 hydrogenation by NTP activation (at 5.5 kV and 27.0 kHz).

Under the NTP-off condition, with the reaction gas feed (*i.e.*, 3% CO_2/9% H_2/Ar), in addition to the CO_2 gas-phase peak (at ~2360 and 2342 cm^{-1}, as shown in Figure 4.12), surface carbon species were not detected by DRIFTS and no reaction was observed (according to MS in Figure 4.13). Upon the ignition of plasma, the MS profile showed the instantaneous appearance of CH_4 signal (Figure 4.13a), confirming the formation of CH_4 over the catalyst under NTP activation. At the same time, surface formyl species (CH_xO, at about 1284, 1270, and 1111 cm^{-1}) and carbonyl species (*i.e.*, linearly

adsorbed CO_{ad} on Ru^0 at 2034 cm^{-1} and linear form $Ru^{\delta+}$-CO at 2084 cm^{-1}) [198], as shown in Figure 4.12b, were measured by DRIFTS. Compared with the CO_{ad} bands formed under CO_2/Ar (Figure 4.11b), the two peaks shifted toward lower frequency by about 10 cm^{-1} and the bridged adsorbed CO_{ad} peak disappeared, which could be attributed to the electron donation of H_{ad} on the Ru surface [199]. On switching off plasma, the CH_4 concentration decreased immediately (Figure 4.13a), while the formyl species decreased slowly (within 4 min) (Figure 4.13b), indicating that the system without plasma discharge was inactive for CH_4 formation. The gradual decrease of formyl band (within 4 min) reflects its desorption under the NTP-off condition. CO_2 hydrogenation can undergo the formyl pathway over Ru-based catalysts [175, 200], which involves the direct CO_2 dissociation to carbonyl (CO_{ad}) and O_{ad}, followed by the hydrogenation of CO_{ad}. The subsequent hydrogenation of CO_{ad} will form the formyl species as the intermediates for CH_4 production. As compared with the DRIFTS findings from the thermal system (*i.e.*, only carbonyl species were observed, Figure 4.10), the appearance of carbonyl species and formyl species under NTP conditions suggested the presence of an alternative reaction pathway (*i.e.*, formyl pathways) for CO_2 hydrogenation under NTP. Thus, evolution of the surface species as a function of ToS coupled with the change in CH_4 signal intensity (from MS) was correlated, as presented in Figure 4.12d. The CO_{ad} species increased at a steeper rate than gas CH_4, which could be explained by the plasma-assisted CO_2 dissociation in the gas phase and the dissociation of adsorbed CO_2 on the catalyst surface. The same phenomenon was found between the formation rates of surface formyl species and CH_4, indicating CH_xO species originating from reactions between CO_{ad} and H_{ad} and as the surface intermediate for CH_4 production [180, 200]. The findings of this work confirmed the presence of the formyl pathway in CO_2 hydrogenation over Ru/SiO_2 under NTP conditions; *i.e.*, CO_2 was dissociated to CO_{ad} and O_{ad} species on the catalyst surface, then CO_{ad} was hydrogenated with H_{ad} into formyl intermediate (CH_xO) species, and finally, the formyl group reacted toward CH_4 and H_2O. In comparison with the thermally activated CO_2 hydrogenation, the vibrationally activated CO_2 molecules under plasma conditions

could adsorb on the catalyst surface with lower energy barriers, which facilitated the formation of CO_{ad} species [55]. This activation promoted the hydrogenation of CO_2 and formation rate of CH_4, leading to the reaction order of p_{CO_2} increasing slightly. Additionally, the plasma-induced excited/dissociated H radicals in the gas phase might also interact with the adsorbed species to form CH_4 (*i.e.*, the formyl pathway) via the Eley–Rideal mechanism in CO_2 hydrogenation under NTP [55, 80]. Due to the relatively low dissociation energy of H_2 molecules (~4.5 eV) [201], the plasma could activate H_2 more efficiently, which produces more H radicals with an increase in H_2 concentration in the feed. Therefore, under NTP, the H_2 partial pressure has a significant influence on the formation rate of CH_4, leading to a much higher reaction order with respect to p_{H_2} than that in the thermal catalysis.

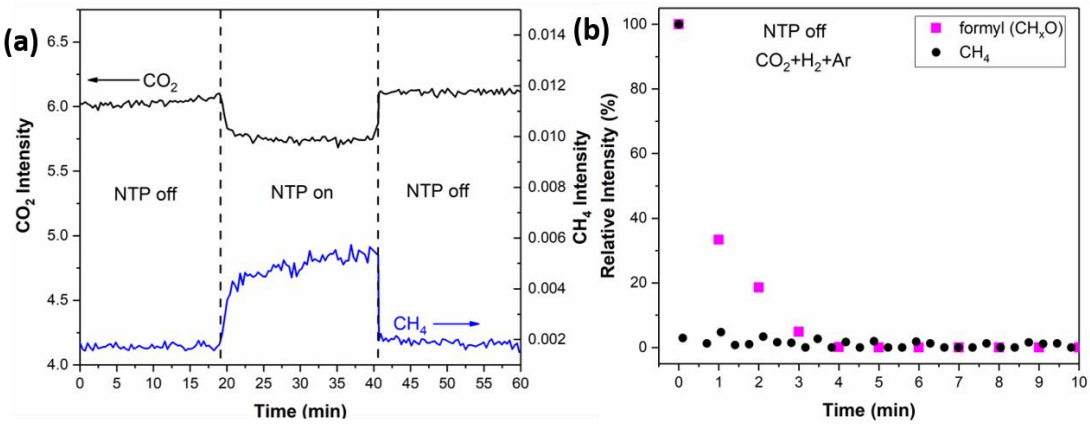

Figure 4.13 (a) Corresponding MS signals collected simultaneously from the DRIFTS cell as a function of time during NTP-assisted CO_2 hydrogenation over the Ru/SiO_2 catalyst. (b) Evolution of formyl species (CH_xO) intensity (by DRIFTS in Figure 4.12c) and CH_4 intensity (by MS) after switching off plasma discharge during CO_2 hydrogenation. (Feed: 3% CO_2 + 9% H_2 + Ar).

4.3.3 Investigation of CO Poisoning on CO_2 Hydrogenation

Catalyst deactivation is complex and significant for practical catalysis. As expected, under the NTP condition (at 6.5 kV, 21.0 kHz), the Ru/SiO_2 catalyst in CO_2

hydrogenation presented excellent stability over 27 h ToS with CO_2 conversions and CH_4 selectivity maintained at 64.7 ± 0.7% and 94.1 ± 0.3%, respectively (Figure 4.14). Comparative TEM analysis of the catalyst before and after the longevity test showed no significant change regarding the particle sizes, neither the sign of metal sintering, which confirmed the anti coking and anti sintering performance of the NTP-catalysis (Figure 4.15).

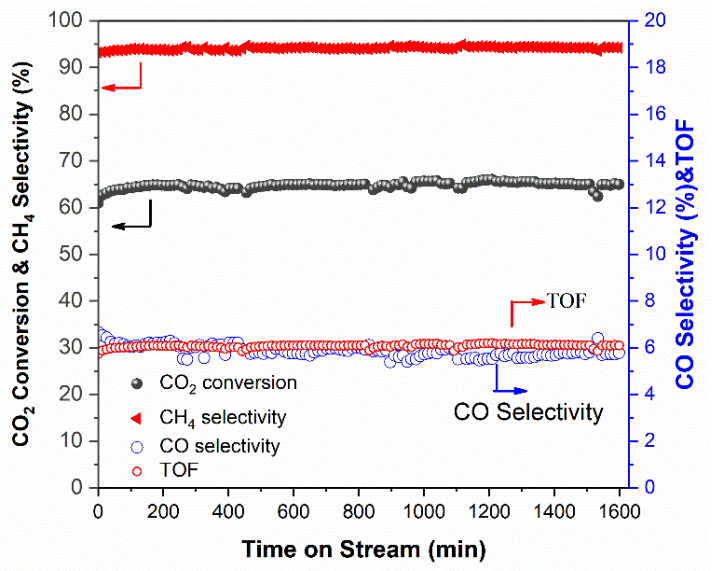

Figure 4.14 Stability test of the Ru/SiO_2 catalyst for CO_2 hydrogenation under the NTP condition (at 6.5 kV, $H_2/CO_2/Ar = 3:1:3$, WHSV = 30,000 mL (STP) g_{cat}^{-1} h^{-1}).

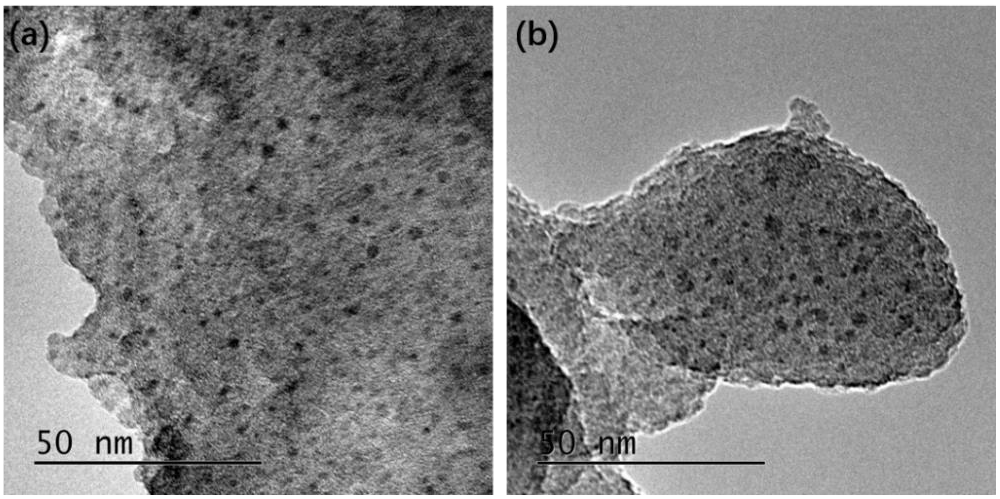

Figure 4.15 TEM image of (a) fresh Ru/SiO_2 catalyst, and (b) spent Ru/SiO_2 catalyst after the longevity test of CO_2 hydrogenation under NTP condition.

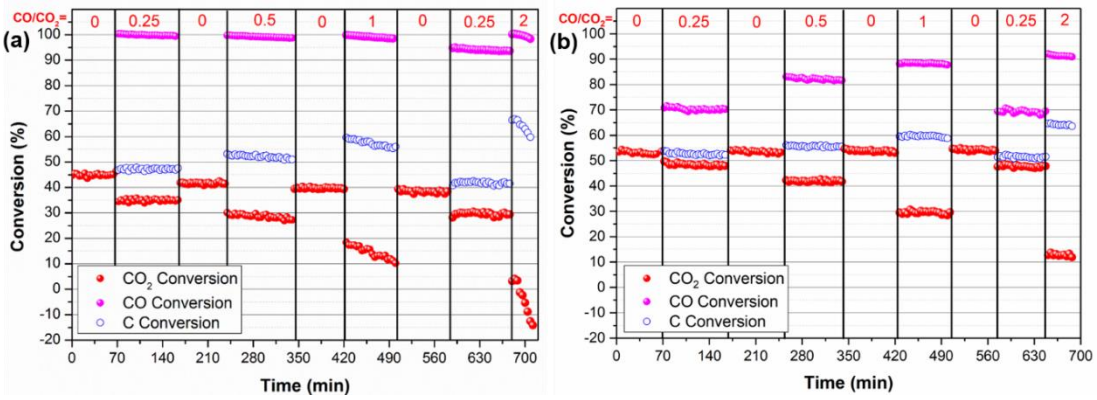

Figure 4.16 CO_2, CO and carbon conversions as a function of ToS in CO poisoning experiments with different CO/CO_2 inlet molar ratios under (a) thermal condition (at 330 °C) and (b) NTP condition (at 6.5 kV and 21.0 kHz). (Experimental conditions: feed gas composition of $H_2/C = 3$, CO/CO_2 =0, 0.25, 0.5, 1.0 and 2.0, and WHSV of 30,000 mL (STP) $g_{cat}^{-1}\,h^{-1}$).

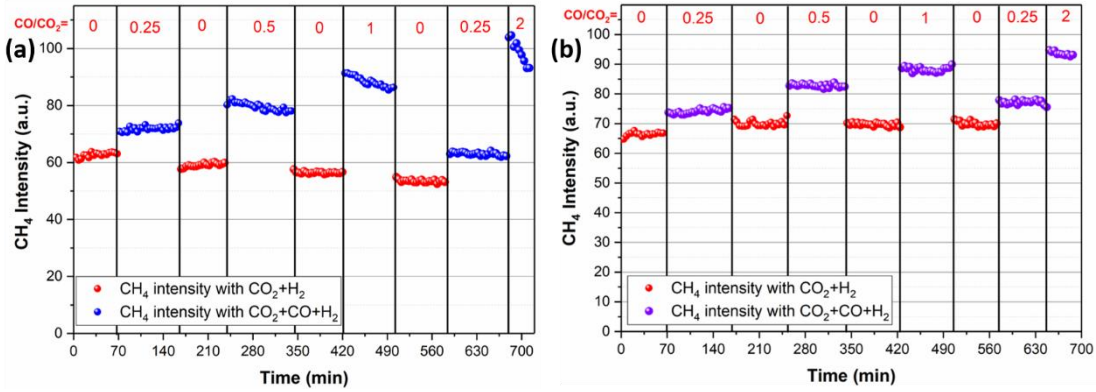

Figure 4.17 Methane intensity as a function of ToS during CO poisoning experiments with different CO/CO_2 inlet molar ratios under (a) thermal condition (at 330 °C), and (b) NTP condition (at 6.5 kV and 21.0 kHz). (Experimental conditions: feed gas composition of $H_2/C = 3$, CO/CO_2 =0, 0.25, 0.5, 1.0 and 2.0, and WHSV of 30,000 mL (STP) $g_{cat}^{-1}\,h^{-1}$).

In addition to coking and sintering, catalyst poisoning is another major factor to deactivate the catalyst. Accordingly, to understand CO poisoning in the catalysis under the thermal and plasma conditions, relevant experiments were performed by varying CO concentration in the gas feed, keeping the H_2/C (*i.e.*, CO_2+CO) inlet molar ratio constant. Figure 4.16 shows the thermal and NTP-activated carbon conversions (CO_2, CO, and overall) as a function of ToS with different CO/CO_2 ratios in the feed gas.

Under the thermal condition at 330 °C (Figure 4.16a), the fresh Ru/SiO_2 catalyst showed a stable CO_2 conversion (~47%) without CO in the feed gas ($CO/CO_2 = 0$, ToS = 0–70 min in Figure 4.16a). When CO ($CO/CO_2 = 0.25$) was introduced in the gas mixture, CO_2 conversion decreased to 35%, while CO was almost completely consumed, promoting the overall carbon conversion and CH_4 production due to CO hydrogenation. By switching back to the "CO-free" feed gas ($CO/CO_2 = 0$, ToS = 165–240 min in Figure 4.16a), catalyst deactivation occurred, and the catalyst could not be fully recovered, as evidenced by the reduced CO_2 conversion (Figure 4.16a) and CH_4 production (Figure 4.17a), in comparison with that of the fresh catalyst. By further increasing the CO/CO_2 ratio to 0.5 and 1.0, the decrease in CO_2 conversion and deactivation of catalyst became more significant, while the CO conversion remained almost complete. The findings showed a strong inhibiting effect of CO on CO_2 conversion. The condition with $CO/CO_2 = 0.25$ in the feed gas (ToS = 590–680 min in Figure 4.16a) was tested again, and carbon conversion and CH_4 production were lower than the previously measured values, suggesting the permanent deactivation of Ru/SiO_2. By adding more CO in the feed (*i.e.,* CO/CO_2 ratio of 2), severe CO poisoning was measured. Specifically, CO_2 conversion dropped rapidly below zero, suggesting that CO_2 become a product. This might be attributed to the presence of CO disproportionation ($2CO \rightarrow C+CO_2$) [202] and/or water gas shift reaction (WGSR, $CO+H_2O \rightarrow H_2+CO_2$) [203] due to the excessive CO in the feed and strong adsorption of CO on the Ru surface. Accordingly, in the thermal catalysis system, a decrease in CO_2 conversion with CO cofeeding was not due to kinetic effect, that is, the diluted CO_2 concentration in the gas feed, as discussed above (Figure 4.9). With the presence of CO in the feed, competitive adsorption of CO and CO_2 on metal active sites occurs [204]. Since the adsorption energy of CO (–2.3 eV) is much lower than that of CO_2 (–0.52 eV) [205], preferential adsorption of CO and inhibited CO_2 adsorption on the Ru surface are expected and, thus, a decrease in CO_2 conversion. It was proposed that the formation of strongly adsorbed carbonyl species [185, 206] due to the presence of CO might be the dominant factor for catalyst deactivation. Therefore, the mechanism of CO

poisoning of the Ru/SiO_2 catalyst was investigated by *in situ* DRIFTS analysis (to be discussed later).

As shown in Figure 4.16b, under the NTP condition at 13.0 kV, 54% CO_2 conversion over the Ru/SiO_2 catalyst was measured with the absence of CO in the feed (*i.e.*, $CO/CO_2 = 0$, ToS = 0–70 min, in Figure 4.16b). By introducing CO in the feed (with $CO/CO_2 = 0.25$), CO_2 conversion decreased slightly to ~49%, and CO conversion was measured at about 70%, being lower than that under the thermal condition (which was close to 100%). By increasing the CO concentration in the feed gas (*i.e.*, $CO/CO_2 = 0.5$, 1.0 and 2.0, respectively), a decrease in CO_2 conversions was measured (due to the change of gas composition); however, catalyst deactivation was insignificant since the carbon conversion remained stable in stream during the cofeeding tests. More importantly, the catalyst activity regarding CO_2 conversion and CH_4 production in CO_2 hydrogenation can be totally recovered when the system was switched back to the "CO-free" feed, regardless of the previous CO concentration in the feed, confirming that (i) NTP could be able to completely regenerate the catalyst and (ii) NTP is able to mitigate CO poisoning on CO_2 hydrogenation (Figure 4.17b). Interestingly, under NTP conditions, in comparison with ~100% CO conversions under the thermal condition, CO conversions increased from 70 to 92% with an increase in the inlet CO/CO_2 ratio from 0.25 to 2. This suggested that the reasons for the decrease in CO_2 conversion in both systems may be different. As discussed above, in thermal catalysis, preferred CO adsorption on the Ru surface and the subsequent CO hydrogenation prevailed, causing the reduction of the CO_2 conversion and almost 100% CO conversion. Conversely, under NTP conditions, the plasma could activate CO_2 molecules in the gas phase and the vibrationally excited CO_2 could adsorb on the catalyst surface with lower energy barriers, which facilitated the adsorption of CO_2 on the catalyst surface [55]. Additionally, the collision of reactive plasma species (such as the vibrationally excited CO_2 and the excited state of CO, H, OH, and CH in the gas phase according to OES and FTIR [58, 80, 187]) might help remove the strongly adsorbed surface CO_{ad} and

then release the active sites for adsorption [55, 207, 208]. Thus, NTP alleviated CO adsorption and facilitated CO_2 adsorption, which result in lower CO conversions and higher CO_2 conversions than those in the thermal catalysis.

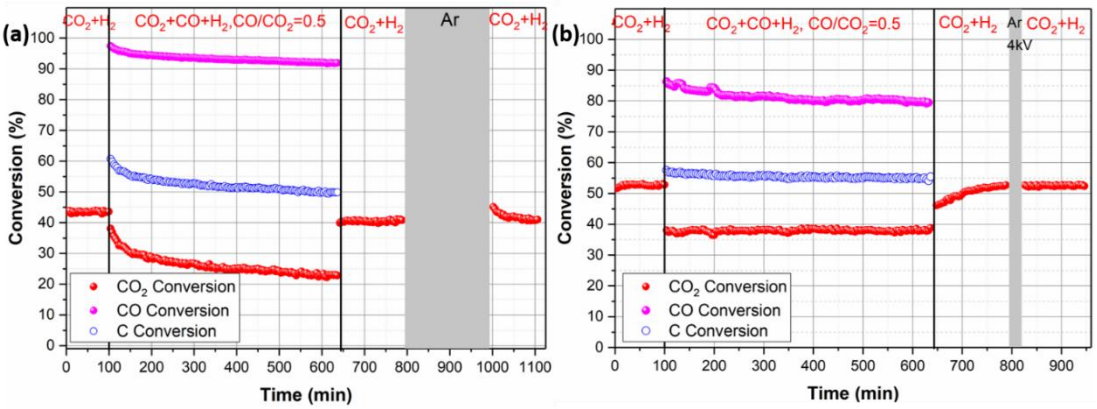

Figure 4.18 Long-term deactivation test with the $CO_2/CO/H_2$ mixtures, regeneration treatment under Ar and catalysis in CO_2/H_2 over the Ru/SiO_2 catalyst under (a) the thermal condition (at 330 °C), and (b) NTP condition (at 6.5 kV and 21.0 kHz). (Experimental conditions: feed gas composition of $H_2/C = 3$, $CO/CO_2 = 0.5$, and WHSV of 30,000 mL (STP) $g_{cat}^{-1}\,h^{-1}$).

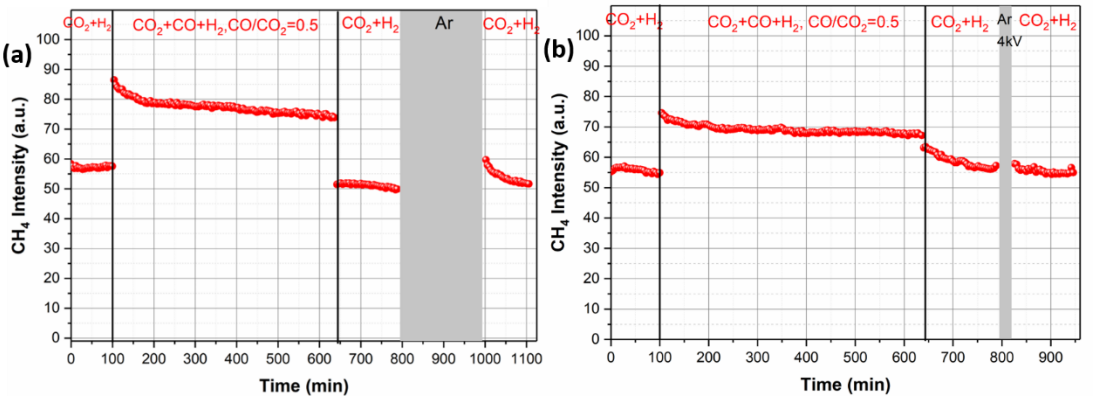

Figure 4.19 Methane intensity in the long-term deactivation test in $CO_2/CO/H_2$ mixture, regeneration treatment under Ar and catalysis in CO_2/H_2 over the Ru/SiO_2 catalyst under (a) thermal condition (at 330 °C), and (b) NTP condition (at 6.5 kV and 21.0 kHz). (Experimental conditions: feed gas composition of $H_2/C = 3$, $CO/CO_2 = 0.5$, WHSV of 30,000 mL (STP) $g_{cat}^{-1}\,h^{-1}$).

The superiority of the NTP-catalysis over the thermal counterpart, regarding the maintenance and regeneration of the catalyst activity, was proved by the long-term CO

poisoning study in Figures 4.18 and 4.19. At 330 °C, the deterioration of the catalyst performance with the presence of CO in the feed was evident during the 9 h test (ToS = 100–640 min in Figure 4.18a). Specifically, CO_2 and CO conversions (Figure 4.18a) and CH_4 formation (Figure 4.19a) dropped by about 42%, 7% and 15%, respectively. By removing CO from the feed (ToS = 640–790 min in Figure 4.18a), CO_2 conversion and CH_4 production over Ru/SiO_2 were recovered to ~93% and ~87% only. Considering that flowing inert gases at high temperature could be used to recover the catalyst reactivity, the deactivated catalyst was regenerated *in situ* at 330 °C by sweeping with Ar for 3.5 h, trying to remove the strongly adsorbed surface species from the catalyst surface. However, as shown in Figure 4.18a and 4.19a, the deactivation of catalyst due to CO poisoning under the thermal condition was permanent. Previous theoretical and experimental studies [209, 210] suggested that the CO molecule could block the active sites for CO_2 and H_2 adsorption, thus decreasing the dissociated H_{ad} on the Ru surface and consequently leading to the deposition of surface carbon species and metal sintering. Conversely, in NTP-catalysis (at 6.5 kV), the catalyst presented stable performance over 9 h, with the constant CO_2 conversion at about 38% and decreased CO conversion (by about 6%). Furthermore, after returning to CO-free feed (ToS = 640–790 min, Figure 4.18b), CO_2 conversion was recovered to ~53% slowly (being comparable with that of the fresh catalyst at ToS = 0–100 min). During the same period (ToS = 640–790 min in Figure 4.19b), the corresponding CH_4 production decreased to the initial level, confirming that NTP could recover the performance of the catalyst. The recovery trend of CO_2 conversion and CH_4 production was attributed to the consumption of residual adsorbed carbon species under NTP, thus regenerating active sites available for CO_2 hydrogenation. The catalyst was further treated *in situ* under Ar and NTP (at 4.0 kV) for 30 min (ToS = 790–820 min, as shown in Figure 4.18b). After that, NTP-activated CO_2 hydrogenation was performed again with the CO-free feed (ToS = 829–945 min in Figure 4.18b), and the NTP-catalysis system showed the fully recovered performance. The corresponding TEM analysis of the catalysts after the long-term deactivation test (Figure 4.20) showed the metal sintering of the catalyst in thermal

catalysis; that is, the Ru particle size increased from ~1.6 nm to ~3.1 nm after the thermal catalysis. Conversely, the Ru particle size showed no significant changes after the NTP-catalysis, confirming the anti sintering ability of the hybrid system.

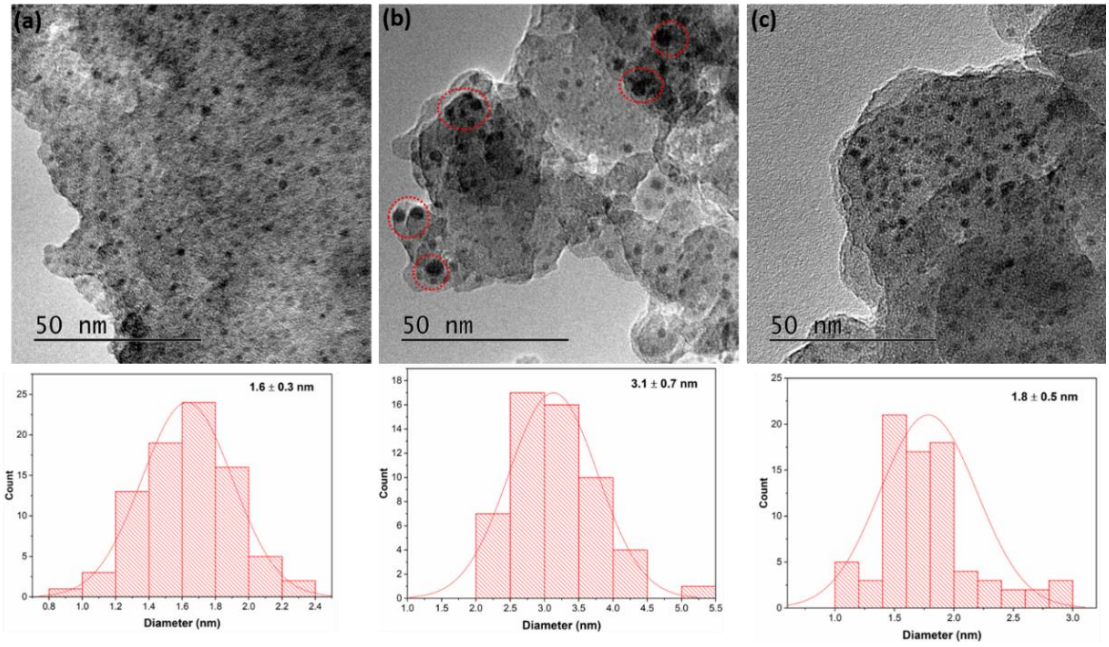

Figure 4.20 TEM image of (a) fresh Ru/SiO_2 catalyst, spent Ru/SiO_2 catalyst under (b) thermal condition (sintered Ni particles in circle) and (c) NTP conditions after the long-term deactivation test in $CO_2/CO/H_2$ mixture.

4.3.4 Mechanisms of CO Poisoning

To understand CO poisoning in the catalysis, comparative *in situ* DRIFTS–MS studies were carried out and compared with the DRIFTS study of CO_2 hydrogenation in Figure 4.10 and 4.12. Under the thermal condition, the DRIFTS spectra measured with CO/H_2 mixture (Figures 4.21) showed that the intensity of the carbonyl bands was significantly enhanced compared with the case of CO_2 hydrogenation (Figure 4.10), suggesting the relatively strong CO binding with Ru surface. Specifically, in addition to the gas-phase CO band (at ~2143 cm^{-1}), the broad carbonyl bands in a range of 2140–1770 cm^{-1} can be deconvoluted into three kinds of CO_{ad} bonds, *i.e.*, the bands at 1775 and 1950–1980 cm^{-1} (for the bridged carbonyls), 2005 cm^{-1} (for the linearly adsorbed CO with mono-

binding configuration), and 2030–2075 cm^{-1} (for the linearly adsorbed CO with multiple-binding configuration) [200]. After changing the feed to inert Ar (Figures 4.21b and 4.21c), the CO_{ad} bands decreased much slower than that in CO_2 hydrogenation (Figure 4.10b), indicating that more strongly adsorbed carbonyl species formed on the surface when CO was in the feed. By switching the feed to H_2 (Figures 4.21e and 4.21f), surface carbonyl species disappeared within 10 min, and the CH_4 concentration at the outlet of the DRIFTS cell showed a maximum (at ~1.3 min, which was followed by a continuous decline untill zero), showing that the adsorbed CO was converted to CH_4 in the presence of H_2. The evolution of the respective surface species as a function of time (Figure 4.21f) showed that the intensity of the carbonyl group at 2030–2050 cm^{-1} quickly decayed (within 2 min) under H_2, being the most reactive surface species, while the bridged carbonyl at 1775 cm^{-1} and linear monocarbonyl at 2005 cm^{-1} disappeared completely with comparatively slow rates. In contrast, the intensity of the peak at 1950–1980 cm^{-1}, corresponding to geminal dicarbonyls adsorbed on the low coordination Ru sites, remained constant within the initial 2 min and then decreased slowly, being relatively stable on the Ru surface and less reactive for hydrogenation [211]. The presence of these stable and less reactive surface species might block the active sites and hence contributed to the catalyst deactivation. Based on the findings from *in situ* DRIFTS–MS, one can conclude that, under the thermal condition, CO hydrogenation proceeded with similar pathways to those of the catalytic CO_2 hydrogenation [212]. However, the strong adsorption of CO on the catalyst surface could saturate the active sites, inhibiting CO_2 and H_2 adsorption.

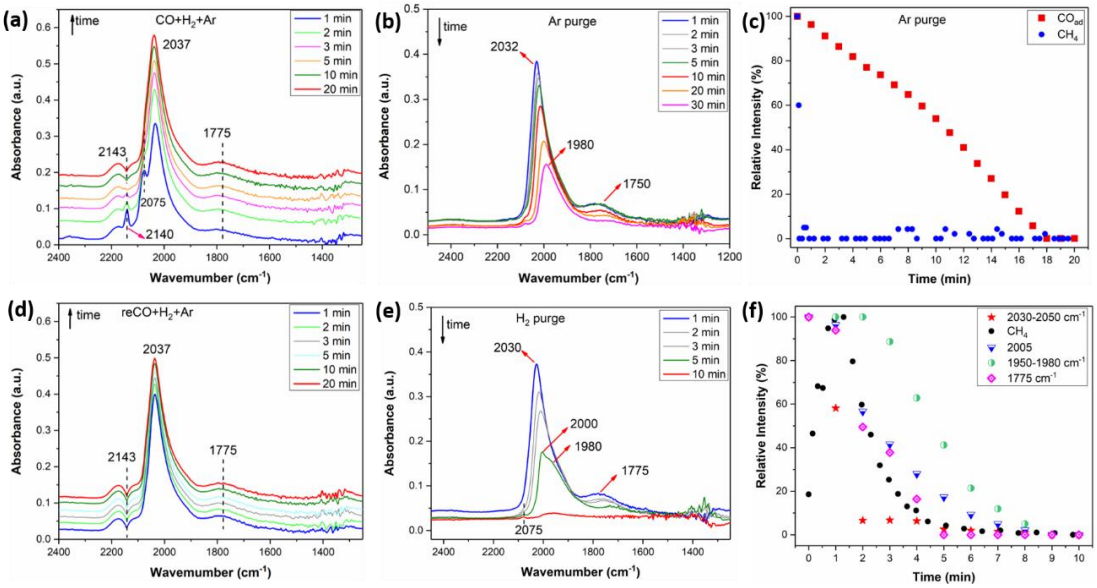

Figure 4.21 In situ DRIFTS spectra of surface species collected at 250 °C in the thermally activated CO hydrogenation over the Ru/SiO_2 catalyst. (a) Initial feed composition: 3% CO+9% H_2+ Ar; (b) change to inert Ar; (c) variations of CO_{ad} intensity from in situ DRIFTS and CH_4 intensity from MS after switching to Ar at 250 °C; (d) change back to the feed: 3% CO+9% H_2+Ar; (e) change to H_2/Ar. (f) variations of CO_{ad} intensity from in situ DRIFTS and CH_4 intensity from MS after switching the feed to H_2/Ar at 250 °C.

With the CO_2+CO+H_2 feed under the thermal condition, the associated DRIFTS spectra showed the combined features of the CO_2-/CO-alone hydrogenation system (as shown in Figure 4.22a and 4.22c), which was substantiated by the presence of strong adsorbed CO_{ad} and C_xH_y species on the surface. Specifically, spectrum for CO_2 hydrogenation (Figure 4.22a) showed that the multi-bonded CO_{ad} and C_xH_y species were adsorbed on the surface, being in line with the DRIFTS in Figure 4.10. After sweeping Ar for 20 min to clean the catalyst surface (20–40 min in Figure 4.22b), by introducing CO in the feed gas (Figure 4.22c), CO coverage increased significantly in comparison with the case of CO_2 hydrogenation and could not be completely removed by Ar sweeping (60–80 min, Figures 4.22d), indicating that the strong adsorbed CO_{ad} occupied the active sites for CO_2 and H_2 adsorption. Thus, when the feed was switched back to the gas mixture containing CO_2 + H_2 again (80–100 min in Figure 4.22e), the intensity of CO_{ad}

species on the catalyst surface is higher than the fresh catalyst in Figure 4.22a, as shown in Figure 4.22f.Accordingly, based on the findings obtained from the thermal catalysis and relevant *in situ* DRIFTS characterisation, it was plausible that the presence of CO in the system produced strongly adsorbed CO species on the Ru sites, which inhibited both CO_2 and H_2 adsorption, and thus suppressing CO_2 hydrogenation. Due to the limited concentration of surface H_{ad} species, the relatively stable and inactive carbon-containing species, such as carbonyls deposition, were encouraged to be formed on the catalyst surface, and they might progressively block the active sites. Thus, the associated carbonaceous species deposit and the metal sintering lead to the permanent catalyst deactivation [213], which confirms the results in Figures 4.16a and 4.18a.

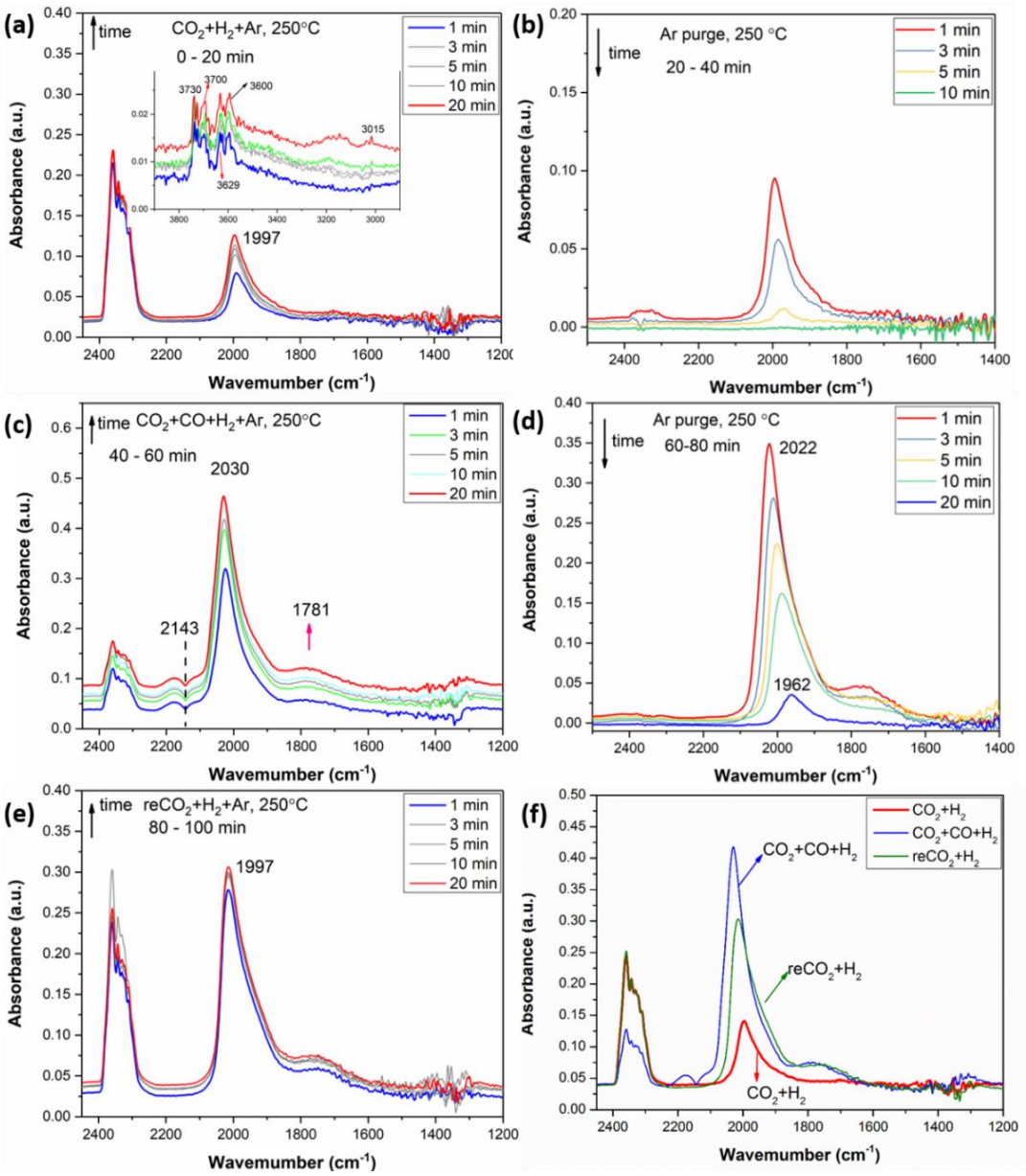

Figure 4.22 In situ DRIFTS spectra of surface species collected at 250 °C in thermal activated CO_2/CO hydrogenation over the Ru/SiO_2 catalyst. (a) CO_2 hydrogenation (3% CO_2 + 9% H_2 + Ar), (b) first Ar purge, (c) CO_2/CO hydrogenation (1.5% CO_2 + 1.5% CO + 9% H_2 + Ar), (d) second Ar purge, (e) back to CO_2 hydrogenation, and (f) the comparison of DRIFTS spectra collected during CO_2+CO hydrogenation. (IR spectra were recorded every 60 s with a resolution of 4 cm^{-1}).

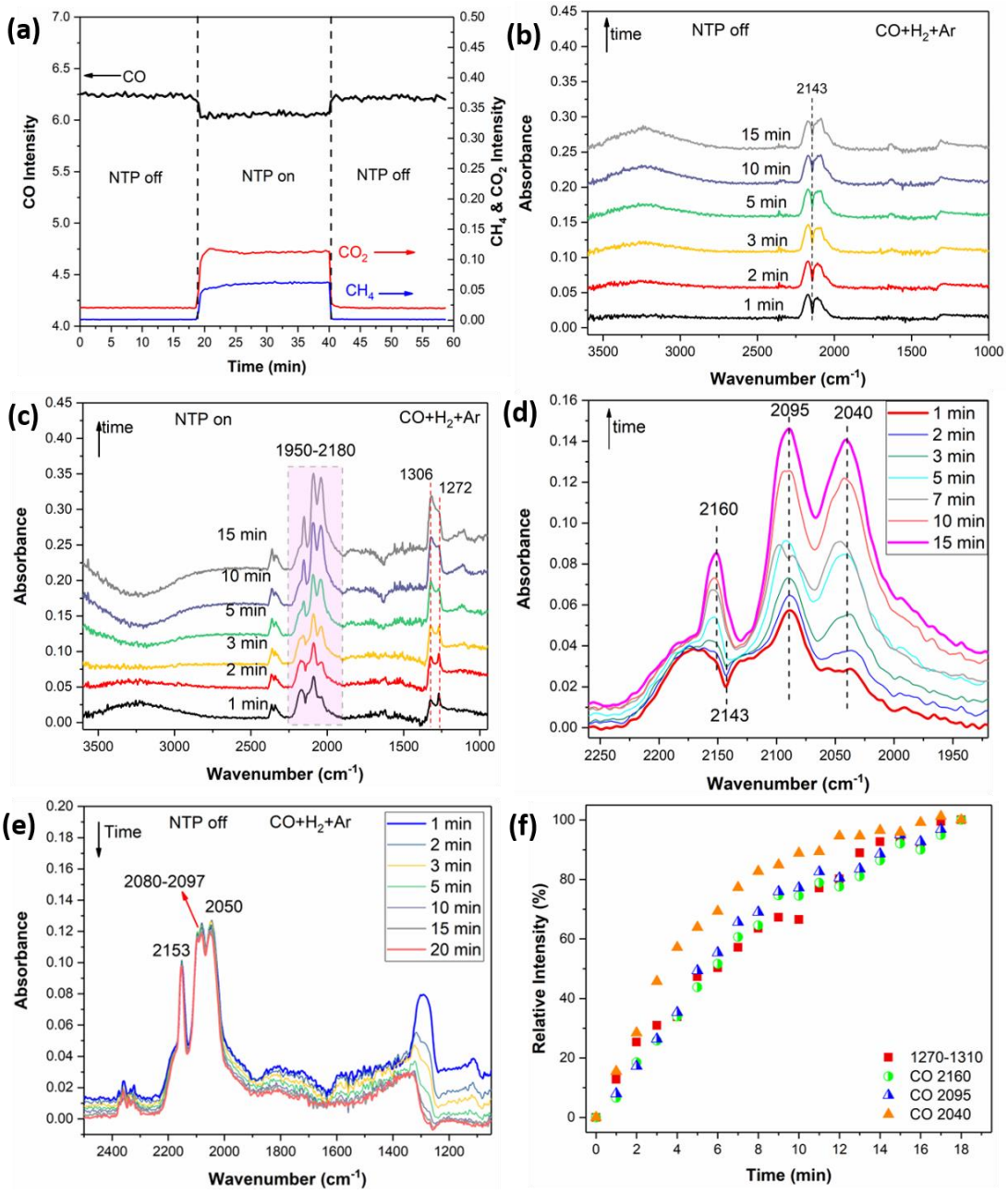

Figure 4.23 (a) Corresponding MS signals collected simultaneously from the DRIFTS cell as a function of time during the NTP-assisted CO hydrogenation over the Ru/SiO_2 catalyst. In situ DRIFTS spectra of surface species for CO hydrogenation over the Ru/SiO_2 catalyst under (b) NTP-off condition with the feed gas of 3% CO + 9% H_2 + Ar; (c and d) NTP-on condition with the feed gas (at 5.5 kV and 27.0 kHz); and (e) NTP-off condition with the feed gas. (f) Relative intensities of surface species as a function of ToS recorded in the *in-situ* DRIFTS from (c) and (d) during CO hydrogenation under NTP (at 5.5 kV and 27.0 kHz).

Without plasma discharge at RT, the Ru/SiO_2 catalyst showed no activity for CO hydrogenation, that is, (i) no CO conversion by MS as shown in Figure 4.23a and (ii) the only presence of gas phase CO (at ~2143 cm^{-1}) according to DRIFTS (Figure 4.23b). Upon the ignition of NTP, the MS profiles (Figure 4.23a) showed the instant decrease of CO signal and the simultaneous increase of CO_2 and CH_4 signals, confirming the production of CH_4 and CO_2 in the NTP-catalysis. CO_2 formation was due to WGSR, which could be activated by NTP [83]. Water were the product from the NTP-activated catalytic CO hydrogenation. As discussed above (Figure 4.16b), when CO was introduced into the feed for NTP-activated CO_2 hydrogenation, a decrease in CO_2 conversion was measured, which might be partly caused by water gas shift reaction. Simultaneously, the gas-phase CO_2 peak at about 2350 cm^{-1} was measured by DRIFTS (Figure 4.23c), in line with the intensity change from MS. In the OCO region (Figure 4.23d), the peak for gas phase CO at 2143 cm^{-1} disappeared, and the continuously development of the IR band at 2095 and 2160 cm^{-1} could be attributed to the linearly adsorbed carbonyl species on $Ru^{\delta+}$ with $Ru^{\delta+}$-CO and $Ru^{\delta+}$-$(CO)_n$ configuration, respectively. Another characteristic peak at 2040 cm^{-1} was assigned to the CO linearly adsorbed on Ru^0, while the gradually increased peaks at about 1272 and 1306 cm^{-1} corresponded to formyl species (CH_xO). The evolution of the surface carbon species recorded by DRIFTS as a function of time are correlated (Figure 4.23f). The increasing rate of carbonyl bands at 2095 and 2160 cm^{-1} was comparable with that of formyl species, which supported that CO is the intermediate towards formyl species. And the formation rate of CO_{ad} band at 2040 cm^{-1} increased relatively fast, which might be due to CO_2 dissociation (formed by water gas shift reaction) and CO adsorption. By switching off NTP, the peak of the gas-phase CO_2 decreased quickly, and the system was not active again for CO hydrogenation, which was in good agreement with the MS profile. Regarding the carbon species, the formyl species disappeared gradually due to the desorption after extinction of plasma (Figure 4.24), whilst CO_{ad} bands intensity barely changed (Figure 4.23e), indicating the strong interaction between the CO_{ad} species and catalyst surface. Besides, when the feed was switched to H_2/Ar (from 3%

CO + 9% H_2 + Ar), DRIFTS characterisation (Figures 4.25a) showed that the surface CO_{ad} species at 2090 cm^{-1} (due to gas phase CO adsorption) decreased immediately, whilst the intensity of formyl species increased initially and then decreased slowly. The initial increase of the formyl species on the catalyst surface could be ascribed to the reaction between CO_{ad} and H_{ad} (to form the formyl), while the subsequent decrease of the formyl species was due to the consumption of residual formyl species to form CH_4. As shown in Figure 4.25b, the rate of decrease of formyl species and CH_4 concentration (at the outlet of the DRIFTS cell by MS) was similar, confirming that the formyl species were originated from the reaction between CO_{ad} and H_{ad} and were the active intermediate for CH_4 formation. DRIFTS analysis of CO hydrogenation under the NTP condition showed that CO hydrogenation to CH_4 proceeded *via* CO adsorption and the formyl pathway, being similar with that of CO_2 hydrogenation (Figure 4.12).

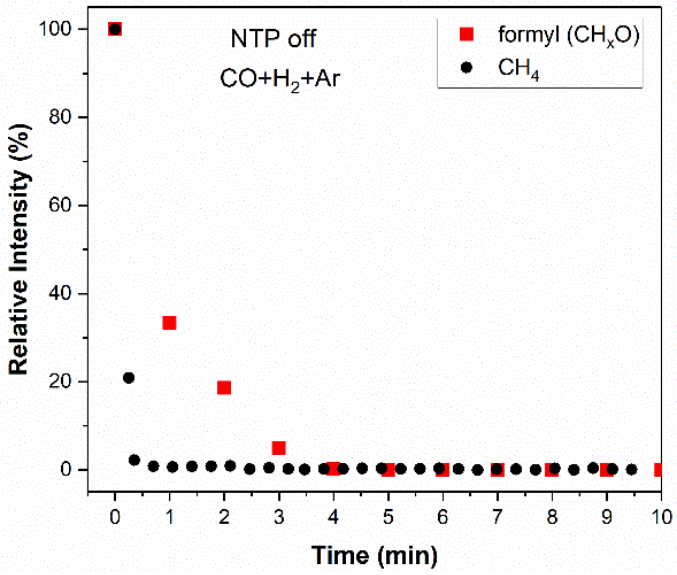

Figure 4.24 Evolution of formyl species (CH_xO) intensity (by DRIFTS, corresponding to Figure 4.23e) and CH_4 intensity (by MS, corresponding to Figure 4.23a) after switching off plasma discharge during CO hydrogenation. (Feed: 3% CO + 9% H_2 + Ar).

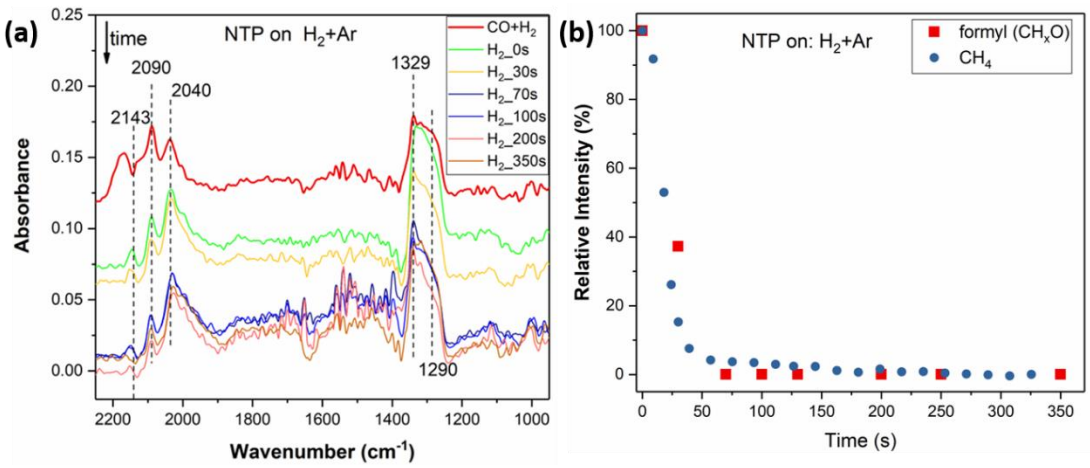

Figure 4.25 (a) In situ DRIFTS spectra of surface species over the Ru/SiO_2 catalyst under NTP (at 5.5 kV and 27.0 kHz) when switching the feed from 3% CO + 9% H_2 + Ar to 9% H_2 + Ar. (b) variations of formyl species (CH_xO) intensity from in situ DRIFTS and CH_4 intensity change from MS after switching the feed to H_2/Ar under NTP (at 5.5 kV and 27.0 kHz). (IR spectra were recorded every 10 s with a resolution of 4 cm^{-1}).

NTP-catalysis with the $CO_2/CO/H_2$ feed was examined by DRIFTS-MS (Figures 4.26 and 4.27). Being different from CO hydrogenation, the CO_{ad} peak at 2080 cm^{-1}, due to CO_2 dissociation, appeared first and then combined with the peak at 2097 cm^{-1} (originating from the gas phase CO adsorption). Accordingly, the evolution profile of the surface carbon species (Figure 4.26c) showed that the CO_{ad} species had higher increasing rates than that of formyl species initially (within 8 min) due to CO_2 dissociation and CO adsorption on the Ru sites. The subsequent change of the increasing rate was due to saturation of relevant active sites on Ru surface by CO_2/CO adsorption [200]. This finding suggested that CO_2 and CO co-adsorption existed in the NTP-catalysis. In contrast, the formyl species presented a constant formation rate, confirming that the formyl species originated from the reaction between CO_{ad} and H_{ad}. Besides, by switching CO feed on and off alternatively, DRIFTS-MS characterisation of the catalysis (Figure 4.28) showed that CO_2 MS signal increased with CO in the feed (*i.e.*, production of CO_2), which confirms the presence of WGSR under the NTP condition with the $CO_2/CO/H_2$ mixture. Therefore, under NTP conditions, the presence

of CO in the feed affected CO_2 conversions, which was due to (i) the occurrence of WGSR in the system for CO_2 formation and (ii) the relatively strong adsorption of CO, in line with the result in Figure 4.16b. Based on the in situ DRIFTS characterisation and relevant discussion, the presence of CO in the feed did not alter the reaction pathways for CO_2 hydrogenation under thermal and NTP conditions. However, in comparison with the CO poisoning under the thermal conditions (as discussed before, *i.e.*, due to strong CO adsorption and associated metal sintering of the catalyst), the collisions between reactive plasma species in NTP could recover the active sites by removing the adsorbed carbon species effectively, which lead to the sites available for CO_2 adsorption [207, 208, 214]. This is confirmed by the comparison of the relevant IR spectra (Figure 4.29), which showed the comparatively low intensity of the adsorbed CO_{ad} on the Ru catalyst under NTP. Therefore, NTP-catalysis promoted the adsorption of CO_2 and alleviated CO adsorption on the catalyst surface in the presence of CO, mitigating the 'CO poisoning' effect on the performance of CO_2 hydrogenation and being opposite to that experienced by the thermal catalysis. More importantly, according to the literature [122, 215, 216], H_2O molecules will occupy the active sites and present an inhibiting effect on the CO_2 hydrogenation. Conversely, NTP enabled WGSR of CO with the produced H_2O, which shifted the equilibrium of CO_2 hydrogenation toward CH_4 production. The phenomenon observed in the system under investigation showed the interesting effect of CO on NTP-catalytic CO_2 hydrogenation, that is, as a reaction promoter rather than a catalyst poison, due to the co-presence of WGSR, CO_2 hydrogenation and CO hydrogenation under NTP conditions.

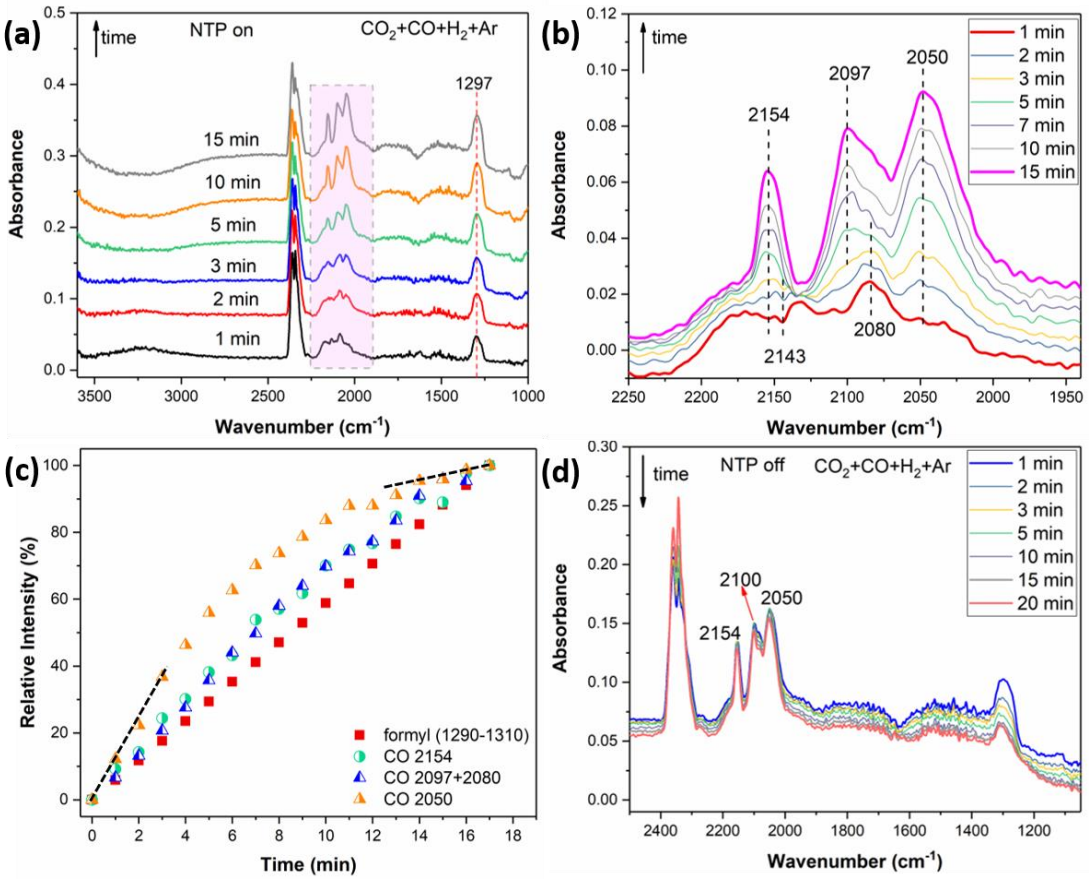

Figure 4.26 In situ DRIFTS spectra of surface species for hydrogenation of CO_2+CO over the Ru/SiO_2 catalyst under (a and b) NTP-on condition with the feed gas of 1.5% CO_2 +1.5% CO + 9% H_2 + Ar (at 5.5 kV and 27.0 kHz), (c) Relative intensities of surface species as a function of ToS recorded in the *in-situ* DRIFTS from (a) and (b), and (d) NTP-off condition with the feed gas.

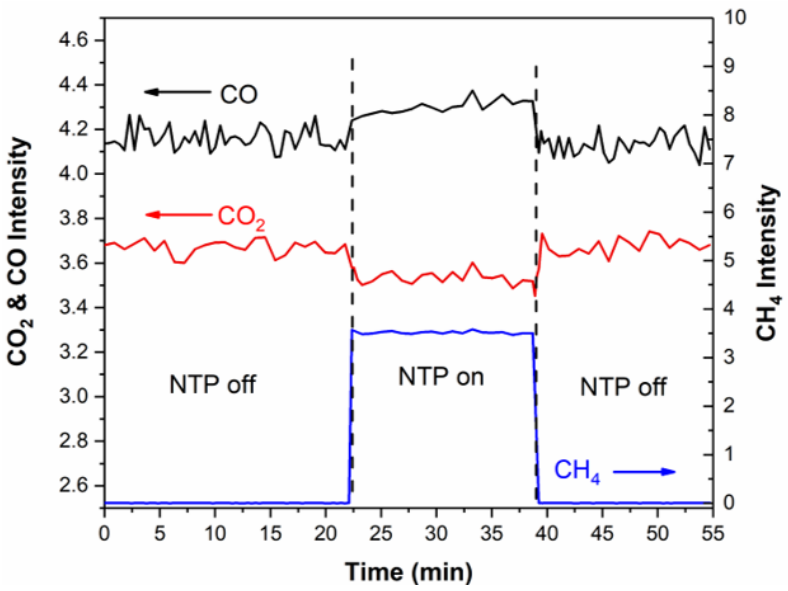

Figure 4.27 Corresponding MS signals collected simultaneously from the DRIFTS cell as a function of time during NTP-assisted CO_2+CO hydrogenation over the Ru/SiO_2 catalyst.

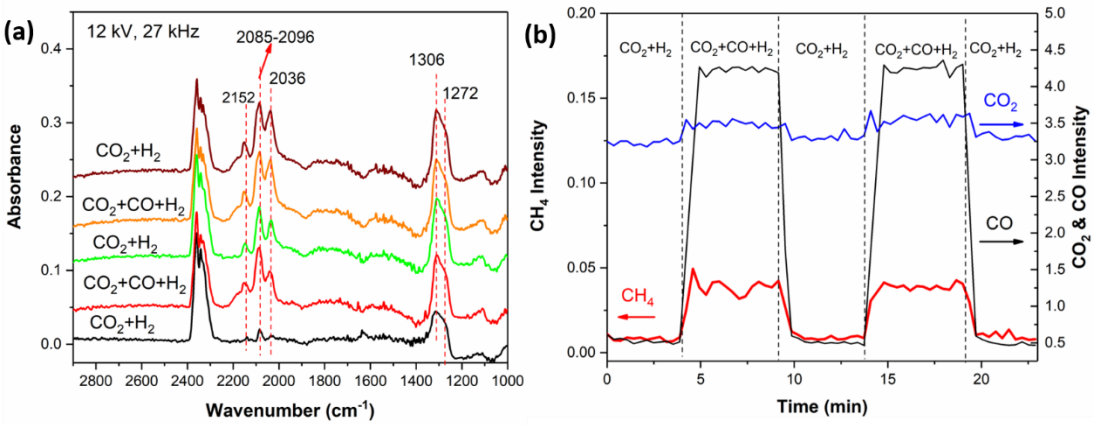

Figure 4.28 (a) In situ DRIFTS spectra of surface species, and (b) corresponding MS profile for CO_2 hydrogenation over the Ru/SiO_2 catalyst with CO feeding in and out. (Condition: 1.5% CO_2 + 1.5% CO + 9% H_2 + Ar, IR spectra were recorded every 60 s with a resolution of 4 cm^{-1}).

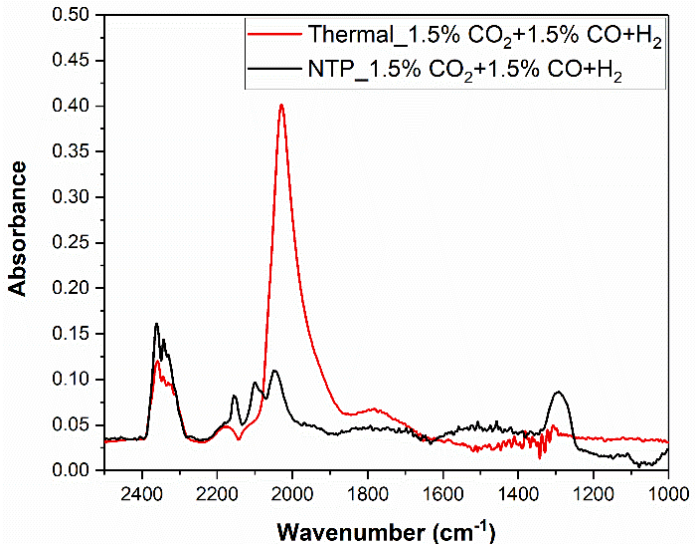

Figure 4.29 Comparison of DRIFTS spectra of surface species collected at 10 min under thermal conditions (at 250 °C) and NTP condition (at 5.5 kV and 27.0 kHz).

4.4 Conclusions

In this study, NTP-catalyst system was demonstrated to be efficient for CO_2 hydrogenations under atmospheric conditions, in which 65% CO_2 conversion and 63% CH_4 yield can be achieved over Ru/SiO_2 catalyst. And the intrinsic nature of catalyst such as surface area is crucial under both thermal and NTP condition. The comparative kinetic and in situ DRIFTS-MS study revealed that the NTP-catalysis could lower the energy barrier required for catalysis and enable both Langmuir-Hinshelwood and Eley-Rideal mechanisms.

The effect of CO on the catalysis under both thermal and NTP condition was investigated for the first time to understand CO poisoning comparatively. In the thermal catalysis, the catalyst suffered from a significant decrease of CO_2 conversion and deactivation due to CO poisoning, whilst in the NTP-catalysis, the CO played a different role in the system, and the catalyst showed the comparatively good stability and regenerability by NTP. In situ DRIFTS-MS study of the thermal catalysis showed that (i) CO preferred to adsorb on the Ru surface strongly to inhibit CO_2 and H_2

adsorption and decrease CO_2 conversion significantly, and (ii) the formation of less reactive and strongly adsorbed carbon species (e.g., CO_{ad}) due to CO strong adsorption and metal sintering deactivate the catalyst permanently. Conversely, in NTP-catalysis, collisions of reactive plasma species contributed to the recovery of the active sites by removing the strongly adsorbed CO_{ad}, which facilitated CO_2 adsorption, and hence CO_2 hydrogenation. Therefore, NTP-catalysis could alleviate the CO effect on CO_2 hydrogenation and regenerate the catalyst in situ in presence of CO during the catalysis. Importantly, the NTP-induced WGSR of CO with the produced H_2O also promoted the equilibrium shift of CO_2 hydrogenation toward CH_4 production. This work demonstrates that, under NTP conditions, the role played by CO in Ru catalysed CO_2 hydrogenation is fundamentally different from its positioning role in thermal catalysis, showing the potential of NTP-catalysis to address some of the challenges in conventional heterogeneous catalysis, specifically, the development of advanced hybrid NTP-catalysis systems to solve the chemical deactivation issues for practical catalysis.

Chapter 5 Silicalite-1 encapsulated Ni nanoparticles prepared by different synthesis methods as sintering-/coking-resistant catalysts for dry reforming of methane

5.1 Introduction

Methane (CH_4) and carbon dioxide (CO_2) are main greenhouse gases, which contribute to current environmental issues (*e.g.,* global warming and climate changes) significantly [37]. Hence, the development of efficient process to activate and convert CH_4 and CO_2 simultaneously into valuable chemicals is a promising and practical solution to achieve the carbon reduction goal [217]. Catalytic dry reforming of methane (DRM) has attracted great interest because it utilises CH_4 and CO_2 for the direct production of syngas (*i.e.,* $CO+H_2$) with the theoretical H_2/CO molar ratio approximately 1, which is the essential feedstock to produce value-added oxygenated chemicals and long-chain hydrocarbons *via* Fischer-Tropsch reactions [218, 219].

Theoretically, DRM (*i.e.,* $CH_4 + CO_2 \rightarrow 2CO + 2H_2$, $\Delta H^{\circ}_{298K} = +247.3$ kJ mol^{-1}) is highly endothermic which requires high temperature (typically >600 °C), and thus high energy consumption [220]. Nickel (Ni)-based catalysts are commonly used catalysts for DRM due to their good catalytic activities and relatively low cost compared to the catalysts based on noble metals (such as Pt, Ru and Rh) [221]. However, Ni-based catalysts commonly suffer from catalyst deactivation during DRM, which is caused by (i) metal particle sintering at high reaction temperatures (*e.g.,* 700 °C) and (ii) carbon deposition induced by methane cracking and CO disproportionation, being the major limitation for the large-scale industrial applications [42, 222]. Therefore, the development of novel Ni-based catalysts with the resistance to metal sintering and coking is urgently needed for progressing the industrial DRM. Various strategies have been proposed and explored to increase the catalyst activity and stability of Ni-based

reforming catalysts, including the methods of (i) reducing the particle sizes [99, 223], (ii) using promoters [224, 225], (iii) developing bimetallic catalysts [221, 226, 227], and (iv) encapsulating metal nanoparticles (NPs) to form unique architectures such as core-shell and yolk-shell structures [228, 229]. In comparison with the metal NPs supported on the external surface of supports, confinement of metal NPs inside the support leads to the improved metal stability (by preventing sintering) and coking resistance (by suppressing carbon diffusion on the metal particles) [230, 231]. For example, core-shell Ni@SiO_2 catalysts with small Ni NPs (~5 nm) showed a good stability of 50 h in DRM, which could be attributed to the confinement of Ni NPs by the silica shell (to avoid sintering) and the small size of Ni NPs (to reduce carbon diffusion in Ni crystals) [232].

Zeolites with uniform micropores, high specific surface area and high thermal stability (especially siliceous zeolites such as silicalite-1) are considered as promising supports to spatially confine the metal particles within their frameworks to form the metal@zeolite catalysts, being able to prevent the aggregation and deactivation of metallic species [233]. For example, Pt, Pd, Rh and Ag NPs encapsulated within Beta and silicalite-1 zeolites have been demonstrated to be sintering resistant at 600–700 °C and showed the long reaction lifetimes in catalytic C1 chemistry including the water-gas shift reaction, oxidative reforming of methane and CO_2 hydrogenation [234]. Although encapsulated catalyst structures have been reported in previous studies, the relevant synthesis methods can strongly affect the physiochemical properties of the catalysts, including metal particle sizes, degree of encapsulation and metal-support interactions, thus influencing the catalytic performance during high-temperature catalysis such as DRM [233]. For example, Ni encapsulated in hollow silicalite-1 developed by a post-treatment method could suppress carbon formation during DRM, showing about 10% carbon deposition after 6 h on stream (compared with ~30% carbon deposition on the impregnated Ni/silicalite-1 catalyst). However, large Ni NPs were still found on the external surface of the zeolite support, which led to coke formation

and a significant decrease (~62%) of the CO_2/CH_4 conversion after the 20 h testing in DRM [235]. By comparison, silicalite-1 encapsulated Pt NPs (<2nm) prepared by a water-in-oil microemulsion successfully achieved the fully encapsulation structure (*i.e.,* encapsulating all the Pt NPs within the zeolite), but with zeolite structure collapsing at the temperature of >620 °C, leading to a decreased accessibility of active sites to reactant. Thus, the catalysts suffered from a severe deactivation at high reaction temperatures [236]. Hence, systematic insights into the synthesis-structure-performance relationships in the encapsulated metal NPs (within zeolite crystals) catalysts are needed for the rational development of stable and high-performing catalysts for DRM.

Herein, encapsulated Ni NPs within silicalite-1 (S-1) catalysts were prepared by different synthesis methods (including post treatment method, direct hydrothermal and seed-directed synthesis) and were investigated comparatively in DRM to assess their catalytic performance. The effect of synthesis methods on the properties of catalysts including degree of encapsulation, Ni dispersion, zeolite shell structure and metal-support interactions and the catalytic performance (in DRM) was investigated. The S-1 supported Ni catalyst prepared by conventional wet impregnation method was used as the reference catalyst for comparison. The longevity (up to 28 h) of the catalysts under investigation showed that 5Ni@SiO_2-S1 catalyst (with the full encapsulation structure) developed by the seed-directed synthesis method presented the significantly improved stability, which was reflected by the reduced metal sintering and carbon formation during the catalysis due to the small Ni particle size and complete confinement of Ni in S-1 zeolite promoted by the method.

5.2 Experimental Section

5.2.1 Preparation of Catalysts

5.2.1.1 Chemicals

Tetrapropylammonium hydroxide solution (TPAOH, 40% in H_2O), tetraethyl orthosilicate (TEOS, 98%), ammonium hydroxide solution (28% in H_2O), urea (BioUltra, >99.5%), nickel nitrate hexahydrate ($Ni(NO_3)_2 \cdot 6H_2O$, ≥97%) and ethylenediamine ($NH_2CH_2CH_2NH_2$, ≥99.5%) were purchased from Sigma-Aldrich. All chemicals were used as received.

5.2.1.2 Synthesis of silicalite-1 (S-1) zeolite

The S-1 zeolite was prepared by a conventional hydrothermal method with a starting molar composition of $1SiO_2$: 0.4TPAOH: $35H_2O$. In a synthesis, 8.32 g of TEOS, 8.125 g of TPAOH aqueous solution, and 25 g of H_2O were mixed and stirred at room temperature (RT) for 6 h to form a clear solution. Then, the mixture was transferred into a 50 mL Teflon-lined autoclave and was hydrothermally treated at 170 °C for 3 days. Centrifugation was used to separate the solid products from the liquid phase, and the obtained solid product was washed with deionized (DI) water several times, and then dried at 110 °C in the oven overnight. Finally, the obtained sample was calcined in a muffle furnace at 550 °C for 8 h (1 °C min^{-1}) to remove the organic template.

5.2.1.3 Synthesis of supported Ni catalyst on S-1 catalyst (Ni/S-1) by impregnation

Supported Ni (theoretical loading of 5.0 wt.%) on S-1 zeolite was prepared by the incipient wetness impregnation method. Typically, 2.5 g of the calcined S-1 zeolite was suspended in water (30 mL), then 0.619 g of $Ni(NO_3)_2 \cdot 6H_2O$ was added to the suspension. After vigorous stirring for 3 h, the precipitate was evaporated at 80 °C under stirring. Finally, the obtained solid was calcined in a muffle furnace at 550 °C for

6 h (1 °C min^{-1}). The resulting sample is denoted as 5Ni/S-1.

5.2.1.4 Synthesis of hollow S-1 encapsulated Ni catalyst (Ni@hol S-1)

Hollow S-1 encapsulated Ni catalyst was prepared by treating the 5Ni/S-1 catalyst hydrothermally with TPAOH solution. Typically, 1.0 g of 5Ni/S-1 was mixed with 0.2 M TPAOH solution (40 mL) and stirred for 1 h at RT. The mixture was then transferred into a 100 mL Teflon-lined autoclave, and the system was left at 170 °C for 2 days. The obtained product was centrifuged, washed with DI water, and dried at 110 °C in an oven overnight. Finally, the obtained sample, denoted as 5Ni@hol S-1, was calcined in a muffle furnace at 550 °C for 6 h (1 °C min^{-1}).

5.2.1.5 Direct hydrothermal synthesis of encapsulated Ni in S-1 catalyst (Ni@EDA-S1)

To enable the encapsulation of Ni species in the framework of S-1, ethylenediamine coordinated Ni, *i.e.,* $[Ni(NH_2CH_2CH_2NH_2)_3](NO_3)_2$, was used as the precursor and introduced directly during the synthesis of S-1 zeolite [237]. Specifically, the molar composition was $1SiO_2$: 0.4TPAOH: $35H_2O$: 0.05 $[Ni(NH_2CH_2CH_2NH_2)_3](NO_3)_2$, and the synthesis condition was similar to that for the preparation of S-1, as described above. $[Ni(NH_2CH_2CH_2NH_2)_3](NO_3)_2$ was prepared by dissolving 0.95 g of $Ni(NO_3)_2{\cdot}6H_2O$ into 2 mL ethylenediamine and 8 mL H_2O mixture under stirring at RT. Then the precursor was added dropwise into the clear solution of TEOS, TPAOH and H_2O under stirring for 30 min. Then, the mixture was transferred into a 50 mL Teflon-lined autoclave for synthesis at 170 °C for 3 days. The prepared solid products were centrifuged, washed with DI water several times, and then dried at 110 °C in the oven overnight. Finally, the obtained sample was calcined in a muffle furnace at 550 °C for 6 h (1 °C min^{-1}) to remove the organic precursor and template. The resulting sample is denoted as 5Ni@EDA-S1.

5.2.1.6 Seed-directed synthesis of encapsulated Ni in S-1 catalyst (Ni@SiO_2-S1)

Preparation of Ni/SiO_2 seeds. SiO_2 seeds were synthesised by a modified Stöber method [238]. Specifically, 12 mL of TEOS was added dropwise into a water/ethanol mixture (24 mL and 160 mL, respectively) under stirring. Then, 5 mL of $NH_3 \cdot H_2O$ was added dropwise into the mixture for further reaction for 7 h. Finally, spherical SiO_2 seeds were centrifuged, washed with water for 3 times, and then dried at 80 °C in the oven overnight. Next, 1.0 g of SiO_2 seeds were dispersed into 60 mL of H_2O. Then, $Ni(NO_3)_2 \cdot 6H_2O$ (0.5 g) and urea (molar ratio of NH_3/Ni = 10:1) were dissolved into 15 mL of H_2O to form nickel ammonia complex. After that, the nickel ammonia complex was added to the silica dispersion and continued to be stirred for 2 h. The mixture was then transferred to the Teflon-lined autoclave and kept at 150 °C for 24 h. The resulting precipitate was centrifuged and washed with DI water to remove the ammonium ions.

Preparation of Ni@SiO_2-S1 catalyst. The catalyst was synthesised with the molar composition of $1SiO_2$: 0.4TPAOH: $35H_2O$. Typically, 1.0 g of the above-prepared Ni/SiO_2 seeds were dispersed in 17 mL of water by sonication for 1 h. Then, TPAOH solution (6.25 g) was added under stirring for 2 h. After that, 2.5 g of TEOS was added into the solution slowly and the resulting solution was continuously stirred for 6 h to fully hydrolyse the TEOS. Subsequently, the resulting gel was transferred into a 50 mL Teflon-lined autoclave for hydrothermal synthesis at 170 °C for 2 days. The obtained solid was washed with water and ethanol for several times, and then dried at 110 °C overnight, followed by calcination in air at 550 °C for 6 h. The obtained catalyst is denoted as 5Ni@SiO_2-S1.

5.2.2 Characterisation of catalysts

The morphology of the catalysts was investigated using a JEOL 7401 high-resolution field scanning electron microscope (SEM) at an accelerating voltage of 20 kV. The bright-field transmission electron microscopy (TEM) and high-angle annular dark field

scanning transmission electron microscopy (HAADF-STEM) were performed on an FEI Tecnai F20 transmission electron microscope operating at 200 kV. X-ray diffraction (XRD) patterns of the materials were performed on a Proto A X-ray diffractometer with a nickel absorber (0.02 mm, K_β = 1.3923 Å) using Cu$K_{\alpha 1}$ radiation (λ = 1.5406 Å) at 40 kV, 40 mA, a scanning rate of 2° min^{-1}, a step size of 0.03° s^{-1}, and 2θ angle from 3 to 100°. X-ray photoelectron spectra (XPS) were recorded on a Kratos AXIS Ultra DLD apparatus with monochromated Al Kα radiation X-rays source, a charge neutraliser and a hemispherical electron energy analyser with a pass energy of 160 eV. The binding energies (B.E) were calibrated by the C 1s peak at 284.8 eV. N_2 physisorption analysis of the samples was conducted at −196 °C using a Micromeritics 3Flex Surface Characterisation Analyser. Prior to N_2 physisorption measurements, the samples (~100 mg) were degassed at 250 °C under vacuum overnight. The Brunauer-Emmett-Teller (BET) method was used to determine the specific surface area of materials, while micropore volumes were obtained by the *t*-Plot and mesopore volumes were calculated by subtracting the micropore volume from the according total pore volume (at p/p^0 = 0.99), respectively. Elemental analysis of metal in the samples was analysed by using ICP-OES (PQ 9000 Elite system). Prior to analysis, the sample (20 mg) was dissolved in concentrated sulfuric acid (6 mL) and concentrated nitric acid (6 mL) by microwave digestion (ETHOS UP microwave digester). Temperature programmed reduction (H_2-TPR) were carried out using Quantachrome ChemBet Pulsar equipped with a thermal conductivity detector (TCD). Typically, 30 mg of the sample was loaded in a quartz tube reactor and then pre-treated with oxygen at 300 °C for 1 h. After cooling to RT, a gaseous mixture of 5% H_2 in Ar was introduced into the reactor (at 50 mL min^{-1}), and the system temperature was increased to 900 °C with a heating rate of 10 °C min^{-1}. Thermogravimetric analyses (TGA) were performed using a thermogravimetric analyser (TGA 550) in the temperature range of 30–900 °C with a heating rate of 10 °C min^{-1} in air (30 mL min^{-1}).

5.2.3 Catalysis

Catalytic DRM was performed in a continuous flow fixed-bed reactor at atmospheric pressure (6 mm O.D. × 4 mm I.D., Figure 5.1). Typically, 60 mg catalysts (pelletised to give particle sizes of 250–425 μm) were loaded in the centre of the reactor between two quartz wool plugs. The temperature of the catalyst bed was measured by a K-type thermocouple embedded in the catalyst bed. Before reaction, the catalyst was reduced at 700 °C for 1 h with 40 vol.% H_2/Ar (at 100 mL min^{-1}). After reduction, the catalyst was cooled down to 500 °C in Ar (50 mL min^{-1}). Subsequently, the gas mixture of CO_2, CH_4 and Ar (molar ratio of 1:1:2) with a total flow rate of 50 mL min^{-1} was fed into the reactor (via three mass flow controllers, Bronkhorst®, F-201CV-500-RAD-11-V). The activity of the catalysts was measured from 500 °C to 750 °C (with 50 °C increments) under the steady state conditions. The stability of the catalysts was assessed at a constant temperature of 700 °C with different durations (*i.e.*, time-on-stream, ToS, up to 28 h). The outlet gas composition was detected by a two-channel on-line gas chromatography (GC) equipped with an Elite-Carbon molecular sieve packed column (N 9303926), a thermal conductivity detector (TCD) and a flame ionisation detector (FID). For each measurement, three consecutive measurements of gas products were analysed to obtain the averaged values (error margins <3%). The liquid products (*e.g.,* water) was removed by a glass water trap cooled by an ice bath and the total flowrate of the gas products was measured by a bubble-flow meter for the calculation of CO_2 conversion (X_{CO_2} , Eq. 5.1) and CH_4 conversion (X_{CH_4} , Eq. 5.2) and the H_2/CO molar ratio (Eq. 5.3).

$$X_{CO_2} = \frac{F_{CO_2}^{in} - F_{CO_2}^{out}}{F_{CO_2}^{in}} \times 100 \qquad \text{Eq. 5.1}$$

$$X_{CH_4} = \frac{F_{CH_4}^{in} - F_{CH_4}^{out}}{F_{CH_4}^{in}} \times 100 \qquad \text{Eq. 5.2}$$

$$\frac{H_2}{CO} = \frac{F_{H_2}^{out}}{F_{CO}^{out}} \qquad \text{Eq. 5.3}$$

where F stands for the molar flow rate in the inlet (superscript in) and outlet (superscript out) of the reactor (mol s^{-1}).

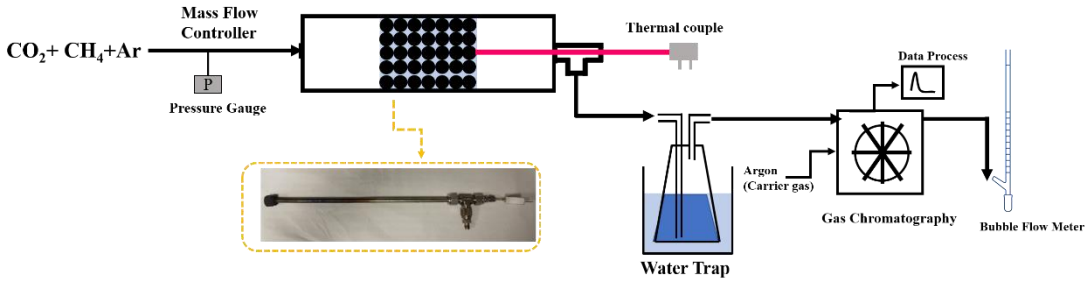

Figure 5.1 Schematic diagram of the system for catalytic DRM.

5.3 Results and discussion

5.3.1 Physiochemical Properties of Catalysts.

Comparative XRD patterns of different catalysts under study (after calcination) are presented in Figure 5.2a. The characteristic peaks of silicalite-1 at 2θ = 7.97°, 8.83°, 23.17°, 24.09° and 24.48°, corresponding to the (011), (200), (501), (033) and (133) facets, were observed for all the catalysts, proving the well-crystallised MFI structure (JCPDS no. 44-0696) [239]. In addition to the strong diffraction peaks of S-1 zeolite, diffraction peaks at about 2θ = 43.5° were also identified in the XRD patterns of 5Ni/S-1 and 5Ni@hol S-1, corresponding to the (200) facets of NiO (JCPDS no. 47-1049). Conversely, diffraction peaks of NiO phase were not observed in 5Ni@EDA-S1 and 5Ni@SiO_2-S1, suggesting the possible presence of highly dispersion of Ni species or encapsulated Ni within the S-1 support. After reduction, XRD diffraction patterns of all S-1 supports were comparable to that of the as-prepared ones, confirming the stability of S-1 support during the reduction treatment. Also, the characteristic peaks for Ni^0 at 2θ = 44.45° in 5Ni/S-1 and 5Ni@hol S-1 were observed, showing the formation of

metallic Ni NPs in the catalysts, whilst Ni^0 phase was again not detected in 5Ni@EDA-S1 and 5Ni@SiO_2-S1, suggesting that metal aggregation of the highly dispersed and encapsulated Ni phases was unlikely during reduction treatment.

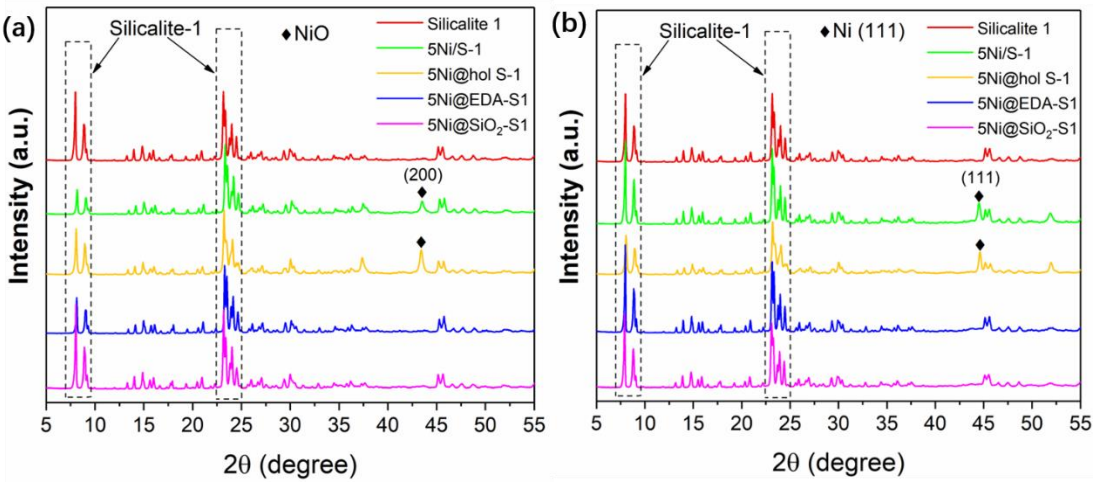

Figure 5.2 XRD patterns of (a) the as-prepared catalysts (after calcination in air at 550 °C for 6 h) and (b) the reduced catalysts (in H_2/Ar at 700 °C for 1 h).

The morphology of the calcined catalysts is shown in Figure 5.3. The 5Ni/S-1 catalyst had an ellipsoid-shape morphology with an average crystal size of 240 nm. For the 5Ni@hol S-1 catalyst, broken zeolite crystals were found by SEM, showing the cavities, which confirm the formation of the hollow structures. Additionally, the average crystal size of 5Ni@hol S-1 was measured to be ~280 nm, and some large crystals were observed, which could be ascribed to the dissolution of the interior of S-1 zeolite and recrystallisation on its outer surface during the TPAOH treatment. The 5Ni@EDA-S1 and 5Ni@SiO_2-S1 catalysts showed a similar coffin-like morphology with larger crystal sizes than that of the catalysts prepared by impregnation. Specifically, for 5Ni@EDA-S1, the average crystal length was ~4.7 μm and some nanosheets were formed (as indicated in Figure 5.3c), which can be the result of adding the $[Ni(NH_2CH_2CH_2NH_2)_3](NO_3)_2$ precursor in the synthesis mixture, affecting the nucleation and crystallisation process of S-1 zeolite [240]. By contrast, 5Ni@SiO_2-S1 showed the well-defined crystal with an average length of ~3.1 μm, suggesting that the seed-directed synthesis method was beneficial to the formation of S-1 zeolite with the

uniform structure.

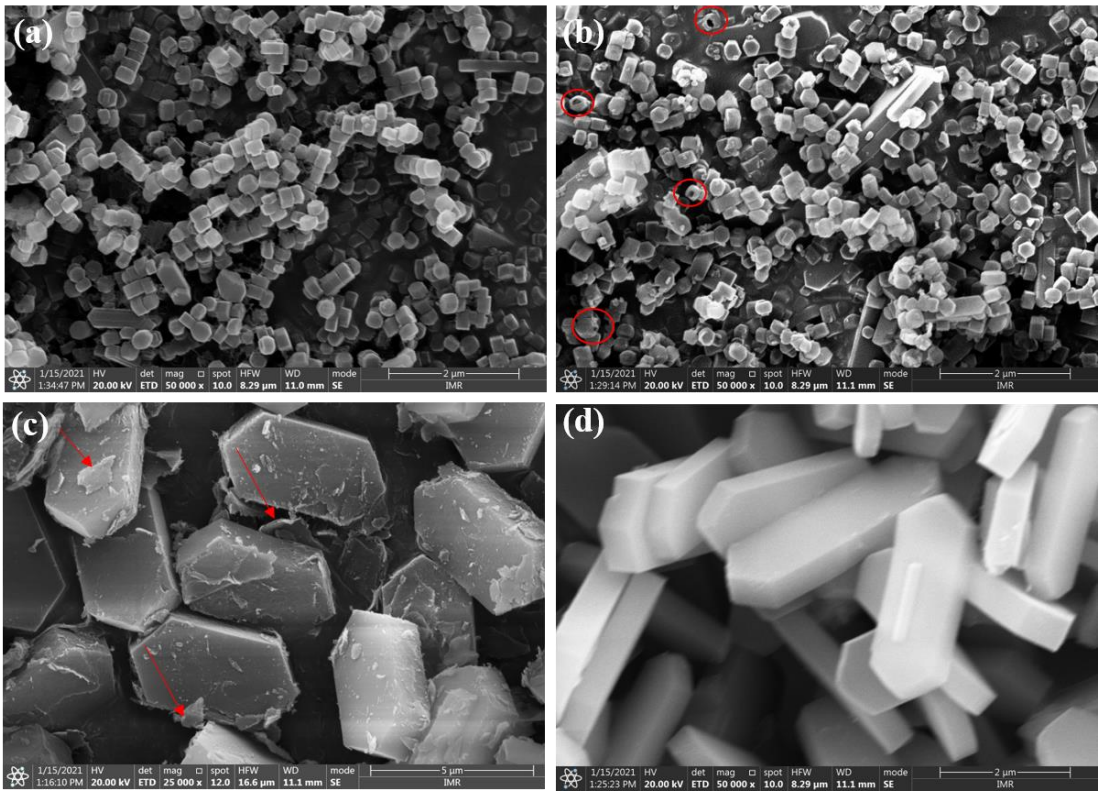

Figure 5.3 SEM micrographs of the calcined (a) 5Ni/S-1, (b) 5Ni@hol S-1, (c) 5Ni@EDA-S1 and (d) 5Ni@SiO_2-S1 catalysts.

The microscopic details of the morphology and size distribution of Ni NPs of the catalysts were further investigated by HRTEM, and the results are shown in Figure 5.4. For 5Ni/S-1, Ni NPs with the average particle size of ~3.7 nm distributed randomly on the external surface of S-1 crystals (Figure 5.4a-c). After the TPAOH treatment, 5Ni@hol S-1 with the hollow structure and thin intact shell (average thickness of ~14 nm) were formed due to the dissolution-recrystallisation of 5Ni/S-1 during the treatment [241], which is in line with the findings by SEM (Figure 5.4d-f). Most of the Ni NPs migrated from the surface into the cavities, and thus are encapsulated by the shells of hollow S-1. The average Ni particle size of 5Ni@hol S-1 was comparable to that of 5Ni/S-1, indicating metal agglomeration was unlikely during the treatment. However, some Ni NPs were found anchored and/or remained on the outer surface of

the cavities (as identified in Figure 5.4d-e), which tended to agglomerate into large particles. For 5Ni@EDA-S1, HRTEM images (Figure 5.4g-i) showed that Ni NPs encapsulated within S-1 zeolite are uniformly dispersed and distributed with an average particle size of 7.3 nm throughout the zeolite crystals, which is in line with the findings of previous studies [237, 242]. However, some Ni NPs were found to be formed on the external surface of zeolite, which might be due to Ni precursors used in the synthesis leading to Ni NPs growth on the internal and external surface of zeolite [243], forming the partially encapsulated Ni structure (Figure 5.5a-c). By contrast, STEM and EDX of 5Ni@SiO_2-S1 catalyst in Figure 5.5d-e showed insignificant Ni species on the surface of the support, confirming that the Ni particles are indeed fully encapsulated within the S-1 crystals. Previous studies demonstrated that a 7 nm minimum threshold for Ni particle size is required for the filamentous carbon formation [244]. Thus, the particle size distribution of 5Ni@SiO_2-S1 showed a comparatively small average Ni nanoparticle size of ~2.9 nm, being potentially able to prevent carbon formation during DRM [96].

Figure 5.6 presents the N_2 physisorption isotherms and relevant pore structures of the 5Ni/S-1, 5Ni@hol S-1, 5Ni@EDA-S1 and 5Ni@SiO_2-S1 catalysts, showing that all the samples possess high surface area (>400 $m^2\ g^{-1}$) and large pore volume (>0.28 $cm^3\ g^{-1}$) (in Table 5.1). The isotherms of all the samples presented a significant increase at relative pressure (p/p_0) of <0.02 due to the micropore filling by N_2 molecules, confirming the presence of microporous structure in the catalysts regardless of their structures. The corresponding average micropore size was calculated to be 0.56±0.1 nm. It is worth noting that a type-IV N_2 adsorption-desorption isotherm with the H_4 type hysteresis loop was measured for 5Ni@hol S-1, 5Ni@EDA-S1 and 5Ni@SiO_2-S1, respectively, suggesting the presence of mesoporous structures. The corresponding average mesopore size of 1.6–2.0 nm was calculated by the BJH method. Additionally, the hysteresis loops with an abrupt step around $p/p_0 = 0.45$ in the 5Ni@hol S-1 catalyst becomes more pronounced, evidencing the existence of large hollow structure inside S-

1 crystals and demonstrating that the large internal voids were connected to the external surface through channels of ~2 nm [241], which is consistent with the TEM results.

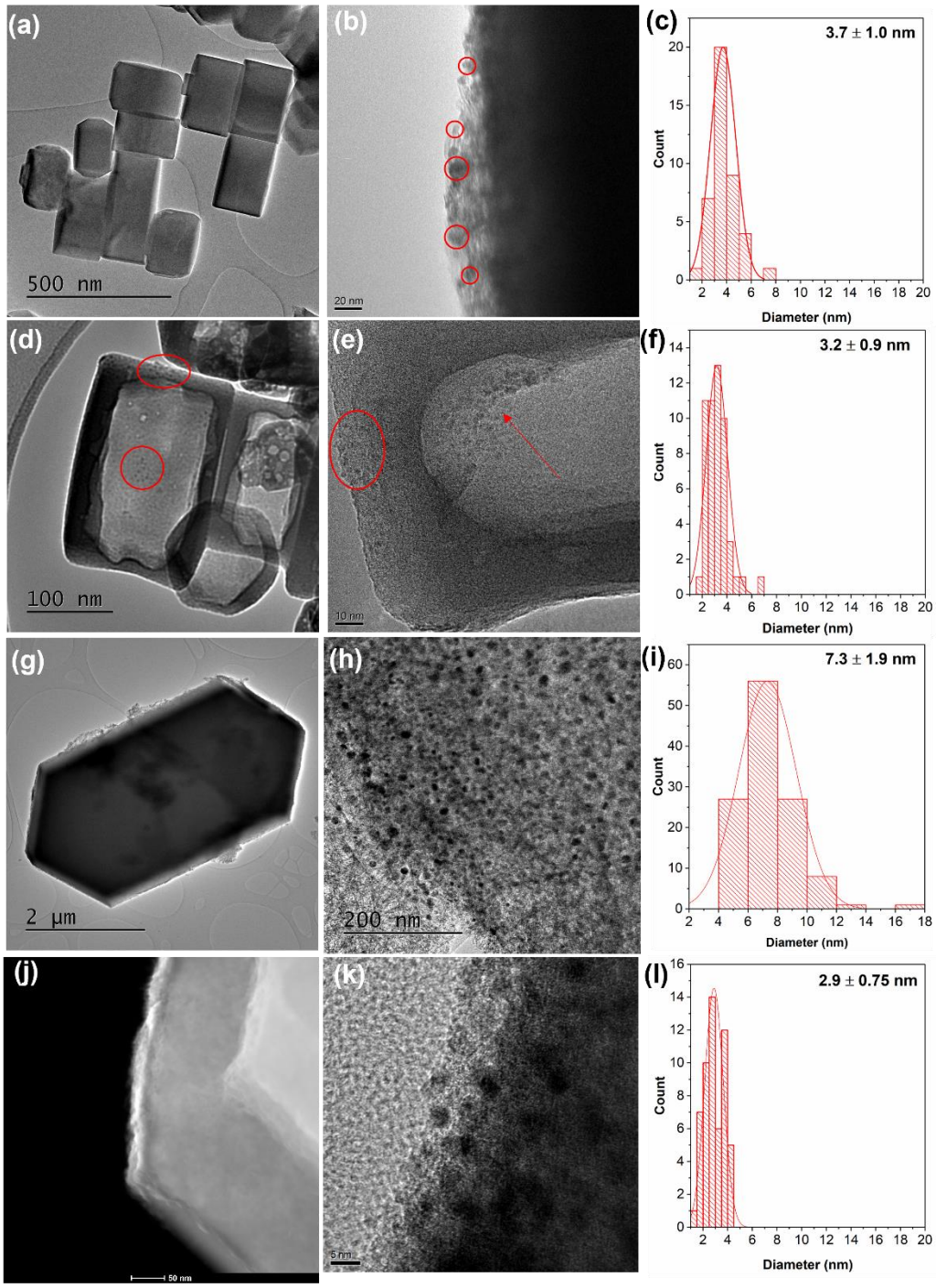

Figure 5.4 HRTEM images and corresponding Ni particle size distribution of (a–c) 5Ni/S-1, (d–f) 5Ni@hol S-1, (g–i) 5Ni@EDA-S1 and (j–l) 5Ni@SiO_2-S1 (after calcination).

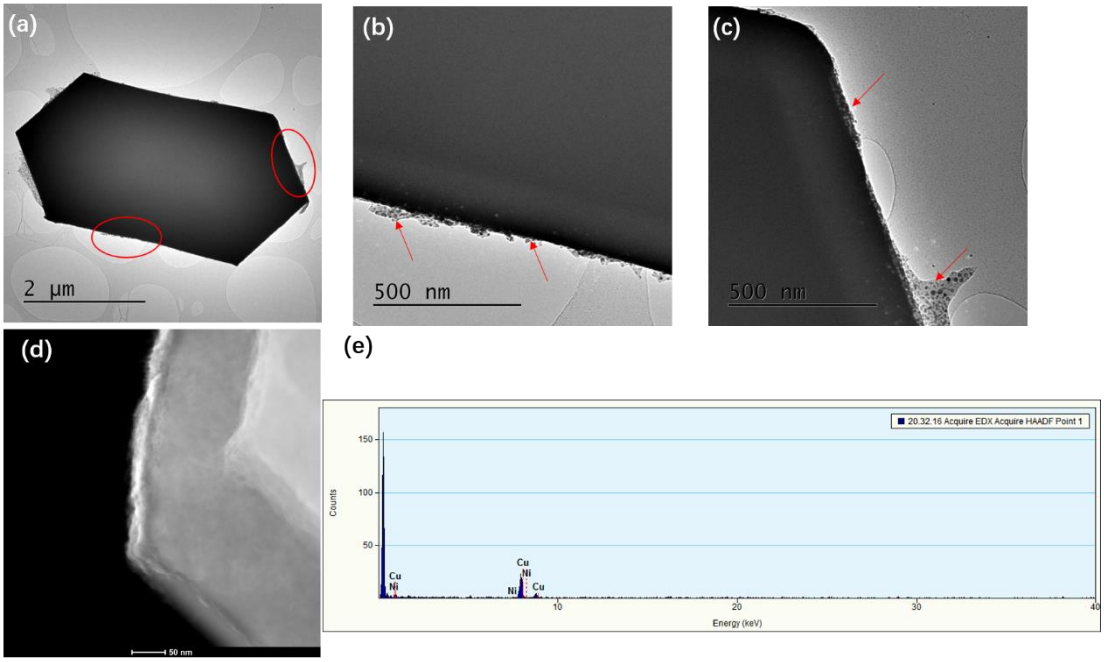

Figure 5.5 (a-c) TEM images of 5Ni@EDA-S1 and (d-e) STEM and EDX of 5Ni@SiO_2-S1 after calcination.

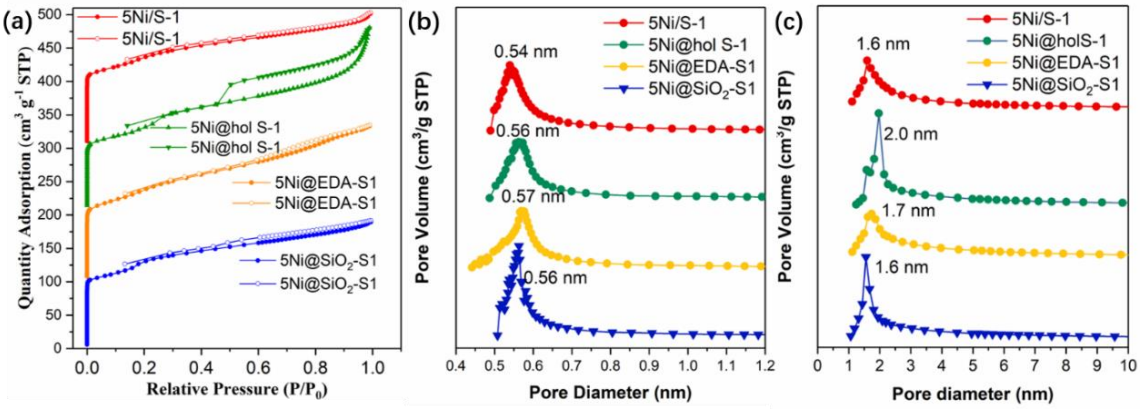

Figure 5.6 (a) N_2 adsorption-desorption isotherms of the calcinated catalysts (solid symbols represent adsorption isotherms and hollow symbols represent desorption isotherms); (b-c) micro/meso- pore size distribution of the catalysts.

Table 5.1 Textual properties of the calcined 5Ni/S-1, 5Ni@hol S-1, 5Ni@EDA-S1 and 5Ni@SiO_2-S1 catalysts.

Sample	Actual Ni content (%)[a]	S_{BET} (m^2 g^{-1})[b]	V_{total} (cm^3 g^{-1})[c]	V_{micro} (cm^3 g^{-1})[d]	V_{meso} (cm^3 g^{-1})[d]
5Ni/S-1	4.25	406	0.290	0.043	0.247
5Ni@hol S-1	6.28	417	0.413	0.034	0.379
5Ni@EDA-S1	4.09	428	0.350	0.039	0.311
5Ni@SiO_2-S1	4.30	401	0.284	0.024	0.26

[a]determined by ICP-OES. [b]determined by the BET method. [c]single point adsorption total pore volume at p/p_0 = 0.99. [d]determined by the BJH method.

The metal-support interaction is an important factor determining the catalytic performance, and thus, H_2-TPR analysis was performed to investigate the interactions between Ni and S-1 support, as shown in Figure 5.7. Only one reduction peak centered at 431 °C was observed in the 5Ni/S-1 catalyst and was assigned to the reduction of NiO on the external surface of zeolite, indicating that the traditional impregnation method was not able to introduce Ni NPs into the zeolite framework. In comparison, another major reduction peak at 461 °C for the 5Ni@hol S-1 catalyst can be ascribed to the reduction of encapsulated NiO in the hollow S-1, suggesting that the encapsulation *via* TPAOH treatment could strengthen the interaction between nickel and support as compared with the impregnated catalyst of 5Ni/S-1 [245]. Regarding the 5Ni@EDA-S1 and 5Ni@SiO_2-S1 catalysts, the peak at 350 °C was attributed to the NiO species weakly interacted with the support, whilst the reduction peak at high temperatures can be related to the NiO particles embedded into the S-1 zeolite with strong metal-support interactions caused by the confinement effect [231]. Specifically, the high temperature reduction peak at 732 °C in the 5Ni@EDA-S1 catalyst can be assigned to nickel phyllosilicate [246], whilst the broad reduction peaks from 426 to 615 °C in 5Ni@SiO_2-S1 are associated with the reduction of the encapsulated NiO species with relatively smaller particle size [231], which is consistent with the metal particle size by TEM analysis. The above results suggest the relatively strong metal-support interaction in 5Ni@EDA-S1 and 5Ni@SiO_2-S1, which can potentially improve

the anti-aggregation ability of Ni species during catalysis, benefiting DRM [247].

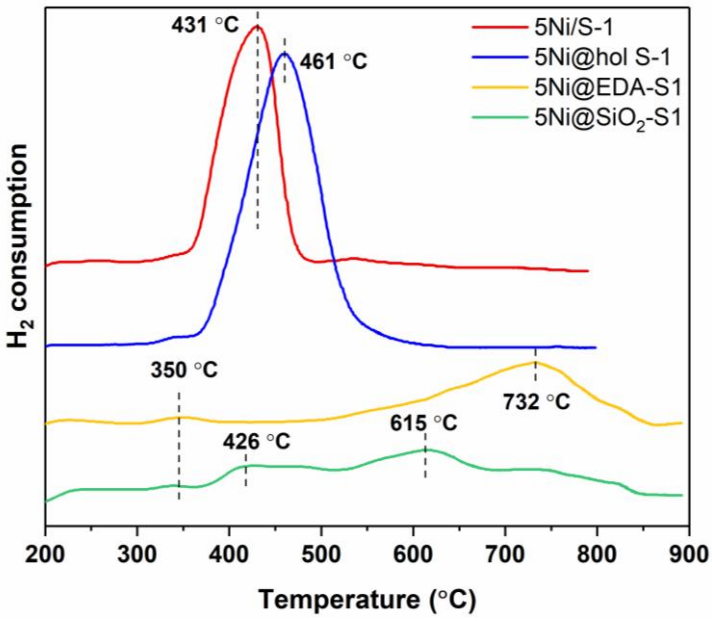

Figure 5.7 H_2-TPR profiles of the calcinated catalyst.

XPS analysis was performed to evaluate the chemical state of Ni species in the catalysts under investigation, and the results are shown in Figure 5.8. The high-resolution XPS spectra of Ni2p can be deconvoluted into four peaks, that is, (i) the peaks at 855.6 and 873.4 eV which are attributed to $Ni2p_{3/2}$ and $Ni2p_{1/2}$ of Ni^{2+} in NiO, and (ii) the peaks at 861.6 and 873.4 eV which are associated with the satellite peaks of Ni^{2+}. It was found that Ni2p spectra shifted to higher binding energy in the following order: 5Ni/S-1 < 5Ni@hol S-1 < 5Ni@EDA-S1 < 5Ni@SiO_2-S1. Such findings indicate that Ni species donate more electrons to the S-1 support in the encapsulated structures, which can be attributed to the relatively strong interactions between encapsulated Ni NPs and S-1 framework [246, 248]. Additionally, for the 5Ni@EDA-S1 catalyst, an additional peak at 858.7 eV, which can be assigned to nickel phyllosilicate [249], was observed, being in line with the H_2-TPR results.

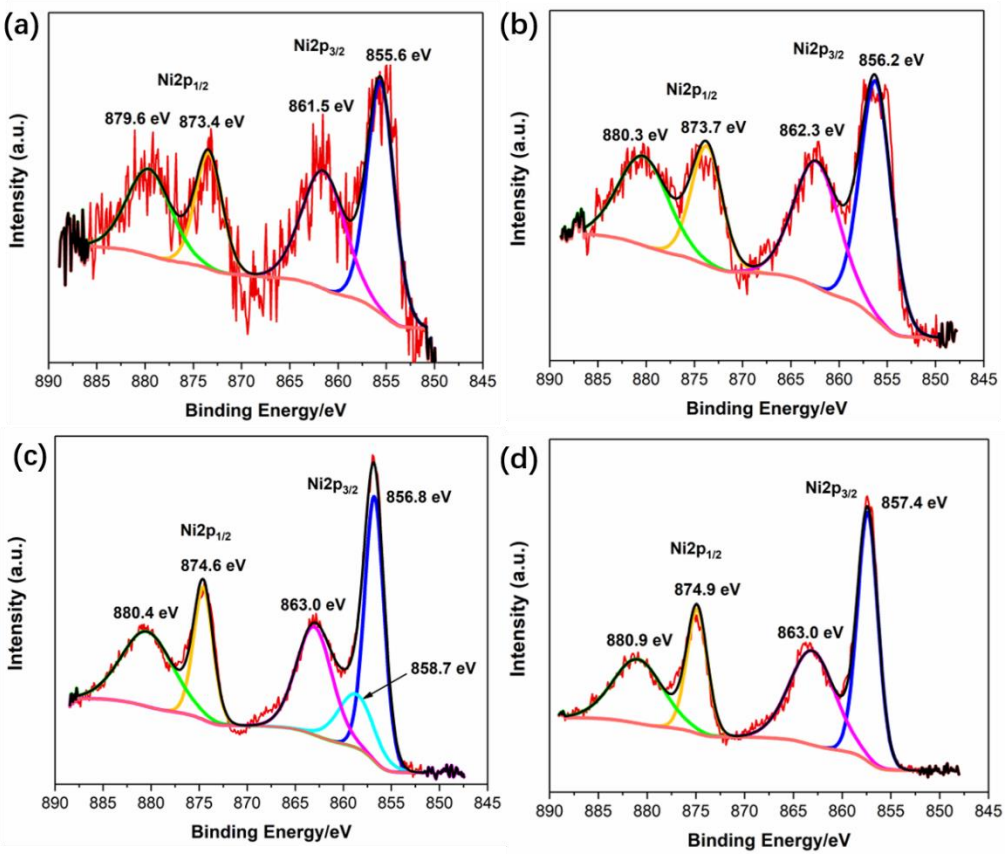

Figure 5.8 Ni_{2p} photoelectron spectra of different catalysts after calcination: (a) 5Ni/S-1, (b) 5Ni@hol S-1, (c) 5Ni@EDA-S1 and (d) 5Ni@SiO_2-S1.

5.3.2 Catalytic performance of the catalysts in DRM.

Catalytic DRM over the catalysts under investigation was first evaluated in the temperature range from 500 to 750 °C to compare their performance regarding the CO_2/CH_4 conversions and H_2/CO molar ratio. As shown in Figure 5.9, for all the catalysts under study, CO_2 and CH_4 reaction rates increased progressively as a function of reaction temperature, showing that the benefit of high temperatures to catalytic DRM over Ni-based catalysts (Figure 5.9a and b). Specifically, the impregnated 5Ni/S-1 catalyst showed the highest CO_2/CH_4 conversion rates due to the easy accessibility of Ni active sites on its external surface, whilst the 5Ni@hol S-1 catalyst presented the lowest activity which might be caused by the diffusion and transport resistance of the reactants to Ni NPs in the cavity through the channels of the S-1 shell. The 5Ni@SiO_2-

S1 catalyst showed slightly better performance than 5Ni@EDA-S1 over the temperature range investigated. Specifically, the CO_2/CH_4 conversions over 5Ni@SiO_2-S1 increased from ~29.7% and ~22.0% at 550 °C to ~83.7% and ~82.2% at 750 °C, respectively (Figure 5.9d). Regarding the H_2/CO molar ratio, all catalysts showed very low initial values, *i.e.*, about 0.2 at 550 °C, suggesting that the H_2 production was significantly lower than the CO production. This could be attributed to the higher conversion of CO_2 (~ 29.7%) than that of CH_4 (~ 22.0%) at low temperature of 550 °C (*e.g.,* in 5Ni@SiO_2-S1, Figure 5.9d), which is caused by the relatively significant occurrence of reverse water-gas shift reaction with relatively low activation barrier (RWGS, $CO_2+H_2 \rightarrow CO+H_2O$, ΔH°_{298K} = + 46.1 kJ mol^{-1}) compared to DRM [250]. The H_2/CO ratio of all catalysts increased rapidly by an increase of the temperature which is due to the increased H_2 production *via* DRM and/or the encouraged methane cracking reaction at high temperatures (*i.e.,* $CH_4 \rightarrow C+2H_2$, ΔH°_{298K} = + 74.9 kJ mol^{-1}). Theoretically, the H_2/CO molar ratio is expected to be unity, whereas in this work, the highest value obtained by the catalysts was around 0.9 at 700 °C (for the 5Ni@SiO_2-S1 catalyst), suggesting the possible occurrence of RWGS [251].

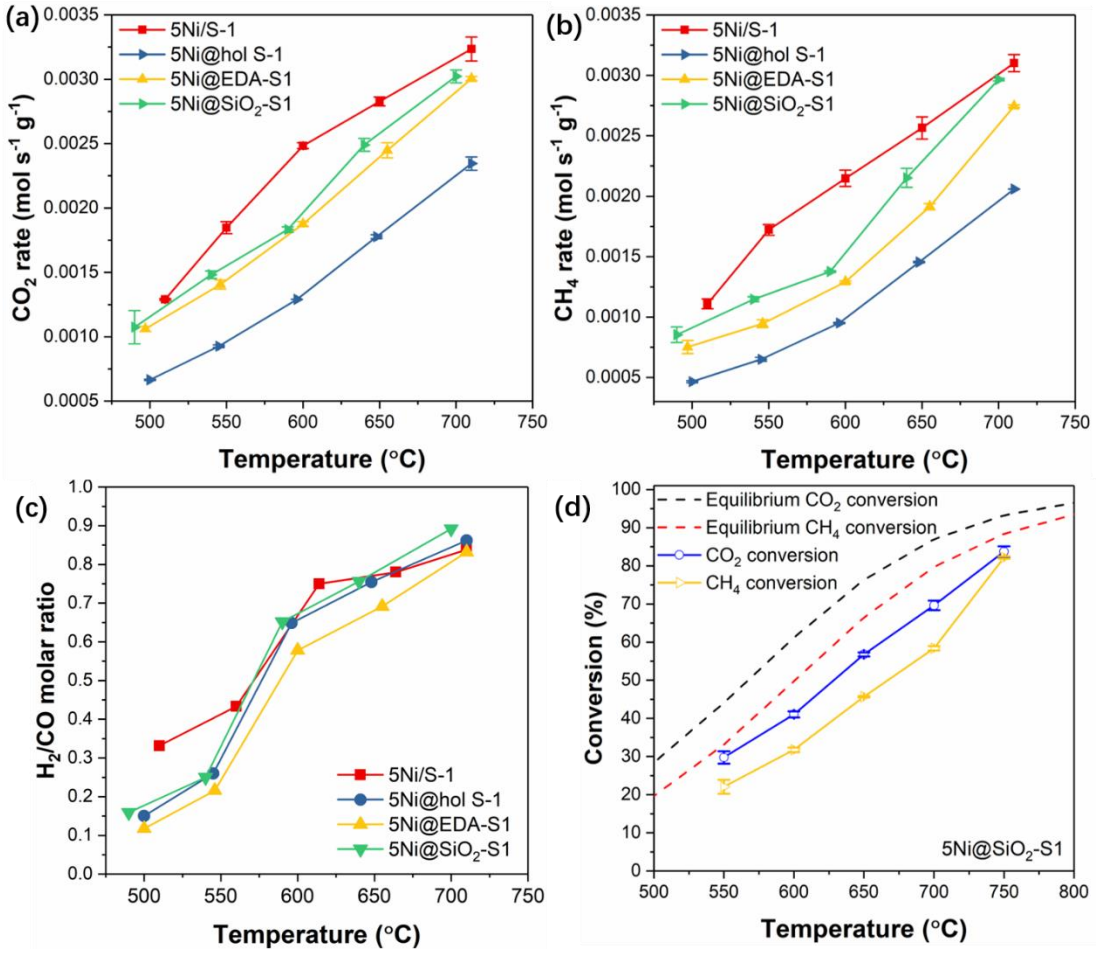

Figure 5.9 (a) CO_2 conversion rate, (b) CH_4 conversion rate, (c) H_2/CO molar ratio as a function of temperature over different catalysts and (d) Equilibrium CO_2/CH_4 conversions, CO_2 and CH_4 conversions as a function of temperature over the 5Ni@SiO_2-S1 catalyst. (reaction conditions: catalyst = 60 mg, total flowrate rate = 50 mL min^{-1}, CO_2/CH_4/Ar = 1:1:2).

Longevity tests were performed to understand the effect of different catalyst structures on coke deposition and associated catalyst deactivation. The tests were performed over the four catalysts under study at 700 °C, and the results are shown in Figure 5.10. The impregnated 5Ni/S-1 catalyst suffered from a significant deactivation after star-up, *i.e.*, CO_2/CH_4 conversions dropped by 28% and 39%, respectively, and the molar ratio of H_2/CO decreased from 0.9 to 0.78 over 8 h on stream. Similarly, the 5Ni@hol S-1 catalyst also showed a decreasing trend for DRM though the encapsulated Ni NPs within the hollow S-1 support were created by the TPAOH treatment, which

theoretically could promote the activity of catalysts by preventing coking and metal sintering. More importantly, the DRM process over the two catalysts halted after 8 h on stream due to physical blocking of the packed bed (with the measured back pressure of >2.0 bar), which was caused by the significant coke formation on the catalyst surface. Comparatively, the 5Ni@hol S-1 catalyst showed a relatively improved stability (*i.e.*, relevant deactivation by 23% and 13% for CO_2/CH_4 conversions over 8 h on stream, respectively). Additionally, TGA profile in Figure 5.10d showed that the spent 5Ni/S-1 catalyst (after 8 h DRM on stream at 700 °C) presented a significant weight loss of ~27.4% between 500 and 750 °C, while the used 5Ni@hol S-1 catalyst showed a lower weight loss of ~9.2%, which confirmed that the encapsulation approach could suppress the carbon deposition during DRM process to some extents. For impregnated 5Ni/S-1 catalyst, TEM images showed that the Ni NPs aggregated into large particles (with average particle size of ~56.7 nm) after reduction treatment, suggesting the metal sintering (Figure 5.12a). And the corresponding SEM (Figure 5.11a) and TEM images of spent 5Ni/S-1 catalyst (Figure 5.12b) confirmed that a large amount of carbon was produced and accumulated on the surface of the spent 5Ni/S-1 catalysts, leading to the deactivation of the catalyst. Comparatively, even though the hollow zeolite shell in 5Ni@hol S-1 catalyst was reported to be able to inhibit aggregation of Ni NPs and coking [235], the Ni NPs which were not encapsulated in the hollow S-1 crystal aggregated into the large particles (as indicated in Figure 5.12c) during the reduction treatment, which could lead to the formation of carbon intermediates and their continuous accumulation of coke on the external catalyst surface (Figure 5.11b and Figure 5.12d). This carbon deposition contributed to the reduced accessibility of Ni active sites to reactant gases, leading to the reduced CO_2/CH_4 conversions for DRM. Therefore, coke deposition on 5Ni@hol S-1 was still inevitable in a long run due to the incomplete encapsulation of Ni NPs in its structure. However, the Ni NPs encapsulated within hollow S-1 zeolite remained active due to the confinement effect during the stability testing (as indicated in Figure 5.12d), leading to an improved coke-resistance compared with the 5Ni/S-1 catalyst. It is also worth mentioning that the over-spacious

interior cavity in 5Ni@hol S-1 could possibly reduce the confinement effect of the S-1 support on Ni NPs, causing the possible migration/aggregation of Ni NPs inside the cavity at high temperatures (as indicated in Figure 5.13), which may lead to the interparticle combination/growth and thus impair the anti-coking capacity of the catalyst [228, 252].

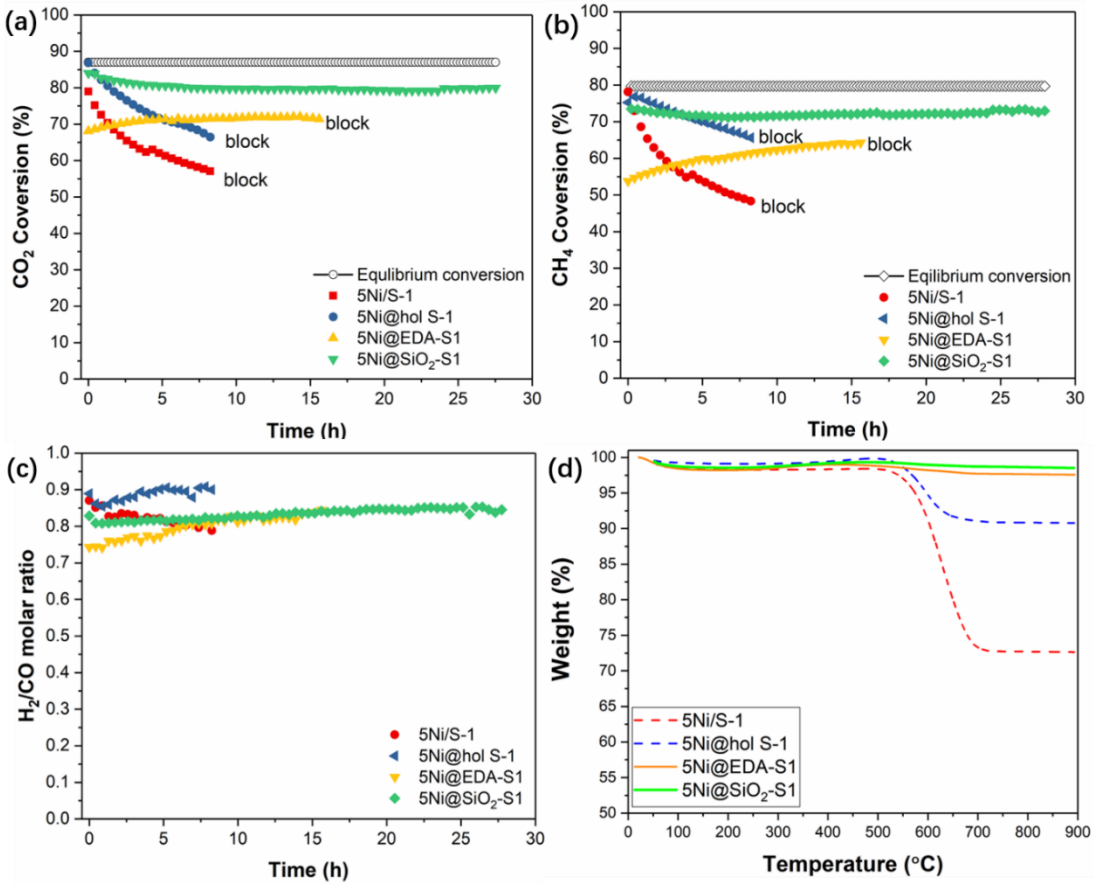

Figure 5.10 Catalytic stability performances of 5Ni/S-1, 5Ni@hol S-1, 5Ni@EDA-S1 and 5Ni@SiO_2-S1 for DRM at 700 °C as a function of ToS: (a) CO_2 conversion, (b) CH_4 conversion and (c) H_2/CO molar ratio; (d) TGA profiles of the spent catalysts after stability testing (reaction conditions: catalyst = 80 mg, T =700 °C, total flowrate rate = 50 mL min^{-1}, CO_2/CH_4/Ar = 1:1:2) (block: physical blocking of the packed bed with the measured back pressure of >2.0 bar).

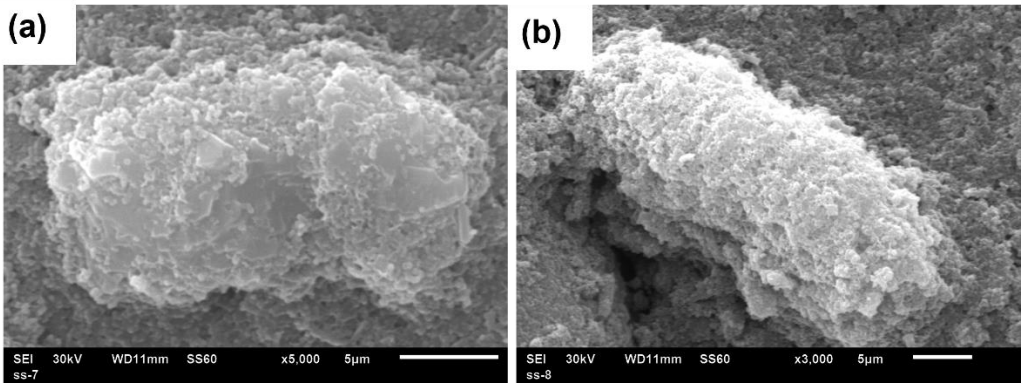

Figure 5.11 SEM image of the spent catalysts after stability testing at 700 °C, (a) 5Ni/S-1 after 8 h testing, (b) 5Ni@hol S-1 after 8 h testing.

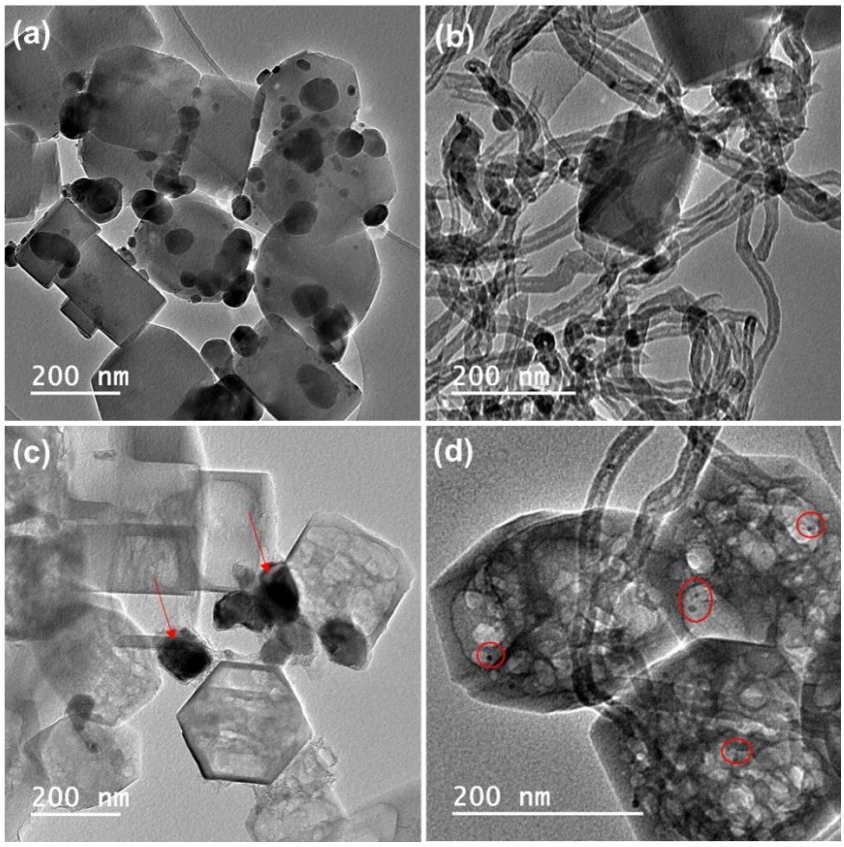

Figure 5.12 HRTEM images of the catalysts after reduction treatment and stability testing at 700 °C. (a) 5Ni/S-1 after reduction at 700 °C, (b) spent 5Ni/S-1 after 8 h testing, (c) 5Ni@hol S-1 after reduction at 700 °C and (d) spent 5Ni@hol S-1 after 8 h testing.

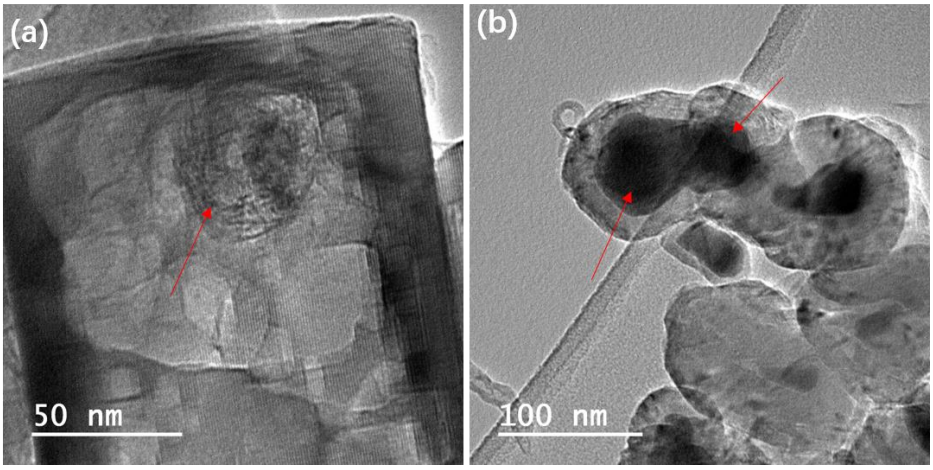

Figure 5.13 HRTEM images of 5Ni@hol S-1 after (a) reduction treatment at 700 °C and (b) 8h stability testing at 700 °C.

The 5Ni@EDA-S1 catalyst presented a relatively low initial activity, which increased gradually within the first 5 h on stream, that is, the CO_2/CH_4 conversions and H_2/CO molar ratio increased from 67%, 53% and 0.73 to 72%, 64% and 0.85, respectively. HRTEM results (Figure 5.5) showed that some Ni NPs exposed on the external surface in the 5Ni@EDA-S1 catalyst might be prone to aggregate into large particles at high reaction temperatures. However, previous study on the particle size effect in DRM over Ni/SiO_2 catalyst demonstrated that the activity of DRM decreased with an increase in Ni particle sizes [223]. Thus, the aggregation of Ni NPs on the external surface of 5Ni@EDA-S1 was not responsible for this increasing trend measured in the first 5 h. STEM images and elemental analysis of the reduced and spent 5Ni@EDA-S1catalyst (Figures 5.14 and 5.15) show that some Ni NPs, which were located inside of the S-1 support, migrated to the external surface of support at high temperatures, especially to the edge of zeolite, leading to more active sites exposed on the external surface and contributing to the initial increase in CO_2/CH_4 conversions. However, these Ni NPs might in turn sinter into large particles, which were prone to encourage the coke formation on the catalyst surface. This can be evidenced by (i) the physical blockage of the packed bed (based on 5Ni@EDA-S1) at 16 h during the stability testing due to the filamentous carbon formation (as indicated in Figure 5.14b), (ii) the corresponding

TGA profile which shows the 2.5% weight loss (suggesting the combustion of deposited coke during TGA) and (iii) the relatively uniform distribution of Ni species on the surface of the spent 5Ni@EDA-S1 (Figures 5.15d and 5.17c). However, in comparison with large cavity in the 5Ni@hol S-1, the surrounding interconnected framework of S-1 zeolite shell in 5Ni@EDA-S1 could provide sufficient isolation for the encapsulated Ni NPs (with strong metal-support interactions, as shown in Figure 5.7), which reduced the accumulation of carbon on the Ni surface [228, 252]. This contributed to the sustained CO_2/CH_4 conversions without deactivation throughout the 16 h longevity test, demonstrating the improved resistance of the 5Ni@EDA-S1 catalyst to deactivation compared to 5Ni@hol S-1.

Comparatively, the 5Ni@SiO_2-S1 catalyst showed the best stability in DRM among the catalysts under investigation, showing the sustained high activity (~80% and ~73% for CO_2/CH_4 conversions, respectively) over 28 h and the stable H_2/CO molar ratio of 0.83 with negligible carbon deposition (~0.5% based on the TGA analysis, as shown in Figure 5.10d). In comparison with the 5Ni@EDA-S1 catalyst, the corresponding STEM images and EDX mapping of the reduced 5Ni@SiO_2-S1 catalyst (indicated in Figure 5.14c and 5.16a-d) show insignificant mitigation of Ni NPs from inside of the zeolite, *i.e.*, the fully encapsulation structure can be remained after reduction. Thus, the spent 5Ni@SiO_2-S1 catalyst (Figure 5.14d) only showed insignificant carbon formation on the external surface of the spent 5Ni@SiO_2-S1 catalyst after 28 h testing. As shown in Figure 5.14d and 5.16e–h, even though it is still inevitable that Ni NPs migrated to the external surface of the support in a long run due to the high reaction temperature, the presence of Ni species on the external surface of the spent 5Ni@SiO_2-S1 catalyst was significantly lower than that of the spent 5Ni@EDA-S1(Figure 5.17). Therefore, the 5Ni@SiO_2-S1 catalyst prepared by seed-directed synthesis demonstrated the comparatively good activity, anti-sintering and anti-coking abilities in DRM. Based on the discussion above, the anti-coking mechanism of the 5Ni@SiO_2-S1 catalyst can be multiple, that is, (i) small Ni NPs (~2.9 nm) could inhibit coke deposition on their

surface, since the nucleation process of the filamentous carbon was suppressed over the small Ni particles of <7 nm [253], (ii) relatively stable encapsulated Ni NPs within the S-1 framework with strong metal-support interactions could impede the movement/aggregation of Ni NPs (due to the confinement incurred by the surrounding zeolite framework), and (iii) the interconnected porous zeolite framework could prohibit the spatial growth and accumulation of coking *via* rapidly gasification of carbon intermediates on the Ni surface, maintaining enough active sites for reaction and making it anti-coking in DRM [252]. Therefore, carbon deposition could be mitigated by the encapsulation approach (*i.e.*, partially/completely encapsulated metal NPs within the S-1 zeolite framework), however, the intrinsic natures of encapsulated Ni catalysts prepared by different methods such as metal particle size, degree of encapsulation, zeolite shell structure and metal-support interactions, significantly affect the catalytic performance regarding the metal sintering and carbon deposition in DRM.

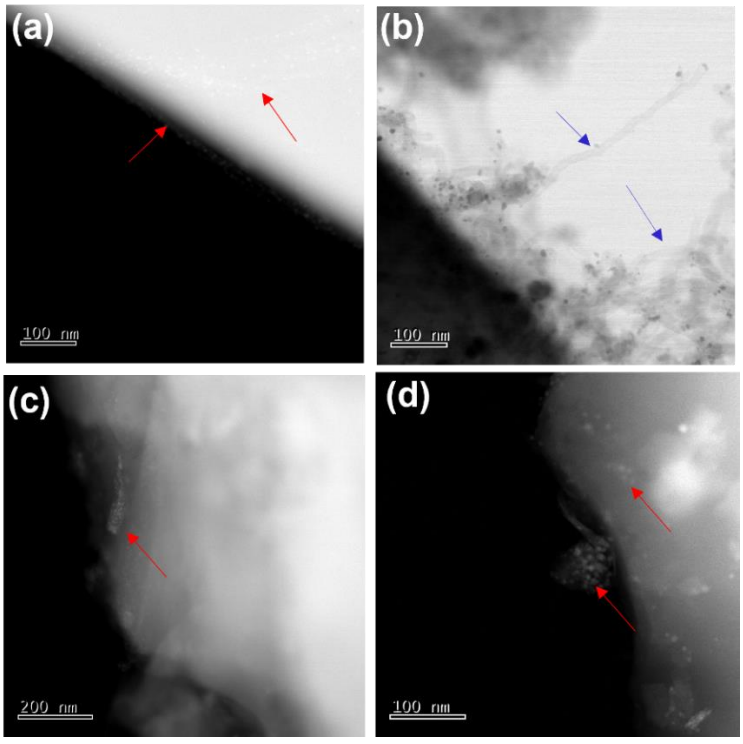

Figure 5.14 STEM/HRTEM images of the catalysts after reduction treatment and stability testing. (a) 5Ni@EDA-S1 after reduction at 700 °C, (b) spent 5Ni@EDA-S1 after 16 h testing at 700 °C, (c) 5Ni@SiO_2-S1 after reduction at 700 °C and (d) spent 5Ni@SiO_2-S1 after 28 h testing at 700 °C.

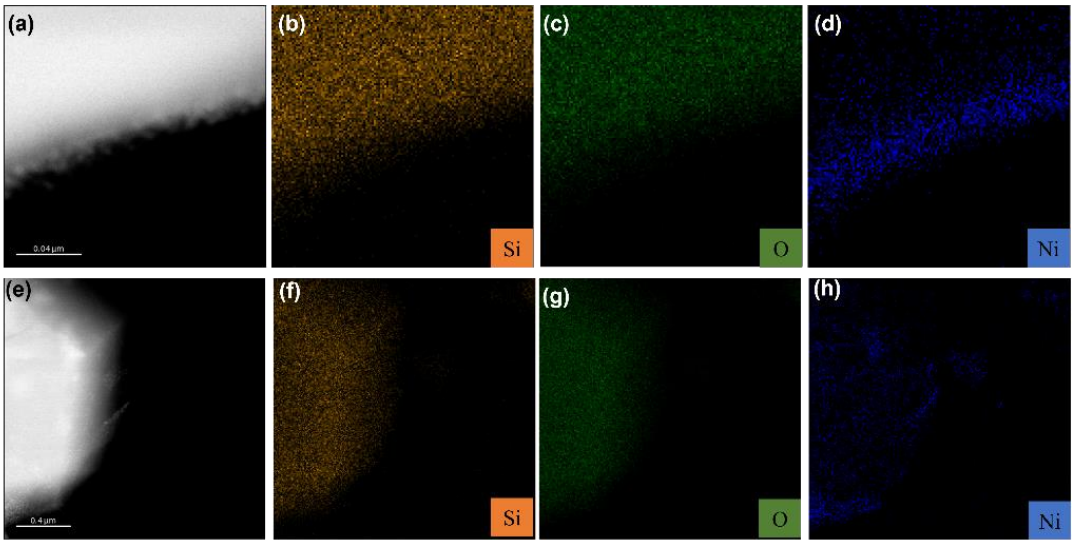

Figure 5.15 HADDF image and selected area for elemental mapping. (a-d) 5Ni@EDA-S1 after reduction at 700 °C; (e-f) spent 5Ni@EDA-S1 after 16 h testing at 700 °C.

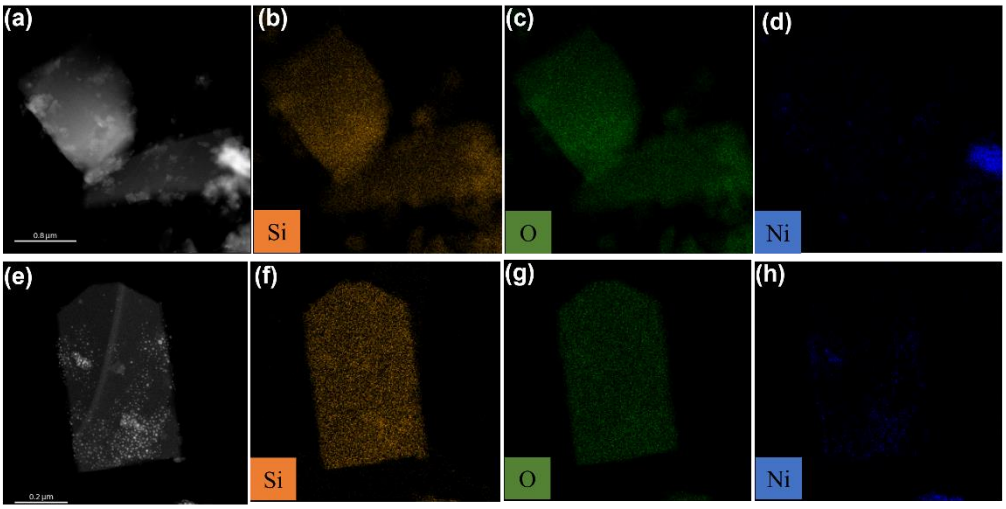

Figure 5.16 HADDF image and selected area for elemental mapping. (a-d) 5Ni@SiO_2-S1 after reduction at 700 °C; (e-f) spent 5Ni@SiO_2-S1 after 28h testing at 700 °C.

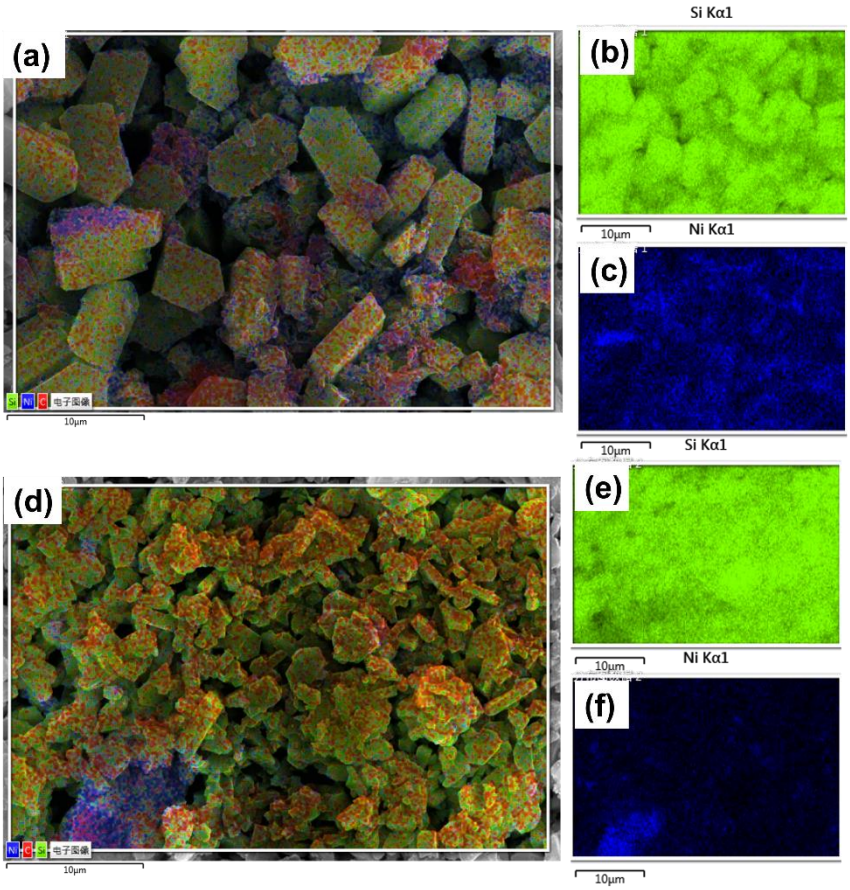

Figure 5.17 SEM image and EDX elemental analysis of (a-c) spent 5Ni@EDA-S1 after 16 h testing at 700 °C; (d-f) spent 5Ni@SiO_2-S1 after 28h testing at 700 °C.

Based on the activity tests above, the 5Ni@SiO_2-S1 catalyst presented the relatively stable CO_2/CH_4 conversions at 700 °C. Accordingly, it was selected for further investigation on the catalytic DRM performance at different total flowrates. As shown in Figure 5.18, when the total flowrate increased from 50 to 200 mL min^{-1}, CO_2 and CH_4 conversions and H_2/CO molar ratio in the control 5Ni/S-1 catalyst (prepared by impregnation) decreased from ~84%, ~80% and ~0.8 to ~59%, ~54% and ~0.6, respectively. Comparatively, CO_2 and CH_4 conversions and H_2/CO molar ratio of the 5Ni@SiO_2-S1 catalyst dropped significantly under the same conditions, *i.e.*, from ~69%, ~60% and ~0.75 to ~39%, ~28% and ~0.55, respectively. The findings suggest that the 5Ni@SiO_2-S1 catalyst experienced significant mass-transfer effect as compared with the 5Ni/S-1 counterpart, which can be attributed to the encapsulated Ni

NPs. Therefore, the trade-off between stability and mass-transfer resistance in the encapsulated catalysts needs to be considered carefully in the process of designing highly efficient catalysts for DRM.

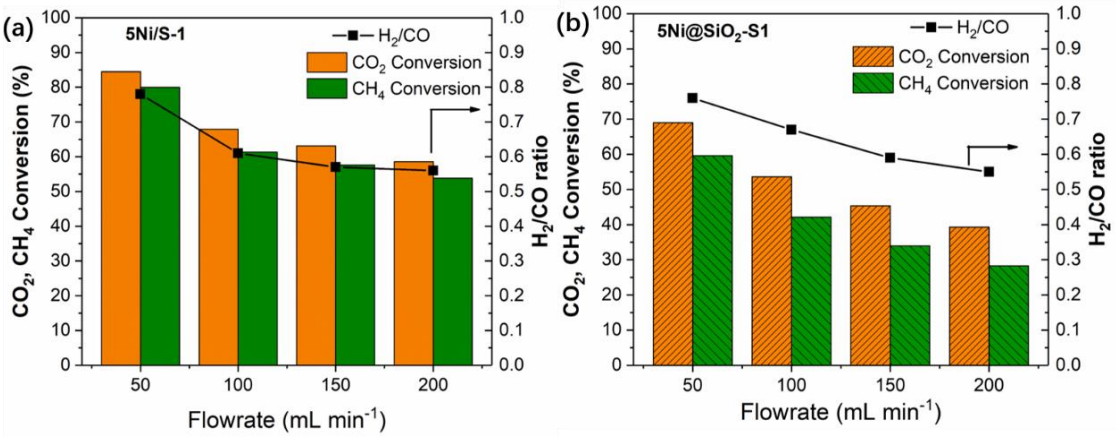

Figure 5.18 Catalytic DRM performance as a function of total flowrate over (a) 5Ni/S-1 and (b) 5Ni@SiO_2-S1. (reaction conditions: catalyst = 60 mg, T = 700 °C, total flowrate rate = 50–200 mL min^{-1}, $CO_2/CH_4/Ar$ = 1:1:2).

5.4 Conclusion

In catalytic dry reforming of CH_4 with CO_2, rapidly deactivation of Ni-based catalysts due to metal sintering and coking is a major challenge. In this study, a series of encapsulated Ni catalysts (by silicalite-1 zeolite) were prepared by different synthesis methods, and comprehensive characterisation revealed that their structural properties varied significantly, such as metal particle size, degree of encapsulation, and metal-support interactions, which affected their catalytic performance in DRM. It was demonstrated that, in general, the encapsulation strategy was effective to improve the stability of the resulting catalysts, however, the intrinsic nature of the catalysts developed by different methods played a key role in suppressing coking and Ni metal sintering during DRM. The developed Ni@SiO_2-S1 catalyst by seed-directed synthesis method showed the complete encapsulation of Ni in its structure and the comparatively best catalytic performance with stable CO_2 and CH_4 conversions of ~80% and ~73%,

respectively, as well as relatively low carbon deposition (about 0.5 wt.% by TGA), during 28 h on stream, outperforming other catalysts under investigation. Conversely, the post treatment and direct hydrothermal methods promoted the incomplete encapsulation of Ni (*i.e.,* the 5Ni@hol S-1 and 5Ni@EDA-S1 catalysts), being prone to deactivate due to the presence of Ni phases on their external surface. By contrast, the impregnated Ni catalyst (with Ni particles only on the external surface of S-1 support) suffered from rapid deactivation and severer carbon deposition after the 8 h test.

This work aimed to understand the synthesis-structure-performance relationships of Ni-S-1 catalysts. Its findings show clearly that the full encapsulated Ni in the support with small Ni particle sizes and strong metal-support interactions in the Ni@SiO_2-S1 catalyst could protect Ni aggregation and inhibit coke formation during DRM, providing design rationales for developing stable metal-based catalyst with coking- and sintering-resistance for high-temperature heterogeneous catalysis such as DRM.

Chapter 6 Summary and recommendations for future work

6.1 Summary

Catalytic conversion of CO_2 to valuable chemicals and fuels offers a practical and viable solution to mitigate issues associated with climate change and energy supply deficiency and contributes to the development of sustainable carbon cycling processes. Especially, catalytic CO_2 hydrogenation and DRM have been regarded as the promising routes for potential practical CO_2 utilisation. CO_2 molecular is thermodynamically and chemically stable. Thus, high temperatures and/or pressures are required to activate CO_2 in the conventional thermocatalytic CO_2 conversions which are associated with high energy input and cause catalyst deactivation. Specifically, under the thermal conditions, catalysts stability against metal sintering, coke deposition and poisoning needs to be considered and addressed carefully during the development of highly active catalysts for advancing catalytic CO_2 conversion technologies towards practical applications. In addition to the thermal catalysis, NTP-catalysis systems have been proposed and demonstrated as a promising alternative to enable the easy activation of CO_2 and promote thermodynamically and/or kinetically limited catalytic reactions at comparatively mild conditions, such as ambient conditions, benefiting energy-efficient conversion of CO_2. Catalysts play an important role in both the thermal and the hybrid NTP catalytic systems regarding efficiency and selectivity, especially NTP catalysis, in which the intrinsic gas phase reactions are non-selective. Therefore, dedicated investigations on the establishment of the correlation between catalysts' structure, composition and activity in the hybrid NTP-catalysis system is necessary for the rational design cost-effective and efficient catalysts bespoke for NTP-catalysis. Additionally, NTP-catalysis is highly complex and require further understanding to advance the technology towards practical applications. In this PhD project, catalytic CO_2 conversions, *i.e.,* CO_2 hydrogenation and DRM, were studied with special focus

on the mechanistic understanding of the catalysis. The work was carried out in order to (i) design highly efficient catalysts for CO_2 conversion and demonstrate the application of NTP-catalysis system for CO_2 hydrogenation, (ii) comparatively study of the mechanism of CO_2 hydrogenation under thermal and plasma conditions to provide some guidance on the designing suitable catalysts for NTP-catalysis, (iii) further understand the catalyst deactivation in CO_2 hydrogenation, especially due to CO poisoning, under thermal and plasma condition, progressing the development of mature catalytic systems towards the practical applications for CO_2 conversion, and (iv) develop the relationship of synthesis-structure-performance of encapsulated Ni catalysts (with a spatial confined Ni nanoparticles within S-1 zeolite framework) to provide design rationales for further development of stable catalysts with coking- and sintering-resistance for DRM.

In Chapter 3, NTP-activated CO_2 hydrogenation over Ru catalysts supported on the MgAl LDHs was performed. The synergy of NTP-catalysts enabled significantly higher CO_2 conversions (~85%) and CH_4 yield (~84%) at relatively low temperatures, which demonstrated NTP-catalysis is efficient for catalytic CO_2 conversion. Regarding the catalyst, the reduction temperature during the preparation process can affect the chemical state of the metal and metal-support interaction significantly, and thus altering the activity of the catalysts in NTP-driven catalytic CO_2 hydrogenation. Additionally, comparative *in situ* DRIFTS-MS study on the mechanism of CO_2 hydrogenation under thermal and NTP conditions confirmed the alternative reaction pathways in NTP-catalysis and identified more active species both in gas-phase and in catalysts-surface including CO*, O*, H*, formates, carbonate, formyl, carbonyl and water compared with the conventional thermally activated counterpart, explaining the improved performance of the NTP-catalysis system as compared with thermal catalysis.

In addition to the activity, the stability and longevity of the catalysts are important issues for practical catalysis under both thermal and NTP conditions. In Chapter 4, the intrinsic nature of catalysts (*e.g.,* surface area and metal dispersion) was demonstrated to play a

key role in the catalytic performance of CO_2 hydrogenation. The Ru/SiO_2 catalyst was selected for further investigation of catalyst deactivation due to its high activity and stability in CO_2 hydrogenation among the candidate catalysts. Specifically, comparative study of CO poisoning over the Ru/SiO_2 catalyst under the thermal and NTP conditions showed the advantage of the hybrid NTP-catalysis system over the thermal counterpart to prevent metal sintering and mitigate CO poisoning of the catalyst. Compared to the catalyst deactivation in thermal catalysis due to strong CO adsorption and metal sintering, *in situ* DRIFTS–MS analysis revealed that the collisions of reactive plasma-derived species in NTP-catalysis could remove the strongly adsorbed species to recover the active sites for CO_2 adsorption. Therefore, NTP-catalysis was capable of alleviating CO poisoning in CO_2 hydrogenation and regenerating the catalyst *in situ* during the catalysis.

In addition to CO_2 hydrogenation, DRM has attracted great attention since it co-utilises CO_2 and CH_4 for direct production of syngas (which is the building block for producing valuable oxygenated chemicals and hydrocarbons *via* Fischer-Tropsch reactions). For the Ni based reforming catalysts, the major challenge for practical application of DRM is the rapid deactivation of Ni catalysts due to metal sintering and coking decomposition. To address the deactivation issue of Ni based catalysts, encapsulation strategy has been demonstrated to be effective to improve the stability of catalysts, however, the nature of catalysts developed by different methods is crucial in preventing metal sintering and coking formation. In Chapter 5, a series of encapsulated Ni catalysts (by silicalite-1 zeolite) were prepared by different synthesis methods (including post treatment method, direct hydrothermal and seed-directed synthesis), and their structural properties varied significantly, such as metal particle size, degree of encapsulation, and metal-support interactions, which affected their catalytic performance in DRM. The developed $Ni@SiO_2$-S1 catalyst by the seed-directed synthesis method showed the complete encapsulation of Ni in its structure and the comparatively best catalytic performance with stable CO_2 and CH_4 conversions of ~80% and ~73%, respectively, as well as

relatively low carbon deposition (about 0.5 wt.% by TGA), during 28 h on stream. Comparatively, the post treatment and direct hydrothermal methods promoted the incomplete encapsulation of Ni (*i.e.,* the 5Ni@hol S-1 and 5Ni@EDA-S1 catalysts), being prone to deactivate due to the presence of Ni phases on their external surface. By contrast, the impregnated Ni catalyst (with Ni particles only on the external surface of S-1 support) suffered from rapid deactivation and severer carbon deposition after the 8 h test. This work established the synthesis-structure-performance relationships of Ni-S-1 catalysts, showing that the full encapsulated Ni in the support with small Ni particle sizes and strong metal-support interactions could protect Ni aggregation and inhibit coke formation during DRM.

6.2 Future work

6.2.1 NTP-catalysis for CO_2 hydrogenation to methanol

In Chapter 3, NTP-catalysis system shows the great potential in activating CO_2 hydrogenation to CO and CH_4 under comparatively mild conditions. And Ni-based catalysts were demonstrated to be effective to enable the good efficiency and selectivity in the hybrid NTP-catalysis system. As compared with the production of CO and CH_4, catalytic CO_2 hydrogenation to hydrocarbons and oxygenates, especially methanol (suitable for storage and transportation), in a one-step process circumvent the additional Fisher-Tropsch and methanol synthesis process from the practical point of view of industrial application for CO_2 utilisation. However, CO_2 hydrogenation to hydrocarbons and methanol is usually conducted at elevated temperatures (200–350 °C) and pressures (50–250 Bar) under thermal conditions, thus the integration of plasma with catalysts to enable these conversions efficiently under mild conditions make it more economically attractive and competitive for CO_2 valorisation. Currently, several studies have been reported to improve the yield of methanol in the NTP-catalytic CO_2 conversion by developing innovative reactor configuration (*e.g.,* water-cooled DBD

reactor) [62] and/or careful design of the catalysts [254]. However, the main challenge for NTP-catalytic CO_2 hydrogenation towards liquid fuels is the low selectivity and yield of target products (*e.g.,* <55% selectivity and <12% yield) compared to thermal catalysis (e.g., >70% selectivity and >25% yield) [1, 255]. In the future work, the design of highly selective catalysts, as well as the development of novel reactors for NTP-catalytic CO_2 hydrogenation to methanol and other liquid oxygenates, needs to be conducted to progress CO_2 conversion to methanol technologies. Accordingly, the following research directions are proposed for the purpose:

(i) According to the previous work on the thermal-catalytic CO_2 hydrogenation towards methanol [1], metals such as Cu, Pd and Pt are good candidates for the thermal conversion. Therefore, bespoke catalysts based on these metals can be developed for CO_2 hydrogenation to liquid fuels under plasma conditions.

(ii) Based on the comprehensive characterisation of the catalysts using XRD, XPS, SEM, TEM and TPR, the catalytic composition/structure-activity relationship in NTP-catalysis needs to be established to enable the rational design and optimization of the bespoke catalysts for NTP-catalysis to improve the methanol selectivity and yield.

(iii) The active sites and possible reaction pathways in the production of methanol need to be revealed using the advanced *in situ* techniques (*e.g.,* OES and DRIFTS-MS) under plasma conditions to uncover key intermediates and identify key factors determining the selectivity to methanol in NTP-catalytic CO_2 hydrogenation.

6.2.2 Anti-poisoning study of plasma-catalytic CO_2 conversion

In Chapter 4, NTP-catalysis shows the capability of promoting CO_2 hydrogenation with features such as energy-efficiency, anti-sintering and anti-poisoning. In the thermal catalysis, the catalyst suffered from a significant deactivation due to CO poisoning, whilst, in the NTP-catalysis, the catalyst showed the comparatively good stability and regenerability. Even though the corresponding deactivation mechanisms of Ru catalysts

was revealed, the effect of plasma on the adsorption capacity of CO and CO_2 molecular on the catalyst surface (*e.g.*, adsorption energy barrier and adsorption active sites) is not clear yet, thus the future effort needs to focus on the CO and CO_2 adsorption behaviour by developing the *in situ* techniques (*e.g.*, online GC-MS, in situ DRIFTS-MS) or carrying out relevant modelling investigations (*e.g.*, density functional theory, DFT, calculation). For example, online plasma-MS has been reported to be employed to observe the SO_2 adsorption/desorption behaviour on the γ-Al_2O_3 with the control of plasma discharge (*i.e.*, on/off), thus, it is possible to extend it for the investigation of CO_2/CO adsorption on the catalyst surface [256]. The previous modelling work based on the DFT calculation from Bogaerts' group has revealed the improved CO_2 adsorption and activation over the supported Cu catalyst enabled by plasma discharge, and the binding energy of CO_2 molecular on Cu surfaces increases significantly with an increased electric field strength [257, 258]. These investigations make DFT calculation a promising method to provide microscopic information on the adsorption CO_2 and CO molecues on the catalyst surface under plasma conditions, which can hardly be achieved with the current experimental techniques.

In addition to CO, sulphur species, such as H_2S and SO_2, is also catalyst poison for the supported metal catalysts due to the irreversible adsorption of sulphur compounds, and the strategy to mitigate the sulphur poisoning under thermal conditions has been developed and explored [259]. Till now, the systematic studies on sulphur poisoning in NTP-catalytic CO_2 conversions are not reported yet, which needs to be investigated. To implement the anti-poisoning study of NTP-catalysis, the future work should consider the following aspects:

(i) The development of relevant simulation methods (*e.g.*, DFT calculation) and the use of in situ plasma-MS and DRIFTS-MS system to elucidate the effect of plasma on the behaviors and interactions of sulphur species, CO_2, CO and the surface of the supported metal catalysts under various plasma conditions (such as discharge gas compositions, voltage, etc.).

(ii) The extended study of Chapter 4 by changing the gas feed with sulphur compounds to explore the slphur poisoning under both thermal and plasma conditions comparatively. The *in situ* techniques (*e.g.,* DRIFTS-MS) and *ex situ* techniques (*e.g.,* XPS, TEM and TPD) can be used to reveal the poisoning mechanism and the change of catalyst structure during the deactivation process.

6.2.3 Anti-coking/sintering catalysts design for DRM

Nickel (Ni)-based catalysts are commonly used for reforming reactions due to their good catalytic activity and relatively low cost. In DRM, rational design of the catalysts to alleviate the deactivation of Ni reforming catalysts caused by coke formation and metal sintering remains a major concern for its industrial application. The fully encapsulated Ni NPs within zeolite in chapter 5 were demonstrated to be effective to improve the sintering and coking resistance of the catalyst. However, the intrinsic natures of encapsulated Ni catalysts prepared by different methods such as metal particle size, degree of encapsulation and zeolite shell structure significantly affect the catalytic performance regarding the metal sintering and carbon deposition in DRM. The catalytic performance shows that the coke formation is still inevitable in a long run of DRM. And encapsulated Ni (*e.g.,* 5Ni@SiO_2-S1) may suffer mass-transfer resistance (due to the encapsulation of Ni in the support framework) compared to the conventional impregnated 5Ni/S-1 catalyst. In the future work, the trade-off between stability and mass-transfer resistance in the encapsulated catalysts should be considered in the process of designing bespoke catalysts for DRM. The following experimental work is proposed for future research:

(i) To evaluate the effect of the nature of catalysts (prepared by different synthesis methods) on the metal sintering and coking during catalysis, the characterisation of the spent catalysts (*e.g.,* TEM, XRD and XPS) after the longevity test should be conducted. For example, the TEM of the spent catalysts could give the evidence of the change in Ni particle sizes, identifying the metal sintering; relevant XRD and XPS analysis of the

spent catalysts can present the change of the catalyst structures and Ni chemical states.

(ii) Routine post-reaction characterisations mentioned above can be inadequate to provide the information of the evolution of catalyst structure and the nature of sintering and carbon deposition during DRM reaction. Therefore, to elucidate the detailed relationship between properties of catalysts and improved stability, in situ observation of catalyst behaviour and deactivation during DRM over the developed catalysts using techniques such as near ambient-pressure X-ray photoelectron spectroscopy (NAPXPS) and in situ XRD, should be performed, which can provide more comprehensive and intuitive information on the changes of chemical state, electronic and structure of catalysts, as well as coke formation mechanism, during DRM.

(iii) To mitigate the mass-transfer resistance, the structure of catalyst should be revised and adjusted to optimise the preparation process. For example, by changing the parameters in preparation process (*e.g.,* concentration of TPAOH and hydrothermal treatment temperature/time), the thickness of zeolite shell can be modified, and the optimal thickness could be established by a dedicated investigation to get the best trade-off between the catalyst stability and mass-transfer resistance.

(iv) To mitigate the mass-transfer limit, the creation of hierarchical mesopores within the zeolite *via* the post-synthetic methods (*e.g.*, alkali treatment, hydrothermal/chemical treatment) can be considered for the further development of new DRM catalysts [260].

In summary, this PhD project used CO_2 hydrogenation and DRM as the model systems to demonstrate the comprehensive evaluation of catalyst developments and NTP-catalysis applications for CO_2 utilisation. NTP-catalysis is a promising technique to enable CO_2 conversion under mild conditions as compared with the conventional thermal catalysis. The comparatively study of CO_2 hydrogenation under thermal and NTP conditions regarding the mechanism and catalyst deactivation will contribute to the further development of bespoke catalysts and mature catalytic systems for practical CO_2 valorisation via catalysis in the future. The developed metal@zeolite catalysts show the proof-of-concept of using the confinement effect of microporous supports for

improving the stability of catalysts in the catalysis at high temperatures.

References

[1] X. Jiang, X. Nie, X. Guo, C. Song, J.G. Chen, Recent advances in carbon dioxide hydrogenation to methanol via heterogeneous catalysis, Chem. Rev., 120 (2020) 7984-8034.
[2] J. Artz, T.E. Muller, K. Thenert, J. Kleinekorte, R. Meys, A. Sternberg, A. Bardow, W. Leitner, Sustainable conversion of carbon dioxide: An integrated review of catalysis and life cycle assessment, Chem. Rev., 118 (2018) 434-504.
[3] J. Rogelj, D. Huppmann, V. Krey, K. Riahi, L. Clarke, M. Gidden, Z. Nicholls, M. Meinshausen, A new scenario logic for the Paris Agreement long-term temperature goal, Nature, 573 (2019) 357-363.
[4] A. Goeppert, M. Czaun, J.P. Jones, G.K. Surya Prakash, G.A. Olah, Recycling of carbon dioxide to methanol and derived products-closing the loop, Chem. Soc. Rev., 43 (2014) 7995-8048.
[5] M. Aresta, A. Dibenedetto, A. Angelini, Catalysis for the valorization of exhaust carbon: from CO_2 to chemicals, materials, and fuels. technological use of CO_2, Chem. Rev., 114 (2014) 1709-1742.
[6] S. Roy, A. Cherevotan, S.C. Peter, Thermochemical CO_2 hydrogenation to single carbon products: scientific and technological challenges, ACS Energy Lett., 3 (2018) 1938-1966.
[7] Q. Yi, W. Li, J. Feng, K. Xie, Carbon cycle in advanced coal chemical engineering, Chem. Soc. Rev., 44 (2015) 5409-5445.
[8] S. Ewald, M. Kolbeck, T. Kratky, M. Wolf, O. Hinrichsen, On the deactivation of Ni-Al catalysts in CO_2 methanation, Appl. Catal., A-Gen, 570 (2019) 376-386.
[9] M. Bradford, M. Vannice, CO_2 reforming of CH_4, Catalysis Reviews, 41 (1999) 1-42.
[10] L. Falbo, C.G. Visconti, L. Lietti, J. Szanyi, The effect of CO on CO_2 methanation over Ru/Al_2O_3 catalysts: a combined steady-state reactivity and transient DRIFT spectroscopy study, Appl. Catal. B: Environ, 256 (2019).
[11] A. George, B. Shen, M. Craven, Y. Wang, D. Kang, C. Wu, X. Tu, A review of non-thermal plasma technology: A novel solution for CO_2 conversion and utilization, Renew. Sust. Energ. Rev., 135 (2021) 109702.
[12] S. Chakrabortty, J. Nayak, B. Ruj, P. Pal, R. Kumar, S. Banerjee, M. Sardar, P. Chakraborty, Photocatalytic conversion of CO_2 to methanol using membrane-integrated Green approach: A review on capture, conversion and purification, Journal of Environmental Chemical Engineering, 8 (2020) 103935.
[13] A. Wagner, C.D. Sahm, E. Reisner, Towards molecular understanding of local chemical environment effects in electro- and photocatalytic CO_2 reduction, Nat. Catal., 3 (2020) 775-786.
[14] S. Liu, L.R. Winter, J.G. Chen, Review of plasma-assisted catalysis for selective generation of oxygenates from CO_2 and CH_4, ACS Catal., 10 (2020) 2855-2871.
[15] H. Chen, F. Goodarzi, Y. Mu, S. Chansai, J.J. Mielby, B. Mao, T. Sooknoi, C.

Hardacre, S. Kegnæs, X. Fan, Effect of metal dispersion and support structure of Ni/silicalite-1 catalysts on non-thermal plasma (NTP) activated CO_2 hydrogenation, Appl. Catal. B: Environ, 272 (2020) 119013.
[16] P. Mehta, P. Barboun, D.B. Go, J.C. Hicks, W.F. Schneider, Catalysis Enabled by Plasma Activation of Strong Chemical Bonds: A Review, ACS Energy Lett., 4 (2019) 1115-1133.
[17] E. Neyts, A. Bogaerts, Understanding plasma catalysis through modelling and simulation—a review, J. Phys. D Appl. Phys., 47 (2014) 224010.
[18] Y. Zheng, W. Zhang, Y. Li, J. Chen, B. Yu, J. Wang, L. Zhang, J. Zhang, Energy related CO_2 conversion and utilization: Advanced materials/nanomaterials, reaction mechanisms and technologies, Nano Energy, 40 (2017) 512-539.
[19] A. Fridman, Plasma chemistry, Cambridge university press2008.
[20] R. Snoeckx, A. Bogaerts, Plasma technology - a novel solution for CO_2 conversion?, Chem. Soc. Rev., 46 (2017) 5805-5863.
[21] C. Shi, S. Wang, X. Ge, S. Deng, B. Chen, J. Shen, A review of different catalytic systems for dry reforming of methane: Conventional catalysis-alone and plasma-catalytic system, J. CO2 Util., 46 (2021).
[22] W.J. Lee, C. Li, H. Prajitno, J. Yoo, J. Patel, Y. Yang, S. Lim, Recent trend in thermal catalytic low temperature CO_2 methanation: A critical review, Catal. Today, (2020).
[23] M. Götz, J. Lefebvre, F. Mörs, A. McDaniel Koch, F. Graf, S. Bajohr, R. Reimert, T. Kolb, Renewable Power-to-Gas: A technological and economic review, Renewable Energy, 85 (2016) 1371-1390.
[24] J. Ashok, S. Pati, P. Hongmanorom, Z. Tianxi, C. Junmei, S. Kawi, A review of recent catalyst advances in CO_2 methanation processes, Catal. Today, 356 (2020) 471-489.
[25] M.A.A. Aziz, A.A. Jalil, S. Triwahyono, A. Ahmad, CO_2 methanation over heterogeneous catalysts: recent progress and future prospects, Green Chemistry, 17 (2015) 2647-2663.
[26] R.-P. Ye, Q. Li, W. Gong, T. Wang, J.J. Razink, L. Lin, Y.-Y. Qin, Z. Zhou, H. Adidharma, J. Tang, A.G. Russell, M. Fan, Y.-G. Yao, High-performance of nanostructured Ni/CeO_2 catalyst on CO_2 methanation, Appl. Catal. B: Environ, 268 (2020) 118474.
[27] R. Zhou, N. Rui, Z. Fan, C.-j. Liu, Effect of the structure of Ni/TiO_2 catalyst on CO_2 methanation, Int. J. Hydrog. Energy, 41 (2016) 22017-22025.
[28] D. Wierzbicki, R. Debek, M. Motak, T. Grzybek, M.E. Gálvez, P. Da Costa, Novel Ni-La-hydrotalcite derived catalysts for CO_2 methanation, Catal. Commun., 83 (2016) 5-8.
[29] Z. Fan, K. Sun, N. Rui, B. Zhao, C.-j. Liu, Improved activity of Ni/$MgAl_2O_{-4}$ for CO_2 methanation by the plasma decomposition, J. Energy Chem., 24 (2015) 655-659.
[30] H. Nagase, R. Naito, S. Tada, R. Kikuchi, K. Fujiwara, M. Nishijima, T. Honma, Ru nanoparticles supported on amorphous ZrO_2 for CO_2 methanation, Catal. Sci. Technol., 10 (2020) 4522-4531.

[31] Y. Wang, H. Arandiyan, S.A. Bartlett, A. Trunschke, H. Sun, J. Scott, A.F. Lee, K. Wilson, T. Maschmeyer, R. Schlögl, R. Amal, Inducing synergy in bimetallic RhNi catalysts for CO_2 methanation by galvanic replacement, Appl. Catal. B: Environ, 277 (2020).
[32] J.A.H. Dreyer, P. Li, L. Zhang, G.K. Beh, R. Zhang, P.H.L. Sit, W.Y. Teoh, Influence of the oxide support reducibility on the CO_2 methanation over Ru-based catalysts, Appl. Catal. B: Environ, 219 (2017) 715-726.
[33] G. Zhou, T. Wu, H. Xie, X. Zheng, Effects of structure on the carbon dioxide methanation performance of Co-based catalysts, Int. J. Hydrog. Energy, 38 (2013) 10012-10018.
[34] M. Behrens, S. Zander, P. Kurr, N. Jacobsen, J. Senker, G. Koch, T. Ressler, R.W. Fischer, R. Schlogl, Performance improvement of nanocatalysts by promoter-induced defects in the support material: methanol synthesis over Cu/ZnO:Al, J. Am. Chem. Soc., 135 (2013) 6061-6068.
[35] H. Yang, C. Zhang, P. Gao, H. Wang, X. Li, L. Zhong, W. Wei, Y. Sun, A review of the catalytic hydrogenation of carbon dioxide into value-added hydrocarbons, Catal. Sci. Technol., 7 (2017) 4580-4598.
[36] A. Abdulrasheed, A.A. Jalil, Y. Gambo, M. Ibrahim, H.U. Hambali, M.Y. Shahul Hamid, A review on catalyst development for dry reforming of methane to syngas: Recent advances, Renew. Sust. Energ. Rev., 108 (2019) 175-193.
[37] S. Subramanian, Y. Song, D. Kim, C.T. Yavuz, Redox and nonredox CO_2 utilization: Dry reforming of methane and catalytic cyclic carbonate formation, ACS Energy Lett., 5 (2020) 1689-1700.
[38] S. Li, J. Gong, Strategies for improving the performance and stability of Ni-based catalysts for reforming reactions, Chem. Soc. Rev., 43 (2014) 7245-7256.
[39] A. Beheshti Askari, M. Al Samarai, B. Morana, L. Tillmann, N. Pfander, A. Wandzilak, B. Watts, R. Belkhou, M. Muhler, S. DeBeer, In situ X-ray microscopy reveals particle dynamics in a NiCo dry methane reforming catalyst under operating conditions, ACS Catal, 10 (2020) 6223-6230.
[40] Z. Bian, S. Das, M.H. Wai, P. Hongmanorom, S. Kawi, A review on bimetallic nickel-based catalysts for CO_2 reforming of methane, Chemphyschem, 18 (2017) 3117-3134.
[41] X. Gao, J. Ashok, S. Kawi, Smart designs of anti-coking and anti-sintering Ni-based catalysts for dry reforming of methane: A recent review, Reactions, 1 (2020) 162-194.
[42] D.G. Araiza, D.G. Arcos, A. Gómez-Cortés, G. Díaz, Dry reforming of methane over Pt-Ni/CeO_2 catalysts: Effect of the metal composition on the stability, Catal. Today, 360 (2021) 46-54.
[43] N.A.K. Aramouni, J.G. Touma, B.A. Tarboush, J. Zeaiter, M.N. Ahmad, Catalyst design for dry reforming of methane: Analysis review, Renew. Sust. Energ. Rev., 82 (2018) 2570-2585.
[44] S. Das, J. Perez-Ramirez, J. Gong, N. Dewangan, K. Hidajat, B.C. Gates, S. Kawi, Core-shell structured catalysts for thermocatalytic, photocatalytic, and electrocatalytic

conversion of CO_2, Chem. Soc. Rev., 49 (2020) 2937-3004.
[45] V. Nehra, A. Kumar, H. Dwivedi, Atmospheric non-thermal plasma sources, International Journal of Engineering, 2 (2008) 53-68.
[46] A. Fridman, A. Chirokov, A. Gutsol, Non-thermal atmospheric pressure discharges, J. Phys. D Appl. Phys., 38 (2005) R1.
[47] U. Kogelschatz, Dielectric-barrier discharges: their history, discharge physics, and industrial applications, Plasma Chem. Plasma Process., 23 (2003) 1-46.
[48] A. Bogaerts, E.C. Neyts, Plasma technology: An emerging technology for energy storage, ACS Energy Lett., 3 (2018) 1013-1027.
[49] Y. Zeng, X. Tu, Plasma-catalytic hydrogenation of CO_2 for the cogeneration of CO and CH_4 in a dielectric barrier discharge reactor: effect of argon addition, J. Phys. D Appl. Phys., 50 (2017) 184004.
[50] R. Benrabbah, C. Cavaniol, H. Liu, S. Ognier, S. Cavadias, M.E. Gálvez, P. Da Costa, Plasma DBD activated ceria-zirconia-promoted Ni-catalysts for plasma catalytic CO_2 hydrogenation at low temperature, Catal. Commun., 89 (2017) 73-76.
[51] X. Zhu, J.-H. Liu, X.-S. Li, J.-L. Liu, X. Qu, A.-M. Zhu, Enhanced effect of plasma on catalytic reduction of CO_2 to CO with hydrogen over Au/CeO_2 at low temperature, J. Energy Chem., 26 (2017) 488-493.
[52] E. Jwa, S.B. Lee, H.W. Lee, Y.S. Mok, Plasma-assisted catalytic methanation of CO and CO_2 over Ni–zeolite catalysts, Fuel Process. Technol., 108 (2013) 89-93.
[53] M. Biset-Peiró, J. Guilera, T. Zhang, J. Arbiol, T. Andreu, On the role of ceria in $Ni-Al_2O_3$ catalyst for CO_2 plasma methanation, Appl. Catal., A-Gen, 575 (2019) 223-229.
[54] C.J. Lee, D.H. Lee, T. Kim, Enhancement of methanation of carbon dioxide using dielectric barrier discharge on a ruthenium catalyst at atmospheric conditions, Catal. Today, 293-294 (2017) 97-104.
[55] J.C. Whitehead, Plasma–catalysis: the known knowns, the known unknowns and the unknown unknowns, J. Phys. D Appl. Phys., 49 (2016) 243001.
[56] F. Ahmad, E.C. Lovell, H. Masood, P.J. Cullen, K.K. Ostrikov, J.A. Scott, R. Amal, Low-temperature CO_2 methanation: synergistic effects in plasma-Ni hybrid catalytic system, ACS Sustain. Chem. Eng., 8 (2020) 1888-1898.
[57] E.C. Neyts, Plasma-surface interactions in plasma catalysis, Plasma Chem. Plasma Process., 36 (2015) 185-212.
[58] M. Mikhail, B. Wang, R. Jalain, S. Cavadias, M. Tatoulian, S. Ognier, M.E. Gálvez, P. Da Costa, Plasma-catalytic hybrid process for CO_2 methanation: optimization of operation parameters, React. Kinet. Mech. Catal., 126 (2018) 629-643.
[59] A. Alvarez, A. Bansode, A. Urakawa, A.V. Bavykina, T.A. Wezendonk, M. Makkee, J. Gascon, F. Kapteijn, Challenges in the greener production of formates/formic acid, methanol, and DME by heterogeneously catalyzed CO_2 hydrogenation processes, Chem. Rev., 117 (2017) 9804-9838.
[60] L. Lan, A. Wang, Y. Wang, CO_2 hydrogenation to lower hydrocarbons over ZSM-5-supported catalysts in a dielectric-barrier discharge plasma reactor, Catal. Commun., 130 (2019) 105761.

[61] B. Eliasson, U. Kogelschatz, B. Xue, L.-M. Zhou, Hydrogenation of carbon dioxide to methanol with a discharge-activated catalyst, Ind. Eng. Chem. Res., 37 (1998) 3350-3357.
[62] L. Wang, Y. Yi, H. Guo, X. Tu, Atmospheric pressure and room temperature synthesis of methanol through plasma-catalytic hydrogenation of CO_2, ACS Catal., 8 (2017) 90-100.
[63] Y.-L. Men, Y. Liu, Q. Wang, Z.-H. Luo, S. Shao, Y.-B. Li, Y.-X. Pan, Highly dispersed Pt-based catalysts for selective CO_2 hydrogenation to methanol at atmospheric pressure, Chem. Eng. Sci., 200 (2019) 167-175.
[64] W.-C. Chung, M.-B. Chang, Review of catalysis and plasma performance on dry reforming of CH_4 and possible synergistic effects, Renew. Sust. Energ. Rev., 62 (2016) 13-31.
[65] A.H. Khoja, M. Tahir, N.A.S. Amin, Recent developments in non-thermal catalytic DBD plasma reactor for dry reforming of methane, Energy Convers. Manag., 183 (2019) 529-560.
[66] H. Puliyalil, D. Lašič Jurković, V.D.B.C. Dasireddy, B. Likozar, A review of plasma-assisted catalytic conversion of gaseous carbon dioxide and methane into value-added platform chemicals and fuels, RSC Adv., 8 (2018) 27481-27508.
[67] D. Ray, P.M.K. Reddy, C. Subrahmanyam, Ni-Mn/γ-Al_2O_3 assisted plasma dry reforming of methane, Catal. Today, 309 (2018) 212-218.
[68] A.H. Khoja, M. Tahir, N.A. Saidina Amin, Evaluating the performance of a Ni catalyst supported on La_2O_3-$MgAl_2O_4$ for dry reforming of methane in a packed bed dielectric barrier discharge plasma reactor, Energy Fuels, 33 (2019) 11630-11647.
[69] B. Eliasson, C.-j. Liu, U. Kogelschatz, Direct conversion of methane and carbon dioxide to higher hydrocarbons using catalytic dielectric-barrier discharges with zeolites, Ind. Eng. Chem. Res., 39 (2000) 1221-1227.
[70] Y. Zeng, X. Zhu, D. Mei, B. Ashford, X. Tu, Plasma-catalytic dry reforming of methane over γ-Al_2O_3 supported metal catalysts, Catal. Today, 256 (2015) 80-87.
[71] R. Vakili, R. Gholami, C.E. Stere, S. Chansai, H. Chen, S.M. Holmes, Y. Jiao, C. Hardacre, X. Fan, Plasma-assisted catalytic dry reforming of methane (DRM) over metal-organic frameworks (MOFs)-based catalysts, Appl. Catal. B: Environ, 260 (2020) 118195.
[72] L. Wang, Y. Yi, C. Wu, H. Guo, X. Tu, One-step reforming of CO_2 and CH_4 into high-value liquid chemicals and fuels at room temperature by plasma-driven catalysis, Angew. Chem. Int. Ed. Engl, 56 (2017) 13679-13683.
[73] E.C. Neyts, K.K. Ostrikov, M.K. Sunkara, A. Bogaerts, Plasma catalysis: Synergistic effects at the nanoscale, Chem. Rev., 115 (2015) 13408-13446.
[74] R. Smith, D. Killelea, D. DelSesto, A. Utz, Preference for vibrational over translational energy in a gas-surface reaction, Science, 304 (2004) 992-995.
[75] A. Jafarzadeh, K. Bal, A. Bogaerts, E. Neyts, CO_2 activation on TiO_2-supported Cu_5 and Ni_5 nanoclusters: effect of plasma-induced surface charging, J. Phys. Chem. C, 123 (2019) 6516-6525.
[76] B.-Y. Lee, S.-H. Park, S.-C. Lee, M. Kang, S.-J. Choung, Decomposition of

benzene by using a discharge plasma–photocatalyst hybrid system, Catal. Today, 93-95 (2004) 769-776.
[77] O. Guaitella, F. Thevenet, E. Puzenat, C. Guillard, A. Rousseau, C_2H_2 oxidation by plasma/TiO_2 combination: Influence of the porosity, and photocatalytic mechanisms under plasma exposure, Appl. Catal. B: Environ, 80 (2008) 296-305.
[78] H.-H. Kim, A. Ogata, Nonthermal plasma activates catalyst: from current understanding and future prospects, The European Physical Journal-Applied Physics, 55 (2011) 13806.
[79] H. Chen, Y. Mu, S. Xu, S. Xu, C. Hardacre, X. Fan, Recent advances in non-thermal plasma (NTP) catalysis towards C1 chemistry, Chin. J. Chem. Eng., 28 (2020) 2010-2021.
[80] F. Azzolina-Jury, F. Thibault-Starzyk, Mechanism of low pressure plasma-assisted CO_2 hydrogenation over Ni-USY by microsecond time-resolved FTIR spectroscopy, Top. Catal., 60 (2017) 1709-1721.
[81] C. Stere, S. Chansai, R. Gholami, K. Wangkawong, A. Singhania, A. Goguet, B. Inceesungvorn, C. Hardacre, A design of a fixed bed plasma DRIFTS cell for studying the NTP-assisted heterogeneously catalysed reactions, Catal. Sci. Technol., 10 (2020) 1458-1466.
[82] C.E. Stere, W. Adress, R. Burch, S. Chansai, A. Goguet, W.G. Graham, C. Hardacre, Probing a non-thermal plasma activated heterogeneously catalyzed reaction using in situ DRIFTS-MS, ACS Catal., 5 (2015) 956-964.
[83] C.E. Stere, J.A. Anderson, S. Chansai, J.J. Delgado, A. Goguet, W.G. Graham, C. Hardacre, S.F.R. Taylor, X. Tu, Z. Wang, H. Yang, Non-Thermal Plasma Activation of Gold-Based Catalysts for Low-Temperature Water-Gas Shift Catalysis, Angew. Chem. Int. Ed. Engl, 56 (2017) 5579-5583.
[84] H. Chen, Y. Mu, Y. Shao, S. Chansai, H. Xiang, Y. Jiao, C. Hardacre, X. Fan, Nonthermal plasma (NTP) activated metal–organic frameworks (MOFs) catalyst for catalytic CO_2 hydrogenation, AIChE Journal, 66(4) (2019) 16853.
[85] H. Chen, Y. Mu, Y. Shao, S. Chansai, S. Xu, C.E. Stere, H. Xiang, R. Zhang, Y. Jiao, C. Hardacre, Coupling non-thermal plasma with Ni catalysts supported on BETA zeolite for catalytic CO_2 methanation, Catal. Sci. Technol., 9 (2019) 4135-4145.
[86] Z. Sheng, H.H. Kim, S. Yao, T. Nozaki, Plasma-chemical promotion of catalysis for CH_4 dry reforming: unveiling plasma-enabled reaction mechanisms, Phys. Chem. Chem. Phys., 22 (2020) 19349-19358.
[87] J. Kim, D.B. Go, J.C. Hicks, Synergistic effects of plasma-catalyst interactions for CH_4 activation, Phys. Chem. Chem. Phys., 19 (2017) 13010-13021.
[88] Y. Mu, S. Xu, Y. Shao, H. Chen, C. Hardacre, X. Fan, Kinetic study of nonthermal plasma activated catalytic CO_2 hydrogenation over Ni supported on silica catalyst, Ind. Eng. Chem. Res., 59 (2020) 9478-9487.
[89] K. Ghaib, K. Nitz, F.Z. Ben-Fares, Chemical methanation of CO_2: A review, ChemBioEng Reviews, 3 (2016) 266-275.
[90] M. Younas, L. Loong Kong, M.J.K. Bashir, H. Nadeem, A. Shehzad, S. Sethupathi, Recent advancements, fundamental challenges, and ppportunities in catalytic

methanation of CO_2, Energy Fuels, 30 (2016) 8815-8831.
[91] M.-M. Millet, A.V. Tarasov, F. Girgsdies, G. Algara-Siller, R. Schlögl, E. Frei, Highly dispersed $Ni^0/Ni_xMg_{1-x}O$ catalysts derived from solid solutions: How metal and support control the CO_2 hydrogenation, ACS Catal., 9 (2019) 8534-8546.
[92] Y. Guo, S. Mei, K. Yuan, D.-J. Wang, H.-C. Liu, C.-H. Yan, Y.-W. Zhang, Low-temperature CO_2 methanation over CeO_2-supported Ru single Atoms, nanoclusters, and nanoparticles competitively tuned by strong metal–support interactions and H-spillover effect, ACS Catal., 8 (2018) 6203-6215.
[93] J.H. Kwak, L. Kovarik, J. Szanyi, CO_2 reduction on supported Ru/Al_2O_3 Catalysts: Cluster size dependence of product selectivity, ACS Catal., 3 (2013) 2449-2455.
[94] Y. Yan, Q. Wang, C. Jiang, Y. Yao, D. Lu, J. Zheng, Y. Dai, H. Wang, Y. Yang, Ru/Al_2O_3 catalyzed CO_2 hydrogenation: Oxygen-exchange on metal-support interfaces, J. Catal., 367 (2018) 194-205.
[95] C.-S. Chen, C.S. Budi, H.-C. Wu, D. Saikia, H.-M. Kao, Size-tunable Ni nanoparticles supported on surface-modified, cage-type mesoporous silica as highly active catalysts for CO_2 hydrogenation, ACS Catal., 7 (2017) 8367-8381.
[96] S. Kawi, Y. Kathiraser, J. Ni, U. Oemar, Z. Li, E.T. Saw, Progress in synthesis of highly active and stable nickel-based catalysts for carbon dioxide reforming of methane, ChemSusChem, 8 (2015) 3556-3575.
[97] M. Akri, S. Zhao, X. Li, K. Zang, A.F. Lee, M.A. Isaacs, W. Xi, Y. Gangarajula, J. Luo, Y. Ren, Y.T. Cui, L. Li, Y. Su, X. Pan, W. Wen, Y. Pan, K. Wilson, L. Li, B. Qiao, H. Ishii, Y.F. Liao, A. Wang, X. Wang, T. Zhang, Atomically dispersed nickel as coke-resistant active sites for methane dry reforming, Nat Commun, 10 (2019) 5181.
[98] M. Babucci, A. Guntida, B.C. Gates, Atomically dispersed metals on well-defined supports including zeolites and metal-organic frameworks: Structure, bonding, reactivity, and catalysis, Chem. Rev., 120 (2020) 11956-11985.
[99] H. Peng, X. Zhang, X. Han, X. You, S. Lin, H. Chen, W. Liu, X. Wang, N. Zhang, Z. Wang, P. Wu, H. Zhu, S. Dai, Catalysts in coronas: A surface spatial confinement strategy for high-performance catalysts in methane dry reforming, ACS Catal., 9 (2019) 9072-9080.
[100] G. Garbarino, P. Riani, L. Magistri, G. Busca, A study of the methanation of carbon dioxide on Ni/Al_2O_3 catalysts at atmospheric pressure, Int. J. Hydrog. Energy, 39 (2014) 11557-11565.
[101] R.-P. Ye, W. Gong, Z. Sun, Q. Sheng, X. Shi, T. Wang, Y. Yao, J.J. Razink, L. Lin, Z. Zhou, H. Adidharma, J. Tang, M. Fan, Y.-G. Yao, Enhanced stability of Ni/SiO_2 catalyst for CO_2 methanation: Derived from nickel phyllosilicate with strong metal-support interactions, Energy, 188 (2019) 116059.
[102] A. Kim, D.P. Debecker, F. Devred, V. Dubois, C. Sanchez, C. Sassoye, CO_2 methanation on Ru/TiO_2 catalysts: On the effect of mixing anatase and rutile TiO_2 supports, Appl. Catal. B: Environ, 220 (2018) 615-625.
[103] L.R. Winter, E. Gomez, B. Yan, S. Yao, J.G. Chen, Tuning Ni-catalyzed CO_2 hydrogenation selectivity via Ni-ceria support interactions and Ni-Fe bimetallic formation, Appl. Catal. B: Environ, 224 (2018) 442-450.

[104] I. Graça, L.V. González, M.C. Bacariza, A. Fernandes, C. Henriques, J.M. Lopes, M.F. Ribeiro, CO_2 hydrogenation into CH_4 on NiHNaUSY zeolites, Appl. Catal. B: Environ, 147 (2014) 101-110.
[105] J. Lin, C. Ma, Q. Wang, Y. Xu, G. Ma, J. Wang, H. Wang, C. Dong, C. Zhang, M. Ding, Enhanced low-temperature performance of CO_2 methanation over mesoporous Ni/Al_2O_3-ZrO_2 catalysts, Appl. Catal. B: Environ, 243 (2019) 262-272.
[106] T.A. Le, M.S. Kim, S.H. Lee, T.W. Kim, E.D. Park, CO and CO_2 methanation over supported Ni catalysts, Catal. Today, 293-294 (2017) 89-96.
[107] G. Zhou, H. Liu, K. Cui, A. Jia, G. Hu, Z. Jiao, Y. Liu, X. Zhang, Role of surface Ni and Ce species of Ni/CeO_2 catalyst in CO_2 methanation, Appl. Surf. Sci., 383 (2016) 248-252.
[108] F. Wang, S. He, H. Chen, B. Wang, L. Zheng, M. Wei, D.G. Evans, X. Duan, Active Site Dependent Reaction Mechanism over Ru/CeO_2 Catalyst toward CO_2 Methanation, J. Am. Chem. Soc., 138 (2016) 6298-6305.
[109] A. Cárdenas-Arenas, A. Quindimil, A. Davó-Quiñonero, E. Bailón-García, D. Lozano-Castelló, U. De-La-Torre, B. Pereda-Ayo, J.A. González-Marcos, J.R. González-Velasco, A. Bueno-López, Isotopic and in situ DRIFTS study of the CO_2 methanation mechanism using Ni/CeO_2 and Ni/Al_2O_3 catalysts, Appl. Catal. B: Environ, 265 (2020) 118538.
[110] Y. Zeng, X. Tu, Plasma-catalytic CO_2 hydrogenation at low temperatures, IEEE Trans Plasma Sci, 44 (2016) 405-411.
[111] K. Oshima, T. Shinagawa, Y. Nogami, R. Manabe, S. Ogo, Y. Sekine, Low temperature catalytic reverse water gas shift reaction assisted by an electric field, Catal. Today, 232 (2014) 27-32.
[112] Y. Sun, J. Li, P. Chen, B. Wang, J. Wu, M. Fu, L. Chen, D. Ye, Reverse water-gas shift in a packed bed DBD reactor: Investigation of metal-support interface towards a better understanding of plasma catalysis, Appl. Catal., A-Gen, 591 (2020) 117407.
[113] L. Liu, Z. Zhang, S. Das, S. Xi, S. Kawi, $LaNiO_3$ as a precursor of Ni/La_2O_3 for reverse water-gas shift in DBD plasma: Effect of calcination temperature, Energy Convers. Manag., 206 (2020) 112475.
[114] Z. Wang, Y. Zhang, E.C. Neyts, X. Cao, X. Zhang, B.W.-L. Jang, C.-j. Liu, Catalyst preparation with plasmas: how does it work?, ACS Catal., 8 (2018) 2093-2110.
[115] P. Chawdhury, K.V.S.S. Bhargavi, M. Selvaraj, C. Subrahmanyam, Promising catalytic activity by non-thermal plasma synthesized SBA-15-supported metal catalysts in one-step plasma-catalytic methane conversion to value-added fuels, Catal. Sci. Technol., 10(16) (2020) 5566.
[116] W. Xu, X. Zhang, M. Dong, J. Zhao, L. Di, Plasma-assisted Ru/Zr-MOF catalyst for hydrogenation of CO_2 to methane, Plasma Sci. Technol., 21 (2019) 044004.
[117] W. Xu, M. Dong, L. Di, X. Zhang, A facile method for preparing UiO-66 encapsulated Ru catalyst and its application in plasma-assisted CO_2 methanation, Nanomaterials (Basel), 9 (2019) 1432.
[118] D. Wierzbicki, M.V. Moreno, S. Ognier, M. Motak, T. Grzybek, P. Da Costa, M.E. Gálvez, Ni-Fe layered double hydroxide derived catalysts for non-plasma and DBD

plasma-assisted CO_2 methanation, Int. J. Hydrog. Energy, 45 (2020) 10423-10432.
[119] M. Nizio, A. Albarazi, S. Cavadias, J. Amouroux, M.E. Galvez, P. Da Costa, Hybrid plasma-catalytic methanation of CO_2 at low temperature over ceria zirconia supported Ni catalysts, Int. J. Hydrog. Energy, 41 (2016) 11584-11592.
[120] Y.S. Mok, E. Jwa, H.W. Lee, Production of methane from carbon monoxide and carbon dioxide in a plasma-catalytic combined reactor system, Int. J. Sustain. Dev. Plan., 8 (2013) 186-196.
[121] J. Amouroux, S. Cavadias, Electrocatalytic reduction of carbon dioxide under plasma DBD process, J. Phys. D Appl. Phys., 50 (2017) 465501.
[122] M.C. Bacariza, M. Biset-Peiró, I. Graça, J. Guilera, J. Morante, J.M. Lopes, T. Andreu, C. Henriques, DBD plasma-assisted CO_2 methanation using zeolite-based catalysts: Structure composition-reactivity approach and effect of Ce as promoter, J. CO2 Util., 26 (2018) 202-211.
[123] D. Mei, B. Ashford, Y.-L. He, X. Tu, Plasma-catalytic reforming of biogas over supported Ni catalysts in a dielectric barrier discharge reactor: Effect of catalyst supports, Plasma Process Polym, 14 (2017).
[124] M. Nizio, R. Benrabbah, M. Krzak, R. Debek, M. Motak, S. Cavadias, M.E. Gálvez, P. Da Costa, Low temperature hybrid plasma-catalytic methanation over Ni-Ce-Zr hydrotalcite-derived catalysts, Catal. Commun., 83 (2016) 14-17.
[125] P. Li, F. Yu, N. Altaf, M. Zhu, J. Li, B. Dai, Q. Wang, Two-Dimensional Layered Double Hydroxides for Reactions of Methanation and Methane Reforming in C1 Chemistry, Materials (Basel), 11 (2018) 221.
[126] N. Dewangan, W.M. Hui, S. Jayaprakash, A.-R. Bawah, A.J. Poerjoto, T. Jie, A. Jangam, K. Hidajat, S. Kawi, Recent progress on layered double hydroxide (LDH) derived metal-based catalysts for CO_2 conversion to valuable chemicals, Catal. Today, 356 (2020) 490-513.
[127] N. Masoumifard, R. Guillet-Nicolas, F. Kleitz, Synthesis of engineered zeolitic materials: From classical zeolites to hierarchical core-shell materials, Adv. Mater., 30 (2018) 1704439.
[128] Q. Zhang, J. Yu, A. Corma, Applications of zeolites to C1 chemistry: Recent advances, challenges, and opportunities, Adv. Mater., 32(44) (2020) 2002927.
[129] Y.-R. Zhang, E.C. Neyts, A. Bogaerts, Enhancement of plasma generation in catalyst pores with different shapes, Plasma Sources Sci. Technol., 27 (2018) 055008.
[130] Y.-R. Zhang, K. Van Laer, E.C. Neyts, A. Bogaerts, Can plasma be formed in catalyst pores? A modeling investigation, Appl. Catal. B: Environ, 185 (2016) 56-67.
[131] H. Chen, H. Lee, S. Chen, Y. Chao, M. Chang, Review of plasma catalysis on hydrocarbon reforming for hydrogen production—Interaction, integration, and prospects, Appl. Catal. B: Environ, 85 (2008) 1-9.
[132] J.C. Whitehead, Plasma-catalysis: Is it just a question of scale?, Front Chem Sci Eng, 13 (2019) 264-273.
[133] Y.-B. Huang, J. Liang, X.-S. Wang, R. Cao, Multifunctional metal–organic framework catalysts: synergistic catalysis and tandem reactions, Chem. Soc. Rev., 46 (2017) 126-157.

[134] J.W. Maina, C. Pozo-Gonzalo, L. Kong, J. Schütz, M. Hill, L.F. Dumée, Metal organic framework based catalysts for CO_2 conversion, Mater. Horiz., 4 (2017) 345-361.
[135] M.C. Bacariza, R. Bértolo, I. Graça, J.M. Lopes, C. Henriques, The effect of the compensating cation on the catalytic performances of Ni/USY zeolites towards CO_2 methanation, J. CO2 Util., 21 (2017) 280-291.
[136] A. Petala, P. Panagiotopoulou, Methanation of CO_2 over alkali-promoted Ru/TiO_2 catalysts: I. Effect of alkali additives on catalytic activity and selectivity, Appl. Catal. B: Environ, 224 (2018) 919-927.
[137] B. Liang, H. Duan, T. Sun, J. Ma, X. Liu, J. Xu, X. Su, Y. Huang, T. Zhang, Effect of Na promoter on Fe-based catalyst for CO_2 hydrogenation to alkenes, ACS Sustain. Chem. Eng., 7 (2018) 925-932.
[138] D. Ray, P. Chawdhury, C. Subrahmanyam, Promising utilization of CO_2 for Syngas Production over Mg^{2+} and Ce^{2+}-Promoted Ni/gamma-Al_2O_3 Assisted by Nonthermal Plasma, ACS Omega, 5 (2020) 14040-14050.
[139] M.C. Bacariza, I. Graça, S.S. Bebiano, J.M. Lopes, C. Henriques, Magnesium as Promoter of CO_2 Methanation on Ni-Based USY Zeolites, Energy Fuels, 31 (2017) 9776-9789.
[140] H. Wang, B. Zhao, L. Qin, Y. Wang, F. Yu, J. Han, Non-thermal plasma-enhanced dry reforming of methane and CO_2 over Ce-promoted Ni/C catalysts, Molecular Catalysis, 485 (2020) 110821.
[141] Y.X. Zeng, L. Wang, C.F. Wu, J.Q. Wang, B.X. Shen, X. Tu, Low temperature reforming of biogas over K-, Mg- and Ce-promoted Ni/Al_2O_3 catalysts for the production of hydrogen rich syngas: Understanding the plasma-catalytic synergy, Appl. Catal. B: Environ, 224 (2018) 469-478.
[142] A.H. Khoja, M. Tahir, N.A.S. Amin, Cold plasma dielectric barrier discharge reactor for dry reforming of methane over Ni/ɤ-Al_2O_3-MgO nanocomposite, Fuel Process. Technol., 178 (2018) 166-179.
[143] W.H. Li, H.Z. Wang, X. Jiang, J. Zhu, Z.M. Liu, X.W. Guo, C.S. Song, A short review of recent advances in CO_2 hydrogenation to hydrocarbons over heterogeneous catalysts, RSC Adv., 8 (2018) 7651-7669.
[144] M. Gotz, J. Lefebvre, F. Mors, A.M. Koch, F. Graf, S. Bajohr, R. Reimert, T. Kolb, Renewable Power-to-Gas: A technological and economic review, Renew. Energy, 85 (2016) 1371-1390.
[145] J. Bao, G.H. Yang, Y. Yoneyama, N. Tsubaki, Significant Advances in C1 Catalysis: Highly Efficient Catalysts and Catalytic Reactions, ACS Catal., 9 (2019) 3026-3053.
[146] C. Mebrahtu, S. Abate, S. Perathoner, S.M. Chen, G. Centi, CO_2 methanation over Ni catalysts based on ternary and quaternary mixed oxide: A comparison and analysis of the structure-activity relationships, Catal. Today, 304 (2018) 181-189.
[147] S. Rönsch, J. Schneider, S. Matthischke, M. Schlüter, M. Götz, J. Lefebvre, P. Prabhakaran, S. Bajohr, Review on methanation – From fundamentals to current projects, Fuel, 166 (2016) 276-296.

[148] M. Xu, M. Wei, Layered Double Hydroxide-Based Catalysts: Recent Advances in Preparation, Structure, and Applications, Adv. Funct. Mater., 28 (2018) 1802943-1802963.
[149] K. Mori, T. Taga, H. Yamashita, Isolated Single-Atomic Ru Catalyst Bound on a Layered Double Hydroxide for Hydrogenation of CO_2 to Formic Acid, ACS Catal., 7 (2017) 3147-3151.
[150] S. Abate, K. Barbera, E. Giglio, F. Deorsola, S. Bensaid, S. Perathoner, R. Pirone, G. Centi, Synthesis, Characterization, and Activity Pattern of Ni–Al Hydrotalcite Catalysts in CO_2 Methanation, Ind. Eng. Chem. Res., 55 (2016) 8299-8308.
[151] R. Vakili, R. Gholami, C.E. Stere, S. Chansai, H. Chen, S.M. Holmes, Y. Jiao, C. Hardacre, X. Fan, Plasma-assisted catalytic dry reforming of methane (DRM) over metal-organic frameworks (MOFs)-based catalysts, Appl. Catal. B: Environ., 260 (2020) 118195-118206.
[152] S. Xu, S. Chansai, C. Stere, B. Inceesungvorn, A. Goguet, K. Wangkawong, S.F.R. Taylor, N. Al-Janabi, C. Hardacre, P.A. Martin, X. Fan, Sustaining metal–organic frameworks for water–gas shift catalysis by non-thermal plasma, Nat. Catal., 2 (2019) 142-148.
[153] H.H. Chen, Y.B. Mu, Y. Shao, S. Chansai, S.J. Xu, C.E. Stere, H. Xiang, R.X. Zhang, Y.L. Jiao, C. Hardacre, X.L. Fan, Coupling non-thermal plasma with Ni catalysts supported on BETA zeolite for catalytic CO_2 methanation, Catal. Sci. Technol., 9 (2019) 4135-4145.
[154] E.K. Gibson, C.E. Stere, B. Curran-McAteer, W. Jones, G. Cibin, D. Gianolio, A. Goguet, P.P. Wells, C.R.A. Catlow, P. Collier, P. Hinde, C. Hardacre, Probing the Role of a Non-Thermal Plasma (NTP) in the Hybrid NTP Catalytic Oxidation of Methane, Angew. Chem. Int. Ed. Engl, 56 (2017) 9351-9355.
[155] B. Ashford, X. Tu, Non-thermal plasma technology for the conversion of CO_2, Curr. Opin. Green Sustain. Chem., 3 (2017) 45-49.
[156] X. Zhu, X. Liu, H.-Y. Lian, J.-L. Liu, X.-S. Li, Plasma catalytic steam methane reforming for distributed hydrogen production, Catal. Today, 337 (2019) 69-75.
[157] F. Cavani, F. Trifiro, A. Vaccari, Hydrotalcite-type anionic clays: Preparation, properties and applications, Catal. Today, 11 (1991) 173-301.
[158] M. Zhang, Y. Zhao, Q. Liu, L. Yang, G. Fan, F. Li, A La-doped Mg-Al mixed metal oxide supported copper catalyst with enhanced catalytic performance in transfer dehydrogenation of 1-decanol, Dalton Trans, 45 (2016) 1093-1102.
[159] P. Liu, M. Derchi, E.J.M. Hensen, Synthesis of glycerol carbonate by transesterification of glycerol with dimethyl carbonate over MgAl mixed oxide catalysts, Appl. Catal. A- Gen, 467 (2013) 124-131.
[160] N. Tang, Y. Cong, Q. Shang, C. Wu, G. Xu, X. Wang, Coordinatively Unsaturated Al^{3+} Sites Anchored Subnanometric Ruthenium Catalyst for Hydrogenation of Aromatics, ACS Catal., 7 (2017) 5987-5991.
[161] L. Chen, Y. Zhu, H. Zheng, C. Zhang, Y. Li, Aqueous-phase hydrodeoxygenation of propanoic acid over the Ru/ZrO_2 and $Ru–Mo/ZrO_2$ catalysts, Appl. Catal. A- Gen, 411-412 (2012) 95-104.

[162] A.M. Abdel-Mageed, D. Widmann, S.E. Olesen, I. Chorkendorff, R.J. Behm, Selective CO Methanation on Highly Active Ru/TiO_2 Catalysts: Identifying the Physical Origin of the Observed Activation/Deactivation and Loss in Selectivity, ACS Catal., 8 (2018) 5399-5414.
[163] N. Gupta, V. Kamble, R. Iyer, K.R. Thampi, M. Gratzel, The transient species formed over Ru–RuOx/TiO_2 catalyst in the CO and CO+H_2 interaction: FTIR spectroscopic study, J. Catal., 137 (1992) 473-486.
[164] J. Singh, J.A. van Bokhoven, Structure of alumina supported platinum catalysts of different particle size during CO oxidation using in situ IR and HERFD XAS, Catal. Today, 155 (2010) 199-205.
[165] D.J. Morgan, Resolving ruthenium: XPS studies of common ruthenium materials, Surf. Interface Anal., 47 (2015) 1072-1079.
[166] D. Li, R. Li, M. Lu, X. Lin, Y. Zhan, L. Jiang, Carbon dioxide reforming of methane over Ru catalysts supported on Mg-Al oxides: A highly dispersed and stable Ru/Mg(Al)O catalyst, Appl. Catal. B: Environ, 200 (2017) 566-577.
[167] J. Chen, Y. Song, D. Shan, E.-H. Han, Study of the in situ growth mechanism of Mg–Al hydrotalcite conversion film on AZ31 magnesium alloy, Corros. Sci., 63 (2012) 148-158.
[168] F. Wang, S. Zhang, C. Li, J. Liu, S. He, Y. Zhao, H. Yan, M. Wei, D.G. Evans, X. Duan, Catalytic behavior of supported Ru nanoparticles on the (101) and (001) facets of anatase TiO_2, RSC Adv., 4 (2014) 10834.
[169] P. da Costa Zonetti, R. Landers, A.J.G. Cobo, Thermal treatment effects on the Ru/CeO_2 catalysts performance for partial hydrogenation of benzene, Appl. Surf. Sci., 254 (2008) 6849-6853.
[170] M. Abdellattif, M. Mokhtar, MgAl-Layered Double Hydroxide Solid Base Catalysts for Henry Reaction: A Green Protocol, Catalysts, 8 (2018) 133.
[171] Q. Pan, J. Peng, T. Sun, S. Wang, S. Wang, Insight into the reaction route of CO_2 methanation: Promotion effect of medium basic sites, Catal. Commun., 45 (2014) 74-78.
[172] E. Baraj, S. Vagaský, T. Hlinčik, K. Ciahotný, V. Tekáč, Reaction mechanisms of carbon dioxide methanation, Chemical Papers, 70 (2016) 309-403.
[173] B. Miao, S.S.K. Ma, X. Wang, H. Su, S.H. Chan, Catalysis mechanisms of CO_2 and CO methanation, Catal. Sci. Technol., 6 (2016) 4048-4058.
[174] A. Parastaev, W.F.L.M. Hoeben, B.E.J.M. van Heesch, N. Kosinov, E.J.M. Hensen, Temperature-programmed plasma surface reaction: An approach to determine plasma-catalytic performance, Appl. Catal. B: Environ., 239 (2018) 168-177.
[175] S. Navarro-Jaén, J.C. Navarro, L.F. Bobadilla, M.A. Centeno, O.H. Laguna, J.A. Odriozola, Size-tailored Ru nanoparticles deposited over γ-Al_2O_3 for the CO_2 methanation reaction, Appl. Surf. Sci., 483 (2019) 750-761.
[176] H.-H. Kim, Y. Teramoto, A. Ogata, H. Takagi, T. Nanba, Plasma Catalysis for Environmental Treatment and Energy Applications, Plasma Chem. Plasma Process., 36 (2015) 45-72.
[177] N. Gupta, V. Kamble, V. Kartha, R. Iyer, K.R. Thampi, M. Gratzel, FTIR

spectroscopic study of the interaction of CO_2 and CO_2+ H_2 over partially oxidized $RuTiO_2$ catalyst, J. Catal., 146 (1994) 173-184.
[178] S. Eckle, H.-G. Anfang, R.J. Behm, Reaction Intermediates and Side Products in the Methanation of CO and CO_2 over Supported Ru Catalysts in H_2-Rich Reformate Gases, J. Phys. Chem. C, 115 (2010) 1361-1367.
[179] K. Zhao, L. Wang, M. Calizzi, E. Moioli, A. Züttel, In Situ Control of the Adsorption Species in CO2 Hydrogenation: Determination of Intermediates and Byproducts, J. Phys. Chem. C, 122 (2018) 20888-20893.
[180] J.L.C. Fajín, J.R.B. Gomes, M.N. D. S. Cordeiro, Mechanistic Study of Carbon Monoxide Methanation over Pure and Rhodium- or Ruthenium-Doped Nickel Catalysts, J. Phys. Chem. C, 119 (2015) 16537-16551.
[181] J. Szanyi, J.H. Kwak, Dissecting the steps of CO_2 reduction: 1. The interaction of CO and CO_2 with gamma-Al_2O_3: an in situ FTIR study, Phys. Chem. Chem. Phys., 16 (2014) 15117-15125.
[182] A. Solis-Garcia, J.F. Louvier-Hernandez, A. Almendarez-Camarillo, J.C. Fierro-Gonzalez, Participation of surface bicarbonate, formate and methoxy species in the carbon dioxide methanation catalyzed by ZrO2-supported Ni, Appl. Catal. B: Environ, 218 (2017) 611-620.
[183] A. Bogaerts, X. Tu, J.C. Whitehead, G. Centi, L. Lefferts, O. Guaitella, F. Azzolina-Jury, H.-H. Kim, A.B. Murphy, W.F. Schneider, T. Nozaki, J.C. Hicks, A. Rousseau, F. Thevenet, A. Khacef, M. Carreon, The 2020 plasma catalysis roadmap, J. Phys. D Appl. Phys., 53 (2020).
[184] R. Vakili, R. Gholami, C.E. Stere, S. Chansai, H. Chen, S.M. Holmes, Y. Jiao, C. Hardacre, X. Fan, Plasma-assisted catalytic dry reforming of methane (DRM) over metal-organic frameworks (MOFs)-based catalysts, Appl. Catal. B: Environ, 260 (2020).
[185] N. Gupta, V. Londhe, V. Kamble, Gas-Uptake, Methanation, and Microcalorimetric Measurements on the Coadsorption of CO and H_2 over Polycrystalline Ru and a Ru/TiO_2 Catalyst, J. Catal., 169 (1997) 423-437.
[186] P. Barboun, P. Mehta, F.A. Herrera, D.B. Go, W.F. Schneider, J.C. Hicks, Distinguishing Plasma Contributions to Catalyst Performance in Plasma-Assisted Ammonia Synthesis, ACS Sustain. Chem. Eng., 7 (2019) 8621-8630.
[187] S. Xu, S. Chansai, Y. Shao, S. Xu, Y.-c. Wang, S. Haigh, Y. Mu, Y. Jiao, C.E. Stere, H. Chen, X. Fan, C. Hardacre, Mechanistic study of non-thermal plasma assisted CO_2 hydrogenation over Ru supported on MgAl layered double hydroxide, Appl. Catal. B: Environ, 268 (2020) 118752.
[188] A. Bogaerts, A. Berthelot, S. Heijkers, S. Kolev, R. Snoeckx, S. Sun, G. Trenchev, K. Van Laer, W. Wang, CO_2 conversion by plasma technology: insights from modeling the plasma chemistry and plasma reactor design, Plasma Sources Sci. Technol., 26 (2017) 063001.
[189] D. Mei, X. Zhu, Y.-L. He, J.D. Yan, X. Tu, Plasma-assisted conversion of CO_2 in a dielectric barrier discharge reactor: understanding the effect of packing materials, Plasma Sources Sci. Technol., 24 (2014) 015011.

[190] Y. Zhang, H.-y. Wang, W. Jiang, A. Bogaerts, Two-dimensional particle-in cell/Monte Carlo simulations of a packed-bed dielectric barrier discharge in air at atmospheric pressure, New J. Phys., 17 (2015) 083056.
[191] K. Zhang, G. Zhang, X. Liu, A.N. Phan, K. Luo, A Study on CO_2 Decomposition to CO and O_2 by the Combination of Catalysis and Dielectric-Barrier Discharges at Low Temperatures and Ambient Pressure, Ind. Eng. Chem. Res., 56 (2017) 3204-3216.
[192] Y. Zhang, H.-y. Wang, Y.-r. Zhang, A. Bogaerts, Formation of microdischarges inside a mesoporous catalyst in dielectric barrier discharge plasmas, Plasma Sources Sci. Technol., 26 (2017) 054002.
[193] G.D. Weatherbee, C.H. Bartholomew, Hydrogenation of CO_2 on group VIII metals: II. Kinetics and mechanism of CO_2 hydrogenation on nickel, J. Catal., 77 (1982) 460-472.
[194] M.R. Prairie, A. Renken, J.G. Highfield, K.R. Thampi, M. Grätzel, A fourier transform infrared spectroscopic study of CO_2 methanation on supported ruthenium, J. Catal., 129 (1991) 130-144.
[195] F. Solymosi, A. Erdöhelyi, M. Kocsis, Methanation of CO_2 on supported Ru catalysts, J. Chem. Soc., Faraday Trans., 77 (1981) 1003-1012.
[196] M. Kuśmierz, Kinetic study on carbon dioxide hydrogenation over Ru/γ-Al_2O_3 catalysts, Catal. Today, 137 (2008) 429-432.
[197] J.A.H. Lalinde, P. Roongruangsree, J. Ilsemann, M. Baeumer, J. Kopyscinski, CO_2 methanation and reverse water gas shift reaction. Kinetic study based on in situ spatially-resolved measurements, Chem. Eng. J., (2020) 124629.
[198] G. Garbarino, D. Bellotti, E. Finocchio, L. Magistri, G. Busca, Methanation of carbon dioxide on Ru/Al_2O_3: Catalytic activity and infrared study, Catal. Today, 277 (2016) 21-28.
[199] I.A. Fisher, A.T. Bell, A comparative study of CO and CO_2 Hydrogenation over Rh/SiO_2, J. Catal., 162 (1996) 54-65.
[200] S. Eckle, H.-G. Anfang, R.J.r. Behm, Reaction intermediates and side products in the methanation of CO and CO_2 over supported Ru catalysts in H_2-rich reformate gases, J. Phys. Chem. C, 115 (2011) 1361-1367.
[201] C.-j. Liu, G.-h. Xu, T. Wang, Non-thermal plasma approaches in CO_2 utilization, Fuel Process. Technol., 58 (1999) 119-134.
[202] N. Gupta, V. Kamble, K.A. Rao, R. Iyer, On the mechanism of CO and CO_2 methanation over Ru/molecular-sieve catalyst, J. Catal., 60 (1979) 57-67.
[203] T. Utaka, T. Okanishi, T. Takeguchi, R. Kikuchi, K. Eguchi, Water gas shift reaction of reformed fuel over supported Ru catalysts, Appl. Catal., A-Gen, 245 (2003) 343-351.
[204] N. Gupta, V. Kamble, R. Iyer, K.R. Thampi, M. Gratzel, FTIR studies on the CO, CO_2 and H_2 co-adsorption over Ru-RuOx/TiO_2 catalyst, Catal. Lett, 21 (1993) 245-255.
[205] S.-T. Zhang, H. Yan, M. Wei, D.G. Evans, X. Duan, Hydrogenation mechanism of carbon dioxide and carbon monoxide on Ru(0001) surface: a density functional theory study, RSC Adv., 4 (2014) 30241.
[206] S. Mukkavilli, C. Wittmann, L.L. Tavlarides, Carbon deactivation of Fischer-

Tropsch ruthenium catalyst, Ind. Eng. Chem. Process. Des. Dev., 25 (1986) 487-494.
[207] L. Wang, Y. Zhao, C. Liu, W. Gong, H. Guo, Plasma driven ammonia decomposition on a Fe-catalyst: eliminating surface nitrogen poisoning, Chem Commun, 49 (2013) 3787-3789.
[208] B. Zhu, X.-S. Li, J.-L. Liu, J.-B. Liu, X. Zhu, A.-M. Zhu, In-situ regeneration of Au nanocatalysts by atmospheric-pressure air plasma: Significant contribution of water vapor, Appl. Catal. B: Environ, 179 (2015) 69-77.
[209] P. Zhao, Y. He, D.B. Cao, X. Wen, H. Xiang, Y.W. Li, J. Wang, H. Jiao, High coverage adsorption and co-adsorption of CO and H_2 on Ru(0001) from DFT and thermodynamics, Phys. Chem. Chem. Phys., 17 (2015) 19446-19456.
[210] T. Diemant, H. Rauscher, J. Bansmann, R.J. Behm, Coadsorption of hydrogen and CO on well-defined Pt(35)Ru(65)/Ru(0001) surface alloys--site specificity vs. adsorbate-adsorbate interactions, Phys. Chem. Chem. Phys., 12 (2010) 9801-9810.
[211] X. Wang, Y. Hong, H. Shi, J. Szanyi, Kinetic modeling and transient DRIFTS–MS studies of CO_2 methanation over Ru/Al_2O_3 catalysts, J. Catal., 343 (2016) 185-195.
[212] N.W. Cant, A.T. Bell, Studies of carbon monoxide hydrogenation over ruthenium using transient response techniques, J. Catal., 73 (1982) 257-271.
[213] J.M.G. Carballo, E. Finocchio, S. García-Rodriguez, M. Ojeda, J.L.G. Fierro, G. Busca, S. Rojas, Insights into the deactivation and reactivation of Ru/TiO_2 during Fischer–Tropsch synthesis, Catal. Today, 214 (2013) 2-11.
[214] W. Abou Saoud, A.A. Assadi, M. Guiza, A. Bouzaza, W. Aboussaoud, A. Ouederni, I. Soutrel, D. Wolbert, S. Rtimi, Study of synergetic effect, catalytic poisoning and regeneration using dielectric barrier discharge and photocatalysis in a continuous reactor: Abatement of pollutants in air mixture system, Appl. Catal. B: Environ, 213 (2017) 53-61.
[215] M.A.A. Aziz, A.A. Jalil, S. Triwahyono, M.W.A. Saad, CO_2 methanation over Ni-promoted mesostructured silica nanoparticles: Influence of Ni loading and water vapor on activity and response surface methodology studies, Chem. Eng. J., 260 (2015) 757-764.
[216] L. Falbo, M. Martinelli, C.G. Visconti, L. Lietti, C. Bassano, P. Deiana, Kinetics of CO_2 methanation on a Ru-based catalyst at process conditions relevant for Power-to-Gas applications, Appl. Catal. B: Environ, 225 (2018) 354-363.
[217] W.-J. Jang, J.-O. Shim, H.-M. Kim, S.-Y. Yoo, H.-S. Roh, A review on dry reforming of methane in aspect of catalytic properties, Catal. Today, 324 (2019) 15-26.
[218] Y. Lyu, J. Jocz, R. Xu, E. Stavitski, C. Sievers, Nickel speciation and methane dry reforming performance of $Ni/Ce_xZr_{1-x}O_2$ prepared by different synthesis methods, ACS Catal., 10 (2020) 11235-11252.
[219] T. Stroud, T.J. Smith, E. Le Saché, J.L. Santos, M.A. Centeno, H. Arellano-Garcia, J.A. Odriozola, T.R. Reina, Chemical CO_2 recycling via dry and bi reforming of methane using $Ni-Sn/Al_2O_3$ and $Ni-Sn/CeO_2-Al_2O_3$ catalysts, Appl. Catal. B: Environ, 224 (2018) 125-135.
[220] Y. Wang, L. Yao, Y. Wang, S. Wang, Q. Zhao, D. Mao, C. Hu, Low-temperature catalytic CO_2 dry reforming of methane on $Ni-Si/ZrO_2$ catalyst, ACS Catal., 8 (2018)

6495-6506.
[221] Z. Xie, B. Yan, S. Kattel, J.H. Lee, S. Yao, Q. Wu, N. Rui, E. Gomez, Z. Liu, W. Xu, L. Zhang, J.G. Chen, Dry reforming of methane over CeO_2-supported Pt-Co catalysts with enhanced activity, Appl. Catal. B: Environ, 236 (2018) 280-293.
[222] Z. Liu, F. Zhang, N. Rui, X. Li, L. Lin, L.E. Betancourt, D. Su, W. Xu, J. Cen, K. Attenkofer, H. Idriss, J.A. Rodriguez, S.D. Senanayake, Highly active ceria-supported Ru catalyst for the dry reforming of methane: In situ identification of $Ru^{\delta+}$–Ce^{3+} interactions for enhanced conversion, ACS Catal., 9 (2019) 3349-3359.
[223] D. Baudouin, U. Rodemerck, F. Krumeich, A.d. Mallmann, K.C. Szeto, H. Ménard, L. Veyre, J.-P. Candy, P.B. Webb, C. Thieuleux, C. Copéret, Particle size effect in the low temperature reforming of methane by carbon dioxide on silica-supported Ni nanoparticles, J. Catal., 297 (2013) 27-34.
[224] R. Franz, T. Kühlewind, G. Shterk, E. Abou-Hamad, A. Parastaev, E. Uslamin, E.J.M. Hensen, F. Kapteijn, J. Gascon, E.A. Pidko, Impact of small promoter amounts on coke structure in dry reforming of methane over Ni/ZrO_2, Catal. Sci. Technol., 10 (2020) 3965-3974.
[225] A.A. Abdulrasheed, A.A. Jalil, M.Y.S. Hamid, T.J. Siang, T.A.T. Abdullah, Dry reforming of CH_4 over stabilized Ni-La@KCC-1 catalyst: Effects of La promoter and optimization studies using RSM, J. CO2 Util., 37 (2020) 230-239.
[226] Z. Wu, B. Yang, S. Miao, W. Liu, J. Xie, S. Lee, M.J. Pellin, D. Xiao, D. Su, D. Ma, Lattice strained Ni-Co alloy as a high-performance catalyst for catalytic dry reforming of methane, ACS Catal., 9 (2019) 2693-2700.
[227] T. Margossian, K. Larmier, S.M. Kim, F. Krumeich, C. Müller, C. Copéret, Supported bimetallic NiFe nanoparticles through colloid synthesis for improved dry reforming performance, ACS Catal., 7 (2017) 6942-6948.
[228] C. Wang, X. Jie, Y. Qiu, Y. Zhao, H.A. Al-Megren, S. Alshihri, P.P. Edwards, T. Xiao, The importance of inner cavity space within Ni@SiO_2 nanocapsule catalysts for excellent coking resistance in the high-space-velocity dry reforming of methane, Appl. Catal. B: Environ, 259 (2019).
[229] S. Das, J. Ashok, Z. Bian, N. Dewangan, M.H. Wai, Y. Du, A. Borgna, K. Hidajat, S. Kawi, Silica–Ceria sandwiched Ni core–shell catalyst for low temperature dry reforming of biogas: Coke resistance and mechanistic insights, Appl. Catal. B: Environ, 230 (2018) 220-236.
[230] S.H. Joo, J.Y. Park, C.K. Tsung, Y. Yamada, P. Yang, G.A. Somorjai, Thermally stable Pt/mesoporous silica core-shell nanocatalysts for high-temperature reactions, Nat Mater, 8 (2009) 126-131.
[231] T. Xie, L. Shi, J. Zhang, D. Zhang, Immobilizing Ni nanoparticles to mesoporous silica with size and location control via a polyol-assisted route for coking- and sintering-resistant dry reforming of methane, Chem Commun (Camb), 50 (2014) 7250-7253.
[232] F. Wang, B. Han, L. Zhang, L. Xu, H. Yu, W. Shi, CO_2 reforming with methane over small-sized Ni@SiO_2 catalysts with unique features of sintering-free and low carbon, Appl. Catal. B: Environ, 235 (2018) 26-35.
[233] H. Wang, L. Wang, F.S. Xiao, Metal@zeolite hybrid materials for catalysis, ACS

Cent Sci, 6 (2020) 1685-1697.
[234] J. Zhang, L. Wang, B. Zhang, H. Zhao, U. Kolb, Y. Zhu, L. Liu, Y. Han, G. Wang, C. Wang, D.S. Su, B.C. Gates, F.-S. Xiao, Sinter-resistant metal nanoparticle catalysts achieved by immobilization within zeolite crystals via seed-directed growth, Nat. Catal., 1 (2018) 540-546.
[235] C. Dai, S. Zhang, A. Zhang, C. Song, C. Shi, X. Guo, Hollow zeolite encapsulated Ni–Pt bimetals for sintering and coking resistant dry reforming of methane, Journal of Materials Chemistry A, 3 (2015) 16461-16468.
[236] T. Kobayashi, T. Furuya, H. Fujitsuka, T. Tago, Synthesis of Birdcage-type zeolite encapsulating ultrafine Pt nanoparticles and its application in dry reforming of methane, Chem. Eng. J., 377 (2019) 120203.
[237] B. Zhang, Y. Tian, D. Chen, L. Li, G. Li, L. Wang, X. Zhang, G. Liu, Selective steam reforming of n-dodecane over stable subnanometric NiPt clusters encapsulated in Silicalite-1 zeolite, AIChE Journal, 66 (2020) 16917.
[238] K.M. Kwok, S.W.D. Ong, L. Chen, H.C. Zeng, Transformation of stober silica spheres to hollow hierarchical single-crystal ZSM-5 zeolites with encapsulated metal nanocatalysts for selective catalysis, ACS Appl Mater Interfaces, 11 (2019) 14774-14785.
[239] X. Niu, X. Li, G. Yuan, F. Feng, M. Wang, X. Zhang, Q. Wang, Hollow hierarchical silicalite-1 zeolite encapsulated PtNi bimetals for selective hydroconversion of methyl stearate into aviation fuel range alkanes, Ind. Eng. Chem. Res., 59 (2020) 8601-8611.
[240] T.M. Davis, T.O. Drews, H. Ramanan, C. He, J. Dong, H. Schnablegger, M.A. Katsoulakis, E. Kokkoli, A.V. McCormick, R.L. Penn, M. Tsapatsis, Mechanistic principles of nanoparticle evolution to zeolite crystals, Nat Mater, 5 (2006) 400-408.
[241] C. Dai, A. Zhang, L. Li, K. Hou, F. Ding, J. Li, D. Mu, C. Song, M. Liu, X. Guo, Synthesis of hollow nanocubes and macroporous monoliths of silicalite-1 by alkaline treatment, Chemistry of Materials, 25 (2013) 4197-4205.
[242] N. Wang, Q. Sun, R. Bai, X. Li, G. Guo, J. Yu, In situ confinement of ultrasmall Pd clusters within nanosized silicalite-1 zeolite for highly efficient catalysis of hydrogen generation, J. Am. Chem. Soc., 138 (2016) 7484-7487.
[243] Q. Sun, N. Wang, Q. Bing, R. Si, J. Liu, R. Bai, P. Zhang, M. Jia, J. Yu, Subnanometric Hybrid Pd-$M(OH)_2$, M = Ni, Co, Clusters in Zeolites as Highly Efficient Nanocatalysts for Hydrogen Generation, Chem, 3 (2017) 477-493.
[244] D. Duprez, M. Demicheli, P. Marecot, J. Barbier, O. Ferretti, E. Ponzi, Deactivation of steam-reforming model catalysts by coke formation: I. Kinetics of the Formation of Filamentous Carbon in the Hydrogenolysis of cyclopentane on Ni/Al_2O_3 Catalysts, J. Catal., 124 (1990) 324-335.
[245] Z. Zhang, Q. Xiao, J. Gu, Effective synthesis of zeolite-encapsulated Ni nanoparticles with excellent catalytic performance for hydrogenation of CO_2 to CH_4, Dalton Trans, 49 (2020) 14771-14775.
[246] Z. Li, L. Mo, Y. Kathiraser, S. Kawi, Yolk–satellite–shell structured Ni–Yolk@Ni@SiO_2 nanocomposite: Superb catalyst toward methane CO_2 reforming

reaction, ACS Catal., 4 (2014) 1526-1536.
[247] F. Wang, L. Xu, W. Shi, Syngas production from CO_2 reforming with methane over core-shell Ni@SiO_2 catalysts, J. CO2 Util., 16 (2016) 318-327.
[248] Y. Chen, B. Qiu, Y. Liu, Y. Zhang, An active and stable nickel-based catalyst with embedment structure for CO_2 methanation, Appl. Catal. B: Environ, 269 (2020) 118801.
[249] M. Yang, H. Wu, H. Wu, C. Huang, W. Weng, M. Chen, H. Wan, Preparation and characterization of a highly dispersed and stable Ni catalyst with a microporous nanosilica support, RSC Adv., 6 (2016) 81237-81244.
[250] C. Pichas, P. Pomonis, D. Petrakis, A. Ladavos, Kinetic study of the catalytic dry reforming of CH_4 with CO_2 over $La_{2-x}Sr_xNiO_4$ perovskite-type oxides, Appl. Catal., A-Gen, 386 (2010) 116-123.
[251] H. Chen, Y. Shao, Y. Mu, H. Xiang, R. Zhang, Y. Chang, C. Hardacre, C. Wattanakit, Y. Jiao, X. Fan, Structured silicalite-1 encapsulated Ni catalyst supported on SiC foam for dry reforming of methane, AIChE Journal, 67 (2021) e17126.
[252] C. Wang, Y. Qiu, X. Zhang, Y. Zhang, N. Sun, Y. Zhao, Geometric design of a Ni@silica nano-capsule catalyst with superb methane dry reforming stability: enhanced confinement effect over the nickel site anchoring inside a capsule shell with an appropriate inner cavity, Catal. Sci. Technol., 8 (2018) 4877-4890.
[253] J.-H. Kim, D.J. Suh, T.-J. Park, K.-L. Kim, Effect of metal particle size on coking during CO_2 reforming of CH_4 over Ni–alumina aerogel catalysts, Appl. Catal., A-Gen, 197 (2000) 191-200.
[254] N. Joshi, S. Loganathan, Methanol synthesis from CO_2 using Ni and Cu supported Fe catalytic system: Understanding the role of nonthermal plasma surface discharge, Plasma Process Polym, (2021).
[255] W. Wu, K. Xie, D. Sun, X. Li, F. Fang, CuO/ZnO/Al_2O_3 catalyst prepared by mechanical-force-driven solid-state ion exchange and itseExcellent catalytic activity under internal cooling condition, Ind. Eng. Chem. Res., 56 (2017) 8216-8223.
[256] M.S. AlQahtani, S.D. Knecht, X. Wang, S.G. Bilén, C. Song, One-Step Low-Temperature Reduction of Sulfur Dioxide to Elemental Sulfur by Plasma-Enhanced Catalysis, ACS Catal., 10 (2020) 5272-5277.
[257] K.M. Bal, S. Huygh, A. Bogaerts, E.C. Neyts, Effect of plasma-induced surface charging on catalytic processes: application to CO_2 activation, Plasma Sources Sci. Technol., 27 (2018).
[258] A. Jafarzadeh, K.M. Bal, A. Bogaerts, E.C. Neyts, Activation of CO_2 on copper surfaces: The synergy between electric field, surface morphology, and excess electrons, J. Phys. Chem. C, 124 (2020) 6747-6755.
[259] A. Alarcón, J. Guilera, R. Soto, T. Andreu, Higher tolerance to sulfur poisoning in CO_2 methanation by the presence of CeO_{-2}, Appl. Catal. B: Environ, 263 (2020).
[260] Y. Tao, H. Kanoh, L. Abrams, K. Kaneko, Mesopore-modified zeolites: preparation, characterization, and applications, Chemical reviews, 106 (2006) 896-910.

Appendix A

A.1 GC calibration

A two-channel on-line gas chromatography (PerkinElmer Clarus 590 GC) equipped with an Elite-Carbon molecular sieve packed column (N 9303926), a thermal conductivity detector (TCD) and a flame ionisation detector (FID) was used for the analysis of the outlet gases after catalytic reaction. The GC calibration of CO_2, CH_4, CO and H_2 are listed in Table A.1.

Table A.1 GC calibration data of CO_2, CH_4, CO and H_2.

% CO_2	CO_2 peak area	% CH_4	CH_4 peak area	% CO	CO peak area	% H_2	H_2 peak area
2.5	2025396	2.5	2064606	5.11	2996253	5	3199789
5	3509833	5	3293087	15	6487202	10	6110791
10	5940962	10	5252834	26.337	9050333	30	17216969
15	8110084	15	6837514	35	110003510	50	27668007
20	10106543	20	8349702	42.22	12212864	70	37994582
25	11977017	25	9714535	52.2	14058664	90	46439468
30	13642467	30	10979014				

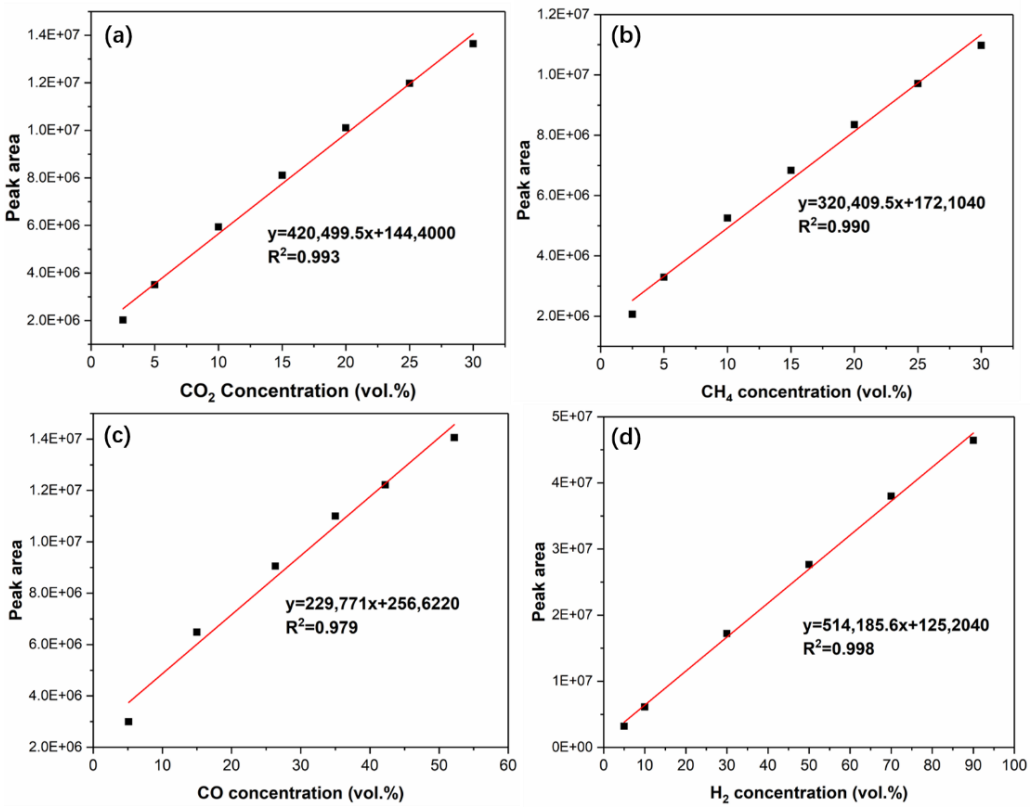

Figure A.1 GC calibration curves of (a) CO_2, (b)CH_4, (c)CO and (d) H_2.

A.2 *in situ* diffuse reflectance infrared Fourier–mass spectrometry (DRIFTS–MS)

The DRIFTS-MS system consists of a IR spectrometer and a mass spectrometer. FTIR can be used to detect a range of functional species in a sample by measuring the absorption of IR frequency. The absorptions only occur at resonant frequency, *i.e.,* the frequency of the IR radiation matches the vibrational frequency of the molecular. The main process for the FTIR analysis is: (i) the beam is emitted from the source and get through the Interferometer where the 'spectral encoding' take place; (ii) the beam reflects from the sample surface and specific adsorption occurs; and (iii) the detector measures the special signals and send the signal to the computer for interpretation. Specifically, the DRIFTS cell used in this PhD project contains a dome with ZnSe windows, collectors consisting of several mirrors, one high voltage electrode and

ground electrode (as shown in Figure 3.2). The mirrors were aligned and rotated to make sure the maximum amplitude of signal. And the high voltage electrode and ground electrode was used to produce non-thermal plasma. The system is operated by OPUS^{TM} software. DRIFTS enables the *in situ* measurement of catalyst surface species during the reaction with the gas feed passing through the catalyst mimicking the real reaction conditions.

The mass spectrometer is connected with the *in situ* system for the measurement of different molecules during reactions. The mass spectrometer consists of three parts: ion source, mass analyser and ion detector. Firstly, the molecular is electrically charged and converted into ions. After that, the ions are sorted by the analyser according to their mass-to-charge ratios. The mass spectrometer used in this PhD project is Hiden^{TM} HPR-20, which was equipped with a heated quartz inlet capillary and a quadrupole analyser. The system is operated by MASsoft software.